GENERATION, DETECTION AND MANIPULATION OF SKYRMIONS IN MAGNETIC NANOSTRUCTURES

EDITED BY: Huaiyang Yuan, Xichao Zhang and Cynthia Reichhardt
PUBLISHED IN: Frontiers in Physics

frontiers Research Topics

ISSN 1664-8714
ISBN 978-2-83250-065-1
DOI 10.3389/978-2-83250-065-1

About Frontiers

Frontiers is more than just an open-access publisher of scholarly articles: it is a pioneering approach to the world of academia, radically improving the way scholarly research is managed. The grand vision of Frontiers is a world where all people have an equal opportunity to seek, share and generate knowledge. Frontiers provides immediate and permanent online open access to all its publications, but this alone is not enough to realize our grand goals.

Frontiers Journal Series

The Frontiers Journal Series is a multi-tier and interdisciplinary set of open-access, online journals, promising a paradigm shift from the current review, selection and dissemination processes in academic publishing. All Frontiers journals are driven by researchers for researchers; therefore, they constitute a service to the scholarly community. At the same time, the Frontiers Journal Series operates on a revolutionary invention, the tiered publishing system, initially addressing specific communities of scholars, and gradually climbing up to broader public understanding, thus serving the interests of the lay society, too.

Dedication to Quality

Each Frontiers article is a landmark of the highest quality, thanks to genuinely collaborative interactions between authors and review editors, who include some of the world's best academicians. Research must be certified by peers before entering a stream of knowledge that may eventually reach the public - and shape society; therefore, Frontiers only applies the most rigorous and unbiased reviews.
Frontiers revolutionizes research publishing by freely delivering the most outstanding research, evaluated with no bias from both the academic and social point of view. By applying the most advanced information technologies, Frontiers is catapulting scholarly publishing into a new generation.

What are Frontiers Research Topics?

Frontiers Research Topics are very popular trademarks of the Frontiers Journals Series: they are collections of at least ten articles, all centered on a particular subject. With their unique mix of varied contributions from Original Research to Review Articles, Frontiers Research Topics unify the most influential researchers, the latest key findings and historical advances in a hot research area! Find out more on how to host your own Frontiers Research Topic or contribute to one as an author by contacting the Frontiers Editorial Office: frontiersin.org/about/contact

GENERATION, DETECTION AND MANIPULATION OF SKYRMIONS IN MAGNETIC NANOSTRUCTURES

Topic Editors:
Huaiyang Yuan, Utrecht University, Netherlands
Xichao Zhang, Shinshu University, Japan
Cynthia Reichhardt, Los Alamos National Laboratory (DOE), United States

Citation: Yuan, H., Zhang, X., Reichhardt, C., eds. (2022). Generation, Detection and Manipulation of Skyrmions in Magnetic Nanostructures.
Lausanne: Frontiers Media. SA doi: 10.3389/978-2-83250-065-1

Table of Contents

frontiers | Frontiers in Physics

TYPE Editorial
PUBLISHED 11 August 2022
DOI 10.3389/fphy.2022.964975

OPEN ACCESS

EDITED BY
Peter Fischer,
Berkeley Lab (DOE), United States

REVIEWED BY
Christopher Marrows,
University of Leeds, United Kingdom
Riccardo Tomasello,
Politecnico di Bari, Italy

*CORRESPONDENCE
H. Y. Yuan,
huaiyangyuan@gmail.com
X. Zhang,
zhangxichao_jsps@shinshu-u.ac.jp
C. J. O. Reichhardt,
cjrx@lanl.gov

SPECIALTY SECTION
This article was submitted to Condensed Matter Physics, a section of the journal Frontiers in Physics

RECEIVED 09 June 2022
ACCEPTED 19 July 2022
PUBLISHED 11 August 2022

CITATION
Yuan HY, Zhang X and Reichhardt CJO (2022), Editorial: Generation, detection and manipulation of skyrmions in magnetic nanostructures. *Front. Phys.* 10:964975. doi: 10.3389/fphy.2022.964975

Editorial: Generation, detection and manipulation of skyrmions in magnetic nanostructures

H. Y. Yuan[1]*, X. Zhang[2]* and C. J. O. Reichhardt[3]*

[1]Institute for Theoretical Physics, Utrecht University, Utrecht, Netherlands, [2]Department of Electrical and Computer Engineering, Shinshu University, Nagano, Japan, [3]Los Alamos National Laboratory, Theoretical Division and Center for Nonlinear Studies, Los Alamos, NM, United States

KEYWORDS

skyrmion, spintronics, spin waves, micromagnetism, pinning effect, racetrack memory

Editorial on the Research Topic
Generation, Detection and Manipulation of Skyrmions in Magnetic Nanostructures

With the rapid accumulation of data in science, technology, and social activity in the development of modern society, it is becoming increasingly urgent and important to find efficient and effective methods to store and process information with low power consumption. The skyrmion, a curling field configuration, was originally proposed by nuclear physicist Skyrme [1] and it was recently realized in a wide class of magnetic materials with chiral exchange interactions [2–4]. Due to their compact shape and small size down to a few nanometers, good thermal stability, and low driven current density, magnetic skyrmions have become promising building blocks for high-density storage and fast information processing applications. In a dozen years, this field dubbed as skyrmionics has attracted significant attention for exploring fundamental physics as well as for practical applications.

This research topic entitled "*Generation, Detection, and Manipulation of Skyrmions in Magnetic Nanostructures*" aims to address the recent developments in the field of skyrmionics. Particularly, the featured topics include the interplay of skyrmions and spin waves, pinning effects of disorder and defects on skyrmion motion, and the design of spintronic devices with information encoded in skyrmions and other magnetic solitons.

Two articles present the interplay of spin waves and magnetic skyrmions. *Guan et al.* show that an antiferromagnetic skyrmion driven by double circularly-polarized spin waves could move along the intersection of the two microwave sources. Here the skyrmion Hall effect is strongly suppressed because the effective transverse forces acting on the skyrmions generated by the left-handed and right-handed spin waves cancel each other. This theoretical proposal may help to guide skyrmion motion in a desirable trajectory. Yao et al. considered skyrmion generation by spin waves reflected from a curved surface. Usually, spin-wave energy is too small to overcome the barrier between a skyrmion and a ferromagnetic state. Here the authors carefully design a parabolic film edge such that the intensity of spin waves totally reflected from the edge is

strongly enhanced to switch the magnetization at the focal point of the system. With continuous excitation of spin waves, more magnetic energy is accumulated and finally leads to the generation of a skyrmion in a transient time. Then the microwave source is switched off and the spins relax toward a steady skyrmion configuration. This finding may enable all magnonic control of skyrmion generation and motion, which in principle works for both magnetic metals and insulators.

Pinning effects of disorder, defects and artificial pits on skyrmion dynamics in a magnetic system are also reported in this research topic. Matsumoto et al. experimentally study the magnetic skyrmions confined to surface-pit corrals with various geometries. They find that skyrmions are deformed in both shape and size under the influence of the boundaries defined by the surface-pit corrals. Deformed skyrmions with opposite polarities may coexist inside a corral even in the absence of external fields. These experimental findings may provide guidance to confine and deform skyrmions in a desirable way. Employing a particle-based approach, Reichhardt and Reichhardt investigate the dynamics of a driven skyrmion interacting with an array of other skyrmions and quenched disorder in a magnetic thin film. In particular, the authors find that the quenched disorder could weaken the drag effect of the skyrmion arrays and thus increase the skyrmion velocity. The nature and amount of noise of skyrmion velocity fluctuations are analysed in detail. These results deepen our understanding of skyrmion dynamics in disordered films, while the essential results may be relevant for other particle-based systems. Wan et al. show that the exchange and fourth-order magneto-crystalline anisotropies can deform a skyrmion lattice and further induce pinning effects to rotate the skyrmion lattice. These findings complement and deepen our understanding on the pinning effects of skyrmions [5–8].

Two articles study potential applications of magnetic skyrmions. Hoffmann et al. theoretically show that a bound state of a skyrmion-antiskyrmion pair could exist in a so-called rank-one magnetic material, where the Dzyaloshinskii-Moriya interaction is reduced to only one non-zero component. This finding suggests that binary information (“0” and “1”) carried by the skyrmion and antiskyrmion pair could form a stable sequence in a magnetic racetrack. By applying a spin current with proper spin polarization, the authors further demonstrate that a skyrmion-antiskyrmion sequence could be collectively displaced along a desired direction without showing the skyrmion Hall effect. The distance of adjacent skyrmions is kept unchanged during propagation because the skyrmion and the antiskyrmion move in step. This finding provides a promising design for skyrmion-based racetrack memory, where the information is coded in the types of magnetic solitons [9], instead of in the appearance or absence of magnetic solitons. It also complements the traditional proposals of magnetic racetrack memory based on magnetic domain walls [10]. A perspective article by Zivieri discusses information storage and coding based on the information entropy of skyrmions.

Besides magnetic skyrmions, a few more magnetic structures are also studied. Chen et al. report an exotic Néel-type kink spin texture stabilized in the corners of square-shaped nanostructures and describe how these kinks can be created, annihilated, and reversed in polarity by spin-polarized currents. Chen et al. observe two types of domains in the kagome metal $DyMn_6Sn_6$, consisting of a type-I domain with a belt structure and a type-II domain with a complex stripe structure. As the temperature changes, the type-II domain may transform into the type-I domain and even disappear, and vice versa. This finding provides a fresh insight into the spin texture in kagome crystals and may further help to understand the relation between novel electronic states and magnetic states in these materials.

In conclusion, this research topic provides a timely update on the recent advances in skyrmion physics and its applications in spintronic devices. We hope that the collection of works will not only advance our understanding of the creation, dynamics, and manipulation of magnetic skyrmions, but will also inspire more interest from the community of science, engineering, and general audience to accelerate the development of skyrmionics.

Author contributions

HY provided the first draft of the editorial. XZ and CR reviewed, revised and finalized the article.

Funding

HY acknowledges the European Union’s Horizon 2020 research and innovation program under Marie Skłodowska-Curie Grant Agreement SPINCAT No. 101018193. XZ was a JSPS International Research Fellow supported by JSPS KAKENHI (Grant No. JP20F20363).

Acknowledgments

We sincerely thank all the authors, reviewers, Editors, and Frontiers editorial staff for their excellent work to make this research topic a reality.

Conflict of interest

The authors declare that the research was conducted in the absence of any commercial or financial relationships that could be construed as a potential conflict of interest.

Publisher's note

References

1. Skyrme THR. A unified field theory of mesons and baryons. *Nucl Phys* (1962) 31:556–69. doi:10.1016/0029-5582(62)90775-7

2. Rößler UK. Spontaneous skyrmion ground states in magnetic metals. *Nature* (2006) 442:797–801. doi:10.1038/nature05056

3. Muhlbauer S, Binz B, Jonietz F, Pfleiderer C, Rosch A, Neubauer A, et al. Skyrmion lattice in a chiral magnet. *Science* (2009) 323:915–9. doi:10.1126/science.1166767

4. Yu XZ, Onose Y, Kanazawa N, Park JH, Han JH, Matsui Y, et al. Real-space observation of a two-dimensional skyrmion crystal. *Nature* (2010) 465:901–4. doi:10.1038/nature09124

5. Iwasaki J, Mochizuki M, Nagaosa. Universal current-velocity relation of skyrmion motion in chiral magnets. *Nat Commun* (2013) 4:1463. doi:10.1038/ncomms2442

6. Kim J-V, Yoo M-W. Current-driven skyrmion dynamics in disordered films. *Appl Phys Lett* (2017) 110:132404. doi:10.1063/1.4979316

7. Gong X, Yuan HY, Wang XR. Current-driven skyrmion motion in granular films. *Phys Rev B* (2020) 101:064421. doi:10.1103/PhysRevB.101.064421

8. Gruber R, Zazvorka J, Brems MA, Rodrigues DR, Dohi T, Kerber N, et al. Skyrmion pinning energetics in thin film systems. *Nat Commun* (2020) 13:3144. doi:10.1038/s41467-022-30743-4

9. Mandru A-O, Yildirim O, Tomasello R, Heistracher P, Penedo M, Giordano A, et al. Coexistence of distinct skyrmion phases observed in hybrid ferromagnetic/ferrimagnetic multilayers. *Nat Commun* (2020) 11:6365. doi:10.1038/s41467-020-20025-2

10. Parkin SSP, Hayashi M, Thomas L. Magnetic domain-wall racetrack memory. *Science* (2008) 320:190–4. doi:10.1126/science.1145799

frontiers in Physics

ORIGINAL RESEARCH
published: 09 June 2021
doi: 10.3389/fphy.2021.685510

Magnetic Domain Structure in Ferromagnetic Kagome Metal $DyMn_6Sn_6$

Zhaohui Chen[1,2†], Miao Li[1,3†], Caixing Liu[1,2], Zongwei Ma[1], Yuyan Han[1], Jianhua Gao[1], Wensen Wei[1], Zhigao Sheng[1] and Haifeng Du[1,4]*

[1]Anhui Key Laboratory of Condensed Matter Physics at Extreme Conditions, High Magnetic Field Laboratory, Hefei Institutes of Physical Science, Chinese Academy of Sciences, Hefei, China, [2]University of Science and Technology of China, Hefei, China, [3]School of Physics and Electronic Information, Huaibei Normal University, Huaibei, China, [4]Institutes of Physical Science and Information Technology, Anhui University, Hefei, China

Two types of magnetic domains, that is, type-I domain belt domain and type-II new stripe domain, are observed in a kagome metal $DyMn_6Sn_6$ by microscopic magneto-optic Kerr imaging technique. From 255 to 235 K, the spin reorientation is observed directly in $DyMn_6Sn_6$. We analyze the structure of two types of domains through brightness distribution of the images. The type-II domain exists from 235 to 160 K by zero-field cooling (ZFC). At the same time, type-I domain and type-II domain coexist and transform into each other with variation of temperature. Type-II domains can easily transform into type-I domains when the temperature and magnetic field changes, and this process is irreversible. These results demonstrate that the type-I domain is more stable than the type-II domain. The phase diagram of magnetic domains in $DyMn_6Sn_6$ is obtained.

Keywords: kagome metal, magnetic domain, microscopic magneto-optical kerr effect technique, perpendicular anisotropy, spin reorientation

OPEN ACCESS

Edited by:
Xichao Zhang,
Shinshu University, Japan

Reviewed by:
Shilei Zhang,
ShanghaiTech University, China
Farhad Sattari,
University of Mohaghegh Ardabili, Iran

***Correspondence:**
Zhaohui Chen
czh177@mail.ustc.edu.cn

†These authors have contributed equally to this work and share first authorship

Specialty section:
This article was submitted to Condensed Matter Physics, a section of the journal Frontiers in Physics

Received: *25 March 2021*
Accepted: *17 May 2021*
Published: *09 June 2021*

Citation:
Chen Z, Li M, Liu C, Ma Z, Han Y, Gao J, Wei W, Sheng Z and Du H (2021) Magnetic Domain Structure in Ferromagnetic Kagome Metal $DyMn_6Sn_6$. Front. Phys. 9:685510. doi: 10.3389/fphy.2021.685510

INTRODUCTION

Novel magnetic domain structure, which is observed in various magnetic materials, is the consequence of competition among various magnetic interactions that are executed on the materials both from intrinsic and extrinsic circumstances [1–4]. In particular, the intrinsic magnetic interactions that occur in materials with kagome crystal is of great complexity and results in complicated magnetic domains, for example, a frustrated circumstance would occur and lead to noncollinear magnetic spin structure [5–10]. Recently, topologically nontrivial skyrmions have been predicted to generate in kagome crystal when the crystal owns both Heisenberg and Dzyaloshinskii–Moriya interactions [11–13], and finally, the skyrmion bubbles are experimented and reported in Fe_3Sn_2 without any Dzyaloshinskii–Moriya interaction [14–17], showing that the uniaxial magnetic anisotropy in kagome crystal can play a vital role in stabilized novel spin structure. On the other hand, the magnetic and electronic structures in kagome crystals are highly entangled, making them show both fruitful spin-orbit and electronic corrected effects. Consequently, the conduction electrons show both an intrinsic anomalous Hall effect which links to reciprocal band structure and a topological Hall effect which related to real space nontrivial spin textures [18–22]. The exotic phenomena are confirmed in many kagome crystals like Fe_3Sn_2 [23, 24], $Co_3Sn_2S_2$ [25, 26], YMn_6Sn_6 [27], etc. Evenly, the kagome lattices may also host Dirac electronic states, which leads to topological and Chern insulating phases, which have been confirmed both by theoretical and experimental investigation on Fe_3Sn_2 [23, 24] and $TbMn_6Sn_6$ [28]. Recently, not only $TbMn_6Sn_6$ but

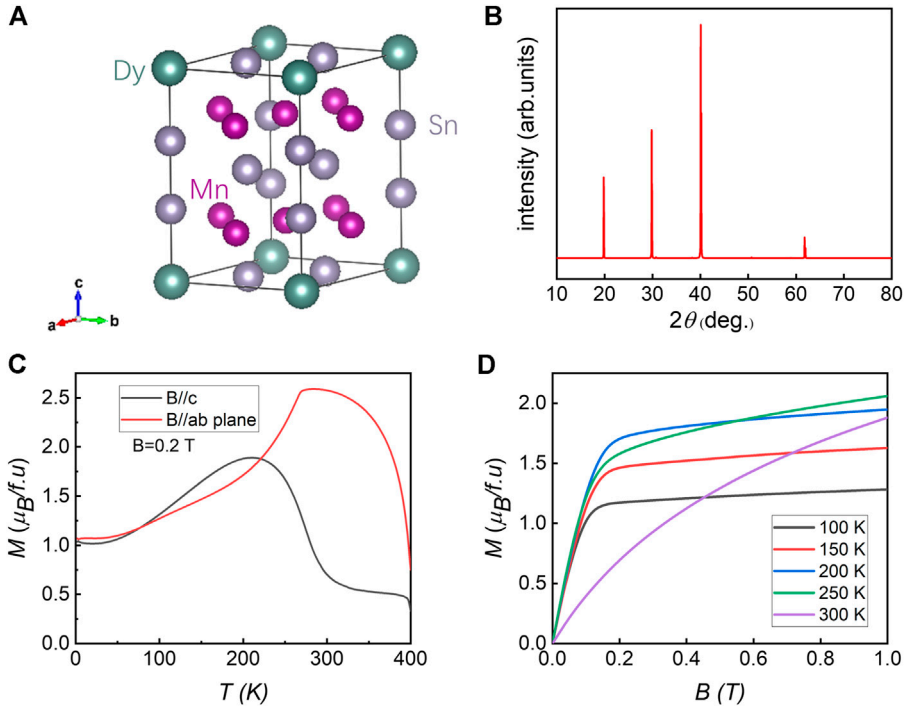

FIGURE 1 | (A) Crystal structure of $DyMn_6Sn_6$. **(B)** XRD pattern of a $DyMn_6Sn_6$ single crystal. **(C)** Temperature-dependent magnetization (M–T) curve with *B//c* and *B//ab* plane. **(D)** Magnetic field-dependent magnetization (M–H) curve with *B//c*.

also RMn_6Sn_6 (R = Y, Dy, Ho, etc.) have been reported to show a very large anomalous Hall effect and a large topological Hall effect [27, 29, 30], stimulating vast investigations in the field and materials of kagome lattices.

$DyMn_6Sn_6$ is a member of kagome metal RMn_6Sn_6 family (R = rare element) which consists of a two-dimensional (2D) Mn layer kagome lattice. It has a hexagonal $HfFe_6Ge_6$-type structure with *P6/mmm* space group [31]. It has a ferrimagnetic behavior below T_C = 393 K with Dy and Mn sublattices ordering simultaneously due to the strong Mn-Dy antiferromagnetic coupling [32]. Neutron diffraction study shows that above room temperature, it possesses a planar anisotropy for the Mn sublattice but with a negative value for Dy, resulting in a partial spin reorientation below T_t ~ 240 K [31]. Considering both the spontaneous magnetization with kagome lattice in $DyMn_6Sn_6$, a conical arrangement of the spin magnetic moment is inferred in the previous report. Recently, the transport, and therefore the electronic structure, has been intensively studied to uncover the possible Dirac and Chern insulating state nature [28]; however, the directional observation of the spin texture has not been reported. The relationship between the complex electronic correlated novel state and the novel spin structure, in other words, the link between the degrees of charge and spin for the electrons in kagome lattices, is highly elusive.

Microscopic magneto-optical Kerr effect (micro-MOKE), which refers to the polarization rotation of a linearly polarized light when reflected by magnetized materials, is widely used to map the magnetic domain patterns and magnetic phase transitions in various materials [33–35]. In this study, the magnetic domain in $DyMn_6Sn_6$ crystal and its evolution with temperature and magnetic field was investigated using the micro-MOKE imaging technique. We evidenced that the spin reorientation occurs between 255 and 235 K. In addition, we observed two types of magnetic domain structures that coexist and compete with each other simultaneously in $DyMn_6Sn_6$. Our results can provide a platform to understand the novel magnetic domain structure in the kagome metal family.

MATERIALS AND METHODS

$DyMn_6Sn_6$ single crystals were grown by the flux method [36]. The constituent elements Dy, Mn, and Sn of better than 3N purity were weighed in the mole ratio of Dy:Mn:Sn = 1:6:30. The sample was placed in an alumina crucible and sealed in an evacuated silica ampoule. The ampoule was heated to 1,273 K and kept at the temperature for 24 h, and then slowly cooled to 1,223 K. It was heated again up to 1,263 K and finally cooled down slowly to 873 K at a rate of 6 K/h. The ampoule was quickly removed from the furnace. Sn flux was removed using a centrifuge. After cooling down to room temperature, the ampoule was broken by tools, and plate-like $DyMn_6Sn_6$ single crystals of about $2 \times 2 \times 0.5\ mm^3$ in size were obtained from the alumina crucible. The quality of the crystals was checked by X-ray diffraction (XRD). Magnetization was carried out using the quantum design magnetic property measurement system (MPMS-XL5) for 1.8 K < T < 400 K and the H < 7 T.

The crystal was exfoliated using Torr seal glue to get smooth sample surface. Then micro-MOKE images of the surface

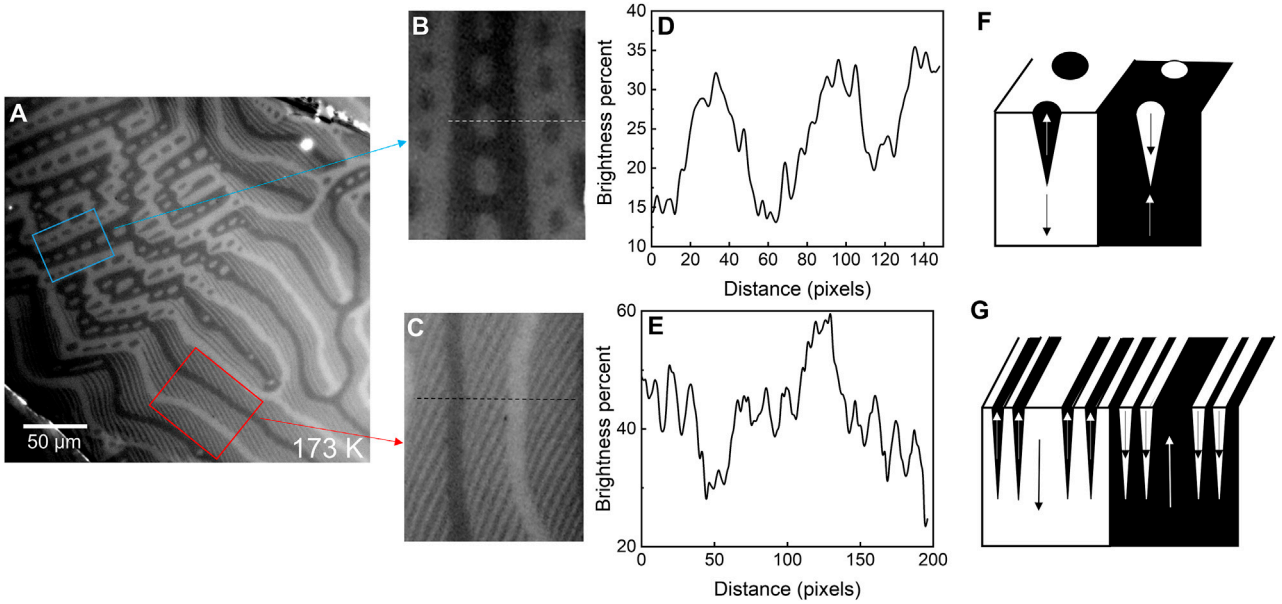

FIGURE 2 | (A) Represented image of the magnetic domains of $DyMn_6Sn_6$ crystal at 173 K. **(B)** Type-I domains in $DyMn_6Sn_6$. **(C)** Type-II domains in $DyMn_6Sn_6$. **(D,E)** Corresponding map of the brightness distribution in two types of magnetic domains. **(F,G)** Corresponding sketch map of two types of magnetic domains structure.

magnetic domains were obtained at several temperatures using a polarizing microscope (Olympus, BX53M) equipped with a homemade option which could provide low temperature circumstances with liquid nitrogen. The magnetic fields executed on the sample during measurements were generated by calibrated permanent magnets.

RESULTS AND DISCUSSIONS

Figure 1A shows the crystal structure of $DyMn_6Sn_6$. It has an hexagonal $HfFe_6Ge_6$-type structure with *P6/mmm* space group with two-dimensional (2D) Mn layer kagome lattice. **Figure 1B** shows the XRD pattern of a $DyMn_6Sn_6$ single crystal. The $DyMn_6Sn_6$ single crystal is high quality due to the very sharp diffraction peaks. Temperature-dependent magnetization (*M–T*) curves with *B*//*c* and *B*//*ab* plane and magnetic field-dependent magnetization (*M–H*) curves with *B*//*c* are shown in **Figure 1C,D**, respectively. There is an obvious spin reorientation transition in $DyMn_6Sn_6$, the same as that in $TbMn_6Sn_6$ and $HoMn_6Sn_6$ [32]. The curve at 300 K in **Figure 1D** is obviously different from the curve at 250 K. It means that the spin reorientation happens between 250 and 300 K.

In order to understand the material behavior of magnetic materials, the direct visualization of the domain structure is required. **Figure 2A** is a MOKE image of the magnetic domain of $DyMn_6Sn_6$ crystal at 173 K. In **Figure 2A**, we discover that there are two types of magnetic domains in $DyMn_6Sn_6$. Type-I domain is the belt domain, while type-II domain is the new stripe domain with complex construction, as shown in **Figure 2B,C**, respectively. The type-I domain shows that there are many white elliptic domains in the black belt domains. The type-II domain shows that the main part is a wide and long domain and the other part is a thin, short domain with the same direction. The thin, short domain locates in the middle of the black main domain and the white main domain. **Figure 2D,E** shows the line profile of the brightness distribution as marked by the dotted lines in **Figure 2B,C**. The intensity of black elliptic domains is stronger than the black belt domains in **Figure 2D**. Inferred from the theory of two-phase branching [37], the elliptic domains could be considered as floating on the belt domains, as shown in **Figure 2F**. Similar to the type-I domains, the intensity of black stripe domains is stronger than the black main domains in **Figure 2E**. It is quite likely that the stripe domains float on the main domains as shown in **Figure 2G**. From the brightness of the magnetic domains, the magnetic structure in $DyMn_6Sn_6$ is reasonably clear, where the sketch map of two types of magnetic domain structures are shown in **Figure 2F,G**, respectively.

From the above observation, one can note that for $DyMn_6Sn_6$, the domain shows refinement structure, reminiscent of the domain branching phenomenon in very large crystals with strongly misoriented surfaces. For $DyMn_6Sn_6$, it shows three-dimensional branching, as shown in **Figure 2**. Based on the theory of two-phase branching, the refinement structure that occurs in $DyMn_6Sn_6$ could be understood when one takes the uniaxial magnetic anisotropy. Usually, the theory of two-phase branching consists of three energy terms [37]: 1) the wall energy that increases toward the surface with increasing wall density, 2) the generalized closure energy depending only on the domain width of the last generation, and 3) the energy connected with the internal stray fields. It is rather complicated and difficult to

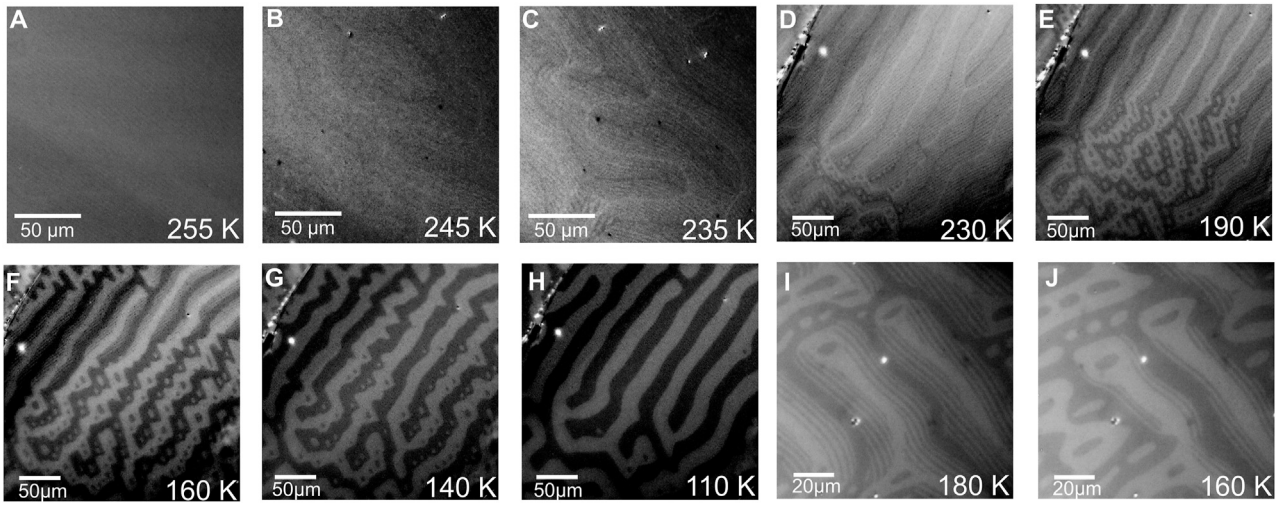

FIGURE 3 | (A–C) Appearance of the magnetic domain of $DyMn_6Sn_6$ crystal from 255 to 235 K. **(D–H)** Magnetic domains of $DyMn_6Sn_6$ crystal from 230 to 110 K. **(D–G)** Type-II domains transform into type-I domains from 230 to 140 K. **(I,J)** Type-II domains of $DyMn_6Sn_6$ crystal from 180 to 160 K.

extract explicit calculation, especially for the three-dimensional structure, as in the case of $DyMn_6Sn_6$. However, the theory applies to both Co- and Dy-modified NdFeB crystals with thickness of about several hundred micrometers. The theory and experimental result confirmed that the occurrence of domain branching has the relationship to both sample thickness and strong enough uniaxial magnetic anisotropy. Based on these previous results, we propose that the branching phenomenon observed in $DyMn_6Sn_6$ has the same mechanism with Dy-modified NdFeB, since $DyMn_6Sn_6$ is a strong uniaxial ferromagnet.

Figure 3 displays the magnetic domain structure as a function of temperature. From 255 to 235 K, the spin reorientation (SR) is observed and shown in **Figure 3A–C**. The magnetic domain is not clear until the temperature decreases to 245 K. When the temperature is below 245 K, the domain appears but is misty. It becomes obvious when the temperature continues decreasing. It is also shown that the spin reorientation in $DyMn_6Sn_6$ occurs gradually.

For investigating these two types of domains, we study the magnetic domains in $DyMn_6Sn_6$ with the temperature decrease. In **Figure 3D–G**, we observe the coexistence of two types of magnetic domains from 230 to 140 K. At the beginning, the type-II domains are in the vast majority at 230 K. When the temperature keeps decreasing, the type-II domains transform into type-I domains. The type-I domain also changes, in which the white elliptic domain in the black belt domain becomes little and disappears with the temperature decrease. At 140 K, all the type-II domains disappear and only a few white elliptic domains are left. The white elliptic domains disappear and the type-I domain does not show any edges nor branches at 110 K. As the temperature continues decreasing, the magnetic domain does not change any more. As shown above, the magnetic domain structure at 110 K is a kind of stripe domain due to the strong perpendicular anisotropy. At the beginning, the type-II domains are in the vast majority due to the weak perpendicular anisotropy. When the temperature decreases, the perpendicular anisotropy becomes strong making the magnetic moment apt to move along the perpendicular plane. We find that type-I domain is less affected than the type-II domain. The domains floating on other domains may reverse under the influence of the perpendicular anisotropy. It is obvious that the type-II domain is more sensitive to the perpendicular anisotropy than that of type-I domain. Consequently, the type-II domains transform into type-I domain when the temperature continues decreasing. The type-I domain also changes because of the perpendicular anisotropy. At last, the perpendicular anisotropy only makes the stripe domain left. The stripe domain is affected by the demagnetizing field.

For investigating the type-II domain in detail, from 180 to 160 K, the structure of the type-II domains is observed. In **Figure 3I,J**, we find that our description of the type-II domains is the same as the domain in **Figure 2A**. It is shown that the structure of the type-II domains changes with temperature. As the temperature decreases, the main domain becomes wider, but the other part keeps the same width. The temperature changes the number of the other part domain. The lower the temperature is, the lower the number is. It is the main reason that the perpendicular anisotropy is enhanced as the temperature decreases. The perpendicular anisotropy can make the magnetic moment apt to move along the perpendicular plane. So, the main domain becomes wider and the number of the other stripe domains decreases. The type-I domain is a kind of manifestation of the branch domain at low temperature [37]. As the temperature increases, the branch structure grows on the type-I domain. The physics behind the domain transformation is the temperature dependence of magnetic anisotropy, especially in kagome lattice with strong uniaxial anisotropy. When the temperature decreases, the coefficients for anisotropy changes,

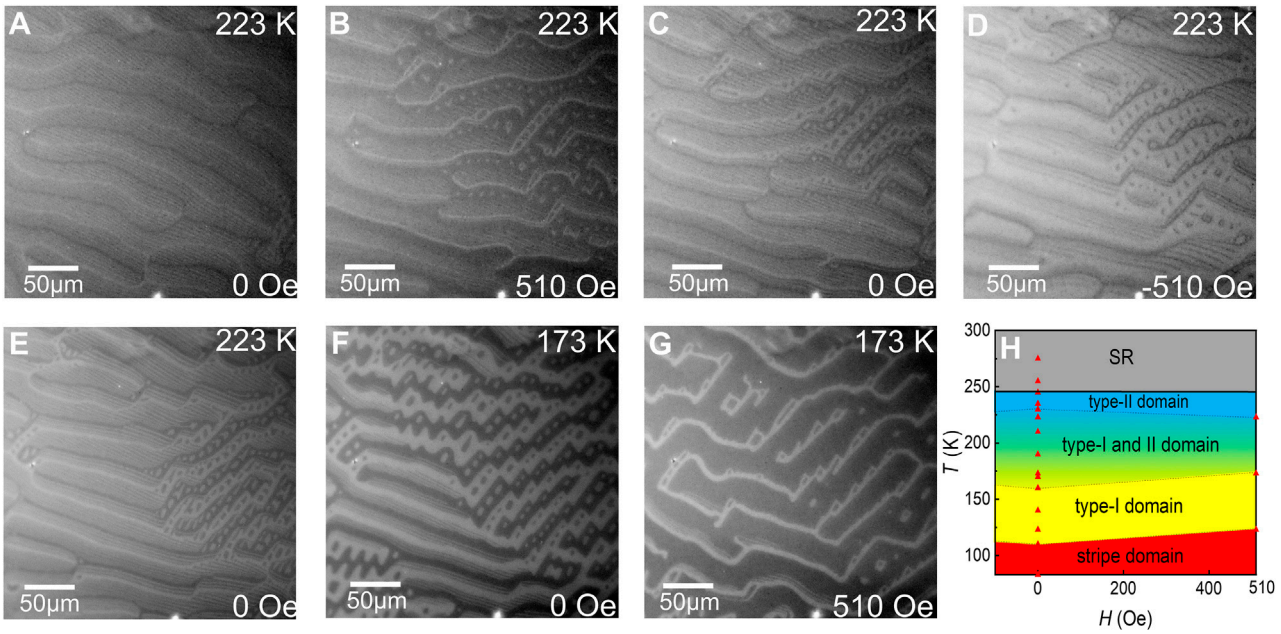

FIGURE 4 | (A–E) Magnetic domains of $DyMn_6Sn_6$ with varying magnetic field at 223 K. **(F–G)** Magnetic domains of $DyMn_6Sn_6$ with varying magnetic field at 173 K. **(H)** Phase diagram of magnetic domain distribution in $DyMn_6Sn_6$.

leading to spin reorientation and domain variations, as shown in **Figure 3**.

To make sense of the domains clearly, we perform the experiment with the various magnetic fields at two representative temperatures, 223 and 173 K, as shown in **Figure 4**. The variable magnetic field of 0 or 510 Oe pointing up (+) or down (−) was applied by a permanent magnet. At 223 K, type-I domains sparsely appear while type-II domains are in the vast majority. One side of the white stripe domains flip to the black domain with the magnetic field increase and the other side of space between the white stripe domains becomes wider. With the magnetic field on, some of the type-II domains transform into the type-I domains. When the magnetic field is removed, the domain recovers. However, the type-I domain to the type-II domain transform does not recover, showing very strong irreversible effect. With the magnetic field reverse, a similar phenomenon happens. One side of the black stripe domains flips to the white domains and the other side of space between the black stripe domains becomes wider. Some type-II domains transform into type-I domain and do not recover without magnetic field assistance. At 173 K, we discover that the type-II domains in **Figure 4F** are far less than the type-II domains in **Figure 2A**. This is because the image in **Figure 2A** is obtained during zero field cooling (ZFC) process, but the image in **Figure 4F** is obtained during cooling process from the state in **Figure 4E**. Both the magnetic field and the temperature can make the type-II domain transform into type-I domain. At 173 K, we observe the same phenomenon. After a loop in the magnetic field, the area of the type-II domain decreases. From the above results, we can conclude that the type-I domain is more stable than the type-II domain.

The phase diagram of magnetic domains is obtained in **Figure 4H**. At T > 235 K, the spin reorientation happens. There is no domain in the gray area. Type-II domain appears, as the temperature decreases, as shown in the light blue part. Type-II domain transforms into type-I domain under the influence of temperature and magnetic field. Type-I domain is shown in the yellow part. Type-II domain and type-I domain coexist locating at the intermediate region, as shown in the figure. As the temperature continues decreasing, only stripe domains are left, as marked by red color in the figure.

CONCLUSION

In summary, the magnetic domains in kagome lattice metal $DyMn_6Sn_6$ are observed using the micro-MOKE technique. Spin reorientation in $DyMn_6Sn_6$ is observed directly by the micro-MOKE technique from 255 to 235 K. There are two types of magnetic domains in $DyMn_6Sn_6$. Type-I domain is the belt domain. Type-II domain is the new stripe domain. The type-II domain exists from 160–235 K (ZFC). We analyze the structure of two types of domains. As the temperature decreases, the perpendicular anisotropy becomes strong, making the type-II domain transform into the type-I domain and even disappear. With a varying magnetic field experiment, we find that the type-II domain is less stable than the type-I domain. The phase diagram of magnetic domains in $DyMn_6Sn_6$ is obtained. However, the formation mechanism of new stripe domain in $DyMn_6Sn_6$ needs to be further investigated in the future.

DATA AVAILABILITY STATEMENT

The original contributions presented in the study are included in the article/Supplementary Material, and further inquiries can be directed to the corresponding author.

AUTHOR CONTRIBUTIONS

ZC and WW grew the single crystal and wrote the paper. YH and ZC did the experiment about the magnetic curves and corrected the paper. ZC, ML, and CL did the experiment about micro-MOKE. ZM and JG corrected the paper and discussed. HD and ZS provided the funding and supervised the research. All authors contributed to the article and approved the submitted version.

FUNDING

This work was supported by the Natural Science Foundation of China (Grants No. 11904368) and the Natural Science Foundation of Anhui Province (Grants No. 2008085QA32).

REFERENCES

1. Takagi R, White JS, Hayami S, Arita R, Honecker D, Rønnow HM, et al. Multiple-q Noncollinear Magnetism in an Itinerant Hexagonal Magnet. *Sci Adv* (2018) 4:eaau3402. doi:10.1126/sciadv.aau3402
2. Nagaosa N, and Tokura Y. Topological Properties and Dynamics of Magnetic Skyrmions. *Nat Nanotech* (2013) 8:899–911. doi:10.1038/NNANO.2013.243
3. Nayak AK, Kumar V, Ma T, Werner P, Pippel E, Sahoo R, et al. Magnetic Antiskyrmions above Room Temperature in Tetragonal Heusler Materials. *Nature* (2017) 548:561–6. doi:10.1038/nature23466
4. Liu YZ, and Zang JD. Overview and Outlook of Magnetic Skyrmions. *Acta Physica Sinica* (2018) 67:131201. doi:10.7498/aps.67.20180619
5. Fert A, Cros V, and Sampaio J. Skyrmions on the Track. *Nat Nanotech* (2013) 8:152–6. doi:10.1038/nnano.2013.29
6. Balents L. Spin Liquids in Frustrated Magnets. *Nature* (2010) 464:199–208. doi:10.1038/nature08917
7. Jo G-B, Guzman J, Thomas CK, Hosur P, Vishwanath A, and Stamper-Kurn DM. Ultracold Atoms in a Tunable Optical Kagome Lattice. *Phys Rev Lett* (2012) 108:045305. doi:10.1103/PhysRevLett.108.045305
8. Zhou Y, Kanoda K, and Ng T-K. Quantum Spin Liquid States. *Rev Mod Phys* (2017) 89:89. doi:10.1103/RevModPhys.89.025003
9. Han T-H, Helton JS, Chu S, Nocera DG, Rodriguez-Rivera JA, Broholm C, et al. Fractionalized Excitations in the Spin-Liquid State of a Kagome-Lattice Antiferromagnet. *Nature* (2012) 492:406–10. doi:10.1038/nature11659
10. Li Y, Che HL, and Sun XF. Syntheses and Magnetic Properties of $RE_3Sb_3Zn_2O_{(14)}$(RE=Tb,Dy and Ho) with a New 2D Kagome Structure. *Chin J Rare Met* (2020) 44(3):333–6. doi:10.13373/j.cnki.cjrm.XY18110010.html
11. Liu C, Zang Y, Ruan W, Gong Y, He K, Ma X, et al. Dimensional Crossover-Induced Topological Hall Effect in a Magnetic Topological Insulator. *Phys Rev Lett* (2017) 119:176809. doi:10.1103/PhysRevLett.119.176809
12. Kurumaji T, Nakajima T, Hirschberger M, Kikkawa A, Yamasaki Y, Sagayama H, et al. Skyrmion Lattice with a Giant Topological Hall Effect in a Frustrated Triangular-Lattice Magnet. *Science* (2019) 365:914–8. doi:10.1126/science.aau0968
13. Batista CD, Lin S-Z, Hayami S, and Kamiya Y. Frustration and Chiral Orderings in Correlated Electron Systems. *Rep Prog Phys* (2016) 79:084504. doi:10.1088/0034-4885/79/8/084504
14. Hou Z, Ren W, Ding B, Xu G, Wang Y, Yang B, et al. Observation of Various and Spontaneous Magnetic Skyrmionic Bubbles at Room Temperature in a Frustrated Kagome Magnet with Uniaxial Magnetic Anisotropy. *Adv Mater* (2017) 29:1701144. doi:10.1002/adma.201701144
15. Tang J, Wu Y, Kong L, Wang W, Chen Y, Wang Y, et al. Two-dimensional Characterization of Three-Dimensional Magnetic Bubbles in Fe3Sn2 Nanostructures. *Natl Sci Rev* (2020) nwaa200. doi:10.1093/nsr/nwaa200
16. Tang J, Kong L, Wu Y, Wang W, Chen Y, Wang Y, et al. Target Bubbles in Fe3Sn2 Nanodisks at Zero Magnetic Field. *ACS Nano* (2020) 14:10986–92. doi:10.1021/acsnano.0c04036
17. Heritage K, Bryant B, Fenner LA, Wills AS, Aeppli G, and Soh YA. Images of a First-Order Spin-Reorientation Phase Transition in a Metallic Kagome Ferromagnet. *Adv Funct Mater* (2020) 30:1909163. doi:10.1002/adfm.201909163
18. Xu G, Lian B, and Zhang S-C. Intrinsic Quantum Anomalous Hall Effect in the Kagome LatticeCs2LiMn3F12. *Phys Rev Lett* (2015) 115:186802. doi:10.1103/PhysRevLett.115.186802
19. Mazin II, Jeschke HO, Lechermann F, Lee H, Fink M, Thomale R, et al. Theoretical Prediction of a Strongly Correlated Dirac Metal. *Nat Commun* (2014) 5:4261. doi:10.1038/ncomms5261
20. Tang E, Mei J-W, and Wen X-G. High-temperature Fractional Quantum Hall States. *Phys Rev Lett* (2011) 106:236802. doi:10.1103/PhysRevLett.106.236802
21. Kida T, Fenner LA, Dee AA, Terasaki I, Hagiwara M, and Wills AS. The Giant Anomalous Hall Effect in the Ferromagnet Fe3Sn2-A Frustrated Kagome Metal. *J Phys Condens Matter* (2011) 23:112205. doi:10.1088/0953-8984/23/11/112205
22. Wang X-L, Liu Y, and Chen X. Tailoring Magnetostriction and Magnetic Domains of -oriented Fe80Ga16Al4 alloy by Magnetic Field Annealing. *Rare Met* (2020) 40:563–9. doi:10.1007/s12598-020-01590-3
23. Baidya S, Mallik AV, Bhattacharjee S, and Saha-Dasgupta T. Interplay of Magnetism and Topological Superconductivity in Bilayer Kagome Metals. *Phys Rev Lett* (2020) 125:026401. doi:10.1103/PhysRevLett.125.026401
24. Ye L, Kang M, Liu J, von Cube F, Wicker CR, Suzuki T, et al. Massive Dirac Fermions in a Ferromagnetic Kagome Metal. *Nature* (2018) 555:638–42. doi:10.1038/nature25987
25. Morali N, Batabyal R, Nag PK, Liu E, Xu Q, Sun Y, et al. Fermi-arc Diversity on Surface Terminations of the Magnetic Weyl Semimetal Co3Sn2S2. *Science* (2019) 365:1286–91. doi:10.1126/science.aav2334
26. Jiao L, Xu Q, Cheon Y, Sun Y, Felser C, Liu E, et al. Signatures for Half-Metallicity and Nontrivial Surface States in the Kagome Lattice Weyl Semimetal Co3Sn2S2. *Phys Rev B* (2019) 99:245158. doi:10.1103/PhysRevB.99.245158
27. Zhang H, Feng X, Heitmann T, Kolesnikov AI, Stone MB, Lu Y-M, et al. Topological Magnon Bands in a Room-Temperature Kagome Magnet. *Phys Rev B* (2020) 101:100405. doi:10.1103/PhysRevB.101.100405
28. Yin J-X, Ma W, Cochran TA, Xu X, Zhang SS, Tien H-J, et al. Quantum-limit Chern Topological Magnetism in TbMn6Sn6. *Nature* (2020) 583:533–6. doi:10.1038/s41586-020-2482-7
29. Asaba T, Thomas SM, Curtis M, Thompson JD, Bauer ED, and Ronning F Anomalous Hall Effect in the Kagome Ferrimagnet GdMn6Sn6. *Phys Rev B* (2020) 101:174415. doi:10.1103/PhysRevB.101.174415
30. Ma W, Xu X, Yin JX, Zhou H, Huang Y, Hasan MZ, et al. *Rare Earth Engineering in RMn_6Sn_6 Topological Kagome Magnets*. arXiv:2007.09913.
31. Fruchart D, Venturini G, and Malaman B. Incommensurate MagneticStructures of RMn_6Sn_6(R = Sc, Y, Lu) Compounds from Neutron Diffraction Study. *J Appl Phys* (1996) 236:102–10. doi:10.1016/0925-8388(95)01998-7
32. Clatterbuck DM, and Gschneidner KA., Jr. Magnetic Properties of RMn6Sn6 (R=Tb, Ho, Er, Tm, Lu) Single Crystals. *J Magnetism Magn Mater* (1999) 207:78–94. doi:10.1016/s0304-8853(99)00571-5
33. McCord J. Progress in Magnetic Domain Observation by Advanced Magneto-Optical Microscopy. *J Phys D Appl Phys* (2015) 48:333001. doi:10.1088/0022-3727/48/33/333001

34. Kustov M, Grechishkin R, Gusev M, Gasanov O, and McCord J. A Novel Scheme of Thermographic Microimaging Using Pyro-Magneto-Optical Indicator Films. *Adv Mater* (2015) 27:5017–22. doi:10.1002/adma.201501859
35. Stupakiewicz A, Chizhik A, Tekielak M, Zhukov A, Gonzalez J, and Maziewski A Direct Imaging of the Magnetization Reversal in Microwires Using All-MOKE Microscopy. *Rev Scientific Instr* (2014) 85:103702. doi:10.1063/1.4896758
36. Kimura S, Matsuo A, Yoshii S, Kindo K, Zhang L, Brück E, et al. High-field Magnetization of RMn6Sn6 Compounds with R=Gd, Tb, Dy and Ho. *J Alloys Compounds* (2006) 408-412:169–72. doi:10.1016/j.jallcom.2005.04.087
37. Hubert A, and Schäfer R. *Magnetic Domains: The Analysis of Magnetic Microstructures*. Berlin: Springer-Verlag Press (1998)

Conflict of Interest: The authors declare that the research was conducted in the absence of any commercial or financial relationships that could be construed as a potential conflict of interest.

frontiers in Physics

ORIGINAL RESEARCH
published: 21 June 2021
doi: 10.3389/fphy.2021.684346

Pinning Effects of Exchange and Magnetocrystalline Anisotropies on Skyrmion Lattice

Xuejin Wan[1], *Yangfan Hu*[1,2]*, *Zhipeng Hou*[3] *and Biao Wang*[1,2]*

[1]School of Materials Science and Engineering, Dongguan University of Technology, Dongguan, China, [2]Sino-French Institute of Nuclear Engineering and Technology, Sun Yat-sen University, Zhuhai, China, [3]Guangdong Provincial Key Laboratory of Optical Information Materials and Technology and Institute for Advanced Materials, South China Academy of Advanced Optoelectronics, South China Normal University, Guangzhou, China

Reorientation of skyrmion crystal (SkX) with respect to crystallographic axes is believed to be insensitive to anisotropies of fourth order in spin-orbit coupling, for which sixth order terms are considered for explanation. Here, we show that this is wrong due to an oversimplified assumption that SkX possesses hexagonal symmetry. When the deformation of SkX is taken into account, fourth order anisotropies such as exchange anisotropy and magnetocrystalline anisotropy have pinning (in this work, the word 'pinning' refers to the reorientation effects of intrinsic anisotropy terms) effects on SkX. In particular, we reproduce some experiments of MnSi and $Fe_{1-x}Co_xSi$ by considering the effect of fourth order magnetocrystalline anisotropy alone. We reproduce the 30° rotation of SkX in Cu_2OSeO_3 by considering the combined effects of the exchange and magnetocrystalline anisotropies. And we use the exchange anisotropy to explain the reorientation of SkX in $VOSe_2O_5$.

Keywords: skyrmion crystal, pinning effect, exchange anisotropy, magnetocrystalline anisotropy, helimagnet

OPEN ACCESS

Edited by:
Cynthia Reichhardt,
Los Alamos National Laboratory (DOE), United States

Reviewed by:
Carles Navau,
Universitat Autònoma de Barcelona, Spain
Anjan Soumyanarayanan,
National University of Singapore, Singapore
Charles Reichhardt,
Los Alamos National Laboratory (DOE), United States

***Correspondence:**
Yangfan Hu
huyf@dgut.edu.cn
Biao Wang
wangbiao@mail.sysu.edu.cn

Specialty section:
This article was submitted to Condensed Matter Physics, a section of the journal Frontiers in Physics

Received: *23 March 2021*
Accepted: *27 May 2021*
Published: *21 June 2021*

Citation:
Wan X, Hu Y, Hou Z and Wang B (2021) Pinning Effects of Exchange and Magnetocrystalline Anisotropies on Skyrmion Lattice. Front. Phys. 9:684346. doi: 10.3389/fphy.2021.684346

1 INTRODUCTION

Helimagnets have attracted extensive interest since the first observation of magnetic skyrmions in 2009 [1]. Magnetic skyrmions in helimagnets are nontrivial spin textures, in which the spins point in all of the directions wrapping a sphere. Their topological protection [2] and facile current driven motion [3, 4] make them possible to be applied in novel spintronic and information storage devices [5, 6].

In helimagnets such as MnSi, $Fe_{1-x}Co_xSi$, and Cu_2OSeO_3, the ferromagnetic exchange interaction (for Cu_2OSeO_3, the exchange interaction consists of ferromagnetic and antiferromagnetic interactions, but the field-induced ground state is closer to ferromagnetic than antiferromagnetic [7, 8]) and the Dzyaloshinsky-Moriya interaction (DMI), which arises due to the broken of space inversion symmetry [9, 10], dominate the free energy when studying bulk material free from any external magnetic field. The former favors parallel spin alignment, while the latter favors the twist of the spins. They compete with each other and result in SkX at appropriate magnetic field just below the Curie temperature [1, 11–14]. In experiments, when the magnetic field is along directions with high symmetry, such as the [001], [111] and [110] directions, the wave vectors of SkX are orientated with respect to the crystallographic axes [1, 12, 15, 16]. This indicates the existence of anisotropy energy. The anisotropies of fourth order in spin-orbit coupling, such as the exchange anisotropy and fourth order magnetocrystalline anisotropy, are widely used to explain the pinning of helical phase, the transition from helical to conical phase and the appearance of tilted conical phase [1, 17–20]. However, according to the perturbation theory [1, 12, 16, 21], which treats the anisotropies

perturbatively and approximates SkX by a triple-Q structure with three equivalent wave vectors forming a regular triangle, they are insensitive to the pinning of SkX. As a consequence, anisotropies with higher order are proposed. In our opinion, ignoring the deformation of SkX is oversimplified, because many experiments show that the structure of SkX is sensitive to anisotropy of the system which destroys its hexagonal symmetry [22–24].

In this work, we study the pinning effects of the exchange anisotropies and the fourth order magnetocrystalline anisotropy on deformable SkX. We apply a rescaled free-energy-density model for T point group and describe Bloch SkX by a three-order Fourier expansion with deformation-related degrees of freedom. Firstly, we study four anisotropies (three types of exchange anisotropies and a fourth order magnetocrystalline anisotropy in helimagnets with T symmetry) separately. It is found that they have different pinning effects on SkX. Then, by plotting the deformation-related parameters as functions of one exchange anisotropy, we figure out that the deformation of SkX is characterized by the change of amplitudes, lengths and azimuth angles of wave vectors. Next, we compare our results with some experiments, the fourth order magnetocrystalline anisotropy may explain the pinning of SkX in MnSi [1, 25, 26] and $Fe_{1-x}Co_xSi$ [12, 27–29]. To reproduce the 30° rotation of SkX in Cu_2OSeO_3 [16], we consider both the exchange and magnetocrystalline anisotropy, and find that at certain conditions 30° rotation of SkX occurs when temperature or magnetic field changes. Lastly, we expand our model so that it is applicable to C_{nv} helimagnets hosting Néel SkX. It is found that exchange anisotropy has pinning effects on Néel SkX in C_{4v} helimagnets but not in C_{3v} or C_{6v} helimagnets.

2 MODEL

Based on the continuum spin model established by Bak and Jensen [17], we write the rescaled free-energy density [30] for helimagnets with the symmetry of T point group in the following form:

$$\omega(\mathbf{m}) = \sum_{i=1}^{3}\left(\frac{\partial \mathbf{m}}{\partial r_i}\right)^2 + 2\mathbf{m}\cdot(\nabla\times\mathbf{m}) - 2\mathbf{b}\cdot\mathbf{m} + \omega_{\mathrm{L}}(\mathbf{m}) + \omega_{\mathrm{a}}(\mathbf{m}). \tag{1}$$

Here, $\mathbf{m}$ is the rescaled magnetization. The first two terms in **Eq. (1)** represent the ferromagnetic exchange interaction and the DMI, respectively. The third term is the Zeeman energy under the rescaled magnetic field $\mathbf{b}$. $\omega_{\mathrm{L}} = t\mathbf{m}^2 + \mathbf{m}^4$ is the Landau expansion with the rescaled temperature t, it consists of the second and the fourth order terms. The last term ω_{a} is the anisotropy energy. In this work, we consider only the exchange anisotropy and the fourth order magnetocrystalline anisotropy, and we express ω_{a} as

$$\omega_{\mathrm{a}} = a_{\mathrm{e}1}\sum_{i=1}^{3}\left(\frac{\partial m_i}{\partial r_i}\right)^2 + a_{\mathrm{e}2}\sum_{i=1}^{3}\left(\frac{\partial m_i}{\partial r_{i+1}}\right)^2 + a_{\mathrm{e}3}\sum_{i=1}^{3}\left(\frac{\partial m_i}{\partial r_{i-1}}\right)^2 + a_{\mathrm{m}}\sum_{i=1}^{3} m_i^4, \tag{2}$$

where $a_{\mathrm{e}1}$, $a_{\mathrm{e}2}$ and $a_{\mathrm{e}3}$ are the coefficients of exchange anisotropy, a_{m} is the coefficient of magnetocrystalline anisotropy, r_{3+1} and r_{1-1} represent r_1 and r_3, respectively.

For bulk B20 materials, the skyrmion plane rotates with respect to the applied magnetic field. To describe the configuration of SkX under magnetic field with different direction, we should choose an appropriate cartesian coordinates system $O\text{-}r_1^*r_2^*r_3^*$ in which the magnetic field is along the r_3^* axis. Let the azimuthal and polar angles that characterize the magnetic field $\mathbf{b}$ be θ and ψ, respectively. We rotate $O\text{-}r_1r_2r_3$ counterclockwise about the r_3 axis by angle θ, and get a new cartesian coordinates system $O\text{-}r_1'r_2'r_3'$. We then perform a second rotation, this time about the r_2' axis by angle ψ, and we get the final cartesian coordinates system $O\text{-}r_1^*r_2^*r_3^*$ [**Figure 1**]. In terms of 3×3 orthogonal matrices, the product of the two operations can be written as $R(\theta,\psi) = R_{r_2'}(\psi)R_{r_3}(\theta)$. Due to the relation $R_{r_2'}(\psi) = R_{r_3}(\theta)R_{r_2}(\psi)R_{r_3}^{-1}(\theta)$, we have

$$R(\theta,\psi) = R_{r_3}(\theta)R_{r_2}(\psi) = \begin{bmatrix}\cos\theta & -\sin\theta & 0\\ \sin\theta & \cos\theta & 0\\ 0 & 0 & 1\end{bmatrix}\begin{bmatrix}\cos\psi & 0 & \sin\psi\\ 0 & 1 & 0\\ -\sin\psi & 0 & \cos\psi\end{bmatrix} \tag{3}$$

In the cartesian coordinates system $O\text{-}r_1^*r_2^*r_3^*$, we apply the n-order Fourier decomposition to describe the magnetization texture of SkX [31],

$$\mathbf{m}^* = \mathbf{m}_0 + \sum_{i=1}^{n}\sum_{j=1}^{n_i}\mathbf{m}_{\mathbf{q}_{ij}}e^{i\mathbf{q}_{ij}^{\mathrm{d}}\cdot\mathbf{r}^*}. \tag{4}$$

Here, $\mathbf{m}_0 = [m_{01}, m_{02}, m_{03}]^{\mathrm{T}}$ is the average magnetization over the entire SkX, and n_i is the number of nth order waves. The ith order waves are characterized by their wave vectors $\mathbf{q}_{ij}^{\mathrm{d}}$ and polarizations $\mathbf{m}_{\mathbf{q}_{ij}}$. In the presence of anisotropy energy, SkX with hexagonal symmetry will go through deformation, and the deformation-related parameters are introduced through the following equation

$$\mathbf{q}_{ij}^{\mathrm{d}} = \begin{bmatrix}1+\varepsilon_{11}^q & \varepsilon_{12}^q+\omega^q\\ \varepsilon_{12}^q-\omega^q & 1+\varepsilon_{22}^q\end{bmatrix}\mathbf{q}_{ij}. \tag{5}$$

In reciprocal space, ε_{11}^q and ε_{22}^q are the normal strains; ε_{12}^q and ω^q reflect the shear deformation and rotation of the plane spanned by $\mathbf{q}_{ij}^{\mathrm{d}}$, respectively. $\mathbf{q}_{ij}$ are the undeformed wave vectors, they all can be expressed as a linear combination of $\mathbf{q}_{11}$ and $\mathbf{q}_{12}$ (without loss of generality, for hexagonal SkX, we set $\mathbf{q}_{11} = [0, 1]^{\mathrm{T}}$, $\mathbf{q}_{12} = \left[-\frac{\sqrt{3}}{2}, -\frac{1}{2}\right]^{\mathrm{T}}$). As to $\mathbf{m}_{\mathbf{q}_{ij}}$, we decompose them along the basis vectors $\mathbf{P}_{ij1} = \frac{1}{\sqrt{2}|\mathbf{q}_{ij}|}[-\mathrm{i}q_{ijy}, \mathrm{i}q_{ijx}, |\mathbf{q}_{ij}|]^{\mathrm{T}}$, $\mathbf{P}_{ij2} = \frac{1}{|\mathbf{q}_{ij}|}[q_{ijx}, q_{ijy}, 0]^{\mathrm{T}}$, and $\mathbf{P}_{ij3} = \frac{1}{\sqrt{2}|\mathbf{q}_{ij}|}[\mathrm{i}q_{ijy}, -\mathrm{i}q_{ijx}, |\mathbf{q}_{ij}|]^{\mathrm{T}}$ (for the chosen of the orthogonal basis, see Ref. [32]), and we have

$$\mathrm{m}_{\mathbf{q}_{ij}} = \sum_{k=1}^{3} c_{ijk}\mathrm{P}_{ijk}, \tag{6}$$

where $c_{ijk} = c_{ijk}^{\mathrm{re}} + \mathrm{i}c_{ijk}^{\mathrm{im}}$ (k = 1, 2, 3) are the complex coefficients.

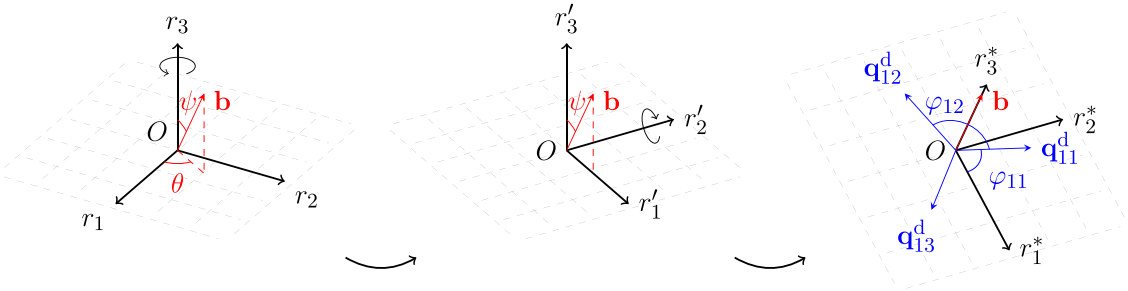

FIGURE 1 | Rotations of coordinates system. θ and ψ are the azimuthal and polar angles of the magnetic field **b**, respectively. φ_{11} is the angle between the wave vector $\mathbf{q}_{11}^{\mathrm{d}}$ and the axis r_1^*, and φ_{12} is the angle between the wave vector $\mathbf{q}_{11}^{\mathrm{d}}$ and $\mathbf{q}_{12}^{\mathrm{d}}$ [see **Eqs. (4, 5)**].

According to **Eqs. (1)** and **(2)**, the free energy density is a functional of m_i and $m_{j,k}$ ($m_{j,k}$ denotes $\frac{\partial m_j}{\partial r_k}$), i.e., $\omega = \omega(m_i, m_{j,k})$. Applying the following coordinate transformation

$$m_i = \sum_{i'=1}^{3} R(\theta,\psi)_{ii'} m_{i'}^*, \tag{7}$$

$$m_{j,k} = \sum_{j',k'=1}^{3} R(\theta,\psi)_{jj'} R(\theta,\psi)_{kk'} m_{j',k'}^*, \tag{8}$$

the free-energy density can be rewritten as, after averaging over a magnetic unit cell

$$\omega = \omega\left(\varepsilon_{11}^q, \varepsilon_{22}^q, \varepsilon_{12}^q, \omega_{11}^q, m_{01}, m_{02}, m_{03}, c_{ijk}^{\mathrm{re}}, c_{ijk}^{\mathrm{im}}\right). \tag{9}$$

At certain temperature t, magnetic field **b**, rotation angles θ and ψ, exchange and magnetocrystalline anisotropies $a_{\mathrm{e}1}$, $a_{\mathrm{e}2}$, $a_{\mathrm{e}3}$ and a_{m}, the parameters describing SkX are calculated *via* minimization of **Eq. (9)**. In this work, we set the order of Fourier expansion $n = 3$.

Our analytical method can only deal with periodic magnetization structure. For the cases where the periodicity of skyrmions is broken, e.g., the thermal-induced disorder or the pinning from impurities, the review [33] and references therein are good to refer to.

3 RESULTS AND DISCUSSION

We first investigate the pinning effects of anisotropies $a_{\mathrm{e}1}$, $a_{\mathrm{e}2}$, $a_{\mathrm{e}3}$ and a_{m} on Bloch SkX, separately. The value of θ is 45°; thus, $\psi = 0°$, 55° and 90° correspond to the directions [001], [111] and [110], respectively. The temperature and the magnetic field are set to be $t = 0.5$ and $\mathbf{b} = [0, 0, 0.2]^{\mathrm{T}}$ (in the O-$r_1^* r_2^* r_3^*$ coordinate system) so that SkX exists as a stable or metastable state. The thermodynamic parameters for MnSi [34] and Cu_2OSeO_3 [7] are available. Using these parameters, we have $(T, B) = (28.0\mathrm{K}, 87\mathrm{mT})$ for MnSi and $(T, B) = (58.1\mathrm{K}, 4.3\mathrm{mT})$ for Cu_2OSeO_3, these points are near the skyrmion stable region in the magnetic field-temperature phase diagram. The anisotropy coefficients of helimagnets are hard to get in experiments. We only find the relative exchange anisotropy for GaV_4O_8, which is about 5% [35]. In this work, the values used for the anisotropy coefficients are 0.005 ~ 0.1. We think, to some extent, the values are within a realistic range.

We change the rotation-related parameter ω^q, minimize the free energy density and then plot ω as a function of φ_{11}, the angle between the wave vector $\mathbf{q}_{11}^{\mathrm{d}}$ and the r_1^* axis, in **Figure 2**. **Figures 2A,B** show the effects of exchange anisotropy $a_{\mathrm{e}1}$ on SkX. For **b**||[001], a negative $a_{\mathrm{e}1}$ (**Figure 2A**) prefers a wave vector along the [100] or [010] direction; while a positive $a_{\mathrm{e}1}$ (**Figure 2B**) prefers a wave vector along the [110] or [1$\bar{1}$0] direction. For **b**||[111] and [110], ω reaches its minimum at $\varphi_{11} = 90°$ and $\varphi_{11} = 60°$, respectively (**Figures 2A,B**), i.e., both negative and positive $a_{\mathrm{e}1}$ prefer a wave vector along the [110] direction for **b**||[111], and along the [001] direction for **b**||[110]. **Figures 1C–F** show the effects of $a_{\mathrm{e}2}$ and $a_{\mathrm{e}3}$ on SkX, respectively. For **b**||[001], a $a_{\mathrm{e}2}$, no matter what its sign is, pins a wave vector of SkX along the [010] direction; while a $a_{\mathrm{e}3}$ pins a wave vector of SkX along the [100] direction. For **b**||[111], φ_{11} is between 45° and 60° or between 60° and 75°, meaning that no wave vector is along any direction with high symmetry. For **b**||[110], both $a_{\mathrm{e}2}$ and $a_{\mathrm{e}3}$ pin a wave vector of SkX along the [001] direction. **Figures 2G,H** show the effects of a_{m} on SkX. For **b**||[001] and [111] , a_{m} has the same the pinning effects on SkX as $a_{\mathrm{e}1}$; while for **b**||[110], a_{m} is different from $a_{\mathrm{e}1}$, it results in a wave vector along the [110] direction.

In **Figure 2**, we give the values of $\Delta\omega$, difference between the maximum and minimum of free energy. They are much smaller than ω (about −0.1), about 10^{-9} for $a_{\mathrm{m}} = \pm 0.05$ and $\psi = 0°$, and about 10^{-7}-10^{-5} for other cases. The strength of a_{m}-induced anisotropy in (001) plane is obviously smaller than that in (111) and (110) planes. Comparing the energy curves for $a_{\mathrm{e}2}$ and for $a_{\mathrm{e}3}$, we find that they have the same $\Delta\omega$ and are symmetric about $\varphi_{11} = 60°$. The similarity between $a_{\mathrm{e}2}$ and $a_{\mathrm{e}3}$ can be inferred from their energy formula in **Eq. 2**, which are related by the coordinate transformation $r_1 \leftrightarrow r_2$. It should be noticed that for **b**||[001], the periodicity of $\omega(\varphi_{11})$ is 30° for $a_{\mathrm{e}1}$ and a_{m}, and is 60° for $a_{\mathrm{e}2}$ and $a_{\mathrm{e}3}$. This can be explained by symmetry analysis. The $a_{\mathrm{e}1}$ and a_{m} terms in **Eq. (2)** have a higher symmetry than T point group, they are invariant with respect to fourfold C_4 rotations around the ⟨001⟩ axes. $a_{\mathrm{e}1}$ and a_{m} terms in **Eq. (2)** have lower symmetry and are invariant with respect ot twofold C_2 rotations around the ⟨001⟩ axes, meaning the broken of the equivalence between [100] and [010].

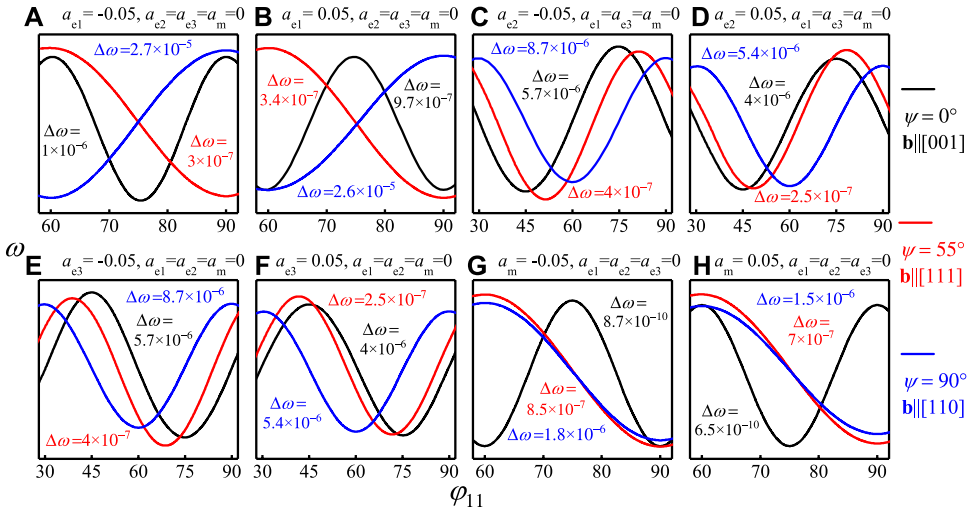

FIGURE 2 | ω as a function of φ_{11}. Pinning effects of **(A,B)** a_{e1}, **(C,D)** a_{e2}, **(E,F)** a_{e3}, and **(G,H)** a_m on SkX. The first and third (second and fourth) are calculated for negative (positive) anisotropy coefficients. The black, red and blue curves are obtained for $\psi = 0°$ [**b**||[001]], $\psi = 55°$ [**b**||[111]] and $\psi = 90°$ [**b**||[110]], respectively. Here, in order to facilitate comparison, three curves which do not correspond to the same y-axis, are plotted in one figure. Δω is the difference between the maximum and minimum of ω. The values of ω are not shown in the figures, they are all about −0.1.

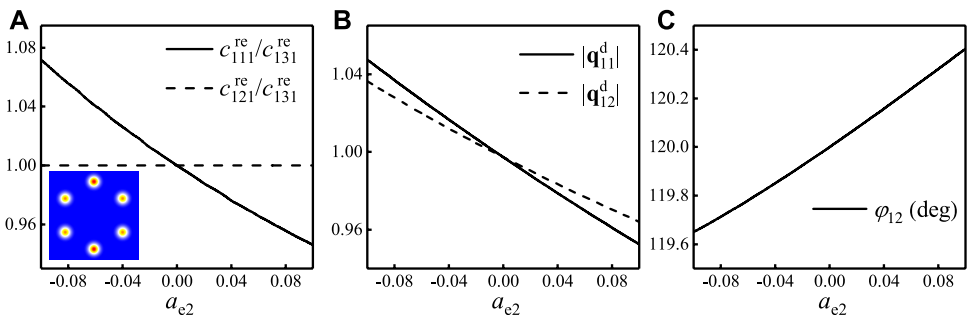

FIGURE 3 | Deformation of SkX induced by a_{e2}. **(A)** the relative wave amplitudes $c^{re}_{111}/c^{re}_{131}$ and $c^{re}_{121}/c^{re}_{131}$, **(B)** the wave lengths $|\mathbf{q}^d_{11}|$ and $|\mathbf{q}^d_{12}|$, and **(C)** the angle φ_{12} between $\mathbf{q}^d_{11}$ and $\mathbf{q}^d_{12}$ as functions of a_{e2}. The results are calculated at $b = 0.2$ and $t = 0.5$. The inset in (a) shows the first-order Bragg spots at $a_{e2} = -0.1$.

SkX is treated as a deformable structure. To reveal how anisotropy energy deforms SkX, we take a_{e2} as an example and plot some deformation-related parameters as functions of a_{e2} in **Figure 3**. It can be found that for nonzero a_{e2}, 1) the wave amplitudes $c^{re}_{111} \neq c^{re}_{131}$ (**Figure 3A**), 2) the wave lengths of $\mathbf{q}^d_{11}$ and $\mathbf{q}^d_{12}$ are not equal to each other (**Figure 3B**), and 3) the angle φ_{12} between $\mathbf{q}^d_{11}$ and $\mathbf{q}^d_{12}$ deviates from 120° (**Figure 3C**). We conclude that anisotropy energy breaks the hexagonal symmetry of SkX by changing the amplitudes of, the lengths of, and the angles between the wave vectors. In many of the small-angle neutron scattering (SANS) experiments (1; 27; 36), the observed Bragg spots have different intensities, this might be explained by our calculation. By energy minimization, we find that the dominant coefficients c_{ijk} are c^{re}_{111}, c^{re}_{121} and c^{re}_{131}, which represent the wave amplitudes of the first order waves with vectors $\mathbf{q}^d_{11}$, $\mathbf{q}^d_{12}$ and $\mathbf{q}^d_{13}$. Their ratios reflect the relative intensities of the first-order Bragg spots. In the inset of the **Figure 3A**, two Bragg spots are brighter than the other four, because $c^{re}_{131} = c^{re}_{121} < c^{re}_{111}$.

We now compare our results with some experiments. The SANS experiments of $Fe_{1-x}Co_xSi$ [12, 27–29] show that for **b**||[111] and [110] directions, two of the six scattering spots are aligned with the $[1\bar{1}0]$ axis; for **b**||[001], two sets of six scattering spots are observed, one is aligned with one the [100] direction, the other one the [010] direction. This is compatible with the results shown in **Figure 2G**. Therefore, a negative a_m may explain the pinning of SkX in $Fe_{1-x}Co_xSi$. Different from $Fe_{1-x}Co_xSi$, MnSi [26] is observed to have a wave vector along the [110] direction for **b**||[001]. This may be explained by a positive a_m (**Figure 2H**. We should point out that at zero magnetic field, a negative (positive) a_m prefers the ⟨100⟩ (⟨111⟩) directions for the helical state, which is indeed the case for $Fe_{1-x}Co_xSi$ (MnSi) [1, 28, 29, 37, 38]. In the work [26], two kinds of sixth order magnetocrystalline anisotropies $\mathbf{m}\cdot$

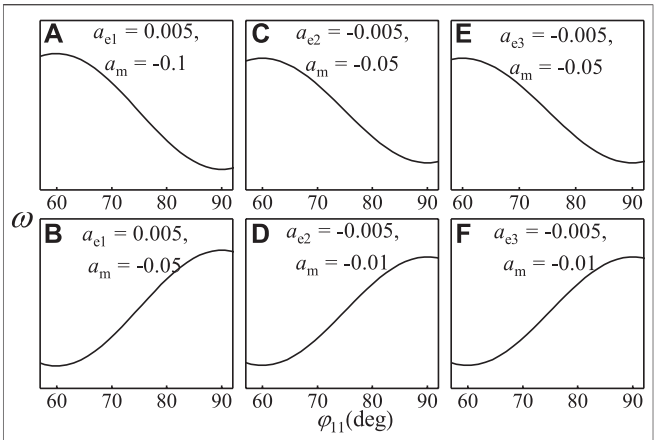

FIGURE 4 | Combined effects of the exchange and fourth order magnetocrystalline anisotropies on SkX. The absolute value of exchange anisotropy coefficient is fixed to be 0.005, the value of magnetocrystalline anisotropy coefficient is fixed to be −0.1 or −0.05 or −0.01. The results are calculated at $\psi = 90^\circ$, $b = 0.2$ and $t = 0.5$.

$(\partial_{r_1}^6 + \partial_{r_2}^6 + \partial_{r_3}^6)\mathbf{m}$ and $\mathbf{m} \cdot (\partial_{r_1}^4\partial_{r_2}^2 + \partial_{r_2}^4\partial_{r_3}^2 + \partial_{r_3}^4\partial_{r_1}^2)\mathbf{m}$ are thought to be responsible for the pinning of SkX in MnSi. However, this is contrary to other works [12, 21] which show that the second sixth order magnetocrystalline anisotropy determines the reorientation of SkX for **b**||[001] and it pins SkX with a wave vector along the [010] or [100] direction depending on the sign of its coefficient. The SANS experiments of MnSi in Ref. [26] can not be explained by the sixth order magnetocrystalline anisotropies.

Cu_2OSeO_3 is another helimagnet hosting SkX, a peculiar experimental phenomenon about it is that for **b**||[110], SkX is reorientated with a wave vector along the $[1\bar{1}0]$ or [001] direction depending on the temperature and magnetic field conditions [16]. To explain this, we should consider the exchange and fourth order magnetocrystalline anisotropies at the same time. As a first step, we determine the signs of anisotropies $a_{e1} > 0$, $a_{e2} < 0$, $a_{e3} < 0$ and $a_m < 0$ according to the fact that [100] is an easy axis for the helical state at zero field [20, 39, 40]. Then we confirm by **Figure 4** that for **b**||[110], a "dominant" magnetocrystalline anisotropy pins SkX with a wave vector along the [001] direction, while a "dominant" exchange anisotropy pins SkX with a wave vector along the $[1\bar{1}0]$ direction. Here, the word "dominant" depends on the type of exchange anisotropy considered. When $a_m = -0.05$, the "dominant" anisotropy is a_{e1} for $a_{e1} = 0.005$ (**Figures 4A,B**), and is a_m for $a_{e2} = -0.005$ or $a_{e3} = -0.005$ (**Figures 4C–F**). Lastly, we take the temperature and magnetic field into account and try to reproduce the 30° rotation of SkX in Cu_2OSeO_3. The anisotropies we considered are a_{e1} and a_m, and their values are 0.005 and −0.1, respectively, the same as that for **Figure 4A**. We fix the magnetic field $b = 0.2$ and change the temperature from 0.5 to 0.8 (**Figure 5A**). It is found that the angle φ_{11}^*, for which the free energy reaches its minimum, drops suddenly from 90° to 60° at $t = 0.66$. Then we fix the temperature $t = 0.65$ and change the magnetic field from 0.15 to 0.27 [**Figure 5B**]. Similar phenomenon is observed, φ_{11}^* drops from 90° to 60° at $b = 0.21$. Our results agree with the experiments of Cu_2OSeO_3 [16].

In another published work [41], we explain the electric-field-induced continuous rotation of SkX [42] by extending the present model. Unlike a previous theory [42] which explains the phenomenon by considering both the fourth and sixth order magnetocrystalline anisotropies, we find that a combination of fourth order exchange anisotropies and magnetocrystalline anisotropies dominates the phenomena. This is because the theory used in [42] obtains a positive coefficient of the fourth order magnetocrystalline anisotropy a_m which is inconsistent with other experiments [20, 39, 40], while our model obtains a negative a_m.

In polar magnets with C_{nv} (n = 3, 4, 6) symmetry, the DMI and the exchange anisotropy are different from that in **Eq. (1)**. By applying the symmetry analysis, we derive the DMI: $\omega_{DM} = 2m_1m_{3,1} - 2m_3m_{1,1} + 2m_2m_{3,2} - 2m_3m_{2,2}$ (in this case, the Néel SkX is stabilized, and the basis vectors in **Eq. (6)** are chosen to be $\mathbf{P}_{ij1} = \frac{1}{\sqrt{2}|\mathbf{q}_{ij}|}[-\mathrm{i}q_{ijx}, -\mathrm{i}q_{ijy}, |\mathbf{q}_{ij}|]^{\mathrm{T}}$, $\mathbf{P}_{ij2} = \frac{1}{|\mathbf{q}_{ij}|}[-q_{ijy}, q_{ijx}, 0]^{\mathrm{T}}$, and $\mathbf{P}_{ij3} = \frac{1}{\sqrt{2}|\mathbf{q}_{ij}|}[\mathrm{i}q_{ijx}, \mathrm{i}q_{ijy}, |\mathbf{q}_{ij}|]^{\mathrm{T}}$ [32]), and the exchange anisotropy:

$$\omega_{ea} = a_{e4}\left(\left(\frac{\partial m_2}{\partial r_1}\right)^2 + \left(\frac{\partial m_1}{\partial r_2}\right)^2\right) + a_{e5}\left(\left(\frac{\partial m_3}{\partial r_1}\right)^2 + \left(\frac{\partial m_3}{\partial r_2}\right)^2\right) \tag{10}$$

Here, we have ignored the terms $(\partial m_i/\partial r_3)^2$ due to the fact that in polar magnets, SkX plane is perpendicular to the n-fold axis no matter what direction the applied magnetic field is along [43, 44]. The term with coefficient a_{e5} is rotationally symmetric, and it has no pinning effects on SkX.

For C_{3v} and C_{6v} point groups, a_{e4} is zero. As a result, the orientation of the wave vector of SkX is insensitive to the exchange anisotropy. In Ref. [44], based on a discrete model and Monte Carlo simulations, the authors attribute the pinning of Néel SkX in C_{3v} polar magnet GaV_4Se_8 to the Dzyaloshinskii-Moriya vectors. However, according to the continuum model, the DMI possesses rotational symmetry and has no pinning effects on Néel SkX. In our opinion, this contradiction is because the

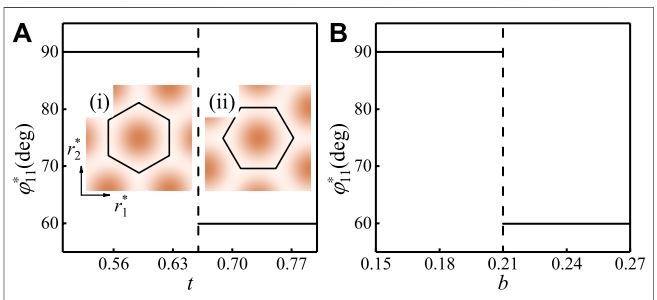

FIGURE 5 | φ_{11}^*, the angle between the wave vector $\mathbf{q}_{11}^{\mathrm{d}}$ and the r_1^* axis, as a function of **(A)** t at $b = 0.2$, **(B)** b at $t = 0.65$. The anisotropies considered are $a_{e1} = 0.005$ and $a_m = -0.1$. The colored density plots i) and ii) show the magnetization along the r_3^* axis at $t = 0.6$ and $t = 0.7$, respectively. The region encircled by black lines is a skyrmion cell.

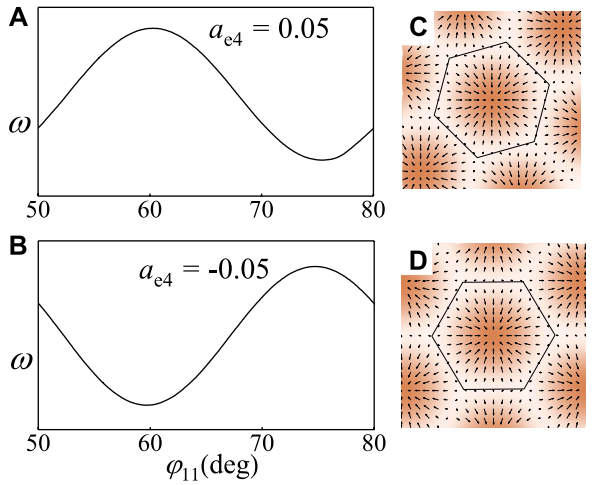

FIGURE 6 | ω as a function of φ_{11} for **(A)** a_{e4} = 0.05 and **(B)** a_{e4} = −0.05. Magnetization structure of Néel SkX for **(C)** a_{e4} = 0.05 and **(D)** a_{e4} = −0.05. The in-plane and out-of-plane components of magnetization are represented by the arrows and the color, respectively. The calculation conditions are b = 0.2 and t = 0.

continuum model ignores higher order DMI terms which emerge during the process of transforming the discrete model to the continuum model. These higher order DMI terms possess lower symmetry C_{3v} or C_{6v} and might reorientate Néel SkX.

For C_{4v} point groups, we have $a_{e4} \neq 0$. The term with coefficient a_{e4} will deform and thus reorientate the Néel SkX. Because it possesses C_{4v} symmetry, which is different from the C_{3v} symmetry possessed by the undeformed SkX. To study the pinning effects of a_4 on Néel SkX, we plot ω as a function of φ_{11} for 1) positive and 2) negative a_{e4} in **Figure 6**. It is found that a positive a_{e4} prefers a wave vector along the [110] or [$1\bar{1}0$] direction, and a negative a_{e4} prefers a wave vector along the [100] or [$0\bar{1}0$] direction. In experiments, very few C_{4v} helimagnets hosting Néel SkX have been found. $VOSe_2O_5$ [45] is one of these C_{4v} helimagnets, in which the Néel SkX is orientated with a wave vector along the [100] or [$0\bar{1}0$] direction. In previous theories, less attention has been paid to the reorientation of Néel SkX in C_{4v} helimagnets. Here, a negative a_{e4} gives a possible explanation for the SkX-reorientation-related phenomena in $VOSe_2O_5$.

4 CONCLUSION

In conclusion, the exchange and fourth order magnetocrystalline anisotropies deform SkX by changing the amplitudes of, the lengths of, and the angles between wave vectors and thus show pinning effects on SkX. The results of magnetocrystalline anisotropy [exchange anisotropy] may explain some experiments of MnSi and $Fe_{1-x}Co_xSi$ [$VOSe_2O_5$]. By considering the exchange and magnetocrystalline anisotropies at the same time, the 30° rotation of SkX in Cu_2OSeO_3 is reproduced.

DATA AVAILABILITY STATEMENT

The original contributions presented in the study are included in the article/Supplementary Material, further inquiries can be directed to the corresponding authors.

AUTHOR CONTRIBUTIONS

XW and YH conceived the idea. XW finished the analytical deduction, and performed all the calculations. XW, YH, ZH, and BW discussed the results for revision and co-wrote the manuscript.

FUNDING

This work was supported by the NSFC (National Natural Science Foundation of China) through fund Nos. 11772360, 11832019, 11572355 and 51901081, the National Key Research and Development Program of China (Grant No. 2020YFA0309300), the Guangdong Basic and Applied Basic Research Foundation (Grant No. 2019A1515012016), and the Pearl River Nova Program of Guangzhou (Grant No. 201806010134).

REFERENCES

1. Mühlbauer S, Binz B, Jonietz F, Pfleiderer C, Rosch A, Neubauer A, et al. Skyrmion Lattice in a Chiral Magnet. *Science* (2009) 323:915–9. doi:10.1126/science.1166767
2. Nagaosa N, and Tokura Y. Topological Properties and Dynamics of Magnetic Skyrmions. *Nat Nanotech* (2013) 8:899–911. doi:10.1038/nnano.2013.243
3. Jonietz F, Mühlbauer S, Pfleiderer C, Neubauer A, Münzer W, Bauer A, et al. Spin Transfer Torques in Mnsi at Ultralow Current Densities. *Science* (2010) 330:1648–51. doi:10.1126/science.1195709
4. Yu XZ, Kanazawa N, Zhang WZ, Nagai T, Hara T, Kimoto K, et al. Skyrmion Flow Near Room Temperature in an Ultralow Current Density. *Nat Commun* (2012) 3:988. doi:10.1038/ncomms1990
5. Zhang X, Ezawa M, and Zhou Y. Magnetic Skyrmion Logic gates: Conversion, Duplication and Merging of Skyrmions. *Sci Rep* (2015a) 5:9400. doi:10.1038/srep09400
6. Zhang X, Zhao GP, Fangohr H, Liu JP, Xia WX, Xia J, et al. Skyrmion-skyrmion and Skyrmion-Edge Repulsions in Skyrmion-Based Racetrack Memory. *Sci Rep* (2015b) 5:7643. doi:10.1038/srep07643
7. Janson O, Rousochatzakis I, Tsirlin AA, Belesi M, Leonov AA, Rößler UK, et al. The Quantum Nature of Skyrmions and Half-Skyrmions in Cu2oseo3. *Nat Commun* (2014) 5:5376–11. doi:10.1038/ncomms6376
8. Yang JH, Li ZL, Lu XZ, Whangbo M-H, Wei S-H, Gong XG, et al. Strong Dzyaloshinskii-Moriya Interaction and Origin of Ferroelectricity inCu2OSeO3. *Phys Rev Lett* (2012) 109:107203. doi:10.1103/physrevlett.109.107203
9. Dzyaloshinsky I. A Thermodynamic Theory of "weak" Ferromagnetism of Antiferromagnetics. *J Phys Chem Sol* (1958) 4:241–55. doi:10.1016/0022-3697(58)90076-3
10. Moriya T. Anisotropic Superexchange Interaction and Weak Ferromagnetism. *Phys Rev* (1960) 120:91–8. doi:10.1103/physrev.120.91
11. Wilhelm H, Baenitz M, Schmidt M, Rößler UK, Leonov AA, and Bogdanov AN. Precursor Phenomena at the Magnetic Ordering of the Cubic Helimagnet Fege. *Phys Rev Lett* (2011) 107:127203. doi:10.1103/physrevlett.107.127203

12. Münzer W, Neubauer A, Adams T, Mühlbauer S, Franz C, Jonietz F, et al. Skyrmion Lattice in the Doped Semiconductor Fe1-Xcoxsi. *Phys Rev B* (2010) 81:041203. doi:10.1103/physrevb.81.041203
13. Ruff E, Widmann S, Lunkenheimer P, Tsurkan V, Bordács S, Kézsmárki I, et al. Multiferroicity and Skyrmions Carrying Electric Polarization in Gav4s8. *Sci Adv* (2015) 1:e1500916. doi:10.1126/sciadv.1500916
14. Omrani A, White J, Prša K, Živković I, Berger H, Magrez A, et al. Exploration of the Helimagnetic and Skyrmion Lattice Phase Diagram in Cu2oseo3 Using Magnetoelectric Susceptibility. *Phys Rev B* (2014) 89:064406. doi:10.1103/physrevb.89.064406
15. Moskvin E, Grigoriev S, Dyadkin V, Eckerlebe H, Baenitz M, Schmidt M, et al. Complex Chiral Modulations in Fege Close to Magnetic Ordering. *Phys Rev Lett* (2013) 110:077207. doi:10.1103/PhysRevLett.110.077207
16. Seki S, Kim J-H, Inosov DS, Georgii R, Keimer B, Ishiwata S, et al. Formation and Rotation of Skyrmion crystal in the Chiral-Lattice Insulator Cu2oseo3. *Phys Rev B* (2012) 85:220406. doi:10.1103/physrevb.85.220406
17. Bak P, and Jensen MH. Theory of Helical Magnetic Structures and Phase Transitions in Mnsi and Fege. *J Phys C: Solid State Phys* (1980) 13:L881–L885. doi:10.1088/0022-3719/13/31/002
18. Park J-H, and Han JH. Zero-temperature Phases for Chiral Magnets in Three Dimensions. *Phys Rev B* (2011) 83:184406. doi:10.1103/physrevb.83.184406
19. Halder M, Chacon A, Bauer A, Simeth W, Mühlbauer S, Berger H, et al. Thermodynamic Evidence of a Second Skyrmion Lattice Phase and Tilted Conical Phase in Cu2oseo3. *Phys Rev B* (2018) 98:144429. doi:10.1103/physrevb.98.144429
20. Chacon A, Heinen L, Halder M, Bauer A, Simeth W, Mühlbauer S, et al. Observation of Two Independent Skyrmion Phases in a Chiral Magnetic Material. *Nat Phys* (2018) 14:936–41. doi:10.1038/s41567-018-0184-y
21. Luo Y, Lin S-Z, Fobes DM, Liu Z, Bauer ED, Betts JB, et al. Anisotropic Magnetocrystalline Coupling of the Skyrmion Lattice in Mnsi. *Phys Rev B* (2018) 97:104423. doi:10.1103/physrevb.97.104423
22. Shibata K, Iwasaki J, Kanazawa N, Aizawa S, Tanigaki T, Shirai M, et al. Large Anisotropic Deformation of Skyrmions in Strained crystal. *Nat Nanotech* (2015) 10:589–92. doi:10.1038/nnano.2015.113
23. Wang C, Du H, Zhao X, Jin C, Tian M, Zhang Y, et al. Enhanced Stability of the Magnetic Skyrmion Lattice Phase under a Tilted Magnetic Field in a Two-Dimensional Chiral Magnet. *Nano Lett* (2017) 17:2921–7. doi:10.1021/acs.nanolett.7b00135
24. Makino K, Reim JD, Higashi D, Okuyama D, Sato TJ, Nambu Y, et al. Thermal Stability and Irreversibility of Skyrmion-Lattice Phases in Cu2oseo3. *Phys Rev B* (2017) 95:134412. doi:10.1103/physrevb.95.134412
25. Grigoriev SV, Potapova NM, Moskvin EV, Dyadkin VA, Dewhurst C, and Maleyev SV. Hexagonal Spin Structure of A-phase in Mnsi: Densely Packed Skyrmion Quasiparticles or Two-Dimensionally Modulated Spin Superlattice?. *Jetp Lett* (2014) 100:216–21. doi:10.1134/s0021364014150065
26. Bannenberg LJ, Qian F, Dalgliesh RM, Martin N, Chaboussant G, Schmidt M, et al. Reorientations, Relaxations, Metastabilities, and Multidomains of Skyrmion Lattices. *Phys Rev B* (2017a) 96:184416. doi:10.1103/physrevb.96.184416
27. Adams T, Mühlbauer S, Neubauer A, Münzer W, Jonietz F, Georgii R, et al. Skyrmion Lattice Domains in Fe1−xCoxSi. *J Phys Conf Ser* (2010) 200:032001. doi:10.1088/1742-6596/200/3/032001
28. Bannenberg LJ, Kakurai K, Qian F, Lelièvre-Berna E, Dewhurst CD, Onose Y, et al. Extended Skyrmion Lattice Scattering and Long-Time Memory in the Chiral magnetFe1−xCoxSi. *Phys Rev B* (2016) 94:104406. doi:10.1103/physrevb.94.104406
29. Bannenberg LJ, Kakurai K, Falus P, Lelièvre-Berna E, Dalgliesh R, Dewhurst CD, et al. Universality of the Helimagnetic Transition in Cubic Chiral Magnets: Small Angle Neutron Scattering and Neutron Spin echo Spectroscopy Studies of Fecosi. *Phys Rev B* (2017b) 95:144433. doi:10.1103/physrevb.95.144433
30. Wan X, Hu Y, and Wang B. Exchange-anisotropy-induced Intrinsic Distortion, Structural Transition, and Rotational Transition in Skyrmion Crystals. *Phys Rev B* (2018) 98:174427. doi:10.1103/physrevb.98.174427
31. Hu Y. Wave Nature and Metastability of Emergent Crystals in Chiral Magnets. *Commun Phys* (2018) 1:82. doi:10.1038/s42005-018-0071-y
32. Hu Y, and Wan X. Thermodynamics and Elasticity of Emergent Crystals. *arXiv:1905.02165* (2019).
33. Reichhardt C, Reichhardt C, and Milosevic M. Statics and Dynamics of Skyrmions Interacting with Pinning: A Review. *arXiv:2102.10464* (2021).
34. Hu Y, and Wang B. Unified Theory of Magnetoelastic Effects in B20 Chiral Magnets. *New J Phys* (2017) 19:123002. doi:10.1088/1367-2630/aa9507
35. Ehlers D, Stasinopoulos I, Kézsmárki I, Fehér T, Tsurkan V, von Nidda H-AK, et al. Exchange Anisotropy in the Skyrmion Host Gav4s8. *J Phys Condens Matter* (2016) 29:065803. doi:10.1088/1361-648x/aa4e7e
36. Adams T, Mühlbauer S, Pfleiderer C, Jonietz F, Bauer A, Neubauer A, et al. Long-range Crystalline Nature of the Skyrmion Lattice in Mnsi. *Phys Rev Lett* (2011) 107:217206. doi:10.1103/physrevlett.107.217206
37. Grigoriev S, Maleyev S, Dyadkin V, Menzel D, Schoenes J, and Eckerlebe H. Principal Interactions in the Magnetic System Fe1-Xcoxsi: Magnetic Structure and Critical Temperature by Neutron Diffraction and Squid Measurements. *Phys Rev B* (2007) 76:092407. doi:10.1103/physrevb.76.092407
38. Takeda M, Endoh Y, Kakurai K, Onose Y, Suzuki J, and Tokura Y. Nematic-to-smectic Transition of Magnetic Texture in Conical State. *J Phys Soc Jpn* (2009) 78:093704. doi:10.1143/jpsj.78.093704
39. Bannenberg LJ, Wilhelm H, Cubitt R, Labh A, Schmidt MP, Lelièvre-Berna E, et al. Multiple Low-Temperature Skyrmionic States in a Bulk Chiral Magnet. *Npj Quan Mater.* (2019) 4:11. doi:10.1038/s41535-019-0150-7
40. Qian F, Bannenberg LJ, Wilhelm H, Chaboussant G, Debeer-Schmitt LM, Schmidt MP, et al. New Magnetic Phase of the Chiral Skyrmion Material Cu2oseo3. *Sci Adv* (2018) 4:eaat7323. doi:10.1126/sciadv.aat7323
41. Wan X, Hu Y, and Wang B. First and Second Order Rotational Transitions of Skyrmion crystal in Multiferroic Cu2oseo3 under Electric Field. *Appl Phys Lett* (2020) 116:182403. doi:10.1063/5.0003880
42. White JS, Prša K, Huang P, Omrani AA, Živković I, Bartkowiak M, et al. Electric-Field-Induced Skyrmion Distortion and Giant Lattice Rotation in the Magnetoelectric InsulatorCu2OSeO3. *Phys Rev Lett* (2014) 113:107203. doi:10.1103/physrevlett.113.107203
43. Leonov AO, and Kézsmárki I. Skyrmion Robustness in Noncentrosymmetric Magnets with Axial Symmetry: The Role of Anisotropy and Tilted Magnetic fields. *Phys Rev B* (2017) 96:214413. doi:10.1103/physrevb.96.214413
44. Kézsmárki I, Bordács S, Milde P, Neuber E, Eng LM, White JS, et al. Néel-type Skyrmion Lattice with Confined Orientation in the Polar Magnetic Semiconductor GaV4S8. *Nat Mater* (2015) 14:1116–22. doi:10.1038/nmat4402
45. Kurumaji T, Nakajima T, Ukleev V, Feoktystov A, Arima T-h., Kakurai K, et al. Néel-Type Skyrmion Lattice in the Tetragonal Polar Magnet VOSe2O5. *Phys Rev Lett* (2017) 119:237201. doi:10.1103/physrevlett.119.237201

Conflict of Interest: The authors declare that the research was conducted in the absence of any commercial or financial relationships that could be construed as a potential conflict of interest.

frontiers in Physics

ORIGINAL RESEARCH
published: 28 July 2021
doi: 10.3389/fphy.2021.680698

Control of Néel-type Magnetic Kinks Confined in a Square Nanostructure by Spin-Polarized Currents

Ji-Pei Chen[1,2], Jia-Qiang Lin[1], Xiao Song[2], Yuan Chen[1], Zhi-Feng Chen[1], Wen-An Li[1], Ming-Hui Qin[2], Zhi-Peng Hou[2], Xing-Sen Gao[2]* and Jun-Ming Liu[2,3]*

[1]School of Physics and Materials Science and Research Center for Advanced Information Materials, Guangzhou University, Guangzhou, China, [2]Institute for Advanced Materials and Guangdong Provincial Key Laboratory of Quantum Engineering and Quantum Materials, South China Normal University, Guangzhou, China, [3]Laboratory of Solid State Microstructures and Innovative Center of Advanced Microstructures, Nanjing University, Nanjing, China

Magnetic skyrmion in chiral magnet exhibits a variety of unique topological properties associated with its innate topological structure. This inspires a number of ongoing searching for new topological magnetic textures. In this work, we used micromagnetic simulations and Monte Carlo simulations to investigate an exotic Néel-type magnetic kinks in square-shaped nanostructures of chiral magnets, which performs rather stably in the absence of magnetic field. The individual magnetic kink can reside in one of the four possible corners, and carry possibly upward or downward core polarity, constituting eight degenerate states. In addition, these kinks also exhibit unique behaviors of generation, stability and dynamics, as revealed by micromagnetic simulations. It was found that such kinks can be created, annihilated, displaced, and polarity-reversed on demand by applying a spin-polarized current pulse, and are easily switchable among the eight degenerate states. In particularly, the kinks can be switched toward the ferromagnetic-like states and backward reversibly by applying two successive current pulses, indicating the capability of writing and deleting the kink structures. These findings predict the existence of Néel-type magnetic kinks in the square-shaped nanostructures, as well as provide us a promising approach to tailor the kinks by utilizing the corners of the nanostructures, and control these states by spin-polarized currents. The present work also suggests a theoretical guide to explore other chiral magnetic textures in nanostructures of polygon geometries.

Keywords: magnetic kinks, chiral magnets, magnetic dynamics in nanostructures, micromagnetic simulations, spin-polarized currents

OPEN ACCESS

Edited by:
Huaiyang Yuan,
Utrecht University, Netherlands

Reviewed by:
Juliano Denardin,
University of Santiago, Chile
Kiyou Shibata,
The University of Tokyo, Japan

****Correspondence:***
Ji-Pei Chen
chenjp@gzhu.edu.cn,
chankaipui@163.com
Xing-Sen Gao
xingsengao@scnu.edu.cn

Specialty section:
This article was submitted to Condensed Matter Physics, a section of the journal Frontiers in Physics

Received: *15 March 2021*
Accepted: *07 July 2021*
Published: *28 July 2021*

Citation:
Chen J-P, Lin J-Q, Song X, Chen Y, Chen Z-F, Li W-A, Qin M-H, Hou Z-P, Gao X-S and Liu J-M (2021) Control of Néel-type Magnetic Kinks Confined in a Square Nanostructure by Spin-Polarized Currents. Front. Phys. 9:680698. doi: 10.3389/fphy.2021.680698

1 INTRODUCTION

A magnetic skyrmion is a topologically stable configuration often observed in chiral magnets with broken inversion symmetry. The nanoscale skyrmion shows particle-like behavior, as it can be moved, created, and annihilated. These characters make it promising candidate as information carrier for future memory devices and logic devices [1–6]. It has thus aroused intense research efforts in recent years, leading to a series of breakthrough achievements in manipulation of skyrmion states, via injected spin-polarized currents, external electric-field, and so on [7–14]. For the application of skyrmions in spintronic devices, many feasible designs have been proposed for confining the skyrmions in geometric nanostructures, such as nanostripes and nanodisks, which may allow the precise control of individual skyrmions [8–10]. These achievements pave the way towards

all-electrical manipulation schemes [2, 3], and underpin the skyrmion-based information storage concepts, such as the skyrmion-based racetrack memory, high density magnetic random access memory, and logic gates, etc. [2–6, 8, 9].

These fascinating physical properties also inspired an ongoing search for new types of magnetic topological textures, for instance, fractional skyrmion emerging in various chiral and frustrated magnets [15–21], which exhibit some unusual physical phenomena distinctly different from skyrmion-host chiral magnetic materials such as MnSi and $Fe_{1-x}Co_xSi$ systems [22, 23]. Moreover, some recent observations indicated that fractional skyrmions also emerge in geometric nanostructures due to the effects of geometric confinement and shape anisotropy [24–28]. For example, it was observed in Lorentz transmission electron microscopy (TEM) images of FeGe nanostripes that, the skyrmions survive when the width of the nanostripe much larger than the single skyrmion size, whereas some merons form at the edges that are not large enough for accommodating a complete skyrmion [24, 25].

Generally, the presence of edges and corners in nanostructures can be utilized to tailor the magnetic textures and modify their dynamics behaviors. For the skyrmion confined in ultrathin film nanostructures with Dzyaloshinskii-Moriya (DM) interaction, the boundary constrictions naturally make the magnetization orientation undergo the 180° rotation at the edges, forming the so-called kink or π domain wall configurations [2, 15, 29–32]. Depending on the crystal symmetry of chiral magnets, two distinct types of chiral kinks, namely, Néel-type and Bloch-type kinks, are favorable in interfacial and bulk DM interaction systems respectively [29, 30]. It had been theoretically proposed in chiral magnets that the skyrmions, antiskyrmions, and other magnetic configurations can be naturally interpreted in terms of chiral kinks. These kinks carry a topological charge and allow to construct new topological particle-like states [15, 31, 32]. In addition, the previous studies demonstrated that some special magnetic textures often appear in the corners of the polygon geometries like triangles, squares, rectangles, in which the corners may also act as pinning sites for the domain wall motion [33–36]. This indicates that the nanostructure with polygon geometries may provide a unique platform for studying the kink structures, favoring the control of the magnetic states, by utilizing their edges and corners. Certainly, there are more open questions to be explored along this line. For instance, is it possible to realize some new kink structures beyond the skyrmions and merons in nanostructures? Is it possible the kink structures stable in nanostructures without the assistance of external magnetic field? Is it possible to manipulate these kinks by pure electric currents? These issues are very critical for our understanding the physical properties of the new type chiral magnetic structures in confined nanostructures.

Inspired by this motivation, the purpose of our work is to explore new kink structures in nanostructures by using micromagnetic simulations and Monte Carlo simulations. In this work, we aimed at studying the square-shaped nanostructures with width smaller than the single skyrmion size. We demonstrated an exotic Néel-type kink structure, which can stably exist in the corners of the square-shaped nanostructures in the absence of external magnetic field. Such kinks possess eight switchable degenerate states and can be created, annihilated, displaced, and polarity-reversed by applying spin-polarized currents.

2 MODEL AND SIMULATION METHODS

In this work, the magnetic state in an ultrathin square nanostructure of chiral magnets is described by a classical Heisenberg model. The Hamiltonian consists of ferromagnetic exchange interaction (J_{FM}), DM interaction (D), anisotropy (A), and Zeeman term (B_z) [8, 37, 38]:

$$\mathcal{H} = -J_{FM}\sum_i \mathbf{m}_i \cdot \left(\mathbf{m}_{i+\widehat{x}} + \mathbf{m}_{i+\widehat{y}}\right) - D\sum_i \left(\mathbf{m}_i \times \mathbf{m}_{i+\widehat{x}} \cdot \widehat{y} + \mathbf{m}_i \times \mathbf{m}_{i+\widehat{y}} \cdot \widehat{x}\right) - A\sum_i (\mathbf{m}_i \cdot \widehat{z})^2 - \boldsymbol{B}_z \cdot \sum_i \mathbf{m}_i, \quad (1)$$

where the magnetic moments are imposed on a two-dimensional $L \times L$ square lattice with free boundary conditions. $\mathbf{m}_i$ denotes the magnetic moment at site i in the xy-plane, with fixed length $|\mathbf{m}_i| = 1.0$. The magnetic field $\boldsymbol{B}_z = B_z\boldsymbol{e}_z$ is applied normal to the xy-plane and easy-axis anisotropy ($A > 0$) is along the ± z-axis. In the simulations, we have neglected the dipole-dipole interactions. This treatment is suitable for chiral magnets with strong DM interaction and weak dipole-dipole interactions such as Pd/Fe bilayers on Ir(111) substrate [39, 40]. For Pd/Fe/Ir(111) the magnetic dipolar energy is very weak in energy scale in comparison with the ferromagnetic exchange energy and DM interaction, and thus it can be effectively included into the anisotropy energy. We choose typical parameters for Pd/Fe/Ir(111) as $J_{FM} \equiv 2.95$ meV, $D/J_{FM} = 0.27$, $A/J_{FM} = 0.05$, and a typical lattice constant $a = 5$ Å [39, 40].

To investigate the dynamics of the magnetic structures driven by the spin-polarized current, we numerically solved the Landau-Lifshitz-Gilbert (LLG) equation by using fourth-order Runge-Kutta method [8, 10, 41, 42]:

$$\frac{d\mathbf{m}_i}{dt} = -\gamma\mathbf{m}_i \times \boldsymbol{B}_i^{eff} + \alpha\mathbf{m}_i \times \frac{d\mathbf{m}_i}{dt} + \mathbf{T}, \quad (2)$$

with the effective field $\boldsymbol{B}_i^{eff} = -(1/\hbar\gamma)(\partial\mathcal{H}/\partial\mathbf{m}_i)$, the gyromagnetic ratio $\gamma = g_s\mu_B/\hbar$ (here g_s is the electron spin g-factor, and μ_B is the Bohr magneton), and Gilbert damping α. The first and second terms describe respectively the gyromagnetic precession and the Gilbert damping, and the third term $\mathbf{T}$ denotes the spin transfer torque (STT) due to the spin-polarized current.

The skyrmion motion can be driven by spin-polarized current flowing in the nanostructure along either the in-plane or out-of-plane direction. For simulations of the skyrmion dynamics induced by the current-in-plane (CIP) injection, the corresponding torque $\mathbf{T}_{CIP}$ is given by the following form [41]:

$$\mathbf{T}_{CIP} = \frac{P_e a^3}{2eM_s}(\boldsymbol{j}_{CIP} \cdot \nabla)\mathbf{m}_i - \frac{P_e a^3 \beta}{2eM_s}[\mathbf{m}_i \times (\boldsymbol{j}_{CIP} \cdot \nabla)\mathbf{m}_i], \quad (3)$$

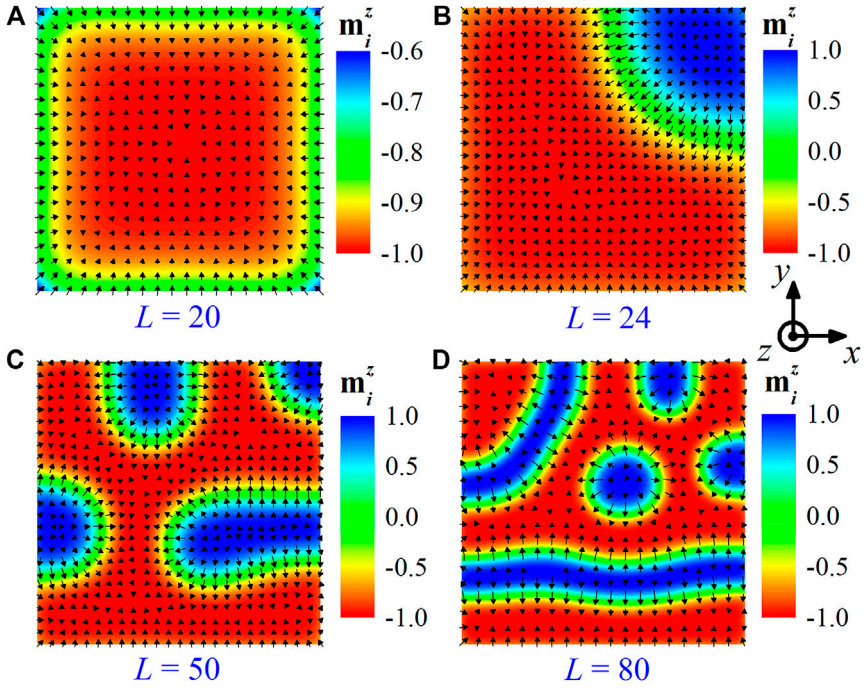

FIGURE 1 | Size effect of nanostructures on the equilibrium magnetic states. Some typical magnetic configurations are shown for square-shaped nanostructures with lateral sizes of **(A)** $L = 20$ (~10 nm), **(B)** $L = 24$ (~12 nm) **(C)** $L = 50$ (~25 nm), and **(D)** $L = 80$ (~40 nm). Here the magnetic field $B_z = -0.008\, J_{FM}$ (~−0.1 T) is applied along the −*z*-axis. To illustrate the magnetic configurations, we used the color map to scale the magnetization components along *z*-axis (out-of-plane) m_i^z, and used the arrows to describe the on-plane *xy* components m_i^{xy}.

where the first and second terms represent the coupling between magnetic moments and spin-polarized current $\boldsymbol{j}_{\mathrm{CIP}}$ via the spin transfer torque and via the non-adiabatic effects, with β the non-adiabaticity factor. M_s is the saturation magnetization, P_e is the polarization rate of the electric current, and e is the elementary charge.

For the current-perpendicular-to-plane (CPP) injection, the current-induced spin transfer torque $\mathbf{T}_{\mathrm{CPP}}$ includes an in-plane Slonczewski torque and an out-of-plane field-like torque [8, 42, 43]:

$$\mathbf{T}_{\mathrm{cpp}} = \gamma u\left(\mathbf{m}_i \times \mathbf{m}_{\mathrm{p}} \times \mathbf{m}_i\right) - \gamma\xi u\left(\mathbf{m}_i \times \mathbf{m}_{\mathrm{p}}\right), \tag{4}$$

where $u = \left|\frac{\hbar}{e}\right| \frac{j_{\mathrm{CPP}} P_e}{2dM_s}$ is the Slonczewski torque coefficient, d the film thickness of FM layer, j_{CPP} the current density, $\mathbf{m}_{\mathrm{p}}$ is the electron polarization direction, and ξ is the amplitude of the out-of-plane torque relative to the in-plane one. In the simulations, we fixed the coefficient $\xi = 0.2$, the polarization rate $P_e = 0.4$, gyromagnetic ratio $\gamma = 1.0$, Gilbert damping $\alpha = 0.3$, and non-adiabaticity factor $\beta = 0.1$, as the typical parameters for studying the current-induced skyrmion dynamics [8, 10, 41]. The simulated time t is measured in the units of $\tau \equiv \hbar/J_{\mathrm{FM}} \sim 0.2$ ps, and current density j are scaled by $\kappa_{\mathrm{CIP}} \equiv 2eJ_{\mathrm{FM}}/P_e a^2\hbar \sim 1.4 \times 10^{13}$ Am^{-2} for the CIP case, and $\kappa_{\mathrm{CPP}} \equiv 2edM_sJ_{\mathrm{FM}}/\hbar^2 P_e\gamma \sim 8.5 \times 10^{13}$ Am^{-2} for the CPP case, respectively [41]. Here we chose the typical parameters for Pd/Fe/Ir(111) as $d = 0.4$ nm and $M_s = 1.1$ MA/m, and used these values to estimate the units of simulated time and current density.

To get the zero-temperature equilibrium state, we adopted a specific simulation scheme: the lattice was initialized as a paramagnetic phase at sufficiently high temperature, and annealed for obtaining the state at a low temperature, by using the Metropolis Monte Carlo simulation combined with over-relaxation algorithm [17, 18, 44]. Then the configuration was further relaxed for the equilibrium state, by solving the LLG equation under $\mathbf{T} = 0$ with long enough equilibration time.

In addition, the kink dynamics is controlled by injecting a CIP-type or CPP-type spin-polarized current pulse on demand. We introduced the schemes in our simulations for setting the amplitude and duration of current pulses as follows: 1) First, we tested the effect of amplitude of current density on the kink dynamics and chose the suitable amplitude of current pulses for control (generation, creation, annihilation, displacement or polarity reversal) of the kink states. 2) Then we carefully tracked its dynamics and turned off the current once the germinal kink appears or kink shifts (in this procedure, the current duration is determined), and further relaxed the system by solving LLG equation under zero-current condition to get an equilibrium kink state.

3 SIMULATION RESULTS

3.1 Size Effect of Nanostructures on the Magnetic Structures

We first investigated the size effect of the nanostructures on magnetic structures. The simulations were carried out on a $L \times L$ square lattice with free boundary conditions. The zero-temperature equilibrium states for the lattices with different sizes were obtained, and some of the typical configurations were presented in **Figure 1**. Here a magnetic field $B_z = -0.008\, J_{FM}$ (corresponding to ~ −0.1 Tesla, as estimated

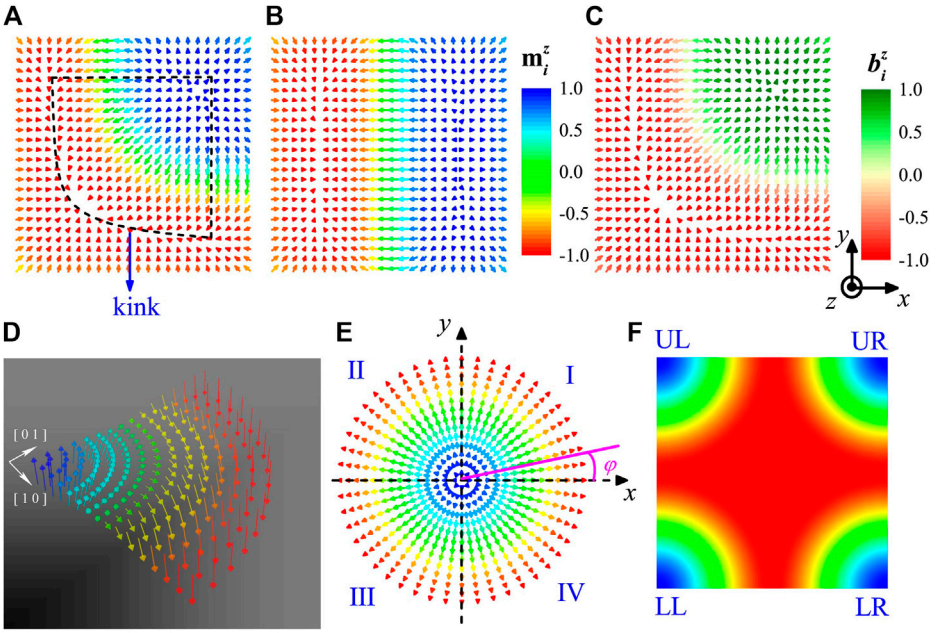

FIGURE 2 | (A) The magnetic structure obtained from the above state in **Figure 1B** after withdrawal of magnetic field. A kink structure is enclosed by the dash lines. **(B)** A spiral structure, as the possible ground state of nanostructure with a size of 24 × 24 square lattices (i.e., ~12 × 12 nm) in the absence of magnetic field. **(C)** The reduced effective field $\boldsymbol{b}_i$ profile corresponding to the magnetic structure in **(A)**. **(D)** Schematic illustrations of the kink structure **(E)** Schematic illustrations of an isolated skyrmion configuration, which can be divided into four quadrants along the dash lines, denoted as kink I, II, III, and IV. **(F)** These kinks may appear in one of the four possible corners (i.e., LL, LR, UR or UL corner) in the nanostructure, corresponding to kinks residing in the four possible quadrants (i.e., quadrant I, II, III or IV).

with the magnetic moment ~3.0 μ_B obtained from density functional theory for Pd/Fe/Ir(111) in Ref. [40]) is applied along the $-z$-axis, which is sufficient for creating the skyrmion states here. In the following, we used an external magnetic field to generate the exotic magnetic kink textures in the nanostructures, and then we demonstrated an alternative way for creating kink by applying spin-polarized current.

As one may see in **Figure 1A**, a bubble domain arises in the square nanostructure at small lateral size L = 20 (~10 nm). As the size increases to L = 24 (~12 nm), a kink-like structure forms in the corner of the square nanostructure, surrounded by the ferromagnetic domain, as will be discussed below. For L = 50 (~25 nm), it was observed that some half-skyrmion-like (meron-like) structures with topological charge $|Q| \approx 1/2$ and elongated stripes (fractional skyrmion) with topological charge $0 < |Q| < 1$ emerges at the edge of the lattice, together with a kink-like structure that appears in the corner. Further increasing the size, the magnetic states evolve into multi-domains composed of spiral domains, edge-merons, and skyrmion as seen in **Figure 1D** for the relatively large size L = 80 (i.e., ~40 nm). It is interesting that the kink-like, meron-like, and skyrmion states tend to nucleate in the corner, the edge, and the inner region of the nanostructure, respectively. These are reasonable likely due to the different boundary constrictions on the formation of magnetic structures, which manifests the strong boundaries and geometric confinement effects in the nanostructures. It is noted that some similar edge states are also found experimentally and theoretically in diverse magnetic materials that host skyrmions with constricted geometry, as a consequence of the effects of geometric boundaries and confinements [37, 45].

3.2 Néel-Type Magnetic Kinks

Now we focus on the intriguing features of kink-like structures and analyzing their current-induced dynamics in this paper. For this, we adopted a small square shaped nanomagnet consisting of 24 × 24 square lattices (~12 × 12 nm) for studying the kink-like structure, in the rest part of this work. We first tested the stability of the kink-like structure in **Figure 1B** once the magnetic field was removed. For this, the magnetic structure was relaxed for the equilibrium state by solving the LLG equation, in which we used the kink-like state shown in **Figure 1B** as the initial state, and set $B_z = 0$ in the calculation. It was found that the kink-like structure remains stable without the assistance of an external magnetic field, as presented in **Figure 2A**. Note that the magnetic structure enclosed by the dash lines in **Figure 2A** is called Néel-type magnetic kink in this work, in which the magnetic moments undergo 180° rotation from the upward direction at its center to the downward direction in the periphery. The schematic magnetic configuration for a Néel-type kink is displayed in **Figure 2D**. For simplicity, we call the kink-like state as the kink state hereafter.

To explore the possible ground state for the nanomagnet of 24 × 24 square lattices at $B_z = 0$, the system was initialized from a the paramagnetic state at sufficiently high temperature T, and cooled down gradually until it reaches a very low T under $B_z = 0$, using Monte Carlo simulations with simulated annealing technique [17, 18, 44]. Then the system was further relaxed for the zero-temperature equilibrium state by solving LLG equation. As a result, a spiral structure forms as shown in **Figure 2B**. The numerical calculations indicate that the total

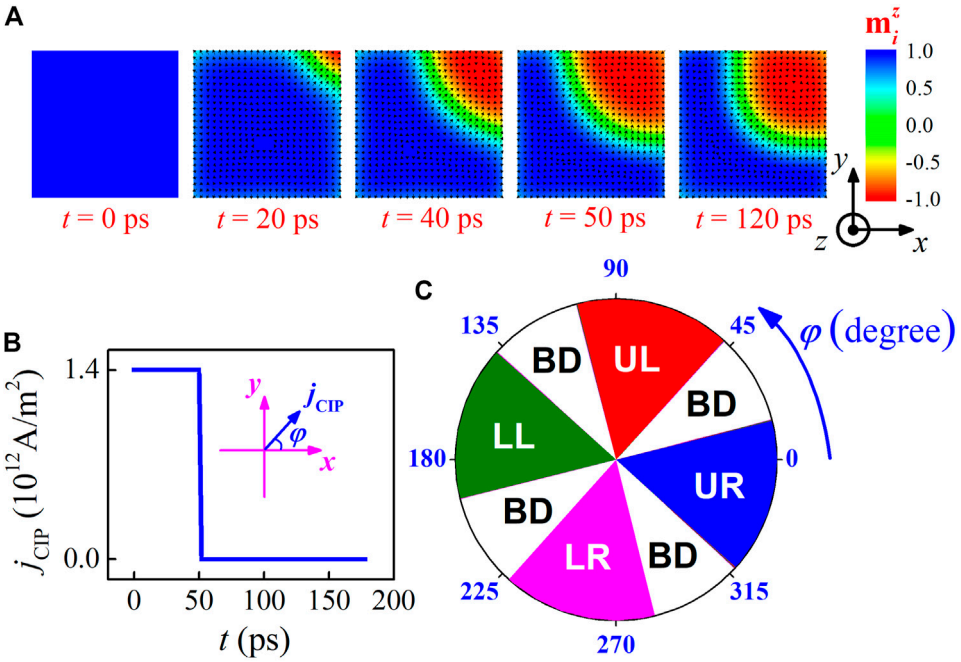

FIGURE 3 | The generation of kink from the initial ferromagnetic state, by injecting into the nanostructure an in-plane spin-polarized current pulse. **(A)** Snapshots show the formation process of the UR kink, driven by the current pulse with injection angle $\varphi = 10^{\circ}$. **(B)** A current pulse with current density $j_{CIP} = 1.4 \times 10^{12}$ Am^{-2} and duration $t_{dur} = 50$ ps. The insert shows the direction of the CIP injection, defined by the angle φ with respect to the x-axis. **(C)** A pie chart shows four colored sections, with the sections colored red, green, pink and blue representing the angle conditions for generation of UL, LL, LR, and UR kinks, respectively. The white region on the pie chart corresponds to angle conditions for the formation of bubble domain (abbreviated to "BD") like that shown in **Figure 1A**. Here the pie chart is generated from a set of data points for $\varphi = 2, 4, \ldots, 360^{\circ}$ at intervals of 2°.

energy of the spiral structure is a little smaller than that of the Néel-type kink structure. These results suggest the spiral structure to be the possible zero-field ground state, while the Néel-type kink structure to be a metastable state at $B_z = 0$, other than the minimum-energy state.

To further estimate the stability of the metastable Néel-type kink state under $B_z = 0$, we calculated the reduced local effective field $\boldsymbol{b}_i \equiv \boldsymbol{B}_i^{eff}/\left|\boldsymbol{B}_i^{eff}\right|$ acting on the i-th magnetic moment $\mathbf{m}_i$. Interestingly, it was found in **Figure 2C** that the $\boldsymbol{b}_i$ distribution and the magnetic kink state in **Figure 2A** are similar in spatial profile, and almost all the magnetic moments in the kink structure are oriented in parallel to the local field $\boldsymbol{b}_i$, making the metastable kink structure self-sustaining. In addition, it was noted that the anisotropy energy $\mathcal{H}_{ani} = -A\sum_i (\mathbf{m}_i \cdot \hat{z})^2$ contributes to the effective field in terms of $-(1/\hbar\gamma)(\partial\mathcal{H}_{ani}/\partial\mathbf{m}_i) = (2/\hbar\gamma)A\mathrm{m}_i^z\boldsymbol{e}_z$. This suggests that the anisotropy plays an important role in guaranteeing the robustness of the metastable kink state, since the effective field $(2/\hbar\gamma)A\mathrm{m}_i^z\boldsymbol{e}_z$ makes the stabilization of the out-of-plane magnetization component m_i^z [46, 47]. In this regard, we reckon that the kink structure is a robust state after the withdrawal of the magnetic field, due to the kink state is trapped in an energy valley in the configurational energy landscape [47].

In fact, one may take account of the kink structures from the prototypical Néel skyrmion, whose configuration can be viewed as a coplanar spiral with magnetic moments lying in a plane perpendicular to the xy plane [1, 38]:

$$\begin{cases} \mathbf{m}(\mathbf{r}) = \sin(\mathbf{q}\cdot\mathbf{r})\boldsymbol{e}_q + \cos(\mathbf{q}\cdot\mathbf{r})\boldsymbol{e}_z & |\text{core}-\text{up}, p = 1 \\ \mathbf{m}(\mathbf{r}) = \sin(\mathbf{q}\cdot\mathbf{r}+\pi)\boldsymbol{e}_q + \cos(\mathbf{q}\cdot\mathbf{r}+\pi)\boldsymbol{e}_z & |\text{core}-\text{down}, p = -1 \end{cases}, \tag{5}$$

where the spatial variables of magnetization are defined in polar coordinates $\mathbf{r} = (\mathrm{r}\cos\varphi, \mathrm{r}\sin\varphi)$, and the magnitude of spiral wave vector is $|\mathbf{q}| = \pi/R$, with the direction denoted by unit vector $\boldsymbol{e}_q = \cos\varphi\boldsymbol{e}_x + \sin\varphi\boldsymbol{e}_y$. For the isolated Néel skyrmion configuration, the core magnetization points upward or downward, and smoothly changes to the opposite direction in the peripheral circle with radius R. We considered skyrmion structure with core-up (core-down) magnetization carries core polarity $p = 1$ ($p = -1$), as the skyrmion with $p = 1$ depicted in **Figure 2E**. Here, R is used to define the radius of skyrmion, with $0 \le \mathrm{r} \le R$ and the azimuthal angle $0 \le \varphi \le 2\pi$ for a single skyrmion.

To proceed, one may divide an isolated skyrmion configuration into four quadrants along the dash lines, as illustrated in **Figure 2E**. The magnetic structures in quadrant I, II, III, and IV can be described by **Eq. 5**, with the azimuthal angle $0 \le \varphi_{\mathrm{I}} \le \pi/2$, $\pi/2 \le \varphi_{\mathrm{II}} \le \pi$, $\pi \le \varphi_{\mathrm{III}} \le 3\pi/2$, $3\pi/2 \le \varphi_{\mathrm{IV}} \le 2\pi$, respectively. The kink may appear in one of the four possible corners, i.e., the upper left (UL), upper right (UR), lower left (LL) or lower right (LR) corner of the nanostructure in the simulations, as shown in **Figure 2F**. The LL, LR, UR, and UL kink structures correspond to the well-defined kinks residing in the quadrant I, II, III, and IV, respectively. In addition, we define the polarity of the kink with core-up (core-down) as $p = 1$ ($p = -1$). Therefore, the kinks in the nanostructure can carry the core polarity

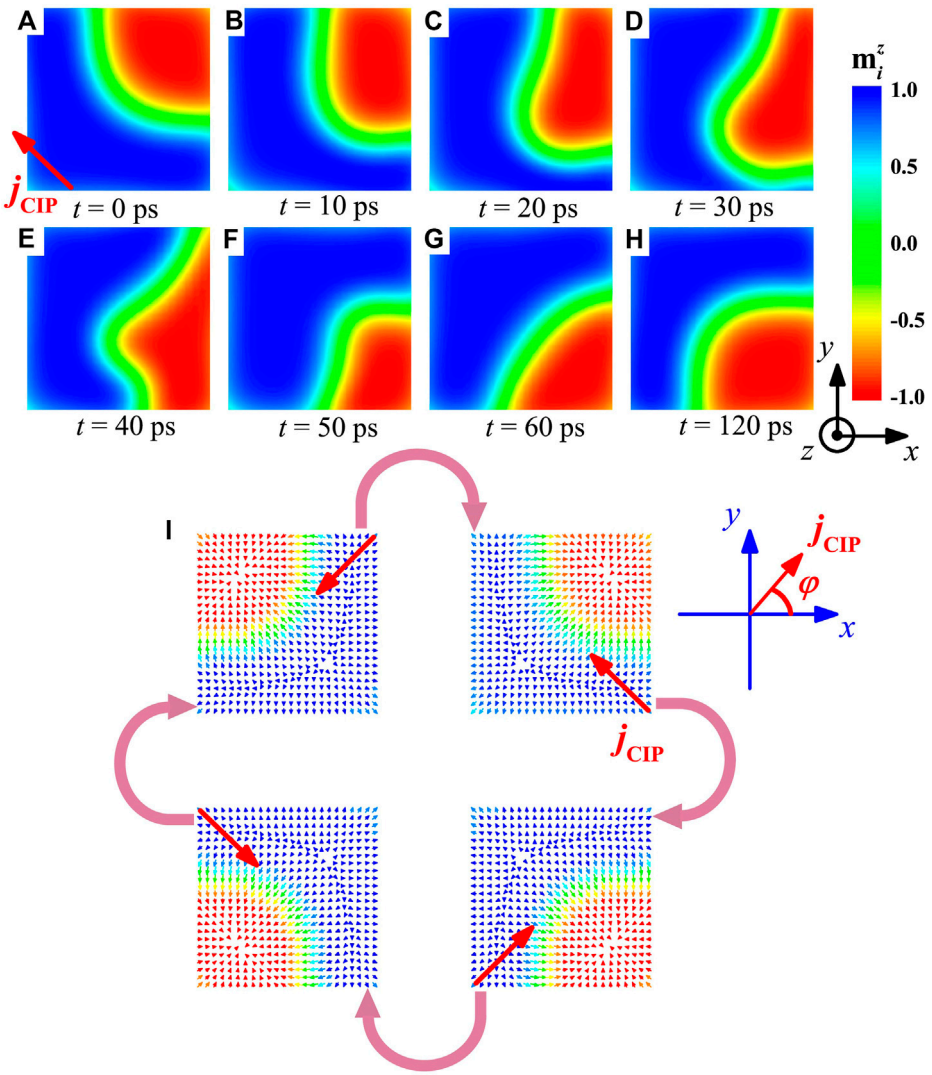

FIGURE 4 | (A)–(H) The gradual shift of kink from UR to LR corner, driven by in-plane current pulse with current density J_{CIP} = 1.4 × 10^{12} Am^{-2}, current duration t_{dur} = 50 ps, and injection angle φ = 135°. **(I)** Schematic illustrations of switching sequences for the kinks driven by in-plane current pulse. Here we used the straight red arrows to mark the injection direction of current J_{CIP}, and the curved pink arrows to denote the switching sequences of magnetic kinks.

$p = \pm 1$, and can reside in one of the four possible corners, constituting 8 degenerate kink states. By comparison, the single skyrmion often appears in circular shaped nanodisks, and possesses only two degenerate states with core polarity $p = \pm 1$ [8, 48–50]. In this sense, the kinks in the square shaped nanostructure have the special feature of multiple degenerate states.

3.3 Generation and Switching of Kinks by In-Plane Current Pulse

In this section, we studied the generation of kinks by injecting into the nanostructure an in-plane spin-polarized current pulse. Here, the direction of the CIP injection is defined by the angle φ with respect to the x-axis (see in **Figure 3B**), and φ is tunable. Note that in the following study, no external magnetic field was applied.

The simulations start from the initial ferromagnetic phase, with all magnetic moments aligning along z-axis at t = 0.0 ps (see **Figure 3A**). We first tested the effect of CIP on the kink dynamics, using a moderate current density $j_{CIP} = 0.1\kappa_{CIP} \sim 1.4 \times 10^{12}\,Am^{-2}$ with current duration $t_{dur} = 250\,\tau \sim 50$ ps. **Figure 3A** shows the formation process of the UR kink for a typical case of $\varphi = 10^{\circ}$. At the beginning (t = 20 ps) of the current duration, the embryo of kink pattern emerges in the UR corner of the nanostructures. This pattern gradually enlarges, and becomes a rough kink at t = 50 ps. Subsequently, the current is turned off and the system evolves into an equilibrated kink state at t = 120 ps.

Further simulations demonstrated that the generation of kinks is sensitive to injection angle φ, with the simulated results summarized in **Figure 3C**. It was found that the UR, UL, LL, and LR quarters can also be created respectively for −42°

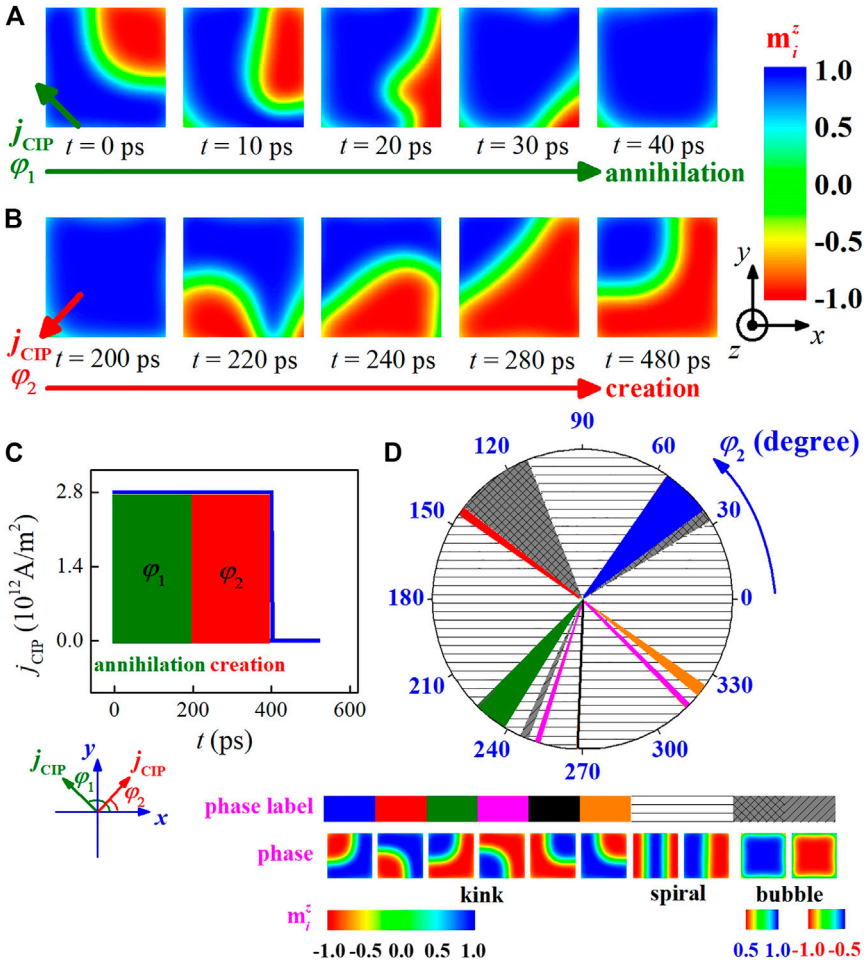

FIGURE 5 | The annihilation and creation of kink is achieved by applying CIP current pulses. **(A)** and **(B)** Snapshots show a typical case for the annihilation and creation process of kink induced by two successional current pulses with injection angle φ_1 = 135° and φ_2 = 230°. Simulations start from the initial UR kink state with p = −1. **(C)** Here two successional current pulses with injection angle φ_1 = 135° and tunable injection angle φ_2, current density j_{CIP} = 2.8 × 10^{12} Am^{-2} and duration t_{dur} = 20 ps is considered. These two pulses are used to annihilate and create the kink state, respectively. **(D)** The phase diagram for the equilibrated states at t = 520 ps after relaxation as a function of angle φ_2 was summarized. The various kinks, spiral states, and bubble states are marked by the colored pieces, striped pattern and grid pattern, respectively. The color map below is used to scale the magnetization components along z-axis m_i^z. Here the pie chart is generated from a set of data points for φ_2 = 1, 2, . . ., 360° at intervals of 1°.

≤ φ ≤ 14°, 48° ≤ φ ≤ 104°, 138° ≤ φ ≤ 194°, and 228° ≤ φ ≤ 284°, while some bubble domain states form beyond these angles φ (see the while region in the **Figure 3C**). Note that the kinks with p = −1 presented here are generated from the initial ferromagnetic phase with magnetization along the z-axis. If the initial ferromagnetic phase is magnetized along the −z-axis, the lattices will evolve to the kinks with p = 1. Therefore, all the eight degenerate kink states can be created by tuning the direction of CIP injection with two different initial ferromagnetic orientations.

Next, we investigated the switching between these kinks using in-plane current pulse, which is fundamental to understand their dynamics properties. The current pulse (j_{CIP} = 1.4 × 10^{12} Am^{-2}, current duration t_{dur} = 50 ps) with varying angle φ is exerted on the initial UR kink state with p = −1. Simulated results reveal that the kink can transfer from UR corner to the LR corner in a clockwise (CW) direction, driven by current with 116° ≤ φ ≤ 178°. However, it was noted that the UR kink cannot move to LL corner in a counterclockwise (CCW) direction or to diagonal UL corner with the adopted simulation parameters. **Figures 4A–H** show the dynamic process for the typical case of φ = 135°. We can see clearly that the upper part of the UR kink is pushed towards the right-edge of the nanostructures, and the lower part is simultaneously dragged to the bottom of the nanostructures (see **Figures 4A–D**). Although the entire kink pattern deforms largely in this process, it gradually turns in a CW direction and eventually moves to the LR corner at t = 50 ps (see **Figures 4E,F**). After that the current is switched off to zero for reaching the equilibrated kink state in the relaxation procedure. Moreover, simulations for the kinks with p = −1 indicate that their switching sequences can be summarized as follows: UR kink → LR kink → LL kink → UL kink with suitable angle φ, as shown schematically

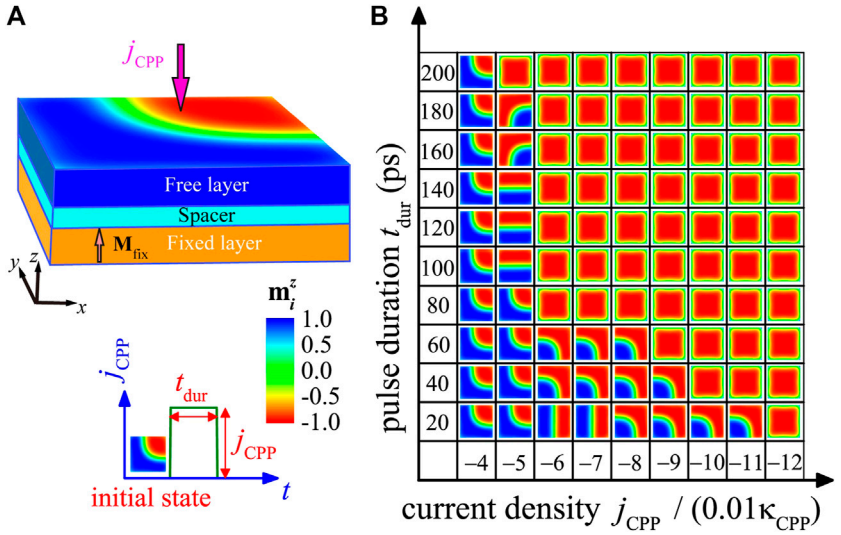

FIGURE 6 | (A) Sketch of a MTJ nanopillar consisting of the top and bottom layers of ferromagnet, and the spacer layer of insulator. **(B)** Simulations for the evolutions of kink driven by a CPP pulse, starting from an initial kink with $p = -1$ in UR corner of the nanostructure. A phase diagram for the equilibrated states obtained after the current pulses, as a function of current density j_{CPP} and duration time t_{dur}.

in **Figure 4I**. In this procedure, the switching sequences is in a CW direction, and the kink polarity has not been reversed by the CIP injection.

3.4 Annihilation and Creation of Kinks by In-Plane Current Pulses

In this section, we presented an effective way to annihilate and create the kink by applying two successive CIP pulses, as the results shown in **Figure 5**. Our simulations start from the initial UR kink state with $p = -1$ in **Figure 5A**. We first found that the kink can be annihilated by applying a CIP current pulse, with a larger current density $j_{CIP} = 2.8 \times 10^{12}$ Am^{-2} and an appropriate injection angle $\varphi_1 = 135^\circ$. Here two successive current pulses are used to annihilate and create the kink states respectively, with injection angle $\varphi_1 = 135^\circ$ for the first pulse, and tunable injection angle φ_2 for the second one. The current duration $t_{dur} = 200$ ps is considered for both two pulses, as shown in **Figure 5C**. **Figure 5A** displays the annihilation of the kink driven by the first current pulse with angle φ_1, whose pattern rotates along a CW direction and disappears at the LR corner of the nanostructure, forming the ferromagnetic-like state at $t =$ 40 ps. The ferromagnetic-like state remains at 40 ps $\leq t \leq$ 200 ps, and we may see that most magnetic moments orientate along the z-axis in the ferromagnetic-like state, though some remaining magnetic moments align in the xy-plane at the LR and LL corners of the nanostructure.

More interestingly, the simulated results reveal that some other kink states can be created from the ferromagnetic-like state, by applying the second current pulse with varying injection angle φ_2. The typical case for $\varphi_2 = 230^\circ$ is presented in **Figure 5B**, in which the domains first appear and gradually grow in the LL, and LR corners during 200 ps $\leq t \leq$ 240 ps. The new embryonic kink forms at $t = 280$ ps and remains during 280 ps $\leq t \leq$ 400 ps, and it finally evolves into a core-up kink in the UL corners after the relaxation with $j_{CIP} = 0$. In this process, the kink has been annihilated and created by two successive current pulses, in which the switching between the kink and ferromagnetic-like states is reversible. This indicates the capability of reversible writing and deleting the kink states.

Further simulations generate the phase diagram for the equilibrated states at $t = 520$ ps as a function of φ_2, as summarized in **Figure 5D**. It was noted that current pulses with $37^\circ \leq \varphi_2 \leq 55^\circ$, $143^\circ \leq \varphi_2 \leq 145^\circ$, and $320^\circ \leq \varphi_2 \leq 325^\circ$ may create the kinks with $p = -1$ in the UL, LL, and UR corners of the nanostructure, while current pulses with $226^\circ \leq \varphi_2 \leq 238^\circ$, $252^\circ \leq \varphi_2 \leq 253^\circ \cup 314^\circ \leq \varphi_2 \leq 315^\circ$, and $\varphi_2 = 268^\circ$ generate the kinks with $p = 1$ in the UL, LL, and UR corners, respectively. In addition, some bubble or spiral states form beyond these angles φ (see the striped-pattern and grid-pattern region in **Figure 5D**), with some typical configurations shown at the bottom of **Figure 5D**. Regarding early investigations on magnetic vortex, it was demonstrated that the vortex polarity reversal may be triggered by a CIP pulse through the formation of a vortex-antivortex pair [51], or by an alternating CIP through the resonant dynamics [52]. However, for the skyrmion in chiral magnets, CIP is usually used for displacing the skyrmion, while cannot change the skyrmion polarity in the dynamics [8, 41, 42]. In this sense, the core polarity reversal of kink can be achieved by CIP pulse, which is analogous to that of vortex system [51, 52]. From the simulation results and analyses in *Generation and Switching of Kinks by In-Plane Current Pulse and Annihilation and Creation of Kinks by In-Plane Current Pulses*, one may create, annihilate, displace, and reverse the kink on demand by adjusting the CIP pulse injections.

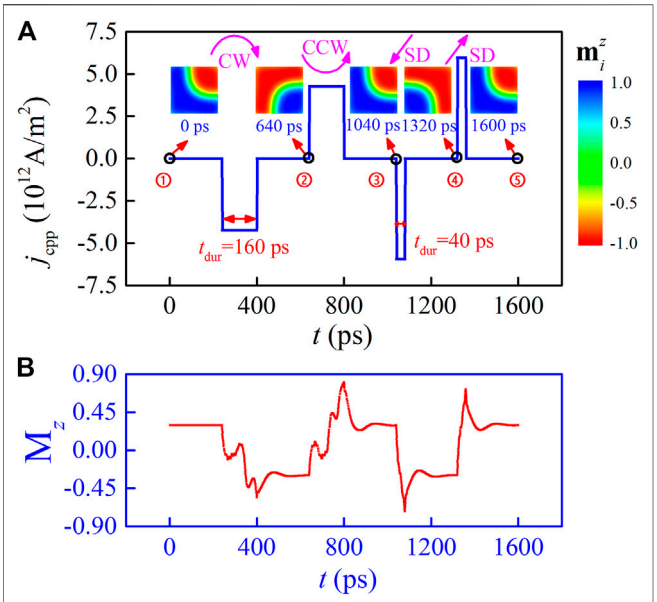

FIGURE 7 | (A) The polarity reversal of kinks induced by CPP pulses, accompanying with the displacements of kinks. The first and second CPP pulses with $j_{CPP} = \pm 0.05\kappa_{CPP} \sim \pm 4.3 \times 10^{12}$ Am^{-2} and $t_{dur} = 160$ ps result in the rotation of kink along CW and CCW directions respectively, while the third and fourth CPP pulses with $j_{CPP} = \pm 0.07\kappa_{CPP} \sim \pm 6.0 \times 10^{12}$ Am^{-2} and $t_{dur} = 40$ ps shifts diagonally (SD) the kink to the diagonal corner of the nanostructure. Snapshots show the kink states (①–⑤) at some typical time before and after the pulses in the evolutions. **(B)** Plots of variations of out-of-plane magnetization M_z as a function of time t, responding to the polarity reversal of kinks.

3.5 Manipulation of Kinks by Out-of-Plane Current Pulse

In this section, we investigated the core polarity reversal of the kinks with out-of-plane current, which is also a fundamental issue for understanding their dynamics properties. One may build a magnetic tunnel junction (MTJ) or spin valve to locally address the kinks [5, 53]. As schematically shown in **Figure 6A**, a typical MTJ structure consists of the top and bottom two layers of ferromagnet, which is separated by an ultrathin spacer of insulator. The top ferromagnetic layer is a free layer which presents a kink state, while the bottom one is a fixed layer with the magnetization $\mathbf{M}_{fix}$ fixed along the z direction. When a spin current is injected into the bottom fixed layer along the z direction, the spin is polarized along z direction. The polarized spin current then flows through the insulating layer to the free layer, acting on its magnetizations with CPP-type STT, described by **Eq. 4**. One may reverse the polarization direction of the spin current, by injecting the spin current into the top free layer along the $-z$ direction. Here we defined the current density $j_{CPP} > 0$ and $j_{CPP} < 0$ in **Eq. 4** corresponding to the injection of spin current flowing along z and $-z$ direction, respectively. Our simulations start from an initial UR kink with polarity $p = -1$ as a general representative. Note that the CPP-type STT induced by current $j_{cpp} < 0$ tends to align the magnetic moments in the free layer along the $-z$ direction, thus the kink may be reversed to its image structure with polarity $p = 1$. Contrarily, the kink with polarity $p = 1$ can be reversed, once the spin current is injected along the z direction.

We first studied the dynamics of the kink driven by various current densities j_{CPP} and duration time t_{dur}, and the phase diagram for the equilibrated states obtained after the current pulses was summarized in **Figure 6B**. The results show that the kink is immovable under low current densities $|j_{CPP}| < 0.04\kappa_{CPP}$ ($\sim 3.4 \times 10^{12}$ Am^{-2}), due to the weak STT strength. It was seen that the kink may be pulled at current densities larger than the critical value $|j_{CPP}| = 0.05\kappa_{CPP}$ ($\sim 4.3 \times 10^{12}$ Am^{-2}). At an intermediate current density $j_{CPP} \sim -4.3 \times 10^{12}$ Am^{-2} and duration time $t_{dur} =$ 160 ps – 180 ps, the kink moves in a CW direction to near LR corner of the nanostructure, accompanying with the kink polarity reverse. For the current pulse with a relatively large current density $0.06\kappa_{CPP} \leq |j_{CPP}| \leq 0.11\kappa_{CPP}$ (i.e., 5.1×10^{12} Am$^{-2} \leq |j_{CPP}| \leq 9.4 \times 10^{12}$ Am^{-2}) and duration ~20 ps $\leq t_{dur} \leq \sim$ 60 ps, it was found that the kink polarity is also reserved, while the UR kink shifts diagonally to the LL corner of the nanostructure. It was also seen in the phase diagram that the large j_{CPP} and large t_{dur} usually lead to the bubble domains, and some spiral states appear at $0.06\kappa_{CPP} \leq |j_{CPP}| \leq 0.07\kappa_{CPP}$ with a short pulse duration.

To further investigate the repeatability of polarity reversals of kink driven by CPP pulses, we took an examination on injecting some discontinuous current pulses to the system, as presented in **Figure 7A**. The insert shows the kink states at some typical time before and after the pulse injections in the evolutions. It was observed that all the four CPP pulses reverse the kink polarity, and the pulse with spin current $j_{CPP} < 0$ ($j_{CPP} > 0$) is used to reverse the kink with polarity $p = -1$ ($p = 1$). The first and second CPP pulses with $j_{CPP} = \pm 4.3 \times 10^{12}$ Am^{-2} and $t_{dur} = 160$ ps rotate the kink in CW and CCW directions respectively (see state transitions ① → ② → ③), which is a reversible switching. Note that the CW and CCW rotational directions here depend on the core polarity of the pre-evolutionary kink. The third and fourth CPP pulses with $j_{CPP} = \pm 0.07\kappa_{CPP} \sim \pm 6.0 \times 10^{12}$ Am^{-2} and $t_{dur} = 40$ ps move the kink to the diagonal corner of the nanostructure (see state transitions ③ → ④ → ⑤), which is also repeatable. For tracking the variations of the magnetic structures, the out-of-plane magnetization $M_z = \sum_i m_i^z/N$ is used to characterize the reversal of kink, where N is the total number of magnetic moments. Although some fluctuant variations appear in the $M_z - t$ curve in **Figure 7B**, it is clear that M_z flips to the opposite direction after every current pulse, in response to the core polarity reversal of the kinks. Therefore, we may use the CPP current to reverse the kink polarity and displace their position.

4 DISCUSSION AND CONCLUSION

Before concluding this work, we briefly discuss the experimental observations and thermal stability of the kink states. The X-ray holography allow the imaging of ultrafast magnetization dynamics in magnetic nanostructure with sub-10 nm spatial resolution time-resolved [6]. Using time-resolved X-ray microscopy, a number of experimental studies reported the direct observation of nanoscale skyrmions, current-driven

skyrmions dynamics, and the detailed evolution of magnetic configuration during the writing and deleting a skyrmion process [54, 55].

On the other hand, all simulations in present study were calculated under zero temperature in which the thermal effect is neglected. However, the thermal stability of magnetic kink structure is also a crucial issue for a detailed understanding of their underlying physical properties. For this, we tested the effect of thermal fluctuation on the magnetic structure by using Monte Carlo simulation with ladder cooling protocol [44]. It was found that the magnetic structure may forms at a very low-temperature $T \leq 1.2J_{FM}/k_B$ (k_B is the Boltzmann constant), under a magnetic field $B_z = -0.008J_{FM}$. Note that temperature T in Monte Carlo simulations is scaled in the unit of J_{FM}/k_B. Thus the kink structures are estimated to be stable below a critical temperature of $\sim$ 40 K, with a typical exchange constant J_{FM} = 2.95 meV adopted for Pd/Fe/Ir(111). This suggests that the kink structures in nanostructures can only exist at cryogenic temperatures, in agreement with the latest experimental investigations on Néel skyrmion in Pd/Fe/Ir(111) [56]. In this regard, the previous studies on skyrmions [57–60] may provide us an enlightened approach to enhance the thermal stability of kinks, which would be an interesting challenge for our further studies.

In summary, we used micromagnetic simulations and Monte Carlo simulations to investigate an exotic Néel-type kink texture in square-shaped nanostructures, which may stably exist in the absence of magnetic field. It was interesting to find that individual kinks hold eight degenerate states as they can reside in one of the four possible corners of a nanostructure, and carry upward or downward polarity. In addition, we proposed some effective schemes to control their dynamics by means of injecting spin-polarization current pulses. It was found that kinks can be created, annihilated, displaced and reversed polarity on demand by applying an in-plane or an out-of-plane spin-polarized current pulse, and are facile switchable among the degenerate kink states. In particularly, the kinks can be switched toward the ferromagnetic-like states and backward reversibly by applying two successive current pulses, indicating the capability of writing and deleting the kink states. These findings predict the existence of Néel-type kinks in the square-shaped nanostructures, as well as provide us a promising approach to tailor the kinks by utilizing the corners of the nanostructures, and control these states by spin-polarized currents. This study also suggests a theoretical guide to explore other chiral magnetic textures in nanostructures of polygon geometries.

DATA AVAILABILITY STATEMENT

The original contributions presented in the study are included in the article/Supplementary Material, further inquiries can be directed to the corresponding author.

AUTHOR CONTRIBUTIONS

J-PC and X-SG conceived the research project, and J-PC performed the computations. J-PC, J-QL, XS, YC, Z-FC, W-AL, M-HQ, Z-PH, X-SG, and J-ML commented the modeling and discussed the results. J-PC and X-SG wrote the manuscript.

FUNDING

This work was supported by the Natural Science Foundation of China (11604059), the Natural Science Foundation of Guangdong Province, China (2017A030313020), Scientific Research Project of Guangzhou Municipal Colleges and Universities (1201630455) and the Guangzhou University's Training Program for Excellent New-recruited Doctors (YB201715).

REFERENCES

1. Nagaosa N, and Tokura Y. Topological Properties and Dynamics of Magnetic Skyrmions. *Nat Nanotech* (2013) 8:899–911. doi:10.1038/nnano.2013.243
2. Fert A, Reyren N, and Cros V. Magnetic Skyrmions: Advances in Physics and Potential Applications. *Nat Rev Mater* (2017) 2:17031. doi:10.1038/natrevmats.2017.31
3. Wiesendanger R. Nanoscale Magnetic Skyrmions in Metallic Films and Multilayers: a New Twist for Spintronics. *Nat Rev Mater* (2016) 1:16044. doi:10.1038/natrevmats.2016.44
4. Jiang W, Chen G, Liu K, Zang J, te Velthuis SGE, and Hoffmann A. Skyrmions in Magnetic Multilayers. *Phys Rep* (2017) 704:1–49. doi:10.1016/j.physrep.2017.08.001
5. Kang W, Huang Y, Zhang X, Zhou Y, and Zhao W. Skyrmion-electronics: an Overview and Outlook. *Proc IEEE* (2016) 104:2040–61. doi:10.1109/JPROC.2016.2591578
6. Zhang X, Zhou Y, Mee Song K, Park T-E, Xia J, Ezawa M, et al. Skyrmion-electronics: Writing, Deleting, reading and Processing Magnetic Skyrmions toward Spintronic Applications. *J Phys Condens Matter* (2020) 32:143001. doi:10.1088/1361-648X/ab5488
7. Romming N, Hanneken C, Menzel M, Bickel JE, Wolter B, von Bergmann K, et al. Writing and Deleting Single Magnetic Skyrmions. *Science* (2013) 341:636–9. doi:10.1126/science.1240573
8. Sampaio J, Cros V, Rohart S, Thiaville A, and Fert A. Nucleation, Stability and Current-Induced Motion of Isolated Magnetic Skyrmions in Nanostructures. *Nat Nanotech* (2013) 8:839–44. doi:10.1038/nnano.2013.210
9. Fert A, Cros V, and Sampaio J. Skyrmions on the Track. *Nat Nanotech* (2013) 8:152–6. doi:10.1038/nnano.2013.29
10. Iwasaki J, Mochizuki M, and Nagaosa N. Current-induced Skyrmion Dynamics in Constricted Geometries. *Nat Nanotech* (2013) 8:742–7. doi:10.1038/nnano.2013.176
11. Hsu P-J, Kubetzka A, Finco A, Romming N, von Bergmann K, and Wiesendanger R. Electric-field-driven Switching of Individual Magnetic Skyrmions. *Nat Nanotech* (2017) 12:123–6. doi:10.1038/nnano.2016.234
12. Jiang W, Upadhyaya P, Zhang W, Yu G, Jungfleisch MB, Fradin FY, et al. Blowing Magnetic Skyrmion Bubbles. *Science* (2015) 349:283–6. doi:10.1126/science.aaa1442
13. Wang Y, Wang L, Xia J, Lai Z, Tian G, Zhang X, et al. Electric-field-driven Non-volatile Multi-State Switching of Individual Skyrmions in a Multiferroic Heterostructure. *Nat Commun* (2020) 11:3577. doi:10.1038/s41467-020-17354-7
14. Yao X, Chen J, and Dong S. Controlling the Helicity of Magnetic Skyrmions by Electrical Field in Frustrated Magnets. *New J Phys* (2020) 22:083032. doi:10.1088/1367-2630/aba1b3

15. Göbel B, Mertig I, and Tretiakov OA. Beyond Skyrmions: Review and Perspectives of Alternative Magnetic Quasiparticles. *Phys Rep* (2021) 895: 1–28. doi:10.1016/j.physrep.2020.10.001
16. Lin S-Z, Saxena A, and Batista CD. Skyrmion Fractionalization and Merons in Chiral Magnets with Easy-Plane Anisotropy. *Phys Rev B* (2015) 91:224407. doi:10.1103/PhysRevB.91.224407
17. Chen JP, Zhang D-W, and Liu J-M. Exotic Skyrmion Crystals in Chiral Magnets with Compass Anisotropy. *Sci Rep* (2016) 6:29126. doi:10.1038/srep29126
18. Chen JP, Zhang D-W, Chen Y, Gao XS, and Liu J-M. Compass-anisotropy-modulated Helical States and Skyrmion Crystals in Chiral Magnets. *Phys Lett A* (2018) 382:2944–51. doi:10.1016/j.physleta.2018.06.035
19. Kanazawa N, Kim J-H, Inosov DS, White JS, Egetenmeyer N, Gavilano JL, et al. Possible Skyrmion-Lattice Ground State in theB20chiral-Lattice Magnet MnGe as Seen via Small-Angle Neutron Scattering. *Phys Rev B* (2012) 86: 134425. doi:10.1103/PhysRevB.86.134425
20. Yu XZ, Koshibae W, Tokunaga Y, Shibata K, Taguchi Y, Nagaosa N, et al. Transformation between Meron and Skyrmion Topological Spin Textures in a Chiral Magnet. *Nature* (2018) 564:95–8. doi:10.1038/s41586-018-0745-3
21. Gao S, Rosales HD, Gómez Albarracín FA, Tsurkan V, Kaur G, Fennell T, et al. Fractional Antiferromagnetic Skyrmion Lattice Induced by Anisotropic Couplings. *Nature* (2020) 586:37–41. doi:10.1038/s41586-020-2716-8
22. Yu XZ, Onose Y, Kanazawa N, Park JH, Han JH, Matsui Y, et al. Real-space Observation of a Two-Dimensional Skyrmion crystal. *Nature* (2010) 465: 901–4. doi:10.1038/nature09124
23. Mühlbauer S, Binz B, Jonietz F, Pfleiderer C, Rosch A, Neubauer A, et al. Skyrmion Lattice in a Chiral Magnet. *Science* (2009) 323:915–9. doi:10.1126/science.1166767
24. Du H, Che R, Kong L, Zhao X, Jin C, Wang C, et al. Edge-mediated Skyrmion Chain and its Collective Dynamics in a Confined Geometry. *Nat Commun* (2015) 6:8504. doi:10.1038/ncomms9504
25. Jin C, Li Z-A, Kovács A, Caron J, Zheng F, Rybakov FN, et al. Control of Morphology and Formation of Highly Geometrically Confined Magnetic Skyrmions. *Nat Commun* (2017) 8:15569. doi:10.1038/ncomms15569
26. Xing X, Pong PWT, and Zhou Y. Current-controlled Unidirectional Edge-Meron Motion. *J Appl Phys* (2016) 120:203903. doi:10.1063/1.4968574
27. Leonov AO, and Mostovoy M. Edge States and Skyrmion Dynamics in Nanostripes of Frustrated Magnets. *Nat Commun* (2017) 8:14394. doi:10.1038/ncomms14394
28. Zhou Y, and Ezawa M. A Reversible Conversion between a Skyrmion and a Domain-wall Pair in a junction Geometry. *Nat Commun* (2014) 5:4652. doi:10.1038/ncomms5652
29. Rohart S, and Thiaville A. Skyrmion Confinement in Ultrathin Film Nanostructures in the Presence of Dzyaloshinskii-Moriya Interaction. *Phys Rev B* (2013) 88:184422. doi:10.1103/PhysRevB.88.184422
30. Heinonen O, Jiang W, Somaily H, te Velthuis SGE, and Hoffmann A. Generation of Magnetic Skyrmion Bubbles by Inhomogeneous Spin Hall Currents. *Phys Rev B* (2016) 93:094407. doi:10.1103/PhysRevB.93.094407
31. Kuchkin VM, Barton-Singer B, Rybakov FN, Blügel S, Schroers BJ, and Kiselev NS. Magnetic Skyrmions, Chiral Kinks, and Holomorphic Functions. *Phys Rev B* (2020) 102:144422. doi:10.1103/PhysRevB.102.144422
32. Cheng R, Li M, Sapkota A, Rai A, Pokhrel A, Mewes T, et al. Magnetic Domain wall Skyrmions. *Phys Rev B* (2019) 99:184412. doi:10.1103/PhysRevB.99.184412
33. Zheng Y, and Chen WJ. Characteristics and Controllability of Vortices in Ferromagnetics, Ferroelectrics, and Multiferroics. *Rep Prog Phys* (2017) 80: 086501. doi:10.1088/1361-6633/aa5e03
34. Cowburn RP, and Welland ME. Micromagnetics of the Single-Domain State of Square Ferromagnetic Nanostructures. *Phys Rev B* (1998) 58:9217–26. doi:10.1103/PhysRevB.58.9217
35. Jaafar M, Yanes R, Perez de Lara D, Chubykalo-Fesenko O, Asenjo A, Gonzalez EM, et al. Control of the Chirality and Polarity of Magnetic Vortices in Triangular Nanodots. *Phys Rev B* (2010) 81:054439. doi:10.1103/PhysRevB.81.054439
36. Yao J, Song X, Gao X, Tian G, Li P, Fan H, et al. Electrically Driven Reversible Magnetic Rotation in Nanoscale Multiferroic Heterostructures. *ACS Nano* (2018) 12:6767–76. doi:10.1021/acsnano.8b01936
37. Keesman R, Leonov AO, van Dieten P, Buhrandt S, Barkema GT, Fritz L, et al. Degeneracies and Fluctuations of Néel Skyrmions in Confined Geometries. *Phys Rev B* (2015) 92:134405. doi:10.1103/PhysRevB.92.134405
38. Banerjee S, Rowland J, Erten O, and Randeria M. Enhanced Stability of Skyrmions in Two-Dimensional Chiral Magnets with Rashba Spin-Orbit Coupling. *Phys Rev X* (2014) 4:031045. doi:10.1103/PhysRevX.4.031045
39. Romming N, Kubetzka A, Hanneken C, von Bergmann K, and Wiesendanger R. Field-dependent Size and Shape of Single Magnetic Skyrmions. *Phys Rev Lett* (2015) 114:177203. doi:10.1103/PhysRevLett.114.177203
40. von Malottki S, Dupé B, Bessarab PF, Delin A, and Heinze S. Enhanced Skyrmion Stability Due to Exchange Frustration. *Sci Rep* (2017) 7:12299. doi:10.1038/s41598-017-12525-x
41. Iwasaki J, Mochizuki M, and Nagaosa N. Universal Current-Velocity Relation of Skyrmion Motion in Chiral Magnets. *Nat Commun* (2013) 4:1463. doi:10.1038/ncomms2442
42. Zhang X, Zhou Y, and Ezawa M. Magnetic Bilayer-Skyrmions without Skyrmion Hall Effect. *Nat Commun* (2016) 7:10293. doi:10.1038/ncomms10293
43. Zhang S, Levy PM, and Fert A. Mechanisms of Spin-Polarized Current-Driven Magnetization Switching. *Phys Rev Lett* (2002) 88:236601. doi:10.1103/PhysRevLett.88.236601
44. Chen JP, Wang ZQ, Gong JJ, Qin MH, Zeng M, Gao XS, et al. Stripe-vortex Transitions in Ultrathin Magnetic Nanostructures. *J Appl Phys* (2013) 113: 054312. doi:10.1063/1.4790483
45. Hagemeister J, Iaia D, Vedmedenko EY, von Bergmann K, Kubetzka A, and Wiesendanger R. Skyrmions at the Edge: Confinement Effects in Fe/Ir(111). *Phys Rev Lett* (2016) 117:207202. doi:10.1103/PhysRevLett.117.207202
46. Wilson MN, Butenko AB, Bogdanov AN, and Monchesky TL. Chiral Skyrmions in Cubic Helimagnet Films: The Role of Uniaxial Anisotropy. *Phys Rev B* (2014) 89:094411. doi:10.1103/PhysRevB.89.094411
47. Chen JP, Xie YL, Chu P, Wang ZQ, Wang YL, Gao XS, et al. Manipulation of Magnetic State in Nanostructures by Perpendicular Anisotropy and Magnetic Field. *J Appl Phys* (2014) 115:243910. doi:10.1063/1.4885158
48. Büttner F, Moutafis C, Schneider M, Krüger B, Günther CM, Geilhufe J, et al. Dynamics and Inertia of Skyrmionic Spin Structures. *Nat Phys* (2015) 11: 225–8. doi:10.1038/nphys3234
49. Liu Y, Du H, Jia M, and Du A. Switching of a Target Skyrmion by a Spin-Polarized Current. *Phys Rev B* (2015) 91:094425. doi:10.1103/PhysRevB.91.094425
50. Kim J-V, Garcia-Sanchez F, Sampaio J, Moreau-Luchaire C, Cros V, and Fert A. Breathing Modes of Confined Skyrmions in Ultrathin Magnetic Dots. *Phys Rev B* (2014) 90:064410. doi:10.1103/PhysRevB.90.064410
51. Liu Y, Gliga S, Hertel R, and Schneider CM. Current-induced Magnetic Vortex Core Switching in a Permalloy Nanodisk. *Appl Phys Lett* (2007) 91:112501. doi:10.1063/1.2780107
52. Yamada K, Kasai S, Nakatani Y, Kobayashi K, Kohno H, Thiaville A, et al. Electrical Switching of the Vortex Core in a Magnetic Disk. *Nat Mater* (2007) 6:270–3. doi:10.1038/nmat1867
53. Finocchio G, Büttner F, Tomasello R, Carpentieri M, and Kläui M. Magnetic Skyrmions: from Fundamental to Applications. *J Phys D: Appl Phys* (2016) 49: 423001. doi:10.1088/0022-3727/49/42/423001
54. Büttner F, Lemesh I, Schneider M, Pfau B, Günther CM, Hessing P, et al. Field-free Deterministic Ultrafast Creation of Magnetic Skyrmions by Spin-Orbit Torques. *Nat Nanotech* (2017) 12:1040–4. doi:10.1038/nnano.2017.178
55. Woo S, Song KM, Han H-S, Jung M-S, Im M-Y, Lee K-S, et al. Spin-orbit Torque-Driven Skyrmion Dynamics Revealed by Time-Resolved X-ray Microscopy. *Nat Commun* (2017) 8:15573. doi:10.1038/ncomms15573
56. Lindner P, Bargsten L, Kovarik S, Friedlein J, Harm J, Krause S, et al. Temperature and Magnetic Field Dependent Behavior of Atomic-Scale Skyrmions in Pd/Fe/Ir(111) Nanoislands. *Phys Rev B* (2020) 101:214445. doi:10.1103/PhysRevB.101.214445
57. Büttner F, Lemesh I, and Beach GSD. Theory of Isolated Magnetic Skyrmions: From Fundamentals to Room Temperature Applications. *Sci Rep* (2018) 8: 4464. doi:10.1038/s41598-018-22242-8
58. Boulle O, Vogel J, Yang H, Pizzini S, de Souza Chaves D, Locatelli A, et al. Room-temperature Chiral Magnetic Skyrmions in Ultrathin Magnetic

Nanostructures. *Nat Nanotech* (2016) 11:449–54. doi:10.1038/nnano.2015.315
59. Desplat L, Suess D, Kim J-V, and Stamps RL. Thermal Stability of Metastable Magnetic Skyrmions: Entropic Narrowing and Significance of Internal Eigenmodes. *Phys Rev B* (2018) 98:134407. doi:10.1103/PhysRevB.98.134407
60. Varentcova AS, von Malottki S, Potkina MN, Kwiatkowski G, Heinze S, and Bessarab PF. Toward Room-Temperature Nanoscale Skyrmions in Ultrathin Films. *npj Comput Mater* (2020) 6:193. doi:10.1038/s41524-020-00453-w

Conflict of Interest: The authors declare that the research was conducted in the absence of any commercial or financial relationships that could be construed as a potential conflict of interest.

Publisher's Note: All claims expressed in this article are solely those of the authors and do not necessarily represent those of their affiliated organizations, or those of the publisher, the editors and the reviewers. Any product that may be evaluated in this article, or claim that may be made by its manufacturer, is not guaranteed or endorsed by the publisher.

frontiers in Physics

ORIGINAL RESEARCH
published: 30 September 2021
doi: 10.3389/fphy.2021.729967

Magnetic Skyrmion Generation by Reflective Spin Wave Focusing

Xianglong Yao[1], Zhenyu Wang[1], Menghua Deng[2], Z.-X. Li[1], Zhizhi Zhang[1], Yunshan Cao[1] and Peng Yan[1]**

[1]School of Electronic Science and Engineering and State Key Laboratory of Electronic Thin Films and Integrated Devices, University of Electronic Science and Technology of China, Chengdu, China, [2]School of Physics and Electronics, Hunan University, Changsha, China

We propose a method to generate magnetic skyrmions by focusing spin waves totally reflected by a curved film edge. The edge contour is derived to be parabolic and frequency-independent based on the identical magnonic path length principle. We performed micromagnetic simulations to verify our theoretical design. Under proper conditions, the reflected spin waves first converge at the focal point with the enhanced intensity leading to the emergence of magnetic droplets, which are then converted to magnetic skyrmion accompanied by a change in the topological charge. We numerically obtain the phase diagram of skyrmion generation with respect to the amplitude and frequency of the driving field. Our finding would be helpful for the design of spintronic devices combining the advantage of skyrmionics and magnonics.

Keywords: magnetic skyrmion, magnon, magnetic droplet, spin-wave focusing, total reflection

OPEN ACCESS

Edited by:
Xichao Zhang,
Shinshu University, Japan

Reviewed by:
Jan Masell,
RIKEN Center for Emergent Matter Science (CEMS), Japan
Marijan Beg,
Imperial College London, United Kingdom

****Correspondence:***
Zhenyu Wang
zhenyuw@uestc.edu.cn
Peng Yan
yan@uestc.edu.cn

Specialty section:
This article was submitted to Condensed Matter Physics, a section of the journal Frontiers in Physics

Received: *24 June 2021*
Accepted: *23 August 2021*
Published: *30 September 2021*

Citation:
Yao X, Wang Z, Deng M, Li Z-X, Zhang Z, Cao Y and Yan P (2021) Magnetic Skyrmion Generation by Reflective Spin Wave Focusing. Front. Phys. 9:729967. doi: 10.3389/fphy.2021.729967

1 INTRODUCTION

Magnetic skyrmions are topologically protected spin textures with a high thermal stability [1, 2]. They normally emerge in chiral bulk magnets or magnetic thin films with broken inversion symmetry, which gives rise to the Dzyaloshinskii–Moriya interaction (DMI) [3, 4]. In contrast to skyrmions, magnons are low-energy excitations in magnetic systems and can be easily generated and destroyed because of their bosonic nature. Both skyrmions and magnons have been extensively investigated and applied in information transmission and procession, which gives birth to two emerging subfields of magnetism: skyrmionics [5–8] and magnonics [9–11].

The interaction between skyrmions and magnons has been widely studied in magnon–skyrmion scattering [12, 13], magnon-driven skyrmion motion [14, 15], skyrmion-based magnonic crystal [16, 17], and skyrmion-induced magnon frequency comb [18]. Recently, the conversion between skyrmions and magnons has been attracting much attention. For example, the spin wave emission is often observed during the annihilation and core switching of magnetic skyrmions [19, 20]. However, it is quite hard to convert magnons to skyrmions because the energy carried by spin waves is much lower than the barrier between the skyrmion and the uniform ferromagnetic state. To create skyrmions by spin waves, the spin wave energy should be accumulated to overcome the energy barrier, which has been realized by the combination of the geometry change and the DMI-induced effective magnetic field [21] and by spin wave focusing [22]. In previous studies, the spin wave focusing is achieved by constructing a spin wave lens, which can be designed by a curved interface [22–24], a local graded-index region [25, 26], and a metasurface [27, 28]. In these methods, the spin wave reflection at the interface would decrease the efficiency of spin wave focusing. In this regard, one should avoid the spin wave reflection as much as possible, intuitively.

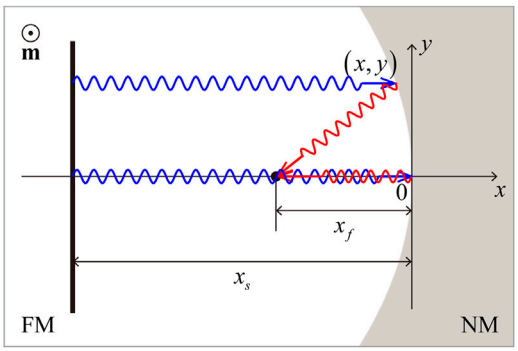

FIGURE 1 | Schematic of the film edge for total-reflection focusing of spin waves. The static magnetization **m** is oriented along the + *z* direction. FM and NM denote the ferromagnetic and non-magnetic regions, respectively. The black bar located at $x = -x_s$ is the spin wave source. A parallel incident spin wave (blue wavy lines with arrow) propagates towards the curved edge, and the reflected spin wave (red wavy lines with arrow) converges on the focal point at $x = -x_f$ (black point).

However, it is known that the spin wave can transmit through an interface without reflection only in rare cases [29]. On the contrary, spin wave can be completely reflected under more loose conditions, such as at the magnetic–non-magnetic interface. One natural issue is how to accumulate all reflected spin waves. In this study, we design a curved film edge based on the principle of identical magnonic path length, which suggests that the parabolic film edge can focus all reflected spin waves independent of their frequencies. At the focal point, the spin wave intensity can be significantly enhanced and the focal point magnetization oscillates strongly and might even be locally reversed, which is considered as the precursor for the skyrmion formation.

2 ANALYTICAL MODEL

We consider a chiral ferromagnetic film with a curved boundary, which is magnetized along the $+\hat{z}$ direction. The spin wave dynamics are governed by the Landau–Lifshitz–Gilbert (LLG) equation,

$$\frac{\partial \mathbf{m}}{\partial t} = -\gamma\mu_0 \mathbf{m} \times \mathbf{H}_{\text{eff}} + \alpha \mathbf{m} \times \frac{\partial \mathbf{m}}{\partial t}, \tag{1}$$

where $\mathbf{m} = \mathbf{M}/M_s$ is the unit magnetization vector with the saturated magnetization M_s, γ is the gyromagnetic ratio, μ_0 is the vacuum permeability, and α is the Gilbert damping constant. The effective field $\mathbf{H}_{\text{eff}}$ comprises the exchange field, the DM field, the anisotropy field, and the dipolar field. In the following discussion, the interfacial DMI is considered.

The film edge for total-reflection focusing can be designed based on the identical magnonic path length (MPL) principle [22]. We first consider a plane spin wave incident from the left source ($x = -x_s$), which is reflected by the film edge and converges into a focal point ($-x_f$, 0), as shown in **Figure 1**. The identical MPL principle yields the following:

$$x + x_s + \sqrt{(x + x_f)^2 + y^2} = x_s + x_f, \tag{2}$$

and the edge contour is described as

$$y^2 = -2px, \tag{3}$$

where $p = 2x_f$. One can see that the shape of the film edge is parabolic for the total-reflection focusing of the plane spin waves.

3 NUMERICAL RESULTS AND DISCUSSIONS

To verify our theoretical design, we numerically solve the full LLG equation (**Equation 1**) using the micromagnetic simulation code MuMax3 [30]. Magnetic parameters of the adopted Co are as follows: $M_s = 5.8 \times 10^5$ A/m, $A_{ex} = 15$ pJ/m, $D = 2.5$ mJ/m^2, and $K_u = 6 \times 10^5$ J/m^3. The cell size $2 \times 2 \times 1$ nm^3 is used to discretize the film in simulations. The Gilbert damping constant $\alpha = 10^{-3}$ is used to ensure a long-distance propagation of spin waves, and absorbing boundary conditions are adopted to avoid the spin wave reflection by the film edges except for the curved edge [31].

We first set the focal length as $x_f = 400$ nm in simulations and design a parabolic edge to focus the reflected spin waves. A sinusoidal monochromatic microwave field $\mathbf{H}_{\text{ext}} = h_0 \sin(\omega t)\hat{x}$ is applied in a narrow rectangular area (black bar in **Figure 2A**) to excite the incident plane spin waves. Numerical results for focusing spin waves with 60 GHz are shown in **Figure 2A**. Using the equation $I_{SW} = \frac{1}{T}\int_0^T \left(\delta m_x^2 + \delta m_y^2\right)dt$, we calculate the spin wave intensity, as plotted in **Figure 2B**. The profiles of the spin wave intensity are also shown (black curve in **Figure 2B**). One can see that spin waves are reflected from the film edge and focused, leading to a significantly enhanced intensity around the focal point. However, it is found that the focal point obtained from the numerical simulation is shifted slightly along the $+x$ direction from the theoretical position of the focal point (black point shown in **Figure 2B**). It may be attributed to two reasons: one is the ray optic approximation for analyzing the spin wave propagation, which requires the spin wave wavelength (about tens of nanometers) to be much smaller than the size of the film edge. The other is the spin canting at the curved edge (**Figure 3D**), which would influence the propagation of the reflected spin waves. **Eq. 3** suggests that the shape of the parabolic edge for the total-reflection focusing is independent of the spin wave frequency. **Figures 2C,D** indeed confirm this result, which would promote the applications of the spin wave focusing in magnonic devices.

A close inspection shows that there is a sharp kink of the spin wave intensity at the magnon source (**Figures 2B,D,F**). It results from the change in the coherence of spin waves through the magnon source. On the right side of the magnon source, the emitted spin waves and reflected spin waves are coherent, leading to a strong interference with a significant interference fringe. The phase of the reflected spin wave would change when it propagates through the magnon source. The coherence between the reflected and emitted spin waves on the left side is destroyed, which shows a

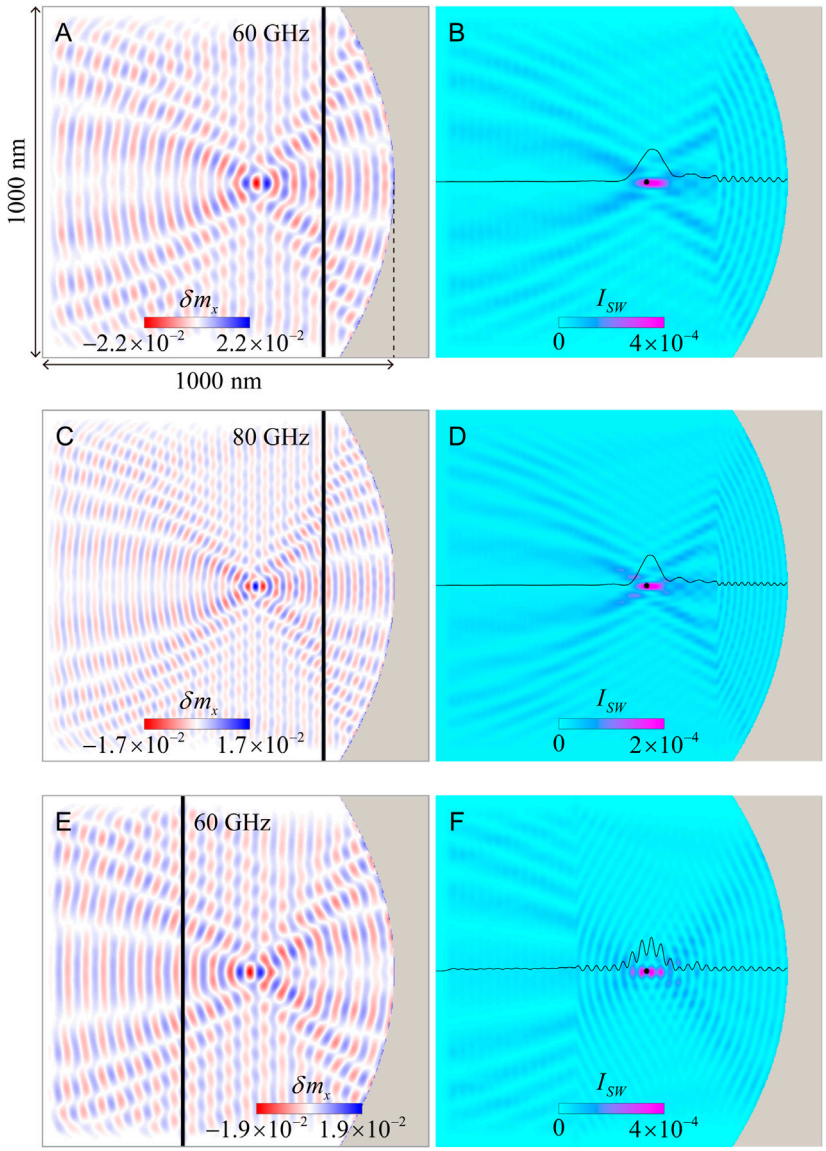

FIGURE 2 | (A) Snapshot of the spin waves reflected from the parabolic edge. The spin wave frequency is $\omega/2\pi$ = 60 GHz. The black bar in **(A)** denotes the spin wave source located at x = −200 nm, which is excited by a microwave field with $\mu_0 h_0$ = 10 mT. **(B)** The spin wave intensity in **(A)**. The black point represents the ideal position of the focal point. The black curve shows the profile of the spin wave intensity along the x axis at y = 0. **(C)** and **(D)** Snapshot of total-reflection focusing of spin waves and the corresponding intensity for $\omega/2\pi$ = 80 GHz. **(E)** and **(F)** Snapshot of spin waves and their intensity for the exciting source located at x = −600 nm.

slight fluctuation in the spin wave intensity. Different fluctuations in spin wave intensities on both sides of the magnon source induce a sharp kink. Therefore, the spin wave intensity at the focal point would fluctuate drastically when the magnon source is located at the left side of the focal point, as shown in **Figures 2E,F**. This severe fluctuation of the spin wave intensity would destroy the localized spin wave soliton (droplet) around the focal point, which hinders the generation of skyrmion. In what follows, we focus on the case of the magnon source locating at the right side of the focal point for generating skyrmion by spin wave focusing.

To generate magnetic skyrmions, we increase the amplitude of the microwave field to $\mu_0 h_0$ = 360 mT. The spin wave intensity around the focal point is enhanced significantly, which shows a strong magnetization oscillation, as plotted in **Figure 3A**. With the continuous excitation of spin waves, more energy is harvested, leading to the local switching of the magnetization and the formation of magnetic droplets, which can be easily driven by spin waves (**Figure 3B**). The magnetic droplet is a non-topological localized spin wave soliton [32, 33] and is unstable in a chiral ferromagnetic film because of high DMI energy. Under the disturbance of spin waves, the magnetic droplet is converted to a dynamical skyrmion at t = 0.6 ns, as shown in **Figure 3C**. Then, we turn off the microwave field at t = 0.7 ns and the system is relaxed toward an equilibrium state with a stable skyrmion state (**Figure 3D**). Moreover, it is noted that the skyrmion is not created exactly at the focal point. This is

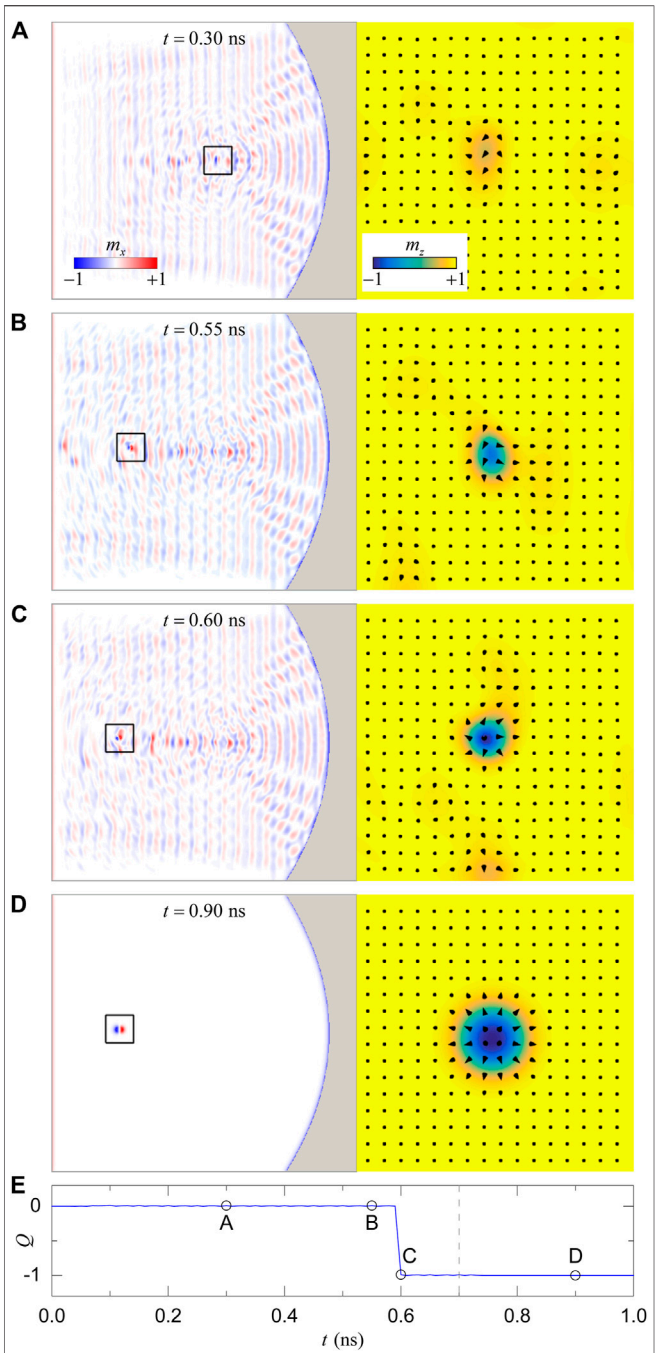

FIGURE 3 | The creation process of the magnetic skyrmion induced by the total-reflection focusing. The exciting field with $\mu_0 h_0$ = 360 mT is applied in **(A–C)** and is turned off in **(D)**. The z-component magnetization of the rectangular area in the left column is enlarged in the right column. **(E)** Temporal evolution of the topological number Q. The microwave field starts at t = 0 and ends at t = 0.7 ns, indicated by the gray dashed line.

because the first nucleated droplet driven by spin waves moves faster than the skyrmion during which the transformation from the droplet to skyrmion happens. This would lead to the skyrmion nucleation site developing far away from the focal point.

The topological charge, which is given by

$$Q = \frac{1}{4\pi}\iint \mathbf{m}\cdot\left(\frac{\partial \mathbf{m}}{\partial x}\times\frac{\partial \mathbf{m}}{\partial y}\right)dxdy, \tag{4}$$

can be used to characterize the topology of skyrmions in two-dimensional systems. However, the large spatial variations of **m** in the process of the skyrmion nucleation and annihilation reduce the accuracy of the finite difference approximation of **Eq. 4** and result in non-integer values of Q [22]. To avoid this spurious deviation, we follow the definition of the topological charge given by Berg and Lüscher [34], which is expressed as

$$Q = \frac{1}{4\pi}\sum_{\langle ijk\rangle} q_{ijk}, \tag{5}$$

with

$$\tan\left(\frac{q_{ijk}}{2}\right) = \frac{\mathbf{m}_i\cdot(\mathbf{m}_j\times\mathbf{m}_k)}{1+\mathbf{m}_i\cdot\mathbf{m}_j+\mathbf{m}_i\cdot\mathbf{m}_k+\mathbf{m}_j\cdot\mathbf{m}_k}, \tag{6}$$

where q_{ijk} is the local topological charge density of elementary-signed triangles, which is invariant under a cyclic permutation of the indices ijk. This lattice-based approach has been employed in

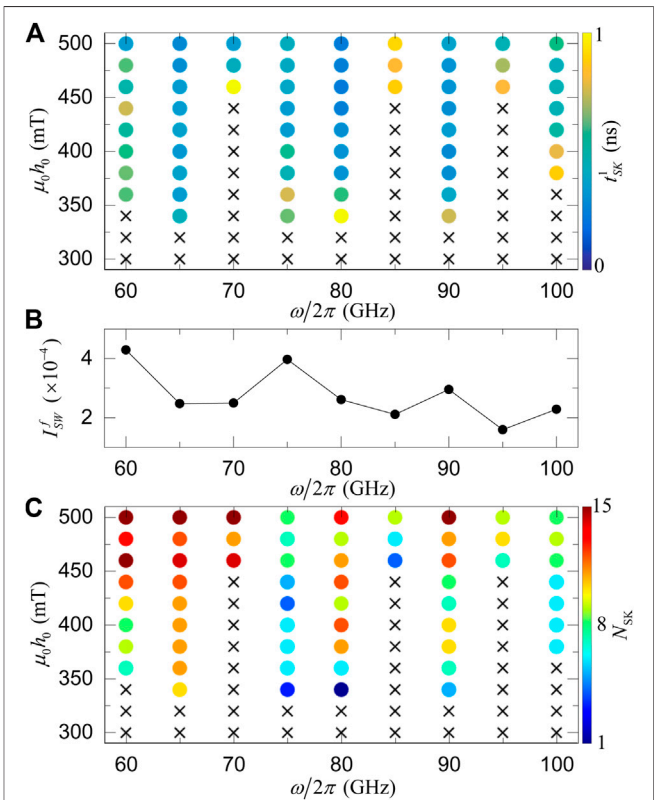

FIGURE 4 | (A) The nucleation time of the first skyrmion t^1_{SK} as a function of the field amplitude and frequency. The black crosses represent no skyrmion creation. **(B)** The frequency dependence of the spin wave intensity at the focal point under the microwave field with $\mu_0 h_0$ = 10 mT. **(C)** Phase diagram of skyrmion generation with respect to the amplitude and frequency of the exciting field with the duration time 10 ns.

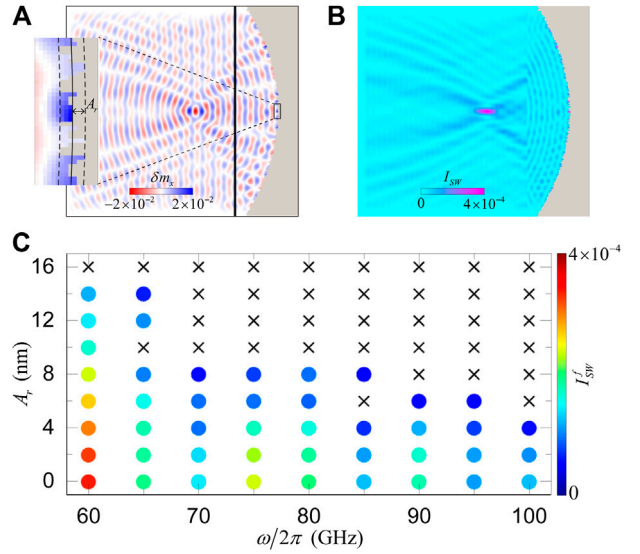

FIGURE 5 | (A) Snapshot of spin waves reflected from the parabolic edge with a random roughness, which is depicted by the formula $x = -y^2/(4x_f) + A_r I_r$, where A_r is the roughness amplitude and I_r is a random value in the interval (−1, 1). The black bar shows the exciting source of spin waves with $\mu_0 h_0$ = 10 mT and $\omega/2\pi$ = 60 GHz. The enlarged image of the rectangular area is shown on the left. The solid line in the inset denotes the ideal parabolic edge, and the dashed lines show the amplitude of the roughness (A_r = 6 nm). **(B)** The spin wave intensity in **(A)**. **(C)** Phase diagram of the spin wave intensity at the focal point as a function of the roughness amplitude and the spin wave frequency. The black crosses represent no spin wave focusing, and the colored dots are the spin wave intensity.

quantifying the topological charge in micromagnetics recently [35–37]. Based on this scheme, we calculate the time evolution of the topological charge Q in the process of the skyrmion generation (**Figure 3E**), where nonphysical values of Q are excluded. An abrupt change in Q from 0 to −1 is observed at t = 0.6 ns, which confirms the skyrmion creation.

From the generation process of the skyrmion, one can see that the magnetic droplet is an indispensable intermediate between ferromagnetic and skyrmion states. Although the energy of the magnetic droplet is higher than the skyrmion, the skyrmion cannot be created directly from the ferromagnetic state. This is because the droplet is non-topological and can be transformed continuously from a ferromagnetic state. However, the continuous transformation from a ferromagnetic state to the skyrmion state is highly unlikely, which is due to the topological protection of the skyrmion. Compared to the droplet, a change in the topological charge is accompanied for the skyrmion creation, which requires more energy input from the external driving.

Figure 4A plots the nucleation time of the first skyrmion t_{SW}^1 induced by the total-reflection focusing of spin waves. It is found that the skyrmion creation at the field frequency with $\omega/2\pi$ = 70, 85, and 95 GHz needs a longer time and requires a higher amplitude of the exciting field. To find the reason for such a frequency dependence of the skyrmion generation, we plot the spin wave intensity at the focal point for different frequencies, as shown in **Figure 4B**. We find that these three frequencies correspond to the local minima of the spin wave intensity, which is due to the destructive interference between the reflected spin waves and emitted spin waves from the magnon source at the focal point. In addition, we also plot a phase diagram of skyrmion generation induced by the total-reflection focusing of spin waves within 10 ns (**Figure 4C**). As in the spin wave focusing for the transmitted waves [22], the generated skyrmion number N_{Sk} is not monotonically increased with the field amplitude h_0, owing to the skyrmion annihilation induced by the interaction between the magnetic droplet and skyrmion. It should be stressed that the generated skyrmion is not able to arrive at the magnon source and is destroyed at the duration time (10 ns) considered in our study, although it moves towards the magnon source driven by spin waves [12–14, 38]. This is because the velocity of the magnon-driven skyrmion motion is very slow (<10 m/s). It has been demonstrated that the number of the nucleated skyrmion depends on the duration time of the microwave field [22]. Thus, we can tune the duration time of the microwave field pulse to generate a single skyrmion (**Figure 3**).

The above micromagnetic simulations are all performed for the idealized edge, which is often not the case in practical applications, due to edge roughness. To make the roughness effect on the total-reflection focusing clear, we performed additional simulations with random roughness, which is close to the rough edge in real cases. For the roughness amplitude A_r = 6 nm, the reflected spin waves with 60 GHz can be well focused with a reduced intensity (≈81%), as shown in **Figures 5A,B**. With the increase in A_r, the focal point intensity of spin waves I_{SW}^f decreases. For a large amplitude of roughness, the reflected spin waves are disordered and cannot be focused (black crosses in **Figure 5C**). We also investigate the frequency dependence of the roughness effect and find that the roughness influence becomes weak with the decrease in the spin wave frequency. This result suggests that our method is valid for spin waves with long wavelength ($\lambda \gg A_r$), for which the roughness effect can be ignored.

The results in this study are obtained in magnetic metals, which usually have high perpendicular magnetic anisotropy and high damping. A large-amplitude microwave field is needed for the skyrmion creation, which is difficult to achieve in experiments. Fortunately, magnetic insulators with perpendicular anisotropy and ultra-low damping have been demonstrated to host skyrmions [39–41], which makes our method more applicable from the view of materials realizations. In a previous study, we proposed a method to generate skyrmion by focusing the transmitted spin waves, which is realized by constructing a spin wave lens with a curved interface [22]. The shape of the interface depends on the relative refraction index of spin waves, which is frequency-dependent. Thus, that method is only feasible for focusing spin waves with one certain frequency. For spin wave focusing with a different frequency, a new curved interface should be designed, which hinders the practical application of that method. We, therefore, believe that the total-reflection focusing in the present study provides a promising way to generate the skyrmion.

4 CONCLUSION

In summary, we theoretically investigated the skyrmion generation induced by the total-reflection focusing of spin waves. The shape of the film edge was derived based on the identical magnonic path length principle. Micromagnetic simulations were performed to

confirm the focusing effect of spin waves reflected from the parabolic edge. By increasing the field amplitude, we observed the nucleation of magnetic droplet induced by the total-reflection focusing and the transformation to the skyrmion with a change in the topological charge. Our results provide a method to generate skyrmion by reflective focusing of spin waves, which is frequency-independent and would promote the development and application of spintronic devices combing magnons and skyrmions.

DATA AVAILABILITY STATEMENT

The original contributions presented in the study are included in the article/Supplementary Material; further inquiries can be directed to the corresponding authors.

AUTHOR CONTRIBUTIONS

ZW and PY conceived the idea and wrote the paper. ZW and XY finished the analytical deduction and performed all the simulations. MD, Z-XL, ZZ, and YC corrected the paper and discussed.

FUNDING

This work was supported by the National Natural Science Foundation of China (Grants No. 12074057 and No. 11704060). ZW acknowledges financial support from the China Postdoctoral Science Foundation (Grant No. 2019M653063). Z-XL acknowledges financial support from the China Postdoctoral Science Foundation (Grant No. 2019M663461) and the NSFC (Grant No. 11904048). ZZ acknowledges financial support from the China Postdoctoral Science Foundation (Grant No. 2020M673180).

ACKNOWLEDGMENTS

We thank H. Yang and L. Song for helpful discussions.

REFERENCES

1. Wild J, Meier TNG, Pöllath S, Kronseder M, Bauer A, Chacon A, et al.Entropy-limited Topological protection of Skyrmions. *Sci Adv* (2017) 3:e1701704. doi:10.1126/sciadv.1701704
2. Desplat L, Suess D, Kim J-V, and Stamps RL. Thermal Stability of Metastable Magnetic Skyrmions: Entropic Narrowing and Significance of Internal Eigenmodes. *Phys Rev B* (2018) 98:134407. doi:10.1103/PhysRevB.98.134407
3. Dzyaloshinsky I. A Thermodynamic Theory of "Weak" Ferromagnetism of Antiferromagnetics. *J Phys Chem Sol* (1958) 4:241–55. doi:10.1016/0022-3697(58)90076-3
4. Moriya T. Anisotropic Superexchange Interaction and Weak Ferromagnetism. *Phys Rev* (1960) 120:91–8. doi:10.1103/PhysRev.120.91
5. Nagaosa N, and Tokura Y. Topological Properties and Dynamics of Magnetic Skyrmions. *Nat Nanotech* (2013) 8:899–911. doi:10.1038/nnano.2013.243
6. Fert A, Cros V, and Sampaio J. Skyrmions on the Track. *Nat Nanotech* (2013) 8:152–6. doi:10.1038/nnano.2013.29
7. Krause S, and Wiesendanger R. Skyrmionics Gets Hot. *Nat Mater* (2016) 15: 493–4. doi:10.1038/nmat4615
8. Zhang X, Zhou Y, Mee Song K, Park T-E, Xia J, Ezawa M, et al.Skyrmion-electronics: Writing, Deleting, reading and Processing Magnetic Skyrmions toward Spintronic Applications. *J Phys Condens Matter* (2020) 32:143001. doi:10.1088/1361-648x/ab5488
9. Serga AA, Chumak AV, and Hillebrands B. YIG Magnonics. *J Phys D: Appl Phys* (2010) 43:264002. doi:10.1088/0022-3727/43/26/264002
10. Lenk B, Ulrichs H, Garbs F, and Münzenberg M. The Building Blocks of Magnonics. *Phys Rep* (2011) 507:107–36. doi:10.1016/j.physrep.2011.06.003
11. Chumak AV, Vasyuchka VI, Serga AA, and Hillebrands B. Magnon Spintronics. *Nat Phys* (2015) 11:453–61. doi:10.1038/nphys3347
12. Iwasaki J, Beekman AJ, and Nagaosa N. Theory of Magnon-Skyrmion Scattering in Chiral Magnets. *Phys Rev B* (2014) 89:064412. doi:10.1103/PhysRevB.89.064412
13. Schütte C, and Garst M. Magnon-skyrmion Scattering in Chiral Magnets. *Phys Rev B* (2014) 90:094423. doi:10.1103/PhysRevB.90.094423
14. Zhang X, Müller J, Xia J, Garst M, Liu X, and Zhou Y. Motion of Skyrmions in Nanowires Driven by Magnonic Momentum-Transfer Forces. *New J Phys* (2017) 19:065001. doi:10.1088/1367-2630/aa6b70
15. Jiang Y, Yuan HY, Li Z-X, Wang Z, Zhang HW, Cao Y, et al.Twisted Magnon as a Magnetic Tweezer. *Phys Rev Lett* (2020) 124:217204. doi:10.1103/physrevlett.124.217204
16. Ma F, Zhou Y, Braun HB, and Lew WS. Skyrmion-based Dynamic Magnonic crystal. *Nano Lett* (2015) 15:4029–36. doi:10.1021/acs.nanolett.5b00996
17. Moon KW, Chun BS, Kim W, and Hwang C. Control of Spin-Wave Refraction Using Arrays of Skyrmions. *Phys Rev Appl* (2016) 6:064027. doi:10.1103/physrevapplied.6.064027
18. Wang Z, Yuan HY, Cao Y, Li Z-X, Duine RA, and Yan P. Magnonic Frequency Comb through Nonlinear Magnon-Skyrmion Scattering. *Phys Rev Lett* (2021) 127:037202. doi:10.1103/PhysRevLett.127.037202
19. Zhang X, Xia J, Zhou Y, Liu X, Zhang H, and Ezawa M. Skyrmion Dynamics in a Frustrated Ferromagnetic Film and Current-Induced Helicity Locking-Unlocking Transition. *Nat Commun* (2017) 8:1717. doi:10.1038/s41467-017-01785-w
20. Zhang B, Wang W, Beg M, Fangohr H, and Kuch W. Microwave-induced Dynamic Switching of Magnetic Skyrmion Cores in Nanodots. *Appl Phys Lett* (2015) 106:102401. doi:10.1063/1.4914496
21. Liu Y, Yin G, Zang J, Shi J, and Lake RK. Skyrmion Creation and Annihilation by Spin Waves. *Appl Phys Lett* (2015) 107:152411. doi:10.1063/1.4933407
22. Wang Z, Li Z-X, Wang R, Liu B, Meng H, Cao Y, et al.Spin-wave Focusing Induced Skyrmion Generation. *Appl Phys Lett* (2020) 117:222406. doi:10.1063/5.0029401
23. Toedt J-N, Mundkowski M, Heitmann D, Mendach S, and Hansen W. Design and Construction of a Spin-Wave Lens. *Sci Rep* (2016) 6:33169. doi:10.1038/srep33169
24. Bao W, Wang Z, Cao Y, and Yan P. Off-axial Focusing of a Spin-Wave Lens in the Presence of Dzyaloshinskii-Moriya Interaction. *Phys Rev B* (2020) 102: 014423. doi:10.1103/PhysRevB.102.014423
25. Whitehead NJ, Horsley SAR, Philbin TG, and Kruglyak VV. A Luneburg Lens for Spin Waves. *Appl Phys Lett* (2018) 113:212404. doi:10.1063/1.5049470
26. Vogel M, Pirro P, Hillebrands B, and von Freymann G. Optical Elements for Anisotropic Spin-Wave Propagation. *Appl Phys Lett* (2020) 116:262404. doi:10.1063/5.0018519
27. Zelent M, Mailyan M, Vashistha V, Gruszecki P, Gorobets OY, Gorobets YI, et al.Spin Wave Collimation Using a Flat Metasurface. *Nanoscale* (2019) 11: 9743–8. doi:10.1039/C8NR10484K
28. Gräfe J, Gruszecki P, Zelent M, Decker M, Keskinbora K, Noske M, et al.Direct Observation of Spin-Wave Focusing by a Fresnel Lens. *Phys Rev B* (2020) 102: 024420. doi:10.1103/PhysRevB.102.024420
29. Yan P, Wang XS, and Wang XR. All-magnonic Spin-Transfer Torque and Domain wall Propagation. *Phys Rev Lett* (2011) 107:177207. doi:10.1103/physrevlett.107.177207

30. Vansteenkiste A, Leliaert J, Dvornik M, Helsen M, Garcia-Sanchez F, and Van Waeyenberge B. The Design and Verification of Mumax3. *AIP Adv* (2014) 4: 107133. doi:10.1063/1.4899186
31. Venkat G, Fangohr H, and Prabhakar A. Absorbing Boundary Layers for Spin Wave Micromagnetics. *J Magnetism Magn Mater* (2018) 450:34–9. Perspectives on magnon spintronics. doi:10.1016/j.jmmm.2017.06.057
32. Chaves-O'Flynn GD, and Stein DL. Thermal Activation Barriers for Creation and Annihilation of Magnetic Droplet Solitons in the Presence of Spin Transfer Torque. *Phys Rev B* (2020) 101:184421. doi:10.1103/PhysRevB.101.184421
33. Macià F, and Kent AD. Magnetic Droplet Solitons. *J Appl Phys* (2020) 128: 100901. doi:10.1063/5.0018251
34. Berg B, and Lüscher M. Definition and Statistical Distributions of a Topological Number in the Lattice O(3) σ-model. *Nucl Phys B* (1981) 190: 412–24. doi:10.1016/0550-3213(81)90568-X
35. Böttcher M, Heinze S, Egorov S, Sinova J, and Dupé B. B-T Phase Diagram of Pd/Fe/Ir(111) Computed with Parallel Tempering Monte Carlo. *New J Phys* (2018) 20:103014. doi:10.1088/1367-2630/aae282
36. Müller GP, Hoffmann M, Dißelkamp C, Schürhoff D, Mavros S, Sallermann M, et al.Spirit : Multifunctional Framework for Atomistic Spin Simulations. *Phys Rev B* (2019) 99:224414. doi:10.1103/PhysRevB.99.224414
37. Kim J-V, and Mulkers J. On Quantifying the Topological Charge in Micromagnetics Using a Lattice-Based Approach. *IOP SciNotes* (2020) 1: 025211. doi:10.1088/2633-1357/abad0c
38. Yu X, Kagawa F, Seki S, Kubota M, Masell J, Yasin F, et al.Real-space Observations of 60-nm Skyrmion Dynamics in an Insulating Magnet under Low Heat, *Nat Commun* (2021) 12:5079, 2021 . PREPRINT (Version 1) available at Research Square doi:10.1038/s41467-021-25291-2
39. Soumah L, Beaulieu N, Qassym L, Carrétéro C, Jacquet E, Lebourgeois R, et al.Ultra-low Damping Insulating Magnetic Thin Films Get Perpendicular. *Nat Commun* (2018) 9:3355. doi:10.1038/s41467-018-05732-1
40. You C-Y. Skyrmions in Magnetic Insulators Warm up. *Nat Electron* (2019) 2: 176–7. doi:10.1038/s41928-019-0250-1
41. Caretta L, Rosenberg E, Büttner F, Fakhrul T, Gargiani P, Valvidares M, et al.Interfacial Dzyaloshinskii-Moriya Interaction Arising from Rare-Earth Orbital Magnetism in Insulating Magnetic Oxides. *Nat Commun* (2020) 11: 1090. doi:10.1038/s41467-020-14924-7

Conflict of Interest: The authors declare that the research was conducted in the absence of any commercial or financial relationships that could be construed as a potential conflict of interest.

Publisher's Note: All claims expressed in this article are solely those of the authors and do not necessarily represent those of their affiliated organizations, or those of the publisher, the editors, and the reviewers. Any product that may be evaluated in this article, or claim that may be made by its manufacturer, is not guaranteed or endorsed by the publisher.

frontiers in Physics

ORIGINAL RESEARCH
published: 03 November 2021
doi: 10.3389/fphy.2021.754869

Suppression of Skyrmion Hall Motion in Antiferromagnets Driven by Circularly Polarized Spin Waves

*S. H. Guan, Y. Yang, Z. Jin, T. T. Liu, Y. Liu and M. H. Qin**

Guangdong Provincial Key Laboratory of Quantum Engineering and Quantum Materials and Institute for Advanced Materials, South China Academy of Advanced Optoelectronics, South China Normal University, Guangzhou, China

An investigation of spin waves interacting with antiferromagnetic spin textures is meaningful for future spintronic and magnonic-based memory and logic applications. In this work, we numerically study the skyrmion dynamics driven by circularly polarized spin waves in antiferromagnets and propose a method of suppressing the Hall motion. It is demonstrated that the application of two circularly polarized spin waves with opposite chirality allows the skyrmion motion straightly along the intersection line of the two spin wave sources. The skyrmion speed depending on these parameters of the spin waves and system is estimated, and a comparison with other methods is provided. Furthermore, two depinning behaviors of the skyrmion related to the strengths of the defect are also observed in the simulations. Thus, the proposed method could be used in precisely modulating the skyrmion dynamics, contributing to skyrmion-based memory device design.

Keywords: antiferromagnetic skyrmion, spin waves, dynamics, Hall motion, speed

OPEN ACCESS

Edited by:
Huaiyang Yuan,
Utrecht University, Netherlands

Reviewed by:
Farhad Sattari,
University of Mohaghegh Ardabili, Iran
Rafael A. Molina,
Consejo Superior de Investigaciones Científicas (CSIC), Spain

****Correspondence:***
M. H. Qin
qinmh@scnu.edu.cn

Specialty section:
This article was submitted to Condensed Matter Physics, a section of the journal Frontiers in Physics

Received: *07 August 2021*
Accepted: *27 September 2021*
Published: *03 November 2021*

Citation:
Guan SH, Yang Y, Jin Z, Liu TT, Liu Y and Qin MH (2021) Suppression of Skyrmion Hall Motion in Antiferromagnets Driven by Circularly Polarized Spin Waves. Front. Phys. 9:754869. doi: 10.3389/fphy.2021.754869

INTRODUCTION

Skyrmion, a topologically protected particle-like magnetic structure, is considered as a promising candidate for spintronic applications like racetrack memories due to some of its attractive features including nanoscale in size, low critical driving current, and high stability [1–6]. Skyrmion dynamics driven by spin-polarized current in ferromagnets has been widely studied, and the so-called skyrmion Hall motion induced by the Magnus force is reported. In this case, the skyrmion moves deviating from the direction of the driving force and could be restricted or even annihilated by element edges of related devices [7–10]. Thus, the Hall motion brings a great challenge to the skyrmion-based applications.

Recently, antiferromagnetic (AFM) skyrmion has been predicted theoretically [11] and observed experimentally at room temperatures in synthetic antiferromagnets [12]. AFM skyrmion is comprised of two coupled spin configurations with opposite topological numbers, and two Magnus forces respectively acting on two sub-lattices under spin-polarized current perfectly cancel with each other, allowing the motion straightly along the driving force [13–16]. Moreover, compared with ferromagnetic skyrmion, AFM skyrmion has more attractive physical properties. For instance, AFM skyrmion is insensitive to external magnetic field [17, 18], and its speed is much larger than ferromagnetic skyrmion under a same driving current density [15]. Importantly, AFM materials are abundant in nature, which include metals comprised Mn-based alloys, insulators, semiconductors, and semimetals [19]. All these merits of AFM skyrmions contribute to the rapid development of AFM spintronics.

Most recently, spin wave driven skyrmion motion draws a lot of attention due to some advantages such as low dissipation and producing less heat [20–22]. In ferromagnets, the spin wave is only right-circularly polarized and drives the skyrmion motion towards the spin wave source in the presence of a Hall motion related to its topological charge, which can be understood from the momentum conservation [23]. In antiferromagnets, however, the spin wave can be fully polarized, providing another degree of freedom in modulating the skyrmion dynamics [24]. For AFM system with uniaxial anisotropy, the spin wave is generally polarized [40], and the scattering of the spin wave is related to its polarization direction, resulting in interesting and complex skyrmion dynamics.

For example, when AFM skyrmion is driven by chiral or isospin charged spin wave with circular or elliptical polarizations, a magnonic topological spin Hall effect is produced resulting from the symmetry breaking of the magnon trajectory [25]. Thus, the skyrmion Hall motion could be also driven by the spin wave even in AFM systems. Interestingly, the scattering direction of the magnon and the deflection direction of skyrmion are determined by the chirality of the spin wave, allowing the skyrmions work as spin splitters in AFM magnon devices [26]. However, skyrmion Hall motion is detrimental for data propagation in future skyrmion-based devices, as discussed above. It is predicted that the linearly polarized spin wave with particular polarization directions drives the AFM skyrmion straightly along its propagation direction without any Hall motion [27], while the strict limitation of the polarization directions affects stable application. Furthermore, the skyrmion speed driven by linearly polarized spin waves is rather low compared with one driven by circularly polarized spin wave. Thus, there is still an urgent need in suppressing the skyrmion Hall motion driven by spin waves in antiferromagnets, considering these particular merits in future magnonic and spintronic device design.

In this work, we propose a method of suppressing skyrmion Hall motion by injecting two kinds of spin waves with opposite chirality in antiferromagnets. The application of the two circularly polarized spin waves drives the skyrmion motion straightly along the intersection line. The skyrmion speed depending on these parameters of the spin waves and system is numerically simulated, and a comparison with those driven by other methods is provided and briefly discussed. Furthermore, the depinning behaviors of the skyrmion from the defects are also investigated.

MODEL AND METHOD

We consider a two-dimensional AFM Heisenberg model in the xy plane with the model Hamiltonian,

$$H = J\sum_{\langle i,j\rangle}\mathbf{m}_i\cdot\mathbf{m}_j + \sum_{\langle i,j\rangle}\mathbf{D}\cdot\left(\mathbf{m}_i\times\mathbf{m}_j\right) - K\sum_i\left(\mathbf{m}_i^z\right)^2, \quad (1)$$

where the first term is the AFM exchange interaction between the nearest neighbors with $J > 0$, $\mathbf{m}_i$ is the local magnetic moment at site i, $\mathbf{m}_i = -\mathbf{S}_i/\hbar$ with the local spin $\mathbf{S}_i$, and the reduced Plank constant $\hbar$, the second term is the Dzyaloshinskii–Moriya interaction (DMI) between the nearest neighbors with the vector $\mathbf{D} = D\,\mathbf{e}_{ij}$, the third term is the perpendicular magnetic anisotropy with the easy z-axis and magnitude K. Considering the canted AFM sample $KMnF_3$, which has been widely used in the study of spin wave propagation theoretically and experimentally [28–30], the parameters are chosen to be $J = 1.0 \times 10^{-21}$ J, $D/J = 0.14$, and $K/J = 0.03$ [31]. In addition, other AFM materials with stable existence of skyrmion and spin wave propagation such as two AFM coupled layers of YIG [26] and Co/Pt bilayer [12, 32] could also be applicable to our simulation.

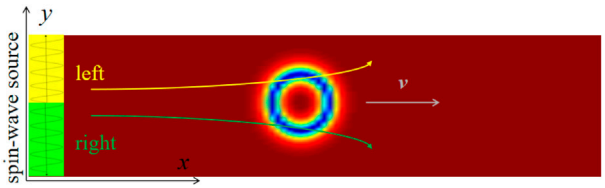

FIGURE 1 | The model of AFM skyrmion driven by double circularly polarized spin waves. The yellow and green regions represent the source of left-handed and right-handed circularly polarized spin waves, respectively. The yellow and green arrows indicate the scattering direction of the spin waves, and the gray arrow indicates the driving direction of the skyrmion.

Subsequently, the time-dependent magnetization dynamics are investigated using the Landau–Lifshitz–Gilbert (LLG) equation,

$$\frac{d\mathbf{m}_i}{dt} = -\gamma\mathbf{m}_i\times\left(\mathbf{H}_i^{eff} + \mathbf{h}\right) + \alpha\mathbf{m}_i\times\frac{d\mathbf{m}_i}{dt}, \quad (2)$$

where $\mathbf{H}_i^{eff} = -(1/\mu_0)\partial H/\partial\mathbf{m}_i$ is the effective field. We set the lattice constant $a = 1.0 \times 10^{-9}$ m, the gyromagnetic ratio $\gamma = -2.211 \times 10^5$ m/(a. s) [13] and the Gilbert damping coefficient $\alpha = 0.005$. $\mathbf{h}$ is the AC magnetic field used to generate stable spin wave, $\mathbf{h}_{LH}/\mathbf{h}_{RH} = h_0(\sin(\omega t)\mathbf{i} \pm \cos(\omega t)\mathbf{j})$ corresponds to left-/right-circularly polarized spin wave, and $\mathbf{h}_x/\mathbf{h}_y = h_0\sin(\omega t)\mathbf{j}/\mathbf{i}$ corresponds to the x/y linearly polarized spin wave with the magnitude h_0. We use the fourth-order Runge–Kutta method for numerical simulation on a system of 200 × 100 lattices. In our simulation, we set time step $\Delta t = 0.01$, $J = 1$, then a reduced time corresponds to the real time $t = 1.0 \times 10^{-13}$ s. Moreover, $\omega = 1$ corresponds to 1.6 THz, and $h_0 = 1$ corresponds to 1.58 Tesla.

As depicted in **Figure 1**, the spin wave sources are set at the left side of the system, and the yellow part and green part represent the left-handed and right-handed spin wave sources, respectively. Unless stated elsewhere, we take the parameters $h_0 = 800$ mT and $\omega = 2$ THz and use absorbing boundary on the right side of the system to avoid reflection of spin wave. Furthermore, the parameters of the two kinds of spin waves are set to be the same, and the balance position of the skyrmion is in the intersection line between the two sources. It is worth noting that the generating of the two kinds of spin waves with opposite chirality in the two halves of the system does not consume more energy than the injecting of single handed spin wave in the whole system.

RESULTS AND DISCUSSION

To some extent, spin wave scattering is similar to the classical motion of a particle subjecting to an effective magnetic field from

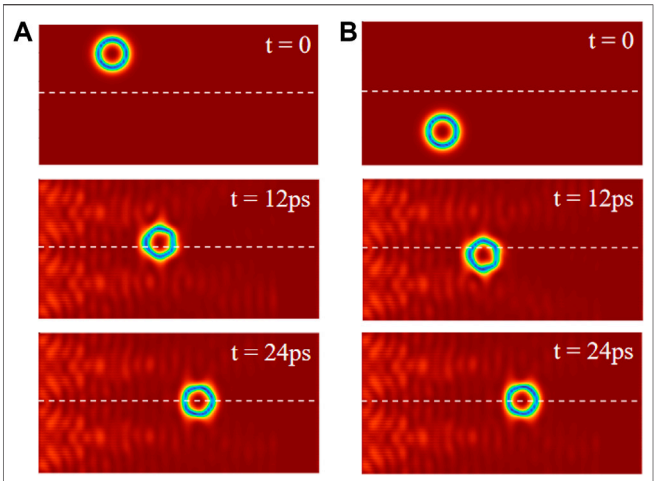

FIGURE 2 | The motion of the AFM skyrmion with different initial positions at **(A)** upside and **(B)** bottom side. The white dashed line indicates the intersection of the two spin wave sources.

the skyrmion [26]. Generally, due to their opposite effective charges, the left-handed and right-handed spin waves are scattered by the skyrmion towards the up side and down side, respectively, as depicted in **Figure 1**. Thus, the momentum exchanges between spin waves and the skyrmions along the longitudinal y-direction are well canceled out, and the skyrmion Hall motion could be suppressed.

This argument has been confirmed in our simulations. **Figure 2A** shows the evolution of the skyrmion position. The AFM skyrmion is initially at the upper side in the absence of the spin wave (up part). When the spin waves are injected, the skyrmion is driven to the right side. In this case, the left-handed spin wave is scattered to the upside and drives the skyrmion downward due to the momentum conservation. Thus, the skyrmion is quickly relaxed to its equilibrium position $y = 50$ at $t = 12$ ps, as shown in the middle part of **Figure 2A**. Subsequently, the forces along the y-direction from the left-handed and right-handed spin waves acting on the skyrmion are well canceled out, and the skyrmion straightly moves along the x direction. More importantly, the suppression of the Hall motion is not affected by the initial position of the skyrmion. **Figure 2B** shows the motion of the skyrmion initially at the bottom side of the system. Attributing to the effect of the right-handed spin wave, the skyrmion is also relaxed to the equilibrium position. Thus, this method is rather efficient in the suppression of the skyrmion Hall motion in antiferromagnets.

The simulated skyrmion position as a function of time is presented in **Figure 3**. On one hand, the skyrmion is quickly relaxed to the equilibrium y-position at $y = 50$ (dashed line in **Figure 3A**) as discussed above, although a weak oscillating behavior is noticeable. On the other hand, the evolutions of the x-position for the two cases are almost the same, as shown in **Figure 3B**. It is noted that the injected spin waves are unavoidable dissipated as it propagates, contributing to the decrease of the skyrmion speed (slope of the position curve).

Subsequently, we investigate the dependence of the speed of the skyrmion on several parameters and present the simulated results in **Figure 4**. Here, the speed is estimated from the average one in the region $x = (110, 130)$. The calculated velocity v_x-Double as a function of ω for $h_0 = 600$ mT is shown with red squares in **Figure 4A**. Two frequencies at $\omega = 1.6$ THz and 2.2 THz are observed with local maximum values $v_x \sim 450$ m/s, which is comparable to the current driven one. The speed of the skyrmion driven by the y linearly polarized spin wave v_x-Linearly is also estimated to be $v_x \sim 200$ m/s, which is rather stable for various ω but much smaller than the maximum value driven by the double circularly polarized spin waves. To have a direction comparison, the speeds along the x direction v_x and y-direction v_y of the skyrmion driven by right-handed spin wave are also presented. Two local maximum $v_x \sim 550$ m/s are estimated at $\omega = 1.7$ THz and 2.0 THz, and the maximum $v_y \sim 850$ m/s is estimated at $\omega = 2.1$ THz. However, in all investigated ω regions, $v_y > v_x$ is estimated, demonstrating the strong skyrmion Hall effect. Thus, particular ω could be chosen in the proposed method to obtain large speed in the absence of skyrmion Hall motion.

The magnitude of the spin wave is mainly controlled by h_0. Thus, with the increase of h_0, the speed of the skyrmion is increased, as shown in **Figure 4B**, which presents the estimated speeds of the skyrmion as functions of magnitude driven by various methods at $\omega = 2$ THz. For $h_0 < 750$ mT, all the estimated speeds increase appropriately with h_0^2 raised from the energy transfer between the spin wave and skyrmion, noting that the energy of the spin wave linearly increases with h_0^2. However, with the further increase of h_0, the skyrmion speed driven by the double circularly polarized spin waves increases much slowly. In some extent, the interference between the two kinds of spin waves is strengthened, strongly limiting the increase of the skyrmion speed.

Furthermore, the skyrmion radius depending on several parameters of the system such as the DMI and anisotropy also affects the skyrmion speed. In **Figure 4C**, the simulated speeds as functions of D driven by various methods for $\omega = 2.0$ THz and $h_0 = 600$ mT are presented. Moreover, the calculated skyrmion radii are also given to help one to understand the results easier. The same as our earlier theoretical calculations, the radius is increased with the increase of D [33, 34]. On one hand, the interacting area between the spin wave and skyrmion is enlarged [35], resulting in the increase of interacting force and skyrmion speed. On the other hand, the mass of the skyrmion is also increased with the increase of the radius [36], decreasing the skyrmion speed. As a result, the competition between the above two factors determines the speed of the skyrmion. For the skyrmion driven by the linearly polarized spin wave, the speed monotonously decreases with the increase of D, demonstrating the dominant effect of the second factor. For the skyrmion driven by double and single circularly polarized spin waves, the oscillating decrease of v_x is observed due to the competition between the two factors. Moreover, the two simulated v_x are almost the same for $D > 0.145$, attributing to the increase of the component from the circularly polarized spin waves in the driving force.

Figure 4D shows the dependence of v_x on the distance between the two spin wave sources for $\omega = 2.0$ THz and

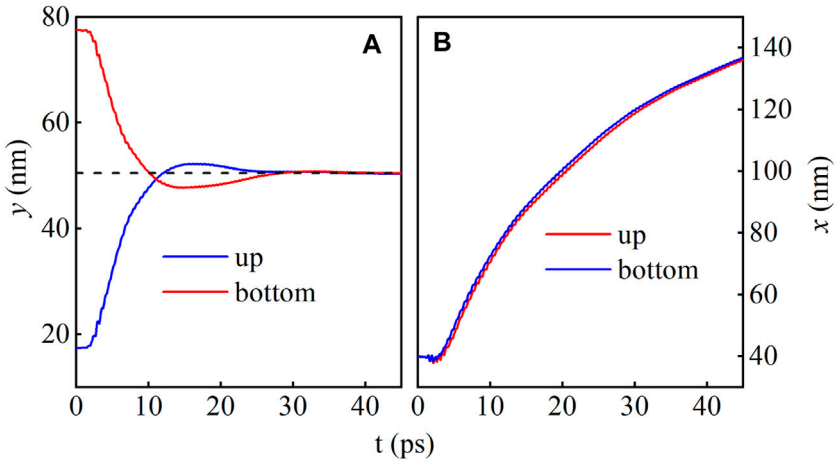

FIGURE 3 | The evolution of the **(A)** *y* and **(B)** *x* coordinates of the AFM skyrmions. The black dashed line represents the intersection of the spin wave sources.

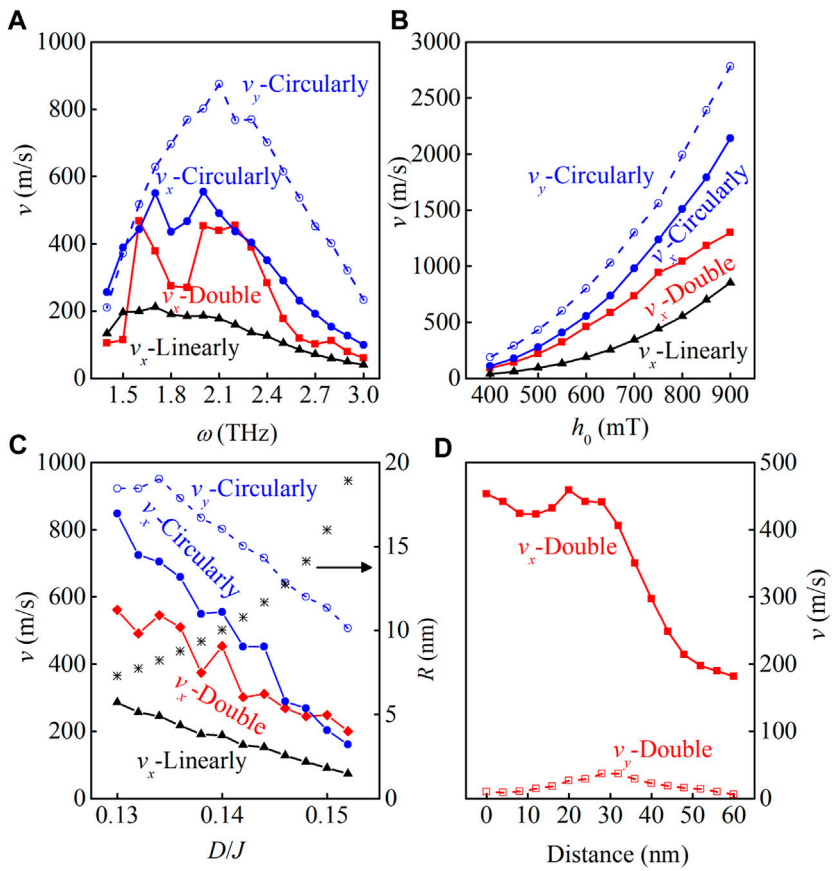

FIGURE 4 | The simulated speeds of the skyrmion driven by the double circularly polarized spin waves v_x-Double, by the *y* linearly polarized spin waves v_x-Linearly, by the right-handed polarized spin waves v_x-Circularly and v_y-Circularly as functions of **(A)** ω for h_0 = 600mT, **(B)** h_0 for ω = 2 THz, and **(C)** *D* for h_0 = 600 mT and ω = 2 THz. **(D)** The simulated v_x and v_y as function of the distance between the two spin wave sources for h_0 = 600 mT and ω = 2 THz. The simulated skyrmion radii are also presented in **(C)**.

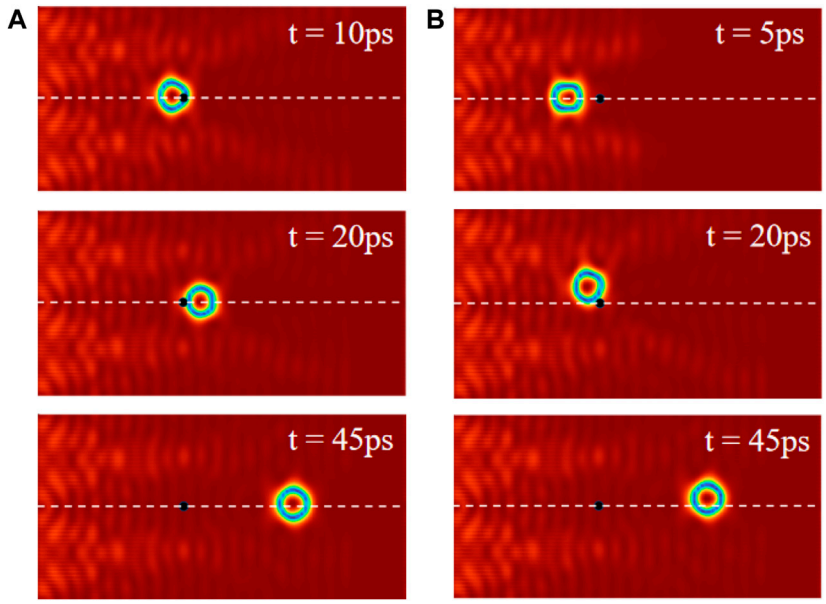

FIGURE 5 | The AFM skyrmion motion in the presence of the defect for **(A)** $A/J = 0.05$ and **(B)** $A/J = 0.15$. The black dots are the defects, and the white dashed lines represent the intersection of the two spin wave sources.

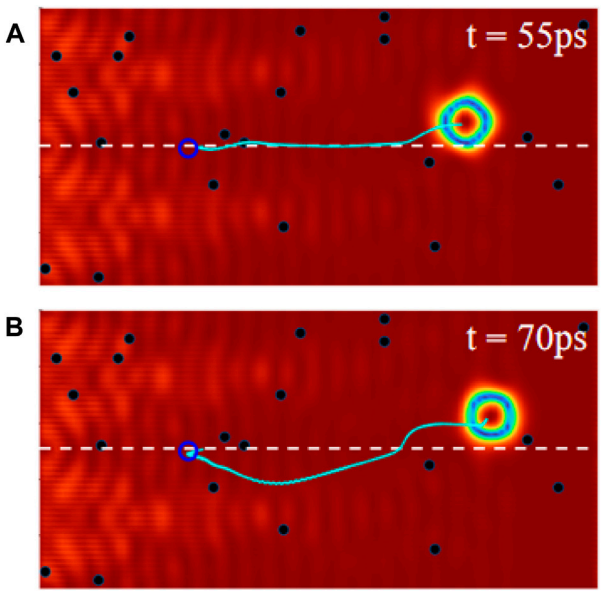

FIGURE 6 | The AFM skyrmion motion trajectories (green curves) with defect concentration 0.1% for **(A)** $A/J = 0.05$ and **(B)** $A/J = 0.15$, where the initial positions of skyrmion are represented by the empty blue circles.

$h_0 = 600$ mT. It is clearly shown that in a rather large distance range 0–30 nm, a rather stable speed $v_x \sim 500$ m/s is obtained. Thus, the skyrmion dynamics is hardly affected by increasing the distance between the two spin wave sources due to the spreading of the spin waves, allowing one to choose proper distance between the two spin wave sources to save energy. Moreover, v_y is rather small in the whole distance range, indicating again the well suppression of the skyrmion Hall motion.

The depinning behavior of skyrmion is a crucial issue considering the fact that there are inevitable defects in real materials. At last, we investigate the depinning behavior from the defect which is set in the intersection line, as shown in **Figure 5**. Here, additional anisotropy $A(\mathrm{m}_i^z)^2$ is used to describe the defect at site i, and we take $D/J = 0.13$. **Figure 5A** shows the trajectory of the skyrmion for $A/J = 0.05$, $\omega = 2$ THz, and $h_0 = 800$ mT. It is clearly shown that the skyrmion can pass through the defect directly. However, the energy barrier is high for large A, prohibiting the skyrmion go straightly through the defect [3]. Interestingly, the skyrmion can bypass the defect and then return to its presupposed orbit, as shown in **Figure 5B**, which presents the motion of the skyrmion for $A/J = 0.15$. More interestingly, the depinning effect still works in the system with randomly distributed defects for a high concentration 0.1%, as demonstrated in **Figures 6A,B**, where presents the skyrmion trajectory (green curve) for $A/J = 0.05$ and $A/J = 0.15$, respectively. Similarly, the skyrmions pass through the weak defects for $A/J = 0.05$ directly, while bypassing the strong defects for $A/J = 0.15$. Thus, the proposed method could be used to precisely drive the skyrmion motion along designed tracks.

Most recently, the AFM skyrmions have been experimentally observed in antiferromagnets with synthetic structures and three sub-lattices [37], which could be used to check our simulations. The generation of the spin wave could be realized through applying an oscillating magnetic field with intensity $h_0 = 400$–800 mT and frequency $\omega \sim 2$ THz [38], or by injecting spin current with intended polarizations [39, 40].

SUMMARY

In summary, we propose a method to suppress the skyrmion Hall motion driven by circularly polarized spin waves in antiferromagnets. The application of the two circularly polarized spin waves drives the skyrmion motion straightly along the intersection line of the two spin wave sources. The skyrmion speed depending on these parameters of the spin waves and system is numerically simulated, and a comparison with those driven by other methods is provided. At last, two depinning behaviors of the skyrmion related to the strengths of the defect are discussed. Thus, the proposed method could be used in precisely modulating the skyrmion dynamics.

DATA AVAILABILITY STATEMENT

The raw data supporting the conclusions of this article will be made available by the authors, without undue reservation.

AUTHOR CONTRIBUTIONS

SG conceived the research project, SG and ZJ performed the computations. SG, YY, ZJ, TL, YL, and MQ commented the modeling and discussed the results. MQ and SG wrote the manuscript.

FUNDING

The work was supported by the Natural Science Foundation of China (Grant No. 51971096), the Science and Technology Planning Project of Guangzhou in China (Grant No. 201904010019), the Natural Science Foundation of Guangdong Province (Grant No. 2019A1515011028), Special Funds for the Cultivation of Guangdong College Students Scientific and Technological Innovation (Grant No. pdjh2020a0148), and National college students' innovation and entrepreneurship training program (Grant No. 202110574049).

REFERENCES

1. Fert A, Cros V, and Sampaio J. Skyrmions on the Track. *Nat Nanotech* (2013) 8:152–6. doi:10.1038/nnano.2013.29
2. Nagaosa N, and Tokura Y. Topological Properties and Dynamics of Magnetic Skyrmions. *Nat Nanotech* (2013) 8:899–911. doi:10.1038/nnano.2013.243
3. Iwasaki J, Mochizuki M, and Nagaosa N. Universal Current-Velocity Relation of Skyrmion Motion in Chiral Magnets. *Nat Commun* (2013) 4:1463. doi:10.1038/ncomms2442
4. Boulle O, Vogel J, Yang H, Pizzini S, de Souza Chaves D, Locatelli A, et al. Room-temperature Chiral Magnetic Skyrmions in Ultrathin Magnetic Nanostructures. *Nat Nanotech* (2016) 11:449–54. doi:10.1038/nnano.2015.315
5. Büttner F, Lemesh I, and Beach GSD. Theory of Isolated Magnetic Skyrmions: From Fundamentals to Room Temperature Applications. *Sci Rep* (2018) 8: 4464. doi:10.1038/s41598-018-22242-8
6. Yuan HY, and Wang XR. Skyrmion Creation and Manipulation by Nano-Second Current Pulses. *Sci Rep* (2016) 6:22638. doi:10.1038/srep22638
7. Silva RL, Silva RC, Pereira AR, and Moura-Melo WA. Antiferromagnetic Skyrmions Overcoming Obstacles in a Racetrack. *J Phys Condens Matter* (2019) 31:225802. doi:10.1088/1361-648x/ab0abd
8. Kim K-W, Moon K-W, Kerber N, Nothhelfer J, and Everschor-Sitte K. Asymmetric Skyrmion Hall Effect in Systems with a Hybrid Dzyaloshinskii-Moriya Interaction. *Phys Rev B* (2018) 97:224427. doi:10.1103/physrevb.97.224427
9. Bessarab PF, Yudin D, Gulevich DR, Wadley P, Titov M, and Tretiakov OA. Stability and Lifetime of Antiferromagnetic Skyrmions. *Phys Rev B* (2019) 99(R):140411. doi:10.1103/physrevb.99.140411
10. Liang JJ, Yu JH, Chen J, Qin MH, Zeng M, Lu XB, et al. Magnetic Field Gradient Driven Dynamics of Isolated Skyrmions and Antiskyrmions in Frustrated Magnets. *New J Phys* (2018) 20:053037. doi:10.1088/1367-2630/aac24c
11. Barker J, and Tretiakov OA. Static and Dynamical Properties of Antiferromagnetic Skyrmions in the Presence of Applied Current and Temperature. *Phys Rev Lett* (2016) 116:147203. doi:10.1103/physrevlett.116.147203
12. Zhang J, Zhang Y, Gao Y, Zhao G, Qiu L, Wang K, et al. Magnetic Skyrmions in a Hall Balance with Interfacial Canted Magnetizations. *Adv Mater* (2020) 32: 1907452. doi:10.1002/adma.201907452
13. Zhang X, Zhou Y, and Ezawa M. Antiferromagnetic Skyrmion: Stability, Creation and Manipulation. *Sci Rep* (2016) 6:24795. doi:10.1038/srep24795
14. Akosa C, Tretiakov O, Tatara G, and Manchon A. Theory of the Topological Spin Hall Effect in Antiferromagnetic Skyrmions: Impact on Current-Induced Motion. *Phys Rev Lett* (2018) 121:097204. doi:10.1103/physrevlett.121.097204
15. Jin C, Song C, Wang J, and Liu Q. Dynamics of Antiferromagnetic Skyrmion Driven by the Spin Hall Effect. *Appl Phys Lett* (2016) 109:182404. doi:10.1063/1.4967006
16. Göbel B, Mook A, Henk J, and Mertig I. Antiferromagnetic Skyrmion Crystals: Generation, Topological Hall, and Topological Spin Hall Effect. *Phys Rev B* (2017) 96:060406(R). doi:10.1103/physrevb.96.060406
17. Buhl PM, Freimuth F, Blügel S, and Mokrousov Y. Topological Spin Hall Effect in Antiferromagnetic Skyrmions. *Phys Status Solidi RRL* (2017) 11:1700007. doi:10.1002/pssr.201700007
18. Yuan HY, Liu Q, Xia K, Yuan Z, and Wang XR. Proper Dissipative Torques in Antiferromagnetic Dynamics. *EPL* (2019) 126:67006. doi:10.1209/0295-5075/126/67006
19. Liang X, Zhao G, Shen L, Xia J, Zhao L, Zhang X, et al. Dynamics of an Antiferromagnetic Skyrmion in a Racetrack with a Defect. *Phys Rev B* (2019) 100:144439. doi:10.1103/physrevb.100.144439
20. Zhang X, Ezawa M, Xiao D, Zhao GP, Liu Y, and Zhou Y. All-magnetic Control of Skyrmions in Nanowires by a Spin Wave. *Nanotechnology* (2015) 26:225701. doi:10.1088/0957-4484/26/22/225701
21. Yu H, Xiao J, and Schultheiss H. Magnetic Texture Based Magnonics. *Phys Rep* (2021) 905:1–59. doi:10.1016/j.physrep.2020.12.004
22. Wang ZY, Yuan HY, Cao YS, Li ZX, Duine RA, and Yan P. Magnonic Frequency Comb through Nonlinear Magnon-Skyrmion Scattering. *Phys Rev Lett* (2021) 127:037202. doi:10.1103/physrevlett.127.037202
23. Iwasaki J, Beekman AJ, and Nagaosa N. Theory of Magnon-Skyrmion Scattering in Chiral Magnets. *Phys Rev B* (2014) 89:064412. doi:10.1103/physrevb.89.064412
24. Shen M, Zhang Y, Ou-Yang J, Yang X, and You L. Motion of a Skyrmionium Driven by Spin Wave. *Appl Phys Lett* (2018) 112:062403. doi:10.1063/1.5010605
25. Proskurin I, Stamps RL, Ovchinnikov AS, and Kishine J-I. Spin-Wave Chirality and its Manifestations in Antiferromagnets. *Phys Rev Lett* (2017) 119:177202. doi:10.1103/physrevlett.119.177202
26. Daniels MW, Yu W, Cheng R, Xiao J, and Xiao D. Topological Spin Hall Effects and Tunable Skyrmion Hall Effects in Uniaxial Antiferromagnetic Insulators. *Phys Rev B* (2019) 99:224433. doi:10.1103/physrevb.99.224433
27. Jin Z, Meng CY, Liu TT, Chen DY, Fan Z, Zeng M, et al. Magnon-driven Skyrmion Dynamics in Antiferromagnets: Effect of Magnon Polarization. *Phys Rev B* (2021) 104:054419. doi:10.1103/physrevb.104.054419
28. Pickart SJ, Collins MF, and Windsor CG. Spin-Wave Dispersion in KMnF3. *J Appl Phys* (1966) 37:1054–5. doi:10.1063/1.1708332
29. Heeger AJ. Spin-Wave Instability and Premature Saturation in Antiferromagnetic Resonance. *Phys Rev* (1963) 131:608–16. doi:10.1103/physrev.131.608

30. Qaiumzadeh A, Kristiansen LA, and Brataas A. Controlling Chiral Domain Walls in Antiferromagnets Using Spin-Wave Helicity. *Phys Rev B* (2018) 97: 020402(R). doi:10.1103/physrevb.97.020402
31. Saiki K. Resonance Behaviour in Canted Antiferromagnet KMnF3. *J Phys Soc Jpn* (1972) 33:1284–91. doi:10.1143/jpsj.33.1284
32. Lan J, Yu W, and Xiao J. Antiferromagnetic Domain wall as Spin Wave Polarizer and Retarder. *Nat Commun* (2017) 8:178. doi:10.1038/s41467-017-00265-5
33. Jin Z, Liu T, Li W, Zhang X, Hou Z, Chen D, et al. Dynamics of Antiferromagnetic Skyrmions in the Absence or Presence of Pinning Defects. *Phys Rev B* (2020) 102:054419. doi:10.1103/physrevb.102.054419
34. Wang XS, Yuan HY, and Wang XR. A Theory on Skyrmion Size. *Commun Phys* (2018) 1:31. doi:10.1038/s42005-018-0029-0
35. Schütte C, and Garst M. Magnon-skyrmion Scattering in Chiral Magnets. *Phys Rev B* (2014) 90:094423. doi:10.1103/physrevb.90.094423
36. Tveten EG, Qaiumzadeh A, Tretiakov OA, and Brataas A. Staggered Dynamics in Antiferromagnets by Collective Coordinates. *Phys Rev Lett* (2013) 110: 127208. doi:10.1103/physrevlett.110.127208
37. Legrand W, Maccariello D, Ajejas F, Collin S, Vecchiola A, Bouzehouane K, et al. Room-temperature Stabilization of Antiferromagnetic Skyrmions in Synthetic Antiferromagnets. *Nat Mater* (2020) 19:34–42. doi:10.1038/s41563-019-0468-3
38. Cheng R, Daniels MW, Zhu J-G, and Xiao D. Antiferromagnetic Spin Wave Field-Effect Transistor. *Sci Rep* (2016) 6:24223. doi:10.1038/srep24223
39. Cheng R, Xiao J, Niu Q, and Brataas A. Spin Pumping and Spin-Transfer Torques in Antiferromagnets. *Phys Rev Lett* (2014) 113:057601. doi:10.1103/physrevlett.113.057601
40. Cheng R, and Niu Q. Dynamics of Antiferromagnets Driven by Spin Current. *Phys Rev B* (2014) 89:081105(R). doi:10.1103/physrevb.89.081105

Conflict of Interest: The authors declare that the research was conducted in the absence of any commercial or financial relationships that could be construed as a potential conflict of interest.

Publisher's Note: All claims expressed in this article are solely those of the authors and do not necessarily represent those of their affiliated organizations, or those of the publisher, the editors, and the reviewers. Any product that may be evaluated in this article, or claim that may be made by its manufacturer, is not guaranteed or endorsed by the publisher.

frontiers in Physics

ORIGINAL RESEARCH
published: 23 November 2021
doi: 10.3389/fphy.2021.769873

Skyrmion-Antiskyrmion Racetrack Memory in Rank-One DMI Materials

Markus Hoffmann[1]*, *Gideon P. Müller*[1,2], *Christof Melcher*[3] and *Stefan Blügel*[1]

[1]Peter Grünberg Institut and Institute for Advanced Simulation, Forschungszentrum Jülich and JARA, Jülich, Germany, [2]Science Institute of the University of Iceland, Reykjavík, Iceland, [3]Department of Mathematics and JARA FIT, RWTH Aachen University, Aachen, Germany

Chiral magnetic skyrmions, localized and topologically protected vortex-like magnetic textures that can be found in chiral magnets, are currently under intense study as an entity for information storage and processing. A recent study showed that so-called rank-one materials can host both skyrmions and antiskyrmions at the same energy. In such systems the Dzyaloshinskii-Moriya interaction, in general a tensorial quantity, is reduced to only one non-zero component. The presence of both skyrmions and antiskyrmions allows for the investigation of the possible interplay between them. Here, we investigate the stability and interaction of skyrmions and antiskyrmions as well as their transport properties subject to spin-orbit torque for a model system described by an atomistic spin-lattice Hamiltonian employing the simulation software Spirit. The spin-orbit torque driven spin-dynamics described by the Landau-Lifshitz-Gilbert equation is compared to the effective one of the Thiele equation. We demonstrate that, even though skyrmions and antiskyrmions can be seen as antiparticles, a rather dense arrangement of both along a memory track is possible, enabling their use as representations of the binary data bits “0” and “1” in a memory device.

Keywords: skyrmion, antiskyrmion, racetrack memory, dzyaloshinskii-moriya interaction, spin-dynamics, Thiele equation

OPEN ACCESS

Edited by:
Xichao Zhang,
Shinshu University, Japan

Reviewed by:
Alexey Kovalev,
University of Nebraska-Lincoln, United States
Joo-Von Kim,
CNRS/Université Paris-Saclay, France

***Correspondence:**
Markus Hoffmann
m.hoffmann@fz-juelich.de

Specialty section:
This article was submitted to Condensed Matter Physics, a section of the journal Frontiers in Physics

Received: *02 September 2021*
Accepted: *25 October 2021*
Published: *23 November 2021*

Citation:
Hoffmann M, Müller GP, Melcher C and Blügel S (2021) Skyrmion-Antiskyrmion Racetrack Memory in Rank-One DMI Materials. Front. Phys. 9:769873. doi: 10.3389/fphy.2021.769873

1 INTRODUCTION

The increasing amount of digital data requires the development of new data storage devices with higher information density at lower energy consumption. So far, magnetic hard disks have been the backbone of mass storage applications in large data centers, where information is read and written using a read-write head that moves across the magnetic disk. However, this technology is approaching its limits, both in terms of information density and the mechanical effort of reading and writing data. A change of paradigm was suggested by the racetrack memory [1], a solid state shift register type memory in which the information is encoded in a pattern of magnetic domains separated by domain walls. These domain walls can be moved by spin-currents either applied in spin-transfer torque (STT) geometry, i.e., a current of spin-polarized electrons is passing in perpendicular geometry through the magnetic layer, or even more efficiently in spin-orbit torque (SOT) geometry, i.e., a charge current is passing through a nonmagnetic heavy metal substrate layer creating a perpendicularly flowing spin current or an accumulation of spin-polarized electrons at the interface to the magnetic domain.

Around 10 years ago, chiral magnetic skyrmions [2] were discovered [3–5], two-dimensional magnetic vortex-like spin textures of topological nature at the nanoscale. They can form in the presence of an applied magnetic field in ferromagnetic films that experience an interfacial

Dzyaloshinskii-Moriya interaction [6, 7] (DMI) as a result of spin-orbit coupling and broken structure-inversion symmetry as introduced at the interface [8]. This finding led to an extension of the racetrack idea towards skyrmion racetracks [9], where the information is now encoded in the presence or absence of such skyrmions on a thin racetrack stripe. Those skyrmions can then be moved by ultra-low electric current densities [10]. Such a possible movement of skyrmions has been shown both theoretically [11, 12] and experimentally [13–16]. In the last years we witnessed significant progress towards the optimization of skyrmion design for technology [17, 18].

Like in ordinary racetrack memories, the information in skyrmion racetrack devices relies on the presence or absence of the skyrmion and the quantization of distances between adjacent skyrmions on a track. However, skyrmions are highly movable, interacting particles that can drift as a result of thermal fluctuations, making it difficult to maintain their distribution along a track. This can lead to difficulties, as e.g., thermal movement can change the distance between neighboring particles, destroying the encoded information. To overcome this problem, several suggestions have been made. One option would be to force the skyrmions to settle on discrete positions, e.g., realized by nano-fabricated arrays of notches or of artificial pinning centers acting as a periodic potential [19]. A more recent proposal is a two-lane racetrack [20], where the choice of track on which the skyrmion settles encrypts the binary information. Those lanes are separated by a finite energy barrier which prevents the loss of data. Both solutions to solve the problem rely on fabrication on the nanoscale. This is a serious challenge that is likely to lead to higher costs. Lately, a powerful alternative approach has been proposed that does not require fixed distances between moving bit carriers because the stream of binary data, which is a sequence of ones and zeros, has been encoded using a sequence of two distinguishable particles: single skyrmions and bobbers [21]. The proposed concept of data encoding promises the realization of a new generation of magnetic solid-state storage devices, where a higher data density can be achieved compared to the existing skyrmion-based racetrack storage concept.

Recently, it was shown on theoretical grounds that in magnetic thin layers of particular point-group symmetry classes, not only magnetic skyrmions but also antiskyrmions can exist [22, 23]. The latter can occur when symmetry allows an anisotropic Dzyaloshinskii-Moriya interaction (DMI), i.e., its strength is different in different spatial directions as experimentally evidenced for thin films of Co. on W (110) [24]. In this case, and resorting to the micromagnetic formulation of the energy landscape, the DMI can no longer be described by a single scalar quantity, the so-called *spiralization D*, but must be replaced by a two-dimensional spiralization tensor $\mathcal{D}$, corresponding to the thin layer geometry. In Ref. [23] it was rigorously shown that under these conditions magnetic skyrmions and antiskyrmions can coexist and the sign of the determinant of $\mathcal{D}$ determines which of the two is the least energy configuration over all non-trivial homotopy classes.

Antiskyrmions [23, 25, 26], like skyrmions, are localized magnetic particles with a topologically non-trivial magnetization texture specified by the same magnitude of the topological charge, $|Q| = 1$, but an opposite sign and an opposite $\mathbb{S}^1$ winding number. The winding number is obtained by means of a line integral over the inplane components of the magnetization along a path enclosing the origin of the particle. It is a secondary topological charge and the defining index to distinguish between skyrmion ($\nu = 1$) and antiskyrmion ($\nu = -1$). In the film geometry, skyrmions are of Néel-type, where the spins rotate in the radial planes from the core to the perimeter. Skyrmions are homochiral particles. The chirality or handedness, i.e., the clockwise or counterclockwise rotational sense of the spin rotation along the radial direction away from the core, is the same for all radial directions. The antiskyrmion is the simplest form of a multichiral skyrmion, characterized by different rotational senses away from the core along different radial directions (see **Figure 1**), and between these directions of different handedness, the magnetization texture varies between Néel-type (chirality vector perpendicular to the radial direction) and Bloch-type (chirality vector parallel to the radial direction) chirality. There is no smooth transformation between a skyrmion and an antiskyrmion. An antiskyrmion is related to a skyrmion by a mirror operation in the spin space, the components of the chirality vector parallel to this mirror plane are conserved whereas the components perpendicular to the mirror plane are inverted (for more details see Supplementary Material of Ref. [23]). In the particular case of a rank-one spiralization tensor, i.e., a vanishing determinant, both the skyrmion and the antiskyrmion are energetically degenerate. Like the skyrmion, the antiskyrmion experiences that a current-driven motion has a transverse component, known as the antiskyrmion Hall effect. Furthermore, in the context of spin-orbit torques, the antiskyrmion Hall angle strongly depends on the current direction. Interestingly, in the context of racetrack memory, the antiskyrmion gyroconstant is opposite to that for the skyrmion, allowing the current-driven propagation of coupled skyrmion-antiskyrmion pairs without an apparent skyrmion Hall effect [27, 28].

In this paper, we combine the two recent development strands: The skyrmion racetrack device and the simultaneous presence and energetic degeneracy of skyrmions and antiskyrmions in rank-one materials, and propose a new type of data storage device, namely a skyrmion-antiskyrmion racetrack memory (see **Figure 1**). It is an alternative to the skyrmion-bobber racetrack memory [21]. In this device, as in Ref. [21], information would be encoded by two distinguishable magnetic particles, e.g., a skyrmion represents the bit "1", whereas an antiskyrmion represents the "0". The distinction between the two is possible, for example, by measuring the sign of the topological Hall effect (THE) [29], which depends on the sign of the topological charge Q, which is opposite for skyrmions and antiskyrmions, or the strength of the chiral Hall effect (CHE) [30] or the noncollinear Hall effect (NHE) [31], which both vary in size depending on the type of particle. We show that skyrmions and antiskyrmions, although they carry the notion of antiparticles, can indeed coexist and even repel each other if the proper geometry of the racetrack is chosen. We focus on SOT driven particle motion as this is

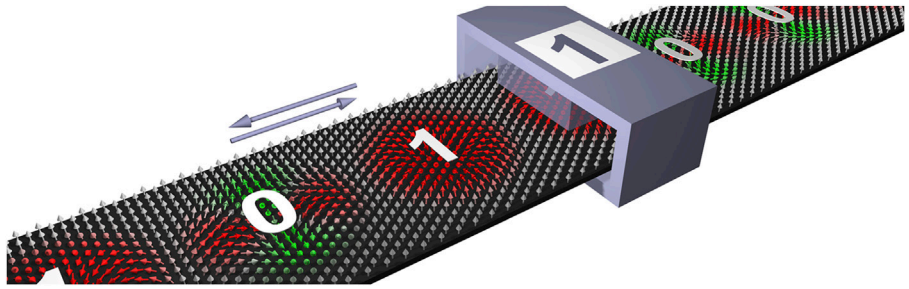

FIGURE 1 | Schematic picture of a skyrmion-antiskyrmion racetrack. Information is encoded in the type of the magnetic particle, i.e., a skyrmion represents the bit "1" and an antiskyrmion represents the bit "0". By applying a current, the magnetic particles can be moved towards a read/write head.

more energy efficient than STT. Using spin-dynamics simulations applied to a model system we demonstrate the feasibility of such a device by showing that a coherent motion of skyrmions and antiskyrmions along the same trackline can be achieved. In order to show the main effects efficiently and to provide a transparent analysis of our simulations, our model system is parameterized to match a ferromagnetic rank-one material with C_{2v}-symmetry of monoatomic layer thickness deposited on a nonmagnetic heavy-metal substrate, e.g. having (110) oriented interfaces in mind, in analogy to atomic-scale skyrmions studied experimentally in the past for (111) oriented interfaces with C_{3v} symmetry [5, 32]. Consistently, the models and simulations are on the atomistic scale.

2 MODELS AND METHODS

2.1 Atomistic Heisenberg Model and Model Parameters

In this paper we study ultrathin ferromagnetic films with an out-of-plane easy axis on a heavy-metal substrate. As underlying model we use the extended Heisenberg Hamiltonian to describe the interactions between localized classical vector spins $\mathbf{S}_i$ of unit length placed on atomic sites i,

$$H = -\sum_{\langle ij\rangle} J_{ij}\left(\mathbf{S}_i \cdot \mathbf{S}_j\right) - \sum_{\langle ij\rangle} \mathbf{D}_{ij} \cdot \left(\mathbf{S}_i \times \mathbf{S}_j\right) + \sum_i K_\perp \left(\mathbf{S}_i \cdot \hat{\mathbf{e}}_z\right)^2, \quad (1)$$

containing exchange and Dzyaloshinskii-Moriya interactions as well as uniaxial anisotropy. The sites i and j are limited to the magnetic film, but the model parameters J_{ij}, $\mathbf{D}_{ij}$, and $K_\perp$ include also the properties of the metal substrate. ($J < 0$) $J > 0$ describes (anti-)ferromagnetic exchange between the sites and $K_\perp < 0$ denotes a magnetic easy axis parallel to the z-direction. For ultrathin magnetic systems, the dipolar interaction between magnetic moments is typically of minor importance and is added as an additional on-site contribution to the magnetic anisotropy constant $K_\perp$. We restrict ourselves to monolayers with a two-dimensional, centered rectangular Bravais lattice as this crystal structure with C_{2v} symmetry offers the possibility of a DMI tensor of rank-one [23]. To obtain such a tensor, $\mathcal{D}$, which is related to the atomistic DMI vectors via

$$\mathcal{D} = -\frac{1}{V}\sum_{\langle ij\rangle} \mathbf{D}_{ij} \otimes \mathbf{R}_{ij}, \quad (2)$$

all atomistic DMI vectors, $\mathbf{D}_{ij}$, have to be aligned in parallel along one of the two lattice vectors of the rectangular unit cell. Without loss of generality we assume that the x-axis is oriented parallel to one of the lattice vectors. The direction along the second lattice vector we call the y-direction. The orientation of the track of the racetrack device on which the information particles move relative to the orientation of the crystal lattice and subsequently the orientation of the DM vector is an important design aspect. This determines the relative chiral orientation of the antiskyrmion with respect to the skyrmion. We will see below that this bears important consequences for the interaction of skyrmions with antiskyrmions. For visualization purposes, we chose the same lattice parameter, a, for both directions of the corresponding rectangular superlattice with two atoms per unit cell.

Magnetic skyrmionic structures can be stabilized by different combinations of parameters in the Heisenberg model (1). On the one hand, it is sufficient to have only nearest neighbor interactions both for the DMI and the exchange interaction and to apply a magnetic field parallel to the ferromagnetic background. By choosing the proper DMI geometry, i.e., a rank-one spiralization tensor, both skyrmions and antiskyrmions can coexist. However, under these assumptions the stabilization of skyrmionic particles becomes problematic when the DMI is not isotropic but anisotropic. In the case of rank-one DMI, i.e., the most anisotropic case possible, the magnetic texture loses its axial symmetry, it becomes elliptically unstable to the point that it decays into a one-dimensional magnetic structure. To counteract, a strong external magnetic field is needed to stabilize the skyrmionic structure, making it unpractical for applications.

An alternative way to stabilize skyrmionic spin textures is to resort to systems with competing magnetic exchange interactions, i.e., systems where more than a nearest neighbor parameter J is needed to describe the system correctly. These Js compete between different neighbors by opposite signs, yet, the magnetic ground state still remains ferromagnetic. Skyrmion stabilization can then be achieved either by counteracting the

previously discussed elliptical instability of the skyrmion by an anisotropic exchange interaction or by purely stabilizing the skyrmionic particles due to exchange. In the following, we will focus on this latter case, since it provides the possibility of studying both skyrmions and antiskyrmions as both of them can be stable independent of the occurring DM interactions. However, we will show later that even though the DMI is not directly responsible for the stabilization, it is quite important for the motion of skyrmions and antiskyrmions, especially the collective motion along a particular direction.

As model parameters for our racetrack ferromagnet, we used $J_1 > 0$, $J_4 = -0.25\,J_1$, $\mathbf{D}_1 = \pm 0.02\ J_1 \cdot \hat{\mathbf{e}}_x$ and $K = -0.025\,J_1$. Index "1" indicates the nearest-neighbor interaction. Taking the centered rectangular lattice structure, J_4 is the interaction with the neighbors lying in the same direction as the first nearest neighbors, but with twice the distance. The sign of J_4 is opposite to J_1 expressing an antiferromagnetic exchange interaction competing with the ferromagnetic nearest-neigbor exchange. From the viewpoint of the rectangular unit cell J_4 contributes to exchange interactions in x- and y-direction. With this choice of parameters, skyrmions and antiskyrmions are metastable with an energy of about 3.5 J_1 above the ferromagnetic ground state. As isolated particle, they have a diameter of about six lattice parameters, 6 a, which corresponds to about 2 nm, a typical size of atomic-scale skyrmions in ultrathin films observed earlier [33]. Lateral boundary conditions as typical for (anti-)skyrmions on a track can modify the particle size as discussed in the results chapter. The diameter is measured by the circle around the origin of the particle on which the z-component of the magnetization changes sign. Assuming the same lattice constant, a, for both directions of the rectangular unit cell, i.e., assuming a square cell, the particles are almost round, yet the anisotropic DM interactions cause a small ellipticity. To simulate a repulsive potential of the boundaries of the racetrack, we add in our simulation additional rows of spins which are pinned to point along the z-direction. Such a ferromagnetic pinning is necessary as the anisotropic DM interaction does not result in a repulsive potential at the boundaries, in isotropic systems caused by the bending of the magnetization at the edges to minimize the DM energy [34, 35]. Such a ferromagnetic pinning, however, can be achieved in experiments by locally enhancing the anisotropy.

2.2 Atomistic Spin Dynamics Simulations of Current-Driven Skyrmion and Antiskyrmion Propagation and Minimum Energy Paths

The time evolution of the atomistic spins subject to the current induced SOT [36] is followed by the numerical solution of the Landau–Lifshitz-Gilbert (LLG) equation presented here in the Landau–Lifshitz form at the atomistic level [37, 38] extend by the SOT,

$$\frac{d\mathbf{S}_i}{dt} = -\gamma_L \mathbf{S}_i \times \mathbf{H}_i^{\text{eff}} - \gamma_L \alpha_G \mathbf{S}_i \times \left(\mathbf{S}_i \times \mathbf{H}_i^{\text{eff}}\right) + \gamma_L \mathbf{T}_i, \qquad (3)$$

were $\mathbf{S}_i = \boldsymbol{\mu}_i/\mu_i$ are normalized magnetic moments located at a lattice site i, $\mu_i \mathbf{H}_i^{\text{eff}} = -\partial H/\partial \mathbf{S}_i$ is the static effective magnetic field acting on spin $\mathbf{S}_i$, $\gamma = g\mu_B/\hbar$ represents the gyromagnetic ratio, $\gamma_L = \gamma/(1+\alpha_G^2)$ is the renormalized gyromagnetic ratio, α_G is the isotropic Gilbert damping constant, and $\mathbf{T}_i$ is the spin-orbit torque acting on site i. The equation of motion is integrated for a set of spins in the two-dimensional, periodic domain by applying an efficient and robust semi-implicit numerical method [39] as implemented in Spirit [40, 41]. If not stated otherwise, we used for our simulations a sufficiently large simulation box for which we tested that no boundary effects occur.

The LLG equation is used in two regimes: (i) the quasi-static regime to determine the minimum energy paths (MEP) and the corresponding energy barriers for the interaction of (anti-) skyrmions with track boundaries as well as the mutual interactions of skyrmions with antiskyrmions and (ii) the dynamical regime to study the current-induced motion of both particles on the track. The importance of the MEP lies in the identification of a transition-state saddle-point and also provides detailed information about the transition mechanism, important quantitative knowledge, which is not easily accessible in the spin dynamics. To follow a MEP means to rotate spins in an optimal way so that the energy is minimal with respect to all degrees of freedom perpendicular to the path. Technically we use the geodesic nudged elastic band (GNEB) method [42] to determine the MEP. The GNEB method gives us precise values for the energy barriers by finding the maximum along any stable transition path and by this also the energetically most favorable transition path. The GNEB is a quasi-static method by which a path is initialized by a set of spin-configurations, called images, that is iteratively optimized using the LLG equation **(3)** without the precession (1. st term on the rhs in **(3)**) and SOT term but additional constraints added to the effective field $\mathbf{H}_i^{\text{eff}}$ to move the system towards the optimum. To obtain the exact saddle point configurations, the climbing image technique [43] is used. Note that the interpolated values between the discrete images can be calculated as cubic Hermite splines using the information on the inclination of the minimum energy path (MEP) at the data points.

In order to study the current-driven (anti-)skyrmion dynamics we express the SOT according to the two qualitatively distinct contributions, the field-like torque $\mathbf{T}^{\text{FL}}(\mathbf{S}) = \mathbf{S} \times \mathbf{H}_{\text{eff}}^{\text{FL}}(\mathbf{S})$ and anti-damping-like torque $\mathbf{T}^{\text{AD}}(\mathbf{S}) = \mathbf{S} \times \mathbf{H}_{\text{eff}}^{\text{AD}}(\mathbf{S})$, relate the effective current-induced fields, $\mathbf{H}_{\text{eff}}^{\text{FL}}$ and $\mathbf{H}_{\text{eff}}^{\text{AD}}$, in linear response theory to the applied electric field $\mathbf{E}$, which is proportional to the electric current density, $\mathbf{j}$, through the conductivity tensor and stay with the lowest order expansion of the induced fields in the orientation of $\mathbf{S}$ [44]. Recently, it was shown that also field-like terms beyond the lowest order in the spin-orientation become important for the motion of skyrmions [45], but this is beyond the scope of this paper. Considering a two-dimensional film and a current density $\mathbf{j} = (j_x, j_y)$ passing through the plane of the nonmagnetic heavy-metal substrate, in the conventional Rashba like symmetry, the fields are related to the current generated electron polarization density $\mathbf{S}_p = S_p\,\hat{\mathbf{e}}_z \times \mathbf{j}$ as $\mathbf{H}_{\text{eff}}^{\text{FL}} \propto \mathbf{S}_p$, and $\mathbf{H}_{\text{eff}}^{\text{AD}} \propto \mathbf{S} \times \mathbf{S}_p$, where $\hat{\mathbf{e}}_z$ is the unit vector pointing normal to the film plane. For interfaces with C_{2v} point-group symmetry, we find that the tensors relating $\mathbf{H}_{\text{eff}}^{\text{FL}}$ and $\mathbf{H}_{\text{eff}}^{\text{AD}}$ to the current density $\mathbf{j}$ is not described by a single material-dependent tensor coefficient as in Rashba-like case, but are

described by 2 and 4 independent tensor coefficients, respectively (for details see mm^2 symmetry in Table 1 of Ref. [46]). The presence of the two independent tensor coefficients for the field-like torque in C_{2v} symmetry is consistent with the two independent coefficients of the anistropic DMI tensor, $\mathcal{D}$, as both transform as axial vectors. To cast this into the commonly used relations between the fields $\mathbf{H}_{\text{eff}}$ and the electron polarization density $\mathbf{S}_{\text{p}}$, the scalar prefactor S_{p} becomes a matrix quantity $\mathcal{S}_{\text{p}}$, which is different for the field- and damping-like torques. For example, invoking the linear combination of a Bychkov-Rashba- and a Dresselhaus model, a minimum microscopic model describing the electronic states of a two-dimensional electron gas with spin-orbit interaction and C_{2v} symmetry, the field-like polarization can be written in the form $\mathcal{S}_{\text{p}}^{\text{FL}} = \text{diag}\,(S_{\text{p}}^{\text{R}} - S_{\text{p}}^{\text{D}}, S_{\text{p}}^{\text{R}} + S_{\text{p}}^{\text{D}})$, where S_{p}^{R} and S_{p}^{D} are the two corresponding material-dependent polarization strengths for the two mechanisms. In order to draw comprehensible conclusions about the feasibility of a Skyrmion-Antiskyrmion racetrack device, we decided to limit the exploration space that the materials allow in the C_{2v} geometry, and work with the same torque strength τ (up to the damping constant α_{G}) and the same polarization matrix $\mathcal{S}$ for both field contributions.

To simplify things we work with the normalized polarization direction $\hat{\mathbf{S}}_{\text{p}} = \hat{\mathcal{S}}_{\text{p}}\,\hat{\mathbf{e}}_{\text{z}} \times \hat{\mathbf{j}}$, with $|\det\hat{\mathcal{S}}_{\text{p}}| = 1$ and $\hat{\mathbf{j}}$ being the direction vector of the applied current. The amplitude becomes part of $\tau(j)$, which is then linearly dependent on the current density j. It is worth noting that the tensorial nature of $\hat{\mathcal{S}}_{\text{p}}$ allows the direction of polarization to be set relative to the direction of current in systems with low symmetry such as C_{2v}, which can be advantageous for engineering applications. Considering the electric current, geometry and material relation, we finally model the torque by the following expression:

$$\mathbf{T}_i = -\alpha_{\text{G}}\,\tau(j)\,\mathbf{S}_i \times \hat{\mathbf{S}}_{\text{p}} + \tau(j)\,\mathbf{S}_i \times \left(\mathbf{S}_i \times \hat{\mathbf{S}}_{\text{p}}\right) \tag{4}$$

In Supplementary Note 1 we demonstrate that the assumption of linear dependent prefactors does not result in a loss of generality when it comes to describing (anti-)skyrmion dynamics.

3 RESULTS

3.1 Energy Barriers of Single Particles

In the following, we will discuss the relevant energy barriers present in the system. At first, energy barriers are discussed which involve only a single particle. To do this, we apply the GNEB method to investigate the minimum energy path for rotation and collapse of both the skyrmion and the antiskyrmion as well as for their disappearance by overcoming the repulsive potential at the boundaries. The latter is caused in our simulations by assuming additional ferromagnetically pinned spins at the boundary of the simulation box. By rotation we mean the local rotation of the atomistic magnetic moments, resulting in the case of the skyrmion in a change from Néel-type with the preferred chirality via Bloch-type to Néel-type with opposite chirality and back, while for the antiskyrmion this is equivalent to a real rotation of the antiskyrmionic structure around its origin on the lattice.

The resulting GNEB paths are illustrated in **Figure 2**. For the paths of the (anti-)skyrmion motion and the collapse, the transition states, i.e., the states at the saddle point of the energy landscape are shown on the right-hand side of **Figure 2**, marked by the same boundary color as the corresponding GNEB path. As can be seen, the energy of the initial state, the final states, the minimum energy paths and thus the energy barriers for the skyrmion and the antiskyrmion are identical, in accordance with the previous statement that in rank-one materials both particles are energetically degenerated. Furthermore, with the chosen parameter set, all relevant single particle energy barriers are in the same order of magnitude which leads to a rather strong robustness against both deformation and rotation. From those results, the influence of the DM interaction becomes obvious: while the stability with respect to the collapse is mainly a result of the competing exchange interactions, the stability with respect to rotation is purely enforced by the DMI.

3.2 Interaction Energies Between Two Particles

The representation of different bit combinations on the racetrack, e.g (0, 0), (0, 1), or (1, 1), requires the knowledge of the interaction behavior between equal and unequal kinds of particles. What might be surprising about the proposed skyrmion-antiskyrmion racetrack memory is the usage of antiparticles as information carriers. The question immediately arises to what extent these particles are mutual antiparticles and whether these particles would not simply annihilate mutually. As we see below, it turns out that the possible annihilation imposes a few restrictions on the fabrication of the resulting racetrack, namely the orientation of the atomistic lattice structure relative to the track direction, but does not prevent a possible realization of a skyrmion-antiskyrmion racetrack memory.

Recalling that an antiskyrmion is not rotationally invariant and thus possesses different properties along different spatial directions, these anisotropic properties need to be considered when one is interested in the interaction of skyrmions and antiskyrmions. As it can be seen in **Figure 2**, in our case the antiskyrmion can be obtained from the skyrmion by inverting the x-component of each atomistic spin, i.e., $S_i^x \rightarrow -S_i^x$, or, considering the symmetry of the skyrmion, by performing a mirror operation on the yz-plane cutting through the center of the skyrmion in real-space, i.e., $\mathbf{S}(\mathbf{r}) \rightarrow \mathbf{S}(\mathbf{r}')$, where $\mathbf{r} = (r_x, r_y) \in \mathbb{R}^2$ located in the film plane is measured relative to the skyrmion center and $\mathbf{r}' = (-r_x, r_y)$. By this, the rotational sense of the component of the atomistic local moments along the y-direction is kept unchanged, in accordance with the choice of our DM vectors pointing along the x-direction thus preferring a certain rotation precisely along this direction. However, the rotation along the perpendicular direction is inverted. Thus, the two distinct cases that need to be studied when skyrmions interact with antiskyrmions are those in which the two particles approach each other along either the x- or the y-axis.

In **Figure 3A** the energy profiles for diskyrmionic interactions as a result of two single particles approaching along the x-axis (axis of direction of DM vector) is illustrated. Here and in the

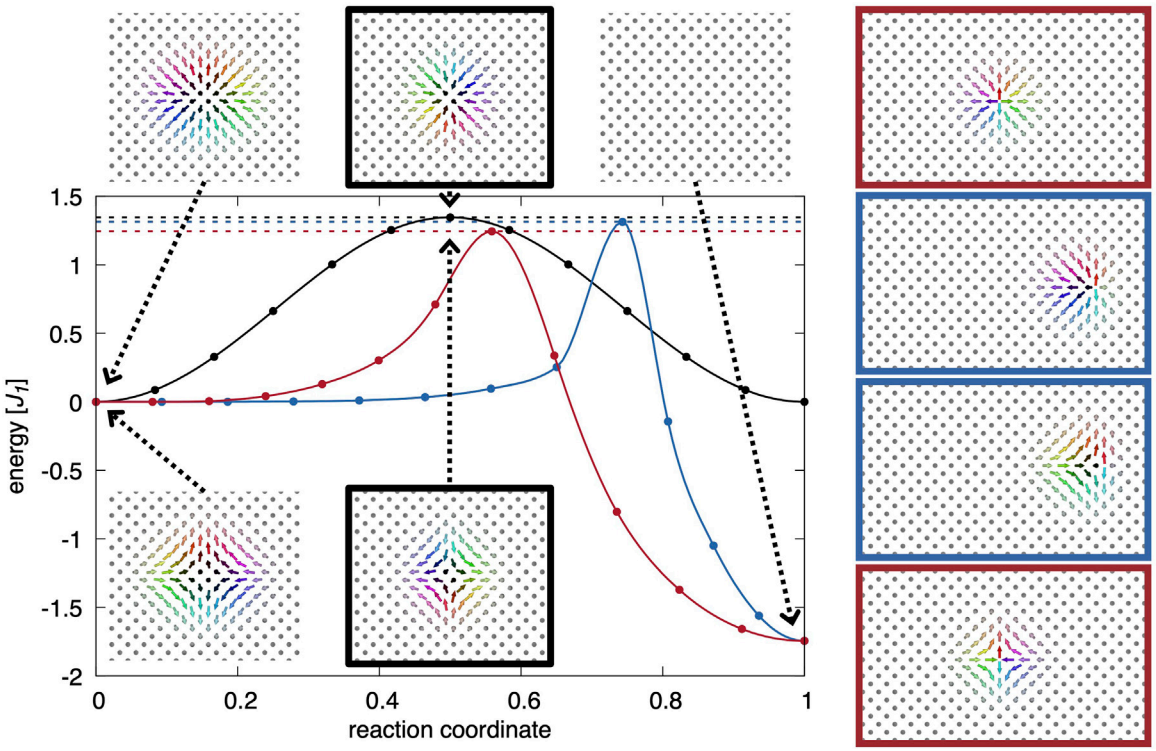

FIGURE 2 | GNEB paths and energy barriers (indicated by dashed lines) given in units of the exchange parameter J_1 for the rotation of an (anti-)skyrmion (black), the collapse of an (anti-)skyrmion (red) and the movement out of the system across the repulsive energy barrier at the boundary of our simulation box created by pinning the boundary spins ferromagnetically (blue). The insets show the relevant states. On the right, transition states are shown for the movement and the collapse. The colored boundary indicates the associated GNEB path degenerated for skyrmion and antiskyrmion. The reference energy refers to a single particle immersed in the ferromagnetic background.

following, the distance between the centers of the particles is taken as measure for the reaction coordinate.

In the case of homoskyrmionic interactions, i.e., both particles are either skyrmions or antiskyrmions, the energy dependence on the distance of the two particles is shown by a black graph. To counteract the repulsive or attractive forces between two particles, we varied the size of the simulation box and placed the two particles such that their distance matched half of the box size along the *x* direction. By using periodic boundary conditions, this approach ensures that the particles remain at their initial position as no net force acts on them. The black graph in the inset of **Figure 3A** describes an energy profile typical for a fast and favorable formation of a homoskyrmionic "molecule," a skyrmion-skyrmion-pair or an antiskyrmion-antiskyrmion-pair. It can be seen that the competing exchange interactions create a small repulsive energy barrier when the particles are approaching followed by the attractive binding potential for the homoskyrmionic molecule. The preferred distance of two particles in the homoskyrmionic molecule is about 10 *a*, slightly smaller than twice the skyrmion diameter of 6 *a*, with *a* being the lattice constant. If the distance between the two particles is decreased, the magnetization textures of the particles deform, and below a critical value of about 5.5 *a*, the pair interaction of the penetrating particles becomes so large that the (anti-)skyrmions become unstable and collapse to the ferromagnetic state. Since the chiral orientation of the antiskyrmion on the racetrack is determined by the DM vector of the underlying crystal lattice which remains unchanged across the racetrack memory, only antiskyrmion of the same chiral orientation will interact on the track.

To investigate the case of heteroskyrmionic interactions of one skyrmion and one antiskyrmion, the previously discussed simulational approach based on the total energy minimization of particles at a given distance is not applicable due to the fact that both particles attract each other and their static distance cannot be controlled anymore. Instead, we performed a GNEB calculation for the related path, meaning the initial state are well-separated particles (see state 1 in **Figure 3B**) at energy of two times the (anti-)skyrmion energy and the final state is the ferromagnetic state (state 5 in **Figure 3B**). The intermediate states represent the continuous nearing of the particles until they merge and finally collapse to the ferromagnetic state (see exemplary states 2-4 in **Figure 3B**). The resulting energy profile is shown by the red graph in **Figure 3A**. As before, the distance between the centers of the two particles is taken as measure for the reaction coordinate as long as they are well separated. Yet, during the merging process of two topologically nontrivial particles with opposite topological charge, a new elongated topologically trivial particle, i.e., with $Q = 0$, is formed (see state 3 in **Figure 3B**). The elongation of the core, i.e., the extend of the region with the

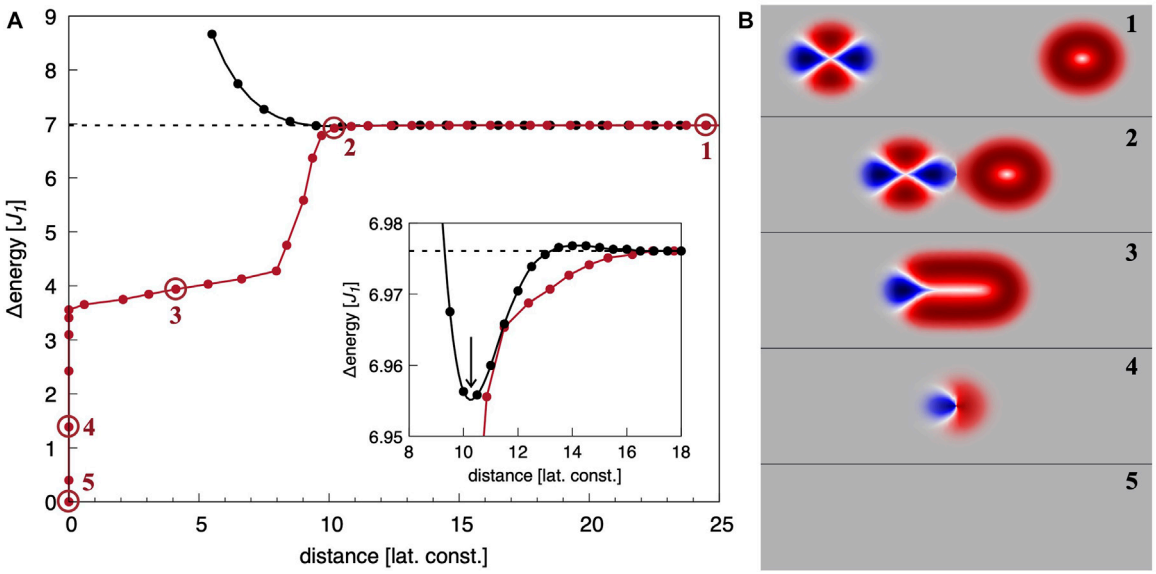

FIGURE 3 | (A) Energy barriers for approaching (anti-)skyrmions along the *x*-direction. The MEP for the fusion of a skyrmion and an antiskyrmion is shown in red and the distance dependent energy for two equivalent particles (either skyrmions or antiskyrmions) is shown in black. The magnetic textures of exemplary intermediate states along the MEP are shown in **(B)**. The corresponding points are highlighted by circles in **(A)** and labeled accordingly. The color code in **(B)** indicates the chirality of the particles. Red and blue represent Néel-type chirality (of opposite sign) while white highlights regions with Bloch-type chirality. State 5 indicates the ferromagnetic ground state, taken as energy zero reference and illustrated as grey background in **(B)**. Distances are measured between the cores of the particles.

magnetization pointing antiparallel to the ferromagnetic background (see central white line in **Figure 3B**, state 3), is taken as a new measure. The color code in **Figure 3B** indicates the chirality of the particles.

As it can be seen, no energy barrier exists if a skyrmion and an antiskyrmion approach along this *x*-direction visualized in state 1 of **Figure 3B**. Instead, the two particles can merge and mutually annihilate, the typical behavior of antiparticles. This is a direct consequence of the opposite chirality along the *x*-direction and is analogous to domain walls between ferromagnetic domains, which can also merge to lower the total energy of the system if they have opposite chirality. The opposite chirality of the antiskyrmion along the *x*-axis is a consequence of the racetrack material, for which we assumed a DMI vector **D** along the *x*-direction that favors in turn a Néel spin rotation along the *y*-direction. Consequently, these results show that a racetrack memory in which an antiskyrmion and a skyrmion are arranged in tandem in an orientation in which the spin chirality of the antiskyrmion is opposite to that of the skyrmion would not work because of data loss over time.

Figure 4 illustrates the energetic situation of a homochiral heteroskyrmionic interaction between an antiskyrmion and a skyrmion, i.e., the antiskyrmion and the skyrmion approach each other in a way that the chiral orientation of the two particles is the same along the reaction coordinate. This is realized by orienting the track direction, i.e., the reaction path in the language of our GNEB studies, along the *y*-axis of the crystal lattice keeping the direction of the DMI along the *x*-direction. Two distinct processes need to be considered for the description of such an interaction path: (i) This is an evasion of the particles by a sideways movement δx on their path along *y*, and (ii) the local change of the chirality of the particles. Both the sideways motion as well as the local rotation result in the possibility that the heteroskyrmionic interaction along the line connecting the centers of the two particles changes from a homo- to a heterochiral one, a condition for the merging and subsequently annihilation of the particles as discussed above. The observed sideways motion is similar to the one observed in Ref. [47] where the merging of two antiskyrmions and the formation of a higher-order state was investigated.

In the case of an infinitely wide racetrack, the sideways movement δx, can become arbitrarily large to avoid the chirality change that would cost energy due to the DM interaction. Effectively, this means that the previously discussed case of the particles approaching along the *x*-axis is repeated, resulting in the situation of a vanishing energy barrier for particle annihilation. To restrict the sideways motion and thus δx, and to explore the optimal track width of a skyrmion-antiskyrmion racetrack memory, we simulate tracks with finite widths. The track boundary is again simulated by embedding the track in a ferromagnetically pinned background, technically achieved in our simulations by adding additional rows of pinned spins at each side of the track, to create the previously discussed repulsive potential, responsible for the discussed energy barrier to avoid the annihilation of the particles at the racetrack boundaries. For track widths between 4 and 26 lattice constants we performed 23 GNEB simulations in steps of one lattice parameter and determined the minimum energy potential barrier for the fusion of the skyrmion with the antiskyrmion. The resulting energy barrier depends on the width of the

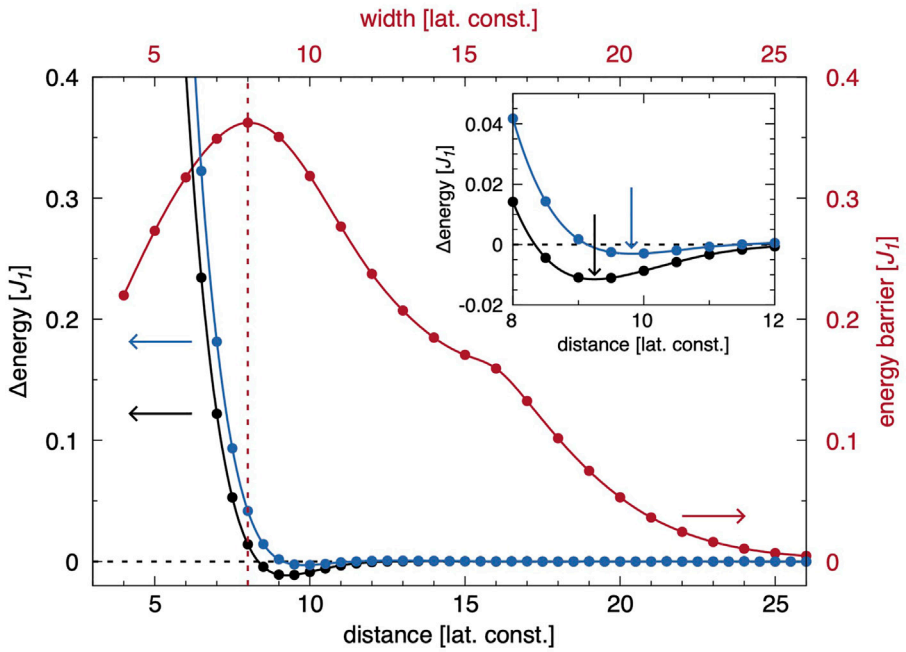

FIGURE 4 | Energy barriers for approaching (anti-)skyrmions on a track oriented along the *y*-direction of the crystal lattice and of finite width in *x*-direction. In red, the energy barrier **(right axis)** for the fusion of a skyrmion and an antiskyrmion in dependence of the width **(top axis)** of the racetrack is given. The track width for which the energy barrier becomes maximum is highlighted by a red, vertical, dashed line. For this particular width, the distance dependent energy profile **(left axis)** for a skyrmion and an antiskyrmion located in the middle of the track is shown in blue calculated with the constraint of fixed chirality, i.e., preventing the local rotation of the atomistic moments within the particles. For two particles of equal type (either skyrmions or antiskyrmions) the profile is shown in black. The reference energy refers to infinitely separated particles at the same track width. The inset provides a higher energy resolution in the region around those two minima. The black and blue arrows indicate the distance of minimal energy.

racetrack as can be seen in **Figure 4** by the red graph. At finite widths, the repulsive force between the particles and the racetrack boundaries sets in. Yet, the skyrmion and antiskyrmion can still approach along the *x*-direction. By reducing the width further, the energy cost caused by the repulsive potential at the boundary gets too large and instead it becomes energetically more favorable to rotate the single particles additionally, which however now costs DMI energy and continues with decreasing width until finally almost no sideways motion occurs anymore. In that case, both in the skyrmion as well as in the antiskyrmion the atomistic magnetic moments need to rotate by 90° resulting in case of the skyrmion in a change from the preferred Néel-type chirality to Bloch-type chirality while the antiskyrmionic structure is effectively rotated by 45° around its origin. The chirality change is then solely responsible for the energy barrier. The energy barrier is about 0.36 J_1, significantly lower than the expected barrier of 1.5 J_1 as estimated based on the rotation barrier of a single particle discussed in **Section 3.1**. This can be understood as following: To reduce the energy cost due to DMI, the chirality change does not occur isotropically over the whole particles, but predominantly along the line connecting the centers of the particles while the chirality along the opposite direction is almost unchanged. Additionally, the particles are already squeezed by the repulsive potential caused by the track boundaries. This results in a destabilization and a reduction of the barrier against a change of chirality. This destabilization is enhanced for even smaller track width, manifesting in the reduction of the energy barrier at lower widths. As it can be seen in **Figure 4**, the optimal energy barrier for application purposes, i.e., the highest barrier as function of the track width, is reached for about 8 lattice constants. In the supplementary materials, we included movies of the annihilation path for different track widths. See Supplementary Note 2 and Supplementary Movies 1-5.

As a skyrmion-antiskyrmion pair feels an repulsive force, which is trying to separate both when they are too close to each other, the range of this repulsive interaction needs to be analyzed. Therefore, in addition, in **Figure 4** the distance dependent energy for two identical particles and for one skyrmion and one antiskyrmion are shown in black and blue, respectively, the later under the constraints that no sidewards movement is allowed, i.e., $\delta x = 0$, and no rotation of the local moments occurs. The track width for those simulations was set to the previously obtained value of 8 lattice constants. As it can be seen, the competing exchange interactions create an optimal distance between the particles, and both a homo-as well as a heteroskyrmionic pair can be formed, a good side effect for application purposes as this reduces the time management for the reading process. The optimal distance varies from about 9.25 lattice constants for identical particles to about 9.8 lattice constants for different ones (see inset in **Figure 4**). The black curve of **Figure 4** should be compared to the black curve in

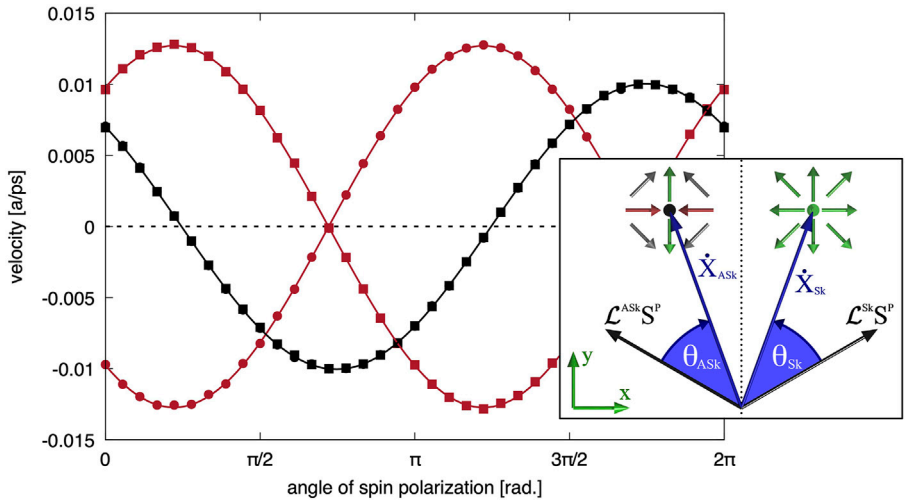

FIGURE 5 | Velocity components along *x*-direction (red) and *y*-direction (black) for different orientations of the spin current polarization (angle measured from the *x*-axis). Circles (squares) represent the skyrmion (antiskyrmion). Inset: schematic representation of the resulting trajectories of skyrmions and antiskyrmions and their symmetry relation according to the Thiele-like **Eq. 6**.

Figure 3. Both describe the binding energy of the homoskyrmionic molecules, the former for reaction paths along the *y*-direction and the latter along the *x*-direction of the lattice. We find that the binding energy and the bond length of homoskyrmionic pairs differ slightly due to the anisotropic DM interaction.

3.3 Motion of Skyrmions and Antiskyrmions Under the Effect of SOT

Here we turn to the atomistic simulation of the SOT enabled electric current induced motion of the skyrmion and the antiskyrmion. A particular challenge is to achieve a coherent and linear motion of the particles independent on the type considering that the skyrmion and the antiskyrmion show an opposite skyrmion Hall angle. Therefore, we simulated the dynamics of both particles by solving the LLG **Equation 3** for SOTs 4) with different orientations of the spin current polarization $\mathbf{S}_p$. We have chosen the current density or torque amplitude so that the relationship of particle velocity and current density stays in the linear regime, thus avoiding the breakdown that would result in a trochoidal motion of the particles [48]. However, it should be highlighted that the rank-one DMI increases the region where current-driven linear motion is possible both for the skyrmion and the antiskyrmion as the relevant energy barrier is increased equivalently for both particles. The results are shown in **Figure 5**, where the velocity components along the two crystallographic directions are plotted as function of the direction of the spin-polarization relative to the current direction. Since we are in the linear regime, both velocity components scale with the torque exerted on the spins or indirectly on the current density. For the simulations presented in **Figure 5**, we used a damping of $\alpha_G = 0.7$ and $\tau(j) = 0.003$ meV. As it can be seen, the *y*-component of the velocity is equivalent for both the skyrmion and the antiskyrmion and follows a sinusoidal shape with respect to the direction of the spin polarization. The *x*-component, however, differs between the skyrmion and the antiskyrmion. More precisely, the velocity component along *x* is inverted for the two particles. Additionally, one can see that this results in a vanishing *x*-component of the velocity for both when the absolute value of the *y*-component is largest, in our case for an angle of the spin polarization relative to the *x*-axis of about 130°. Another important aspect to mention is the different maximal velocity which can be achieved along the two different crystallographic directions which can be explained by the ellipticity of the particles. Note, as before, we assumed the same lattice constant *a* in both directions.

To interpret the obtained results, we go back to the LLG **Equation 3** which can be written in its implicit form as

$$\frac{d\mathbf{S}_i}{dt} = -\gamma \mathbf{S}_i \times \mathbf{H}_i^{\text{eff}} + \alpha \mathbf{S}_i \times \frac{d\mathbf{S}_i}{dt} + \gamma \tau(j) \mathbf{S}_i \times (\mathbf{S}_i \times \mathbf{S}^P). \quad (5)$$

In a first step, we go from the atomistic description to the micromagnetic one by replacing the discrete lattice of localized spins by a normalized continuous vector field, i.e., $\mathbf{S}_i \rightarrow \mathbf{m}(\mathbf{r})$. Assuming that the shape of the magnetic structures remains unchanged during the motion in an applied spin current, i.e., staying within the rigid-body ansatz, $\mathbf{m}(\mathbf{r}, t) = \mathbf{m}(\mathbf{r} - \mathbf{X}(t))$, and further neglecting the ellipticity of the skyrmion one can then find an equation of motion for the center of the (anti-)skyrmion similar to the Thiele equation (49) in an inplane current by projecting **Eq. 5** onto the translational mode. The resulting Thiele-like equation for the position, $\boldsymbol{X}$, of the particle reads as

$$\left(4\pi Q \epsilon_{\alpha\beta} + \mathcal{D}_{\alpha\beta}\right) \dot{X}_\beta = \gamma \tau(j) \mathcal{L}_{\alpha\beta} S_\beta^P \quad (6)$$

(apply summation over common index β) with

$$Q = \frac{1}{4\pi}\int_{\mathbb{R}^2} d\mathbf{r}_\parallel\, \mathbf{m}\cdot\partial_x\mathbf{m}\times\partial_y\mathbf{m}, \tag{7a}$$

$$\mathcal{D}_{\alpha\beta} = \alpha_G\int_{\mathbb{R}^2} d\mathbf{r}_\parallel\, \partial_\alpha\mathbf{m}\cdot\partial_\beta\mathbf{m}, \tag{7b}$$

$$\mathcal{L}_{\alpha\beta} = \int_{\mathbb{R}^2} d\mathbf{r}_\parallel\, (\partial_\alpha\mathbf{m}\times\mathbf{m})\cdot\hat{\mathbf{e}}_\beta, \tag{7c}$$

where $\epsilon_{\alpha\beta}$ is the Levi-Civita symbol, α and β take the values of the x and y components of the magnetic film, $\alpha, \beta \in \{x, y\}$. Q is the integer topological charge, $\mathcal{D}$ the dissipation tensor and $\mathcal{L}$ the chirality tensor.

The Thiele-like equation states that the SOT-driven skyrmion dynamics depends not only on the topology, but also on the chirality. In the case of SOT, the skyrmion Hall effects can be controlled using special DMI and the resulting chiralities of the skyrmions, which we exploit to keep skyrmions and antiskyrmions on the track. The chirality tensor is different for Néel and Bloch-type skyrmions and antiskyrmions, which are typically described in terms of the helicity defined as the angle of the global rotation around the z-axis that relates various skyrmions to the Néel skyrmion by a smooth transformation. The limit of axial and nearly axial skyrmions was discussed by Ritzmann *et al.* in Ref. [48]. In this case, the chirality tensor becomes proportional to the helicity and thus for these systems the choice of the topological charge and the helicity determines the dynamics of skyrmions.

Eq. 6 has two fundamental consequences: (i) the Hall angle is inverted for skyrmions and antiskyrmions due to the opposite topological charge Q and (ii) the "effective" spin polarization, $\mathcal{L}\mathbf{S}^P$, or equivalently the external force felt by the particle depends on $\mathcal{L}$ and therefore on the magnetic structure of the particle. Consequently, for the forces acting on the antiparticles it follows $F^x_{\mathrm{Sk}} = -F^x_{\mathrm{ASk}}$, i.e., the forces are mirrored at the yz-plane. Thus, combining the inverted Hall angle and the mirrored force, the direction of motion of the skyrmion and the antiskyrmion are as well mirrored at the same mirror plane in agreement with our spin-dynamics results. The dynamics of skyrmion and antiskyrmions are schematically sketched in the inset of **Figure 5** where the black arrows represent the effective spin polarization and in blue the resulting direction of motion for the skyrmion and the antiskyrmion, respectively, are shown.

Thus, one can conclude that a parallel motion of skyrmions and antiskyrmions is possible along the y-direction with the same speed and thus the necessary conditions for the possibility of a two-particle racetrack memory are fulfilled.

4 DISCUSSION

A few important conditions need to be fulfilled if one uses more than one type of particles for such a device: i) Both particles should be energetically stable, i.e., they need to be (meta-) stable states of the system with a finite energy barrier preventing them from disappearing. ii) There should exist an energy barrier avoiding the fusion or annihilation of different particles. iii) The involved particles should move a) in the same direction and b) with the same velocity to avoid a change of the stored information for example due to annihilation or other effects.

In this paper we demonstrated, that rank-one DMI materials, materials where the DMI tensor possesses a zero determinant, are good candidates for the analysis of the interplay of skyrmions and antiskyrmions. Although the antiskyrmion carries the notion of the antiparticle of the skyrmion, we found the energy barrier for skyrmion-antiskyrmion annihilation can be large for particles on a track with proper track width and a track oriented properly with respect the anisotropy of the DM interaction of the crystal lattice. The energy profile as function of distant-dependent reaction coordinates for pairs of particles on a track shows the typical behavior for the formation of diskyrmionic molecules with very similar bond lengths, regardless of whether they are skyrmion-skyrmion, skyrmion-antiskyrmion or antiskyrmion-antiskyrmion pairs. This means any string of information encoded in a sequence of "0" and "1" can form a weakly bound chain of skyrmions and antiskyrmions with well-defined distances. This serves a simplification of the reading electronics. We showed, that a collective motion along one particular high-symmetry direction can be achieved if one applies a spin current in SOT geometry. This would allow for the creation of a skyrmion-antiskyrmion racetrack where the data is stored not in the presence or absence of particles but in their type itself, allowing for a more robust and time persistent way of information storage than it can be achieved if the information relies on predefined distances of information carriers. In Supplementary Movie 6 we show the simulation of such a skyrmion-antiskyrmion racetrack which confirms the collective motion of skyrmions and antiskyrmions as well as their even distribution along the racetrack.

The natural question arises whether such a model system of a perfect rank-one material occurs in nature. The main focus of both experimental measurements as well as theoretical investigations on magnetic thin films and multilayers was so far mainly on (111)-oriented surfaces and interfaces of fcc or bcc materials [5, 33, 50], meaning a hexagonal structure, and partially on (001) ones [51], i.e., square alignments. Those, however, do not allow for an anisotropic DM interaction due to their high symmetry, namely C_{3v} and C_{4v}, respectively. Only recently, the possibility of anisotropic DMI in low-symmetry systems was brought into focus [23, 24]. Thus, the determination of a particular rank-one material is still missing. However, it is worth noting that the proposed racetrack memory itself assumes only the possible coexistence of skyrmions and antiskyrmion. Such a coexistence does not rely on a perfect rank-1 DMI, but can be achieved even if the DMI deviates from the rank-1 behaviour. While larger deviations can in fact result in small changes of the velocity as well as the direction of motion, the overall motion is predominantly determined by the helicity of the magnetic object, and thus by the crystal symmetry, here C_{2v}. However, as the deviation of the DMI from the rank-1 behaviour increases, either the stability of the skyrmion or antiskyrmion decreases, in particular with respect to helicity changes, eventually leading to the occurrence of trochoidal motion.

Yet, it should be highlighted that systems with C_{2v} symmetry, and among these in particular those materials that have a rank-1 DMI, should be superior candidates for a skyrmion-antiskyrmion

racetrack memory compared to material classes with higher symmetry. Recently, it was experimentally shown that in tetragonal inverse Heusler alloys, skyrmions and antiskyrmions can coexist [52, 53]. Presumably, however, the mechanism for the stability of the two particles is different, and so are their energetics. While again exchange frustration is the main stabilization mechanism, the DMI, however, exhibits D_{2d} symmetry and thus intrinsically favors antiskyrmions over skyrmions. The observed elliptical deformation of the skyrmion suggests that the dipole interaction is a possible cause for the stability of the particle, and therefore leads to significantly different static and dynamic properties of the two particles.

DATA AVAILABILITY STATEMENT

The raw data supporting the conclusions of this article will be made available by the authors, without undue reservation.

AUTHOR CONTRIBUTIONS

MH performed the spin dynamic simulations. CM provided the mathematical analysis of the micromagnetic functional. SB initiated and supervised this work. All authors took part in the analysis and the discussion of the results and contributed to the writing of the paper.

FUNDING

We acknowledge computing time on supercomputers provided by the Jülich Supercomputing Centre (JSC) and RWTH-Aachen University. We acknowledge funding from the DARPA TEE program (grant MIPR#HR0011831554) from DOI and from the Deutsche Forschungsgemeinschaft (DFG) through CRC 1238 (Project No. C01) and SPP 2137 (DFG grant no. BL 444/16). GM acknowledges funding from the Icelandic Research Fund (grant no.152483-052). CM acknowledges funding from Deutsche Forschungsgemeinschaft (DFG grant no. ME 2273/3-1). CM and SB acknowledge seed-fund support from JARA-FIT.

SUPPLEMENTARY MATERIAL

The Supplementary Material for this article can be found online at: https://www.frontiersin.org/articles/10.3389/fphy.2021.769873/full#supplementary-material

REFERENCES

1. Parkin SSP, Hayashi M, Thomas L. Magnetic Domain-Wall Racetrack Memory. *Science* (2008) 320:190–4. doi:10.1126/science.1145799
2. Bogdanov AN, Yablonskii D. Electrostatic Interaction of Neutral Semi-permeable Membranes. *Zh Eksp Teor Fiz* (1989) 95:178.
3. Mühlbauer S, Binz B, Jonietz F, Pfleiderer C, Rosch A, Neubauer A. Skyrmion Lattice in a Chiral Magnet. *Science* (2009) 323:915–9.
4. Yu XZ, Onose Y, Kanazawa N, Park JH, Han JH, Matsui Y. Real-space Observation of a Two-Dimensional Skyrmion crystal. *Nature* (2010) 465: 901–4. doi:10.1038/nature09124
5. Heinze S, Von Bergmann K, Menzel M, Brede J, Kubetzka A, Wiesendanger R. Spontaneous Atomic-Scale Magnetic Skyrmion Lattice in Two Dimensions. *Nat Phys* (2011) 7:713–8. doi:10.1038/nphys2045
6. Dzyaloshinsky I. A Thermodynamic Theory of "weak" Ferromagnetism of Antiferromagnetics. *J Phys Chem Sol* (1958) 4:241–55. doi:10.1016/0022-3697(58)90076-3
7. Moriya T. Anisotropic Superexchange Interaction and Weak Ferromagnetism. *Phys Rev* (1960) 120:91–8. doi:10.1103/physrev.120.91
8. Bode M, Heide M, Von Bergmann K, Ferriani P, Heinze S, Bihlmayer G. Chiral Magnetic Order at Surfaces Driven by Inversion Asymmetry. *Nature* (2007) 447:190–3. doi:10.1038/nature05802
9. Fert A, Cros V, Sampaio J. Skyrmions on the Track. *Nat Nanotech* (2013) 8: 152–6. doi:10.1038/nnano.2013.29
10. Jonietz F, Mühlbauer S, Pfleiderer C, Neubauer A, Münzer W, Bauer A. Skyrmion Lattice in a Chiral Magnet. *Science* (2010) 330:1648–51. doi:10.1126/science.1166767
11. Sampaio J, Cros V, Rohart S, Thiaville A, Fert A. Skyrmions on the Track. *Nat Nanotechnol* (2013) 8:839–44. doi:10.1038/nnano.2013.29
12. Koshibae W, Nagaosa N. Creation of Skyrmions and Antiskyrmions by Local Heating. *Scientific Rep* (2018) 8:6328. doi:10.1038/ncomms6148
13. Woo S, Litzius K, Krüger B, Im M-Y, Caretta L, Richter K. Observation of Room-Temperature Magnetic Skyrmions and Their Current-Driven Dynamics in Ultrathin Metallic Ferromagnets. *Nat Mater* (2016) 15:501–6. doi:10.1038/nmat4593
14. Hrabec A, Sampaio J, Belmeguenai M, Gross I, Weil R, Chérif SM. Current-induced Skyrmion Generation and Dynamics in Symmetric Bilayers. *Nat Commun* (2017) 8:15765. doi:10.1038/ncomms15765
15. Woo S, Song KM, Han HS, Jung MS, Im MY, Lee KS. *Nat Commun* (2017) 8: 1–8. doi:10.1038/ncomms15573
16. Litzius K, Lemesh I, Krüger B, Bassirian P, Caretta L, Richter K. Skyrmion Hall Effect Revealed by Direct Time-Resolved X-ray Microscopy. *Nat Phys* (2017) 13:170–5. doi:10.1038/nphys4000
17. Back C, Cros V, Ebert H, Everschor-Sitte K, Fert A, Garst M. The 2020 Skyrmionics Roadmap. *J Phys D: Appl Phys* (2020) 53:363001. doi:10.1088/1361-6463/ab8418
18. Hoffmann M, Müller GP, Blügel S. Atomistic Perspective of Long Lifetimes of Small Skyrmions at Room Temperature. *Phys Rev Lett* (2020) 124:247201. doi:10.1103/physrevlett.124.247201
19. Kang W, Huang Y, Zheng C, Lv W, Lei N, Zhang Y. Voltage Controlled Magnetic Skyrmion Motion for Racetrack Memory. *Sci Rep* (2016) 6:23164. doi:10.1038/srep23164
20. Müller J. Magnetic Skyrmions on a Two-Lane Racetrack. *New J Phys* (2017) 19: 025002. doi:10.1088/1367-2630/aa5b55
21. Zheng F, Rybakov FN, Borisov AB, Song D, Wang S, Li Z-A. Experimental Observation of Chiral Magnetic Bobbers in B20-type FeGe. *Nat Nanotech* (2018) 13:451–5. doi:10.1038/s41565-018-0093-3
22. Güngördü U, Nepal R, Tretiakov OA, Belashchenko K, Kovalev AA. , 93 (2016). p. 064428. doi:10.1103/physrevb.93.064428*Phys Rev B*
23. Hoffmann M, Zimmermann B, Müller GP, Schürhoff D, Kiselev NS, Melcher C. Antiskyrmions Stabilized at Interfaces by Anisotropic Dzyaloshinskii-Moriya Interactions. *Nat Commun* (2017) 8:308. doi:10.1038/s41467-017-00313-0
24. Camosi L, Rohart S, Fruchart O, Pizzini S, Belmeguenai M, Roussigné Y. Anisotropic Dzyaloshinskii-Moriya Interaction in Ultrathin Epitaxial Au/Co/W(110). *Phys Rev B* (2017) 95:214422. doi:10.1103/physrevb.95.214422
25. Koshibae W, Nagaosa N. Theory of Antiskyrmions in Magnets. *Nat Commun* (2016) 7:10542. doi:10.1038/ncomms10542
26. Kovalev AA, Sandhoefner S. Orbital Angular Momentum and Topological Charge of a Multi-Vortex Gaussian Beam. *Front Phys* (2018) 6 98:2296–424X. doi:10.1364/JOSAA.401561

27. Huang S, Zhou C, Chen G, Shen H, Schmid AK, Liu K. Stabilization and Current-Induced Motion of Antiskyrmion in the Presence of Anisotropic Dzyaloshinskii-Moriya Interaction. *Phys Rev B* (2017) 96(14):144412. doi:10.1103/physrevb.96.144412
28. Silva RC, Silva RL, Pereira AR. Magnus-force Induced Skyrmion-Antiskyrmion Coupling in Inhomogeneous Racetrack. *J Phys Condens Matter* (2020) 33:105802. doi:10.1088/1361-648x/abd1fa
29. Kumar V, Kumar N, Reehuis M, Gayles J, Sukhanov AS, Hoser A. Detection of Antiskyrmions by Topological Hall Effect in Heusler Compounds. *Phys Rev B* (2020) 101(1):014424. doi:10.1103/physrevb.101.014424
30. Lux FR, Freimuth F, Blügel S, Mokrousov Y. Chiral Hall Effect in Noncollinear Magnets from a Cyclic Cohomology Approach. *Phys Rev Lett* (2020) 124(9): 096602. doi:10.1103/physrevlett.124.096602
31. Bouaziz J, Ishida H, Lounis S, Blügel S. Transverse Transport in Two-Dimensional Relativistic Systems with Nontrivial Spin Textures. *Phys Rev Lett* (2021) 126:147203. doi:10.1103/physrevlett.126.147203
32. Romming N, Hanneken C, Menzel M, Bickel JE, Wolter B, von Bergmann K. Writing and Deleting Single Magnetic Skyrmions. *Science* (2013) 341:636–9. doi:10.1126/science.1240573
33. Romming N, Kubetzka A, Hanneken C, von Bergmann K, Wiesendanger R. Field-Dependent Size and Shape of Single Magnetic Skyrmions. *Phys Rev Lett* (2015) 114(17):177203. doi:10.1103/physrevlett.114.177203
34. Rohart S, Thiaville A. Skyrmion Confinement in Ultrathin Film Nanostructures in the Presence of Dzyaloshinskii-Moriya Interaction. *Phys Rev B* (2013) 88:184422. doi:10.1103/physrevb.88.184422
35. Bessarab PF, Müller GP, Lobanov IS, Rybakov FN, Kiselev NS, Jónsson H. Lifetime of Racetrack Skyrmions. *Scientific Rep* (2018) 8:1–10. doi:10.1038/s41598-018-21623-3
36. Manchon A, Železný J, Miron IM, Jungwirth T, Sinova J, Thiaville A. Relativistic Néel-Order fields Induced by Electrical Current in Antiferromagnets. *Rev Mod Phys* (2019) 91(3):035004. doi:10.1103/revmodphys.91.035004
37. Schieback C, Kläui M, Nowak U, Rüdiger U, Nielaba P. Numerical Investigation of Spin-Torque Using the Heisenberg Model. *Eur Phys J B* (2007) 59:429–33. doi:10.1140/epjb/e2007-00062-2
38. Chureemart P, Evans RFL, Chantrell RW. Dynamics of Domain wall Driven by Spin-Transfer Torque. *Phys Rev B* (2011) 83:184416. doi:10.1103/physrevb.83.184416
39. Mentink JH, Tretyakov MV, Fasolino A, Katsnelson MI, Rasing T. Stable and Fast Semi-implicit Integration of the Stochastic Landau-Lifshitz Equation. *J Phys Condens Matter* (2010) 22:176001. doi:10.1088/0953-8984/22/17/176001
40. Spirit Spin Simulation Framework. Available at: https://spirit-code.github.io.
41. Müller GP, Hoffmann M, Dißelkamp C, Schürhoff D, Mavros S, Sallermann M. Spirit : Multifunctional Framework for Atomistic Spin Simulations. *Phys Rev B* (2019) 99:224414. doi:10.1103/physrevb.99.224414
42. Bessarab PF, Uzdin VM, Jónsson H. Method for Finding Mechanism and Activation Energy of Magnetic Transitions, Applied to Skyrmion and Antivortex Annihilation. *Comp Phys Commun* (2015) 196:335–47. doi:10.1016/j.cpc.2015.07.001
43. Henkelman G, Uberuaga BP, Jónsson H. A Climbing Image Nudged Elastic Band Method for Finding Saddle Points and Minimum Energy Paths. *J Chem Phys* (2000) 113:9901–4. doi:10.1063/1.1329672
44. Hals KMD, Brataas A. Spin-Wave Driven Bidirectional Domain Wall Motion in Kagome Antiferromagnets. *Phys Rev B* (2013) 88(8):085423. doi:10.1103/physrevb.88.085423
45. Hanke JP, Freimuth F, Dupé B, Sinova J, Kläui M, Mokrousov Y. Theory of Current-Induced Angular Momentum Transfer Dynamics in Spin-Orbit Coupled Systems. *Phys Rev B* (2020) 101(1):014428. doi:10.1103/physrevb.101.014428
46. Železný J, Gao H, Manchon A, Freimuth F, Mokrousov Y, Zemen J. Relativistic Néel-Order fields Induced by Electrical Current in Antiferromagnets. *Phys Rev B* (2017) 95(1):014403. doi:10.1103/PhysRevLett.113.157201
47. Ritzmann U, Desplat L, Dupé B, Camley RE, Kim J-V. Asymmetric Skyrmion-Antiskyrmion Production in Ultrathin Ferromagnetic Films. *Phys Rev B* (2020) 102:174409. doi:10.1103/physrevb.102.174409
48. Ritzmann U, von Malottki S, Kim J-V, Heinze S, Sinova J, Dupé B. Trochoidal Motion and Pair Generation in Skyrmion and Antiskyrmion Dynamics under Spin-Orbit Torques. *Nat Electron* (2018) 1:451–7. doi:10.1038/s41928-018-0114-0
49. Thiele AA. Steady-State Motion of Magnetic Domains. *Phys Rev Lett* (1973) 30:230–3. doi:10.1103/physrevlett.30.230
50. Dupé B, Hoffmann M, Paillard C, Heinze S. Tailoring Magnetic Skyrmions in Ultra-thin Transition Metal Films. *Nat Commun* (2014) 5:4030. doi:10.1038/ncomms5030
51. Nandy AK, Kiselev NS, Blügel S. Interlayer Exchange Coupling: A General Scheme Turning Chiral Magnets into Magnetic Multilayers Carrying Atomic-Scale Skyrmions. *Phys Rev Lett* (2016) 116:177202. doi:10.1103/physrevlett.116.177202
52. Peng L, Takagi R, Koshibae W, Shibata K, Arima T-h., Nagaosa N. Real-Space Observation of a Transformation from Antiskyrmion to Skyrmion by Lorentz TEM. *Microsc Microanal* (2019) 25:1840–1. doi:10.1017/s1431927619009930
53. Jena J, Göbel B, Ma T, Kumar V, Saha R, Mertig I. Elliptical Bloch Skyrmion Chiral Twins in an Antiskyrmion System. *Nat Commun* (2020) 11:1–9. doi:10.1038/s41467-020-14925-6

Conflict of Interest: The authors declare that the research was conducted in the absence of any commercial or financial relationships that could be construed as a potential conflict of interest.

Publisher's Note: All claims expressed in this article are solely those of the authors and do not necessarily represent those of their affiliated organizations, or those of the publisher, the editors and the reviewers. Any product that may be evaluated in this article, or claim that may be made by its manufacturer, is not guaranteed or endorsed by the publisher.

frontiers in Physics

ORIGINAL RESEARCH
published: 30 November 2021
doi: 10.3389/fphy.2021.767491

Fluctuations and Pinning for Individually Manipulated Skyrmions

C. J. O. Reichhardt and C. Reichhardt*

Los Alamos National Laboratory, Theoretical Division and Center for Nonlinear Studies, Los Alamos, NM, United States

We numerically examine the dynamics of individually dragged skyrmions interacting simultaneously with an array of other skyrmions and quenched disorder. For drives just above depinning, we observe a broadband noise signal with a 1/*f* characteristic, while at higher drives, narrowband or white noise appears. Even in the absence of quenched disorder, the threshold force that must be applied to translate the driven skyrmion is finite due to elastic interactions with other skyrmions. The depinning threshold increases as the strength of the quenched disorder is raised. Above the depinning force, the skyrmion moves faster in the presence of quenched disorder than in a disorder-free system since the pinning sites prevent other skyrmions from being dragged along with the driven skyrmion. For strong pinning, we find a stick-slip motion of the driven skyrmion which produces a telegraph noise signature. The depinning threshold increases monotonically with skyrmion density in the absence of quenched disorder, but when pinning is present, the depinning threshold changes nonmonotonically with skyrmion density, and there are reentrant pinned phases due to a competition between pinning induced by the quenched disorder and that produced by the elastic interactions of the skyrmion lattice.

Keywords: skyrmion, dynamic phases, broadband noise, telegraph noise, depinning

OPEN ACCESS

Edited by:
Vladimir Dobrosavljevic,
Florida State University, United States

Reviewed by:
Eugene Chudnovsky,
CUNY, United States
Fumitaka Kagawa,
The University of Tokyo, Japan

****Correspondence:***
C. J. O. Reichhardt
cjrx@lanl.gov

Specialty section:
This article was submitted to Condensed Matter Physics, a section of the journal Frontiers in Physics

Received: *30 August 2021*
Accepted: *11 October 2021*
Published: *30 November 2021*

Citation:
Reichhardt CJO and Reichhardt C (2021) Fluctuations and Pinning for Individually Manipulated Skyrmions. Front. Phys. 9:767491. doi: 10.3389/fphy.2021.767491

1 INTRODUCTION

Magnetic skyrmions in chiral magnets are particle-like textures that form a triangular lattice [1,2] and can be set into motion under various types of drives [3-6]. Moving skyrmions can interact with each other as well as with impurities or quenched disorder in the sample [3,7]. One consequence is the presence of a finite depinning threshold or critical driving force needed to initiate skyrmion motion. Depinning thresholds have been observed that span several orders of magnitude depending on the properties of the materials [5-7]. Another interesting aspect of skyrmions is that their motion is strongly influenced by gyrotropic effects or the Magnus force. This force appears in addition to the dissipative effects that can arise from Gilbert damping and other sources. In the absence of quenched disorder, the Magnus force causes a driven skyrmion to move at a finite angle known as the skyrmion Hall angle θ_{sk} with respect to the driving force, where the value of θ_{sk} is proportional to the ratio of the Magnus to the damping forces [3,7-11]. When quenched disorder is present, θ_{sk} becomes velocity or drive dependent, starting from a zero value at low drives and gradually increasing with increasing velocity until it saturates at high drives to a value close to the intrinsic or disorder-free Hall angle [9-14]. Skyrmion depinning and motion can also be probed using the time series of the skyrmion velocity. Both numerical and experimental studies have shown that near the depinning transition, the skyrmion motion is disordered, and the system exhibits large noise fluctuations with broadband or $1/f^{\alpha}$ features, while at higher drives, there is a crossover to white noise or even a narrowband or periodic noise signal [15-17]. The onset of narrowband noise is an indication that the skyrmions have formed a periodic lattice structure. Similar transitions between broadband and narrowband noise as a

function of drive have also been observed for the depinning and sliding dynamics of vortices in type-II superconductors [18,19], driven charge density waves [20], and other driven assemblies of particles moving over random quenched disorder [21].

Interest in skyrmion dynamics and pinning is driven in part by the prospect of using skyrmions in a variety of applications [22,23]. Many of these applications require the manipulation of individual skyrmions or the interaction of skyrmions with a disordered landscape, so understanding the motion and fluctuations of individually manipulated skyrmions would be a valuable step in this direction. There have been numerous studies of methods to manipulate or drag individual particles with and without quenched disorder which focused on the velocity and fluctuations of the manipulated particle. Examples include driving single colloids through assemblies of other colloids [24-28], as well as measuring the changes of the effective viscosity on the driven particle as the system goes through glass [24-27], or jamming transitions [29,30]. Other studies have explored how the depinning threshold changes in a clean system as the system parameters are varied [25,31,32], as well as the effect of quenched disorder on individually manipulated superconducting vortices and magnetic textures [33-37]. It is also possible to examine changes in the fluctuations as a function of drive while the density of the surrounding medium or the coupling to quenched disorder is changed [29,30,37,38]. In experiments on skyrmion systems, aspects of the pinning landscape have been examined by moving individual skyrmions with local tips [39,40]. It is also possible to drag individual skyrmions with optical traps [41] or by other means [42] and to examine the motion of the skyrmions within the traps as well as changes in the velocity and skyrmion Hall angle as a function of driving force. Most of the extensive numerical and experimental studies of the dynamics of individually dragged particles have focused on bulk properties such as the average velocity or effective drag coefficients, and there is little work examining how the time series, noise fluctuations, or depinning threshold of a single probe particle would change when quenched disorder is present. This is of particular interest for skyrmions, since one could expect different fluctuations to appear in the damping dominated regime compared to the strong Magnus or gyrotropic dominated regime.

In this work, we introduce quenched disorder to the system in order to expand on our previous study [42] of driving individual skyrmions through an assembly of other skyrmions. We specifically focus on the time series of the velocity fluctuations, noise power spectra, effective drag, and changes in the depinning threshold while varying the ratio of the Magnus force to the damping. For strong damping, we generally find enhanced narrowband noise signals. We show that although quenched disorder can increase the depinning threshold, it can also decrease the drag experienced by the driven particle and reduce the amount of broadband noise. In the absence of quenched disorder, the depinning threshold monotonically increases with increasing system density [42], but we find that when quenched disorder is present, the depinning becomes strongly nonmonotonic due to the competition between the pinning from the quenched disorder and the pinning from elastic interactions with the surrounding medium. This can also be viewed as an interplay between pinning [21] and jamming [43] behaviors.

2 SIMULATION AND SYSTEM

We consider a modified Thiele equation [44-46] or particle-based approach in which a single skyrmion is driven though a two-dimensional assembly of other skyrmions and a quenched disorder landscape. The initial skyrmion positions are obtained using simulated annealing, so that in the absence of quenched disorder, the skyrmions form a triangular lattice. The equation of motion of the driven skyrmion is given by

$$\alpha_d \mathbf{v}_i + \alpha_m \hat{\mathbf{z}} \times \mathbf{v}_i = \mathbf{F}_i^{ss} + \mathbf{F}_i^{p} + \mathbf{F}_i^{D}. \tag{1}$$

Here, the instantaneous velocity is $\mathbf{v}_i = d\mathbf{r}_i/dt$, $\mathbf{r}_i$ is the position of skyrmion i, and α_d is the damping coefficient arising from dissipative processes. The gyrotropic or Magnus force, given by the second term on the left-hand side, is of magnitude α_m and causes the skyrmions to move in the direction perpendicular to the net applied force. The repulsive skyrmion interaction force has the form [45] $\mathbf{F}_i^{ss} = \sum_{j=1}^{N_s} K_1(r_{ij})\hat{\mathbf{r}}_{ij}$, where $r_{ij} = |\mathbf{r}_i - \mathbf{r}_j|$, $\hat{\mathbf{r}}_{ij} = (\mathbf{r}_i - \mathbf{r}_j)/r_{ij}$, and K_1 is the modified Bessel function which decays exponentially for large r. Within the system are N_p non-overlapping randomly placed pinning sites which are modeled as parabolic traps with a maximum range of r_p that produce a pinning force given by $\mathbf{F}_i^{p} = \sum_{k=1}^{N_p} (F_p/r_p)(\mathbf{r}_i - \mathbf{r}_k^{(p)})\Theta(r_p - |\mathbf{r}_i - \mathbf{r}_k^{(p)}|)\hat{\mathbf{r}}_{ik}^{(p)}$, where F_p is the maximum pinning force, and Θ is the Heaviside step function. The driving force $\mathbf{F}_i^{D} = F_D\hat{\mathbf{x}}$ is applied only to a single skyrmion. Under this driving force, in the absence of pinning or collisions with other skyrmions, the skyrmion would move with an intrinsic skyrmion Hall angle of $\theta_{sk}^{\rm int} = \arctan(\alpha_m/\alpha_d)$. We measure the net skyrmion velocity $\mathbf{V} = N_s^{-1}\sum_{i=1}^{N_s}\mathbf{v}_i$ and its time-averaged components parallel, $\langle V_{\parallel}\rangle$, and perpendicular, $\langle V_{\perp}\rangle$, to the driving force, which is applied along the x direction. The measured skyrmion Hall angle is $\theta_{sk} = \arctan(\langle V_{\perp}\rangle/\langle V_{\parallel}\rangle)$. The sample is of size $L \times L$ with $L = 36$, and in most of this work, we consider $N_s = 648$, giving a skyrmion density of $n_s = N_s/L^2 = 0.5$, and $N_p = 388$, giving a pinning site density of $n_p = N_p/L^2 = 0.3$.

In previous work, we considered a similar model containing no pinning [42], where a finite critical depinning force F_c for motion of the driven skyrmion arises due to elastic interactions with the background skyrmions. There is also a higher second depinning force F_c^{tr} at which the driven skyrmion begins to move transverse to the driving direction, producing a finite skyrmion Hall angle. θ_{sk} increases with increasing drive until, for high drives, it reaches a value close to the intrinsic value $\theta_{sk}^{\rm int}$. This is similar to the behavior found for an assembly of skyrmions driven over random disorder [9-15]. For a fixed drive, the net velocity of the driven skyrmion can actually increase with increasing system density due to the Magnus-induced velocity boost effect, whereas in the overdamped limit, the velocity decreases monotonically with increasing density

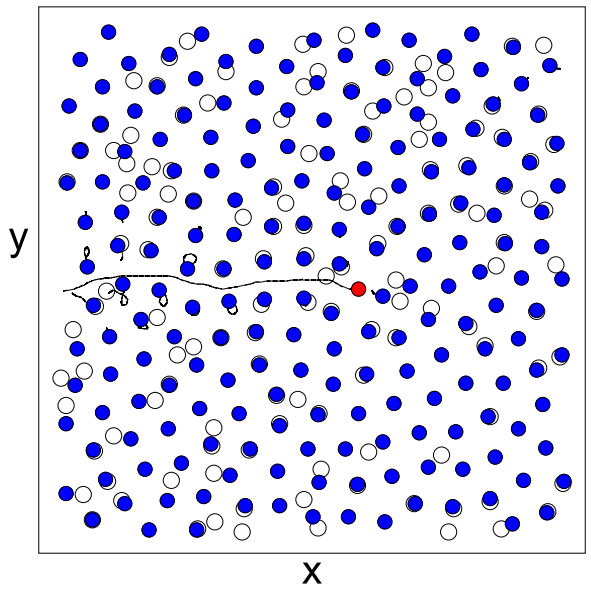

FIGURE 1 | An image of a subsection of the system in which a single skyrmion (red) is driven through an assembly of other skyrmions (blue) in the presence of quenched disorder, generated by randomly placed nonoverlapping local trapping sites (open circles). Black lines indicate the skyrmion trajectories. The driven skyrmion generates motion of the surrounding skyrmions as it passes through the system.

due to enhanced damping from the increased frequency of collisions with background skyrmions [42]. In the present work, we study the effects of adding quenched disorder, and we measure time-dependent velocity fluctuations, velocity overshoots, and the depinning threshold. The time series can be characterized by the power spectrum

$$S(\omega) = \left| \int V(t) \exp(-i\omega) dt \right|^2. \quad (2)$$

Power spectra provide a variety of information on the dynamical properties of the system [47] and have been used extensively to characterize depinning phenomena [18-21,48,49]. In this work, we focus specifically on the fluctuations of the velocity component in the direction of drive.

3 RESULTS

In **Figure 1**, we illustrate a subsection of the system containing a single skyrmion driven through a background of other skyrmions (blue dots) and pinning sites (open circles). The skyrmion trajectories indicate that the driven skyrmion creates a distortion in the surrounding medium as it moves through the system.

In **Figure 2A**, we plot the average velocity parallel to the drive, $\langle V_\parallel \rangle$, versus F_D for the system in **Figure 1** with $n_s = 0.5$, $\alpha_m = 0.1$, and $\alpha_d = 0.995$. Here, we employ the constraint $\alpha_d^2 + \alpha_m^2 = 1.0$ [42], and the intrinsic skyrmion Hall angle is $\theta_{sk}^{\rm int} = -5.74^\circ$. In the absence of quenched disorder, where $n_p = 0$, a depinning threshold appears near $F_c^{np} = 0.1$. For $0.1 < F_D \leq 1.0$, the skyrmion is moving but, as indicated in **Figures 2B,C**, $\langle V_\perp \rangle = 0$ and thus $\theta_{sk} = 0^\circ$. For $F_D > 1.0$, $\langle V_\perp \rangle$ becomes finite, and θ_{sk} begins to grow in magnitude with increasing F_D, until it saturates near $\theta_{sk} = -4.0^\circ$. In a sample containing pinning with $n_p = 0.3$ and $F_p = 0.3$, where the ratio of skyrmions to pinning sites is 5:3, the depinning threshold appears at $F_c = 0.565$. This value is higher than what would be observed in the single skyrmion limit, where $F_c^{ss} = F_p = 0.3$, indicating that the skyrmion-skyrmion interactions are playing an important role in the depinning process. It is also higher than the sum $F_c^{ss} + F_c^{np} = 0.4$ of the single skyrmion and pin-free thresholds, showing that the skyrmions at the pinning sites produce an enhanced pinning effect on the driven skyrmion. In the sample with quenched disorder, $\langle V_\parallel \rangle$ is finite for $0.565 < F_D \leq 1.0$, but the corresponding $\langle V_\perp \rangle = 0$, while for $F_D > 1.0$, both $\langle V_\perp \rangle$ and θ_{sk} increase in magnitude with increasing F_D. In the regime $F_D > 1.0$, $\langle V_\parallel \rangle$ for the system containing pinning is higher than that found in the system without pinning. This is a result of the fact that in the clean system, the driven skyrmion pushes some of the background skyrmions along with it, creating an enhanced drag which reduces $\langle V_\parallel \rangle$, whereas when pinning is present, the surrounding skyrmions are trapped by the pinning sites and cannot be entrained to move along with the driven skyrmion. The reverse trend appears in $\langle V_\perp \rangle$, where both the perpendicular velocity and the skyrmion Hall angle are smaller in magnitude when pinning is present than for the system without pinning. In general, the error in the velocity measurements is less than 10 percent. Near depinning, where the velocity fluctuations are more pronounced, we perform longer time averaging when obtaining

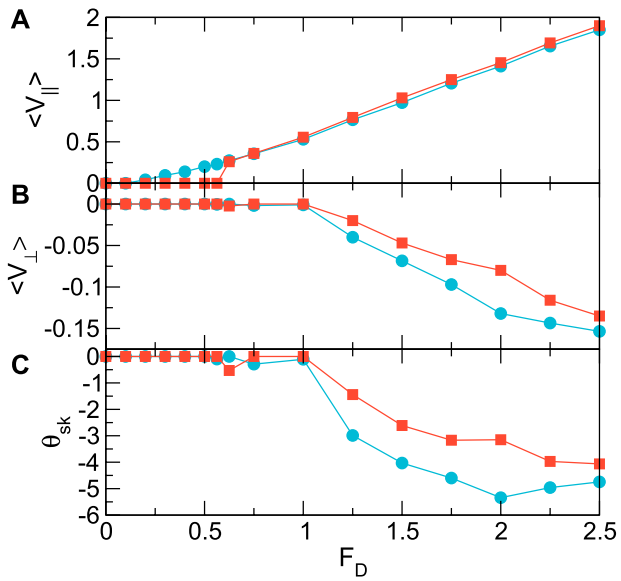

FIGURE 2 | (A) The velocity $\langle V_\parallel \rangle$ parallel to the driving direction versus drive F_D for the system in **Figure 1** with $n_s = 0.5$, $\alpha_m = 0.1$, $\alpha_d = 0.995$, and $\theta_{sk}^{\rm int} = -5.74^\circ$. Blue circles are for a system with no pinning, $n_p = 0$, while red squares are for a system with $n_p = 0.3$ and $F_p = 0.3$. **(B)** The corresponding velocity in the perpendicular direction $\langle V_\perp \rangle$ versus F_D. **(C)** The corresponding measured skyrmion Hall angle θ_{sk} versus F_D.

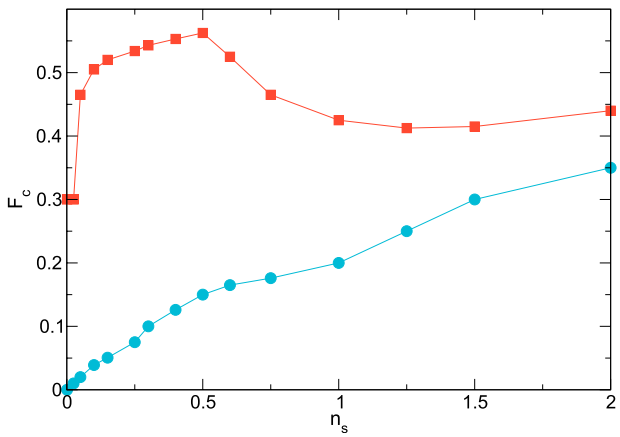

FIGURE 3 | The depinning force F_c versus skyrmion density n_s for the systems in **Figure 2** with $\alpha_m = 0.1$, $\alpha_d = 0.995$, and $\theta_{sk}^{int} = -5.74^{\circ}$. Blue circles are for a pin-free system with $n_p = 0$ while red squares are for a system with $n_p = 0.3$ and $F_p = 0.3$. With no quenched disorder, F_c increases monotonically with n_s.

the average velocity, while at higher drives, the average converges more rapidly to an accuracy of at least 10 percent. The quenched disorder produces a greater reduction in the transverse velocity compared to the longitudinal velocity as a result of the side jump effect which occurs for skyrmions moving over pinning sites. This side jump reduces the Hall angle and thus decreases the transverse velocity but does not modify the longitudinal velocity [9,50-53]. In fact, in some cases, it is possible to obtain an increase in the longitudinal velocity due to a velocity boost effect; however, in the system we consider here, this effect is very weak.

In **Figure 3**, we plot the depinning force F_c versus skyrmion density n_s for the systems in **Figure 2** with and without pinning. In the absence of pinning, F_c starts from zero and increases monotonically with increasing n_s as it becomes more difficult to push the skyrmion through the system. When pinning is present, at low n_s, the driven skyrmion interacts only with the pinning sites, giving $F_c = F_p$; however, once the density increases enough for the driven skyrmion to interact with both pinning sites and other skyrmions, F_c sharply increases and reaches a maximum value near $n_s = 0.5$. The maximum depinning force F_c^{max} should be approximately equal to the force needed to depin the driven skyrmion from a pinning site plus the force required to push the skyrmion directly in front of the driven skyrmion out of a pinning site, $F_c^{max} = 2F_p$, which is close to the value we observe. Up to $n_s = 0.5$, the driven skyrmion can always find an empty pinning site to occupy. If the pinning was periodic, all pins would be filled once $n_s = n_p$, but since the pinning is randomly placed, some pins remain empty and available even when n_s is somewhat larger than n_p. Once $n_s > 0.5$, F_c decreases with increasing n_s because the driven skyrmion is no longer able to find an available pinning site and is instead pinned only by the repulsion from the neighboring pinned skyrmions. This interstitial pinning is weaker than the direct pinning, and as n_s increases above $n_s = 0.5$, a larger and larger number of interstitial skyrmions appear in the sample, decreasing the fraction of directly pinned skyrmions and leading to the decrease in F_c. There is, however, still a nonzero fraction of pinned skyrmions, so F_c remains well above the value found in the sample without pinning sites. At large n_s, F_c begins to increase with increasing density, in line with the trend found for the sample with no quenched pinning, where the interactions with an increasing number of unpinned skyrmions make it more difficult for the driven skyrmion to move through the system. As n_s is increased beyond the range shown in **Figure 3**, we expect that the curves for the pinned and unpinned samples will approach each other as the fraction of directly pinned skyrmions becomes smaller and smaller.

In **Figure 4A**, we plot the time series of the parallel velocity $V_{\parallel}$ for the system in **Figure 2** at $n_s = 0.5$ with no quenched disorder for $F_D = 0.3$, just above depinning. A series of short-period oscillations appear which correspond to elastic interactions in which the driven skyrmion moves past a background skyrmion without generating plastic displacements of the background skyrmions. There are also infrequent larger signals in the form of sharp velocity dips that are correlated with the creation of a plastic distortion or exchange of neighbors among the background skyrmions due to the passage of the driven skyrmion. In **Figure 4B**, we show the time series of $V_{\parallel}$ for the system with quenched disorder at $F_D = 0.625$, just above the depinning threshold. Here, the motion is much more disordered, with strong short-time velocity oscillations. These are produced by the motion of the driven skyrmion over the background pinning sites. The overall structure of the background skyrmions is disordered, destroying the periodic component of motion found in the unpinned system.

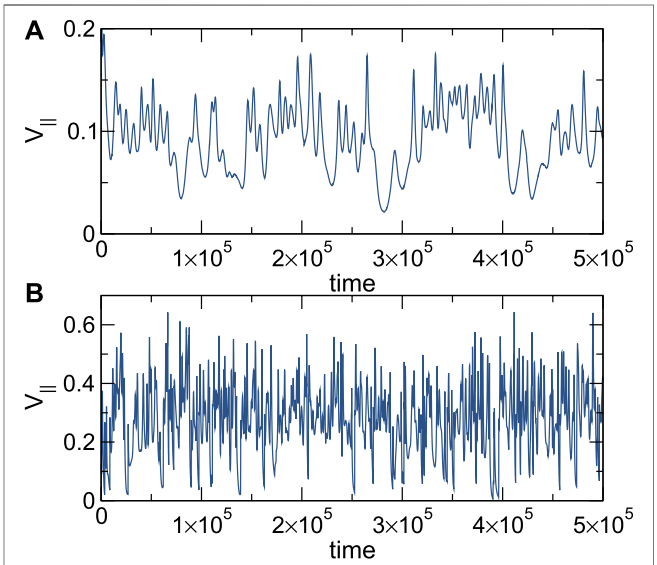

FIGURE 4 | The time series of the velocity $V_{\parallel}$ parallel to the drive for the system in **Figure 2** with $n_s = 0.5$, $\alpha_m = 0.1$, $\alpha_d = 0.995$, and $\theta_{sk}^{int} = -5.74^{\circ}$. **(A)** The disorder-free $n_p = 0$ system at $F_D = 0.3$ just above depinning, showing periodic oscillations and longer time plastic events. **(B)** The quenched disorder system with $n_p = 0.3$ and $F_p = 0.3$ at $F_D = 0.625$ just above depinning, showing less correlated motion.

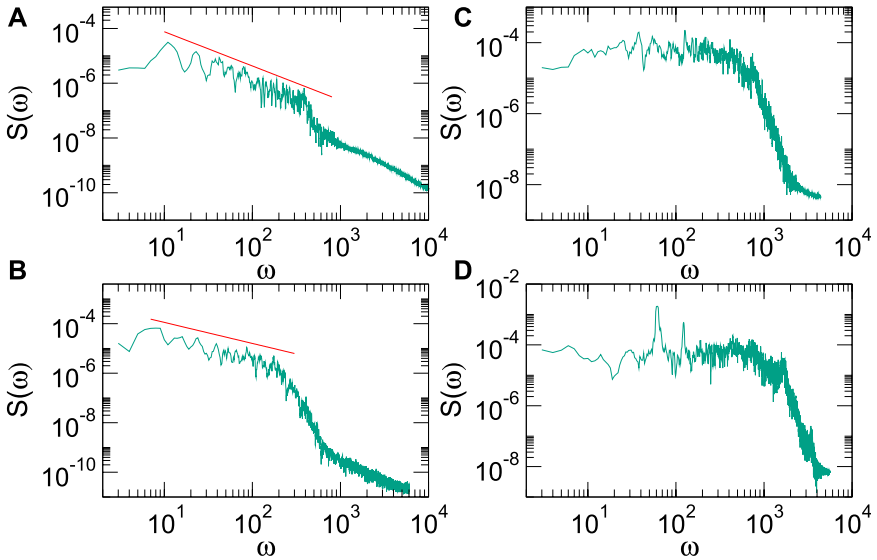

FIGURE 5 | (A) The power spectra $S(\omega)$ for the system in **Figure 2** with $n_s = 0.5$, $\alpha_m = 0.1$, $\alpha_d = 0.995$, $\theta_{sk}^{int} = -5.74°$, and no quenched disorder ($n_p = 0$). **(A)** At $F_D = 0.2$, there is a $1/f^{\alpha}$ signature, where the straight line indicates $\alpha = 1.25$, along with a series of peaks corresponding to the oscillatory portion of the motion due to the periodicity of the skyrmion lattice. **(B)** At $F_D = 0.3$, the red line indicates $\alpha = 0.85$. **(C)** At $F_D = 1.0$, the signal is white noise with $\alpha = 0$. **(D)** At $F_D = 1.5$, there is a narrowband noise signal.

We next examine the power spectra $S(\omega)$ of time series such as those shown in **Figure 4** for different drives for the systems in **Figure 2**. Generically, power spectra can take several forms including $1/f^{\alpha}$, where $\alpha = 0$ indicates white noise with little or no correlation, $\alpha = 2$ is Brownian noise, and $\alpha = 1$ or pink noise can appear when large-scale collective events occur [47]. Noise signatures that are periodic produce narrowband signals with peaks at specific frequencies. It is also possible to have combinations in which the signal is periodic on one time scale but has random fluctuations on longer time scales. For assemblies of particles under an applied drive that exhibit plastic depinning, the power spectrum is typically of $1/f^{\alpha}$ type with α ranging from $\alpha = 1.3$ to $\alpha = 2.0$. A single particle moving over an uncorrelated random landscape typically shows a white noise spectrum, while motion over a periodic substrate produces narrowband noise features [21].

In **Figure 5A**, we plot $S(\omega)$ for the disorder-free system with $n_p = 0$ from **Figure 2** at $F_D = 0.2$, just above the depinning threshold. At low frequencies, we find a series of oscillations or a narrowband noise feature. These periodic velocity oscillations correspond to the driven skyrmion speeding up and slowing down as it moves through the roughly triangular lattice formed by the surrounding skyrmions. The driven skyrmion occasionally generates dislocations or topological defects in the background lattice, so the motion is not strictly periodic but exhibits a combination of periodic motion with intermittent large bursts. This intermittent signal is what gives the spectrum an overall $1/f^{\alpha}$ shape, as indicated by the red line which is a fit with $\alpha = 1.25$. The noise power drops at higher frequencies, which are correlated with the small rotations caused by the Magnus force as the driven skyrmion generates plastic events. In **Figure 5B**, we show the velocity spectrum in the disorder-free sample at $F_D = 0.3$ for the time series illustrated in **Figure 4A**. The overall shape of the spectrum is similar to that found at $F_D = 0.2$ in **Figure 5A**, but the low-frequency oscillations are reduced since more plastic events are occurring in the background skyrmion lattice. A power-law fit with $\alpha = 0.85$ appears as a straight line in **Figure 5B**. In overdamped driven systems with quenched disorder, the power-law exponent is observed to decrease with increasing drive, until it reaches a white noise state with $\alpha = 0$, and a narrowband noise signature appears at high drives [18,19,21]. In **Figure 5C** at $F_D = 1.0$, the response at lower frequencies has become a white noise spectrum with $\alpha = 0$, while at slightly higher frequencies, there is the beginning of a narrowband noise peak. At $F_D = 1.5$ in **Figure 5D**, strong narrowband peaks appear in the spectrum. The narrowband noise arises once the driven skyrmion is moving fast enough that it no longer has time to generate dislocations or other defects in the surrounding lattice, making the system appear more like a single particle moving over a triangular lattice and creating few to no distortions. For high drives, the same narrowband noise signal appears, but the peaks shift to higher frequencies as the driven skyrmion moves faster. The narrowband noise frequencies are related to the time $t = a/v$ between collisions with other skyrmions, where a is the skyrmion lattice constant, and v is the average skyrmion velocity at a specific drive, giving $\omega = v/a$. This implies that for higher F_D, the narrowband noise peak will shift to higher frequencies, consistent with our observations. Similar periodic signals observed for moving superconducting vortices are described in terms of a washboard frequency which is also proportional to v/a, and which appears when the vortices form an ordered lattice [54,19]. In well-ordered lattices, the narrowband noise peaks are sharp, while when the lattice is disordered but large-scale plastic deformations do not occur, narrowband noise peaks are still

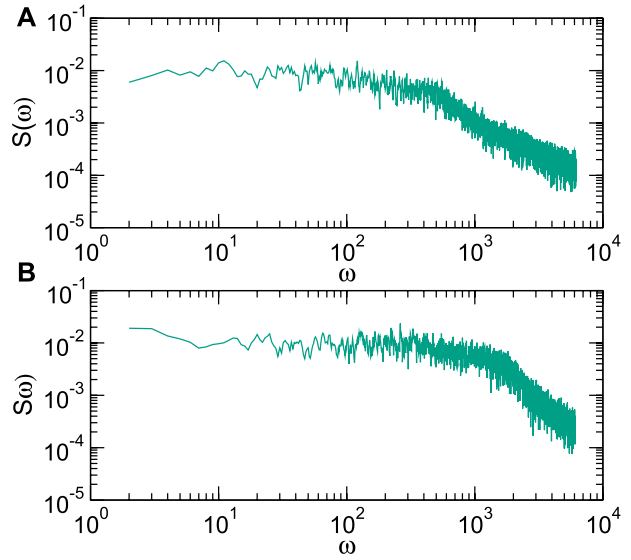

FIGURE 6 | The power spectra $S(\omega)$ for the system in **Figure 2** with quenched disorder at $n_s = 0.5$, $\alpha_m = 0.1$, $\alpha_d = 0.995$, $\theta_{sk}^{\rm int} = -5.74^{\circ}$, $n_p = 0.3$, and $F_p = 0.3$. **(A)** At $F_D = 0.625$, the noise signal is close to white with $\alpha = 0$. **(B)** A similar spectrum appears at $F_D = 1.5$. The high-frequency shoulder above which a $1/f^2$ signature appears shifts to higher drives as F_D increases.

present but become broadened. When the quenched disorder is strong enough to generate large plastic events in which groups of skyrmions move along with the driven probe skyrmion, the noise becomes white and adopts a $\omega^{-\alpha}$ form.

In **Figure 6A**, we plot $S(\omega)$ for the pinned system with $n_p = 0.3$ and $F_p = 0.3$ from **Figure 4B** at $F_D = 0.625$, just above depinning. At low frequencies, the power spectrum is nearly white with $\alpha = 0$, while the noise power drops as $1/f^2$ at high frequencies. Unlike the pin-free system, strong low-frequency oscillations are absent because the lattice structure of the surrounding skyrmions is disordered by the pinning sites. We find no $1/f$ noise, in part due to the reduced mobility of the skyrmions trapped at pinning sites, which reduces the amount of plastic events which can occur. In the absence of pinning, the driven skyrmion can more readily create exchanges of neighbors in the background skyrmions, generating longer range distortions in the system and creating more correlated fluctuations in the driven skyrmion velocity. In **Figure 6B**, we plot $S(\omega)$ for the same system at a higher drive of $F_D = 1.5$, where again similar white noise appears at low frequencies, while the transition from white noise to $1/f^2$ noise has shifted to a higher frequency. Unlike the disorder-free sample, here, we find no narrowband signal since the surrounding skyrmions are trapped in disordered positions by the pinning. The addition of quenched disorder might be expected to increase the appearance of $1/f$ noise due to the greater disorder in the system; however, in this case, the quenched disorder suppresses the plastic events responsible for the broadband noise signature. In a globally driven assembly of particles, the drive itself can induce plastic events [21]. This implies that the fluctuations of a single probe particle driven over quenched disorder are expected to differ significantly from the noise signatures found in bulk-driven systems. The spectra in **Figure 6** have a shape called Lorentzian, $S(f) = A/(\omega_0^2 + \omega^2)$, which is also found for shot noise [47]. In our case, ω_0 corresponds to the average time between collisions of the driven skyrmion with pinning sites, and it shifts to higher frequencies as the drive increases. Here, $\omega_0 \propto v/a$, where a is the skyrmion lattice constant and v is the average skyrmion velocity. At higher drives where v increases, the distortions of the surrounding skyrmion lattice should diminish, leading to the emergence of a sharp narrowband noise signal.

We next consider the influence of the Magnus force on the noise fluctuations of the driven skyrmion. In **Figure 7A**, we plot the time series of $V_{\parallel}$ at $F_D = 1.0$ for a system without quenched disorder in the completely overdamped limit of $\alpha_m = 0.0$ and $\alpha_d = 1.0$. For the equivalent drive in a sample with $\alpha_m = 0.1$ and $\alpha_d = 0.995$, **Figure 5C** shows that white noise is present; however, for the overdamped system, **Figure 7B** indicates that a strong narrowband noise signal appears. In the image in **Figure 8A**, the driven skyrmion moves through the lattice of other skyrmions without creating plastic distortions. In general, we find that in the overdamped limit and in the absence of pinning, a strong narrowband noise signal appears as the driven skyrmion moves elastically through an ordered skyrmion lattice, as shown in the linear-linear plot of $S(\omega)$ in **Figure 7B**. In **Figure 7C**, we plot the time series of $V_{\parallel}$ for the same system in the Magnus-dominated regime with $\alpha_m/\alpha_d = 9.95$ and $\theta_{sk}^{\rm int} = -84.26^{\circ}$. Here, a combination of periodic motion and plastic events occurs, producing the much smaller narrowband noise signal shown in **Figure 7D**. In the corresponding skyrmion trajectories illustrated in **Figure 8B**, the skyrmion moves at an angle to the driving direction due to the Magnus force, and there are significant distortions of the surrounding skyrmion lattice. This additional motion is generated by the increase in spiraling behavior produced by the Magnus force. In previous studies of bulk-driven skyrmions moving over quenched disorder, it was shown that an increase in the Magnus force caused a reduction in the narrowband noise signal [15].

We next consider the effect of the pinning strength on the dynamics. In **Figure 9A**, we plot the time series of $V_{\parallel}$ for a system with $\alpha_m/\alpha_d = 0.1$, $n_s = 0.5$, $n_p = 0.3$, $F_p = 2.0$, and $F_D = 1.6$. Here, the driven skyrmion experiences a combination of sliding and nearly pinned motion, where at certain points, the skyrmion is temporarily trapped by a combination of the pinning and the skyrmion-skyrmion interactions. As the surrounding skyrmions relax, the driven skyrmion can jump out of the pinning site where it has become trapped, leading to another pulse of motion. This stick-slip or telegraph-type motion only occurs just above the critical driving force when the pinning force is sufficiently strong, while for higher drives, the motion becomes continuous. In **Figure 9B**, we show the time series of $V_{\parallel}$ for the same system at $\alpha_m/\alpha_d = 9.95$, where the stick-slip or telegraph motion is lost. We note that the value of $\langle V_{\parallel} \rangle$ in the Magnus-dominated $\alpha_m/\alpha_d = 9.95$ system is smaller than that found in the overdamped $\alpha_m/\alpha_d = 0.1$ system since the increasing Magnus force rotates more of the velocity into the direction perpendicular to the drive; however, a similar continuous flow is observed both parallel and perpendicular to the drive in the Magnus-dominated system. The loss of the stick-slip motion is due to the increasing spiraling

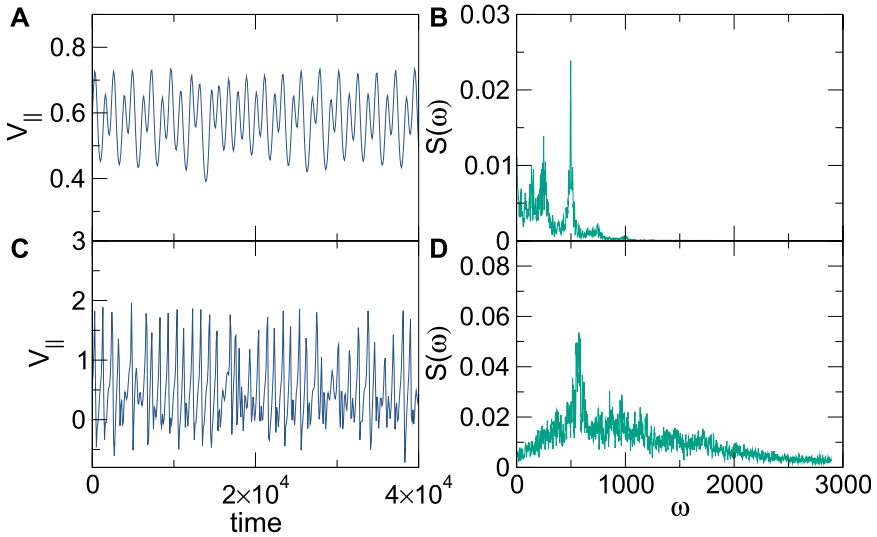

FIGURE 7 | (A) The time series of the velocity $V_{\parallel}$ parallel to the drive at $n_s = 0.5$ and $F_D = 1.0$ for an overdamped system with $\alpha_m/\alpha_d = 0$ and no quenched disorder. **(B)** The corresponding power spectrum $S(\omega)$ contains narrowband peaks. **(C)** The time series for the same system but with $\alpha_m/\alpha_d = 9.95$, where the fluctuations are enhanced. **(D)** The corresponding power spectrum $S(\omega)$ has a reduced amount of narrowband noise.

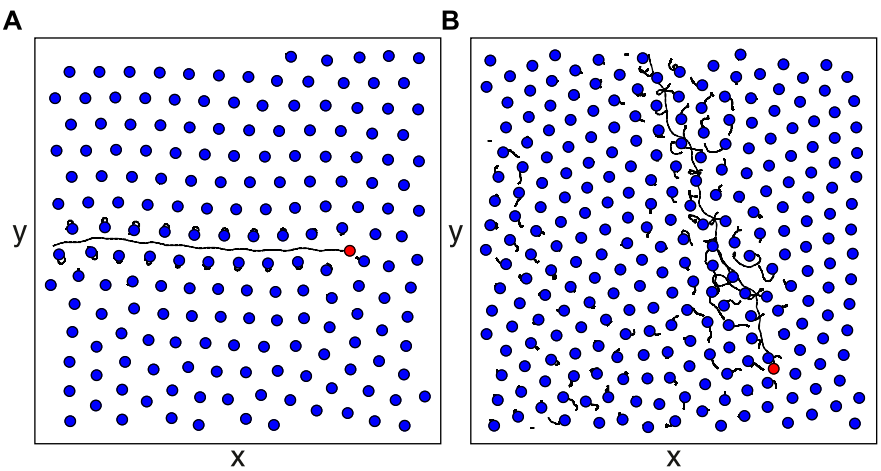

FIGURE 8 | An image of a subsection of the system showing the driven skyrmion (red), background skyrmions (blue), and skyrmion trajectories (black lines) for the samples from **Figure 7** with $n_s = 0.5$ at $F_D = 1.0$. **(A)** For the overdamped system with $\alpha_m/\alpha_d = 0$ from **Figures 7A,B**, the background skyrmions experience elastic distortions, but there are no plastic events. **(B)** For the Magnus-dominated system with $\alpha_m/\alpha_d = 9.95$ from **Figures 7C,D**, the driven skyrmion moves at an angle due to the increased Magnus force, creating significant distortions in the background skyrmion lattice.

motion of both the driven and background skyrmions. In **Figure 9C**, we plot the power spectra corresponding to the time series in **Figures 9A,B**. The stick-slip motion of the $\alpha_m/\alpha_d = 0.1$ system produces a $1/f^{\alpha}$ signature in $S(\omega)$ with $\alpha = 1.3$. For the $\alpha_m/\alpha_d = 9.95$ sample, $S(\omega)$ is much flatter, indicating reduced correlations in the fluctuations, and also has increased noise power at high frequencies. The enhanced high-frequency noise results from the fast spiraling motion of both the driven and the background skyrmions when they are inside pinning sites. The detection of enhanced high-frequency noise could thus provide an indication that strong pinning effects or strong Magnus forces are present. In **Figure 9D**, we plot the distribution $P(V_{\parallel})$ of instantaneous velocity for the samples in **Figures 9A,B**. When $\alpha_m/\alpha_d = 0.1$, $P(V_{\parallel})$ is bimodal with a large peak near $V_{\parallel} = 0$ and a smaller peak near $V = 1.6$, corresponding to the value of the driving force. There is no gap of zero weight in $P(V_{\parallel})$ separating these two peaks. When $\alpha_m/\alpha_d = 9.95$, $P(V_{\parallel})$ has only a single peak at intermediate velocities. Additionally, there is significant weight at negative velocities, which were not present in the strongly damped sample. The negative velocities arise when the skyrmions move in circular orbits due to the Magnus force

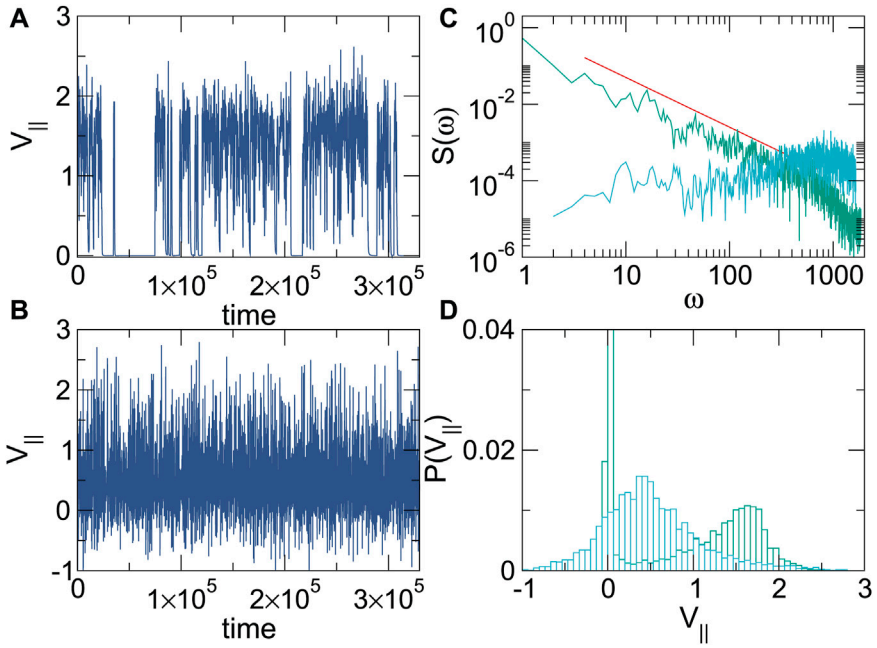

FIGURE 9 | Samples with $n_s = 0.5$, $n_p = 0.3$, $F_p = 2.0$, and $F_D = 1.6$. **(A)** Time series of $V_\parallel$ for a system with $\alpha_m/\alpha_d = 0.1$. **(B)** Time series of $V_\parallel$ for a system with $\alpha_m/\alpha_d = 9.95$. **(C)** The power spectra $S(\omega)$ for the $\alpha_m/\alpha_d = 0.1$ system (green) showing a power-law fit to $1/f^{\alpha}$ with $\alpha = 1.3$ (red line), and $S(\omega)$ for the $\alpha_m/\alpha_d = 9.95$ system (blue). **(D)** Distribution $P(V_\parallel)$ of velocities in the direction parallel to the drive for the $\alpha_m/\alpha_d = 0.1$ system (green), where a bimodal shape appears, and for the $\alpha_m/\alpha_d = 9.95$ system (blue), where the distribution is unimodal.

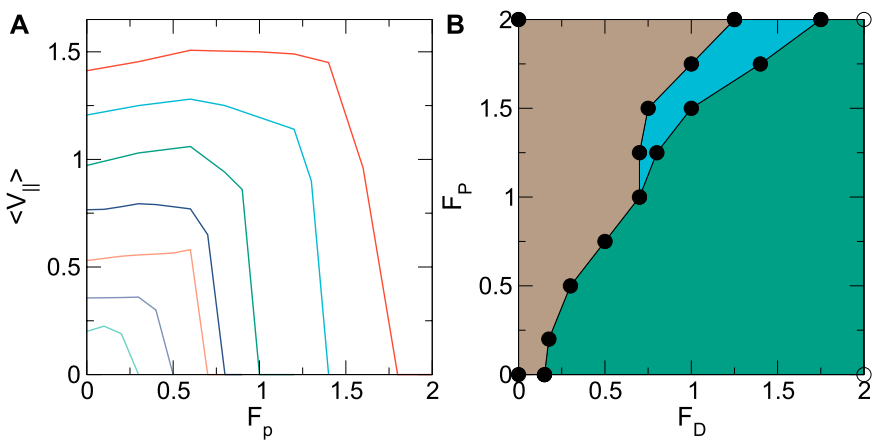

FIGURE 10 | (A) $\langle V_\parallel \rangle$ versus pinning strength F_p for the system in **Figure 9A** with $n_s = 0.5$, $n_p = 0.3$, and $\alpha_m/\alpha_d = 0.1$ at $F_D = 2.0$, 1.75, 1.5, 1.25, 1.0, 0.7, and 0.5, from top to bottom. **(B)** Dynamic phase diagram for the same system as a function of F_p versus F_D. Green: continuous flow regime; blue: stick-slip motion; brown: pinned.

and spend a portion of the orbit moving in the direction opposite to the driving force.

In **Figure 10A**, we plot the average velocity $\langle V_\parallel \rangle$ versus pinning strength F_p for the system in **Figure 9A** with $\alpha_m/\alpha_d = 0.1$, $n_s = 0.5$, and $n_p = 0.3$ at $F_D = 2.0$, 1.75, 1.5, 1.25, 1.0, 0.75, and 0.5. The pinning force at which $\langle V_\parallel \rangle$ reaches zero, indicating the formation of a pinned state, increases as F_D increases. Generally, there is also a range of low F_p over which $\langle V_\parallel \rangle$ increases with increasing F_p. This is due to a reduction in the drag on the driven skyrmion as the background skyrmions become more firmly trapped in the pinning sites, similar to what was illustrated in **Figure 2**. Stick-slip motion appears in the regime where there is a sharp downturn in $\langle V_\parallel \rangle$ and is associated with a bimodal velocity distribution of the type shown in **Figure 9D**. A plot of $\langle V_\parallel \rangle$ versus F_p for the $\alpha_m/\alpha_d = 9.95$ system (not shown) reveals a similar trend, except that the pinning transitions shift to larger values of F_p. Using the features in **Figure 10A** combined with the velocity distributions, we construct a dynamic phase diagram for the

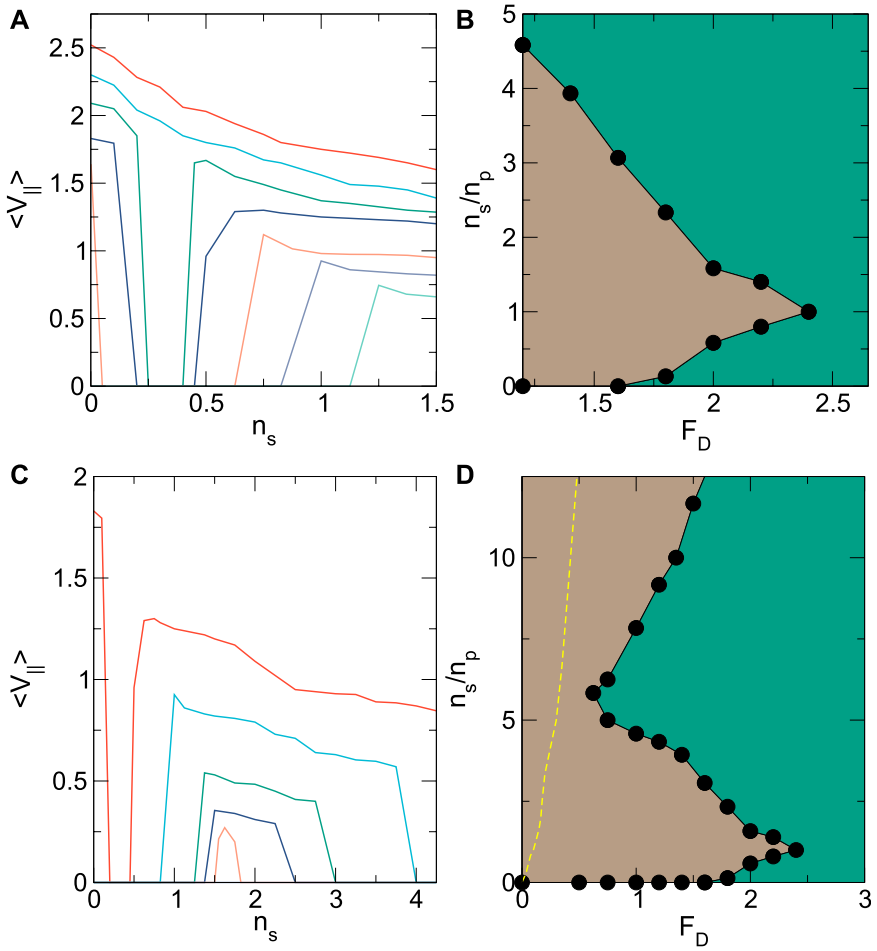

FIGURE 11 | (A) $\langle V_{\parallel}\rangle$ versus skyrmion density n_s for the system in **Figure 9A** with $n_p = 0.3$, $F_p = 1.6$, and $\alpha_m/\alpha_d = 0.1$ at $F_D = 1.4$, 1.6, 1.8, 2.0, 2.2, 2.4, and 2.6, from bottom to top. **(B)** Dynamic phase diagram for the same system as a function of n_s/n_p versus F_D. Green: continuous flow regime; brown: pinned. **(C)** $\langle V_{\parallel}\rangle$ versus n_s for the system in panel **(A)** plotted up to a maximum value of $n_s = 4.0$ for $F_D = 0.75$, 1.0, 1.2, 1.6, and 2.0, from bottom to top. Note that for $F_D = 0.5$, $\langle V_{\parallel}\rangle = 0$ over this entire range of n_s. **(D)** Dynamic phase diagram for the same system as a function of n_s/n_p versus F_D. Green: continuous flow regime; brown: pinned. The yellow dashed line indicates the location of the depinning threshold in systems with no quenched disorder.

$\alpha_m/\alpha_d = 0.1$ system as a function of F_p versus F_D, illustrated in **Figure 10B**. We observe continuous flow, stick-slip motion, and pinned regimes, with stick-slip motion occurring only when $F_p > 0.75$. In general, for increasing Magnus force, the window of stick-slip motion decreases in size.

In **Figure 11A**, we plot $\langle V_{\parallel}\rangle$ versus the skyrmion density n_s for the system in **Figure 9A** with $F_p = 1.6$, $n_p = 0.3$, and $\alpha_m/\alpha_d = 0.1$ at $F_D = 1.4$, 1.6, 1.8, 2.0, 2.2, 2.4, and 2.6. At $F_D = 1.4$, the system is pinned when $n_s \leq 1.0$. For this skyrmion density, all of the skyrmions can be trapped at pinning sites and are therefore unable to move since $F_D < F_p$. As n_s increases, all of the pinning sites become filled and interstitial skyrmions appear which are pinned only by repulsion from other skyrmions directly located at pinning sites. The strength of this interstitial pinning is determined by the elastic properties of the skyrmion lattice, and for these densities, it is weaker than F_p. When $F_D > F_p$, flow can occur even for low n_s, where the driven skyrmion interacts with the pinning sites but has few collisions with background skyrmions. In the limit $n_s = 0$ where only the driven skyrmion is present, the system is always flowing whenever $F_D/F_p > 1.0$. For the $F_D = 2.2$ curve, the system is flowing up to $n_s = 0.2$, and then, a pinned region appears for $0.2 < n_s < 0.5$. At this range of skyrmion densities, even though $F_D > F_p$, the driven skyrmion experiences a combination of direct pinning from the pinning sites it encounters plus interstitial pinning by the nearby directly pinned skyrmions, giving an additive effect which causes the apparent pinning strength to be larger than F_D. For $n_s > 0.5$, all the pinning sites start to become occupied, and the driven skyrmion experiences only the weaker interstitial pinning without becoming trapped directly by any pinning sites. At small F_D, it is possible for the driven skyrmion to become trapped by a pinning site that is already occupied by a background skyrmion, creating a doubly occupied pinning site, which is why the value of n_s below which the driven skyrmion can begin to move again shifts to larger n_s with decreasing F_D. The reentrant pinning effect illustrated in

Figure 11A arises from the combination of the direct and interstitial pinning mechanisms. In **Figure 11B**, we construct a dynamic phase diagram as a function of n_s/n_p versus F_D for the system in **Figure 11A** showing the pinned and flowing phases. Reentrant pinning occurs over the range $F_D = F_p = 1.6$ to slightly above $F_D = 2.2$. The reentrant pinned phase reaches its maximum extent near $n_s/n_p = 1.0$, a density at which the number of directly pinned skyrmions attains its maximum value while the number of interstitially pinned skyrmions is still nearly zero.

For higher values of n_s/n_p, another pinned phase arises at low values of F_D that is produced by the skyrmion-skyrmion interactions. In **Figure 11D**, we plot $\langle V_{\parallel} \rangle$ versus n_s up to $n_s = 4.0$ for $F_D = 0.5$, 0.75, 1.0, 1.2, 1.6, and 2.0 in the same system from **Figure 11**. Note that for $F_D = 0.5$, $\langle V_{\parallel} \rangle = 0$ over the entire range of n_s. At higher n_s, $\langle V_{\parallel} \rangle$ drops to zero again as the system reaches a pinned state. This second pinned phase is produced by the increase in the elastic skyrmion-skyrmion interaction energies at the higher densities. In the absence of quenched disorder, the skyrmion-skyrmion interactions are the only mechanism by which the driven skyrmion can be pinned, and there is a threshold for motion which increases monotonically with increasing n_s. When quenched disorder is introduced, the threshold becomes both nonmonotonic and reentrant. For increasing F_D in **Figure 11C**, the elastic energy-induced pinning transition shifts to higher n_s. In **Figure 11D**, we show a dynamic phase diagram as a function of n_s/n_p versus F_D for the system in **Figure 11C** indicating the locations of the pinned and flowing phases. For $n_s/n_p < 2.0$, the reentrant pinned state produced by a combination of direct and interstitial pinning reaches its maximum extent. As n_s/n_p increases, the pinned state reaches a minimum width near $n_s/n_p = 5.5$, above which the pinned region begins to grow again. The yellow dashed line is the depinning threshold in the absence of quenched disorder, which always falls below the depinning transition of samples with quenched disorder. The increase in the depinning threshold due to the addition of pinning occurs even when the number of skyrmions is significantly larger than the number of pinning sites since even a relatively small number of pins can prevent plastic distortions of the background skyrmions, raising the barrier for motion of the driven skyrmion.

In the phase diagram of **Figure 11B** and **Figure 11D**, for drives just above the pinned phase, there is a small window of stick-slip motion (not shown) which is more prominent for lower values of n_s/n_p. In addition, within the flowing phase, there is another critical drive above which there is an onset of transverse motion, giving a finite Hall angle. This line has a shape similar to that of the depinning curve but falls at higher values of F_D.

In this work, we considered a point-like model for skyrmions. In real skyrmion systems, there is an effective skyrmion size that can change with field or exhibit internal modes. It may be possible that at low fields, the particle picture works well, while at higher fields, the skyrmions will start to change shape. Micromagnetic simulations could capture situations in which the individual spin degrees of freedom become important, such as when the skyrmions become deformed when interacting with a pinning site. Skyrmion deformations could also produce changes in the noise fluctuations or spectral signatures since the internal modes of the skyrmions can be associated with distinct frequencies. A micromagnetic model could also treat systems in which different types of skyrmions are present, such as ferromagnetic skyrmions versus antiferromagnetic skyrmions or antiskyrmions. It would be interesting to study how the effective drag on the driven skyrmion would change in this case. As previously demonstrated experimentally, the system we consider could be realized by dragging an individual skyrmion with a local atomic force microscope or magnetic force microscope tip. There have also been proposals to manipulate individual skyrmions with optical traps. Such local probes would allow the fluctuations and velocity noise of the individual driven skyrmion to be measured. Another method for achieving relative plastic motion of skyrmions on the scale of the skyrmion lattice constant would be to use a sample containing skyrmions of different sizes or different species in which one size or species couples more strongly to the external drive and moves more rapidly than the other sizes or species of skyrmions. In this work, we focus on the strong pinning regime in which interactions with the substrate produce plastic distortions or tearing of the skyrmion lattice. For weaker pinning, an elastic regime can appear in which plastic deformations do not occur, and a single driven skyrmion can drag the entire skyrmion assembly along with it. There could also be a finite range for the elastic interaction, with the driven skyrmion dragging a large elastically stable chunk of skyrmions along with it, and with plastic deformations occurring only on much larger length scales [21]. This would suggest the existence of an elastic to plastic transition that could be detected by varying the driving velocity or other parameters. It would also be interesting to consider driving an individual three-dimensional skyrmion line. Here, only the top portion of the skyrmion might respond to the driving force, while the lower portion of the line is passively dragged by the skyrmion line tension. This type of effect has been studied for three-dimensional superconducting vortex lines.

Another question regards the distinction between pinning-dominated pinned states, where direct pinning is responsible for producing the pinning, and interstitial-dominated or jammed pinned states, where the pinning of the driven skyrmion arises from elastic interactions with directly pinned skyrmions. The fluctuations in the jammed state generally show that there is a greater tendency for large-scale plastic events to occur, leading to a larger amount of low-frequency noise compared to the pinning-dominated state. In work on superconducting vortices with quenched disorder, the presence of pinned, jammed, and clogged phases could be deduced by measuring memory effects [55]. For the single driven skyrmion, memory could be tested by reversing the driving direction. For strong pinning, the trajectory under reversed drive should mirror that of the forward drive, indicating a memory effect, whereas in samples with strong plastic distortions, the trajectory for forward and reversed drive will differ due to the appearance of plastic distortions in the background skyrmions.

4 SUMMARY

We have examined the fluctuations and pinning effects for individually driven skyrmions moving through an assembly of other skyrmions and quenched disorder. We find that in the absence of quenched disorder, there is a depinning force that increases monotonically with increasing skyrmion density. When quenched disorder is introduced, the driven skyrmion experiences a combination of pinning and drag effects from both the pinning sites and the background skyrmions. Both with and without quenched disorder, there is a second, higher driving threshold for the onset of motion transverse to the drive and the appearance of a finite skyrmion Hall angle. For higher drives, the addition of quenched disorder actually increases the velocity of the driven skyrmion since the pinning sites help prevent the background skyrmions from being dragged along by the driven skyrmion. Near depinning, in the absence of quenched disorder, the velocity fluctuations show a combination of periodic oscillations from the elasticity of the ordered background skyrmion lattice along with stronger jumps associated with plastic distortions of the background skyrmions. This produces a velocity power spectrum that has narrowband noise peaks superimposed on a $1/f^{\alpha}$ shape with $\alpha = 1.2$. As the drive increases, the spectrum becomes white, and for very high drives, a strong narrowband signature emerges once the driven skyrmion is moving too rapidly to generate plastic distortions in the background skyrmions. The addition of quenched disorder reduces the frequency of plastic events, giving a white noise spectrum. In the absence of disorder, a damping-dominated system generally shows strong narrowband noise fluctuations as the driven skyrmion moves along one-dimensional paths in the background skyrmion lattice, whereas in the Magnus-dominated limit, the driven skyrmion moves at an angle through the lattice, generating dislocations and reducing the strength of the narrowband signature. When the disorder is strong, the driven skyrmion can undergo stick-slip motion due to a combination of being trapped at pinning sites and interacting elastically with the background skyrmions, which produces a bimodal velocity distribution along with $1/f^{\alpha}$ noise. For systems with quenched disorder, the depinning threshold is highly nonmonotonic as a function of the skyrmion density, passing through both peaks and minima. This is due to a competition between two different pinning effects. The depinning threshold drops when the number of skyrmions becomes larger than the number of pinning sites since the driven skyrmion must be pinned through interstitial interactions with directly pinned skyrmions instead of sitting in a pinning site directly; however, at higher densities, the increasing strength of the elastic interactions between the skyrmions causes the depinning threshold to rise again with increasing density. At low densities, the system can be viewed as being in a pinning-dominated regime, while at higher densities, it is in an interstitial-dominated or jamming regime. Beyond skyrmions, our results should be relevant to fluctuations in other particle-based systems such as individually dragged vortices in type-II superconductors.

DATA AVAILABILITY STATEMENT

The original contributions presented in the study are included in the article/Supplementary Material, and further inquiries can be directed to the corresponding author.

AUTHOR CONTRIBUTIONS

All authors listed have made a substantial, direct, and intellectual contribution to the work and approved it for publication.

FUNDING

We gratefully acknowledge the support of the US Department of Energy through the LANL/LDRD program for this work. This work was supported by the US Department of Energy through the Los Alamos National Laboratory. The Los Alamos National Laboratory is operated by Triad National Security, LLC, for the National Nuclear Security Administration of the US Department of Energy (Contract No. 892333218NCA000001).

REFERENCES

1. Mühlbauer S, Binz B, Jonietz F, Pfleiderer C, Rosch A, Neubauer A, et al. Skyrmion Lattice in a Chiral Magnet. *Science* (2009) 323:915–9. doi:10.1126/science.1166767
2. Yu XZ, Onose Y, Kanazawa N, Park JH, Han JH, Matsui Y, et al. Real-space Observation of a Two-Dimensional Skyrmion crystal. *Nature* (2010) 465:901–4. doi:10.1038/nature09124
3. Nagaosa N, Tokura Y. Topological Properties and Dynamics of Magnetic Skyrmions. *Nat Nanotech* (2013) 8:899–911. doi:10.1038/NNANO.2013.243
4. Iwasaki J, Mochizuki M, Nagaosa N. Universal Current-Velocity Relation of Skyrmion Motion in Chiral Magnets. *Nat Commun* (2013) 4:1463. doi:10.1038/ncomms2442
5. Schulz T, Ritz R, Bauer A, Halder M, Wagner M, Franz C, et al. Emergent Electrodynamics of Skyrmions in a Chiral Magnet. *Nat Phys* (2012) 8:301–4. doi:10.1038/NPHYS2231
6. Woo S, Litzius K, Krüger B, Im M-Y, Caretta L, Richter K, et al. Observation of Room-Temperature Magnetic Skyrmions and Their Current-Driven Dynamics in Ultrathin Metallic Ferromagnets. *Nat Mater* (2016) 15:501–6. doi:10.1038/nmat4593
7. Reichhardt C, Reichhardt CJO, Milosevic MV. Statics and Dynamics of Skyrmions Interacting with Pinning: a Review. *arXiv e-prints* (2021). arXiv:2102.10464
8. Everschor-Sitte K, Sitte M. Real-space Berry Phases: Skyrmion Soccer (Invited). *J Appl Phys* (2014) 115:172602. doi:10.1063/1.4870695
9. Reichhardt C, Ray D, Reichhardt CJO. Collective Transport Properties of Driven Skyrmions with Random Disorder. *Phys Rev Lett* (2015) 114:217202. doi:10.1103/PhysRevLett.114.217202
10. Jiang W, Zhang X, Yu G, Zhang W, Wang X, Benjamin Jungfleisch M, et al. Direct Observation of the Skyrmion Hall Effect. *Nat Phys* (2017) 13:162–9. doi:10.1038/NPHYS3883
11. Litzius K, Lemesh I, Krüger B, Bassirian P, Caretta L, Richter K, et al. Skyrmion Hall Effect Revealed by Direct Time-Resolved X-ray Microscopy. *Nat Phys* (2017) 13:170–5. doi:10.1038/NPHYS4000
12. Reichhardt C, Reichhardt CJO. Thermal Creep and the Skyrmion Hall Angle in Driven Skyrmion Crystals. *J Phys Condens Matter* (2019) 31:07LT01. doi:10.1088/1361-648X/aaefd7

13. Juge R, Je S-G, Chaves Dd. S, Buda-Prejbeanu LD, Peña Garcia J, Nath J, et al. Current-driven Skyrmion Dynamics and Drive-dependent Skyrmion Hall Effect in an Ultrathin Film. *Phys Rev Appl* (2019) 12:044007. doi:10.1103/physrevapplied.12.044007
14. Zeissler K, Finizio S, Barton C, Huxtable AJ, Massey J, Raabe J, et al. Diameter-independent Skyrmion Hall Angle Observed in Chiral Magnetic Multilayers. *Nat Commun* (2020) 11:428. doi:10.1038/s41467-019-14232-9
15. Díaz SA, Reichhardt CJO, Arovas DP, Saxena A, Reichhardt C. Fluctuations and Noise Signatures of Driven Magnetic Skyrmions. *Phys Rev B* (2017) 96: 085106. doi:10.1103/PhysRevB.96.085106
16. Sato T, Koshibae W, Kikkawa A, Yokouchi T, Oike H, Taguchi Y, et al. Slow Steady Flow of a Skyrmion Lattice in a Confined Geometry Probed by Narrow-Band Resistance Noise. *Phys Rev B* (2019) 100:094410. doi:10.1103/physrevb.100.094410
17. Sato T, Kikkawa A, Taguchi Y, Tokura Y, Kagawa F. Mode Locking Phenomena of the Current-Induced Skyrmion-Lattice Motion in Microfabricated MnSi. *Phys Rev B* (2020) 102:180411. doi:10.1103/PhysRevB.102.180411
18. Marley AC, Higgins MJ, Bhattacharya S. Flux Flow Noise and Dynamical Transitions in a Flux Line Lattice. *Phys Rev Lett* (1995) 74:3029–32. doi:10.1103/physrevlett.74.3029
19. Olson CJ, Reichhardt C, Nori F. Nonequilibrium Dynamic Phase Diagram for Vortex Lattices. *Phys Rev Lett* (1998) 81:3757–60. doi:10.1103/physrevlett.81.3757
20. Grüner G. The Dynamics of Charge-Density Waves. *Rev Mod Phys* (1988) 60: 1129–81. doi:10.1103/RevModPhys.60.1129
21. Reichhardt C, Olson Reichhardt CJ. Depinning and Nonequilibrium Dynamic Phases of Particle Assemblies Driven over Random and Ordered Substrates: a Review. *Rep Prog Phys* (2017) 80:026501. doi:10.1088/1361-6633/80/2/026501
22. Fert A, Reyren N, Cros V. Magnetic Skyrmions: Advances in Physics and Potential Applications. *Nat Rev Mater* (2017) 2:17031. doi:10.1038/natrevmats.2017.31
23. Luo S, You L. Skyrmion Devices for Memory and Logic Applications. *APL Mater* (2021) 9:050901. doi:10.1063/5.0042917
24. Hastings MB, Olson Reichhardt CJ, Reichhardt C. Depinning by Fracture in a Glassy Background. *Phys Rev Lett* (2003) 90:098302. doi:10.1103/PhysRevLett.90.098302
25. Habdas P, Schaar D, Levitt AC, Weeks ER. Forced Motion of a Probe Particle Near the Colloidal Glass Transition. *Europhys Lett* (2004) 67:477–83. doi:10.1209/epl/i2004-10075-y
26. Zia RN. Active and Passive Microrheology: Theory and Simulation. *Annu Rev Fluid Mech* (2018) 50:371–405. doi:10.1146/annurev-fluid-122316-044514
27. Dullens RPA, Bechinger C. Shear Thinning and Local Melting of Colloidal Crystals. *Phys Rev Lett* (2011) 107:138301. doi:10.1103/PhysRevLett.107.138301
28. Gazuz I, Puertas AM, Voigtmann T, Fuchs M. Active and Nonlinear Microrheology in Dense Colloidal Suspensions. *Phys Rev Lett* (2009) 102: 248302. doi:10.1103/PhysRevLett.102.248302
29. Candelier R, Dauchot O. Journey of an Intruder through the Fluidization and Jamming Transitions of a Dense Granular media. *Phys Rev E* (2010) 81:011304. doi:10.1103/PhysRevE.81.011304
30. Olson Reichhardt CJ, Reichhardt C. Fluctuations, Jamming, and Yielding for a Driven Probe Particle in Disordered Disk Assemblies. *Phys Rev E* (2010) 82: 051306. doi:10.1103/PhysRevE.82.051306
31. Olson Reichhardt CJ, Reichhardt C. Viscous Decoupling Transitions for Individually Dragged Particles in Systems with Quenched Disorder. *Phys Rev E* (2008) 78:011402. doi:10.1103/PhysRevE.78.011402
32. Gruber M, Puertas AM, Fuchs M. Critical Force in Active Microrheology. *Phys Rev E* (2020) 101:012612. doi:10.1103/PhysRevE.101.012612
33. Straver EWJ, Hoffman JE, Auslaender OM, Rugar D, Moler KA. Controlled Manipulation of Individual Vortices in a Superconductor. *Appl Phys Lett* (2008) 93:172514. doi:10.1063/1.3000963
34. Auslaender OM, Luan L, Straver EWJ, Hoffman JE, Koshnick NC, Zeldov E, et al. Mechanics of Individual Isolated Vortices in a Cuprate Superconductor. *Nat Phys* (2009) 5:35–9. doi:10.1038/NPHYS1127
35. Veshchunov IS, Magrini W, Mironov SV, Godin AG, Trebbia J-B, Buzdin AI, et al. Optical Manipulation of Single Flux Quanta. *Nat Commun* (2016) 7: 12801. doi:10.1038/ncomms12801
36. Kremen A, Wissberg S, Haham N, Persky E, Frenkel Y, Kalisky B. Mechanical Control of Individual Superconducting Vortices. *Nano Lett* (2016) 16:1626–30. doi:10.1021/acs.nanolett.5b04444
37. Ma X, Reichhardt CJO, Reichhardt C. Manipulation of Individual Superconducting Vortices and Stick-Slip Motion in Periodic Pinning Arrays. *Phys Rev B* (2018) 97:214521. doi:10.1103/PhysRevB.97.214521
38. Illien P, Bénichou O, Oshanin G, Sarracino A, Voituriez R. Nonequilibrium Fluctuations and Enhanced Diffusion of a Driven Particle in a Dense Environment. *Phys Rev Lett* (2018) 120:200606. doi:10.1103/PhysRevLett.120.200606
39. Hanneken C, Kubetzka A, von Bergmann K, Wiesendanger R. Pinning and Movement of Individual Nanoscale Magnetic Skyrmions via Defects. *New J Phys* (2016) 18:055009. doi:10.1088/1367-2630/18/5/055009
40. Holl C, Knol M, Pratzer M, Chico J, Fernandes IL, Lounis S, et al. Probing the Pinning Strength of Magnetic Vortex Cores with Sub-nanometer Resolution. *Nat Commun* (2020) 11:2833. doi:10.1038/s41467-020-16701-y
41. Wang X-G, Chotorlishvili L, Dugaev VK, Ernst A, Maznichenko IV, Arnold N, et al. The Optical Tweezer of Skyrmions. *Npj Comput Mater* (2020) 6:140. doi:10.1038/s41524-020-00402-7
42. Reichhardt C, Reichhardt CJO. Dynamics and Nonmonotonic Drag for Individually Driven Skyrmions. *Phys Rev B* (2021) 104:064441. doi:10.1103/physrevb.104.064441
43. Reichhardt C, Reichhardt CJO. Aspects of Jamming in Two-Dimensional Athermal Frictionless Systems. *Soft Matter* (2014) 10:2932–44. doi:10.1039/c3sm53154f
44. Thiele AA. Steady-state Motion of Magnetic Domains. *Phys Rev Lett* (1973) 30: 230–3. doi:10.1103/PhysRevLett.30.230
45. Lin S-Z, Reichhardt C, Batista CD, Saxena A. Particle Model for Skyrmions in Metallic Chiral Magnets: Dynamics, Pinning, and Creep. *Phys Rev B* (2013) 87: 214419. doi:10.1103/PhysRevB.87.214419
46. Brown BL, Täuber UC, Pleimling M. Effect of the Magnus Force on Skyrmion Relaxation Dynamics. *Phys Rev B* (2018) 97:020405. doi:10.1103/physrevb.97.020405
47. Weissman MB. 1fnoise and Other Slow, Nonexponential Kinetics in Condensed Matter. *Rev Mod Phys* (1988) 60:537–71. doi:10.1103/revmodphys.60.537
48. Bullard TJ, Das J, Daquila GL, Täuber UC. Vortex Washboard Voltage Noise in Type-II Superconductors. *Eur Phys J B* (2008) 65:469–84. doi:10.1140/epjb/e2008-00358-7
49. Reichhardt C, Olson Reichhardt CJ. Noise Fluctuations and Drive Dependence of the Skyrmion Hall Effect in Disordered Systems. *New J Phys* (2016) 18: 095005. doi:10.1088/1367-2630/18/9/095005
50. Müller J, Rosch A. Capturing of a Magnetic Skyrmion with a Hole. *Phys Rev B* (2015) 91:054410. doi:10.1103/PhysRevB.91.054410
51. Reichhardt C, Ray D, Reichhardt CJO. Quantized Transport for a Skyrmion Moving on a Two-Dimensional Periodic Substrate. *Phys Rev B* (2015) 91: 104426. doi:10.1103/PhysRevB.91.104426
52. Reichhardt C, Reichhardt CJO. Thermal Creep and the Skyrmion Hall Angle in Driven Skyrmion Crystals. *J Phys Condens Matter* (2018) 31:07LT01. doi:10.1088/1361-648X/aaefd7
53. Fernandes IL, Chico J, Lounis S. Impurity-dependent Gyrotropic Motion, Deflection and Pinning of Current-Driven Ultrasmall Skyrmions in Pdfe/ir(111) Surface. *J Phys Condens Matter* (2020) 32:425802. doi:10.1088/1361-648X/ab9cf0
54. Harris JM, Ong NP, Gagnon R, Taillefer L. Washboard Frequency of the Moving Vortex Lattice in $YBa_2Cu_3O_{6.93}$ Detected by Ac-Dc Interference. *Phys Rev Lett* (1995) 74:3684–7. doi:10.1103/PhysRevLett.74.3684
55. Reichhardt C, Reichhardt CJO. Jamming, Fragility and Pinning Phenomena in Superconducting Vortex Systems. *Sci Rep* (2020) 10:11625. doi:10.1038/s41598-020-68417-0

Conflict of Interest: The authors declare that the research was conducted in the absence of any commercial or financial relationships that could be construed as a potential conflict of interest.

Publisher's Note: All claims expressed in this article are solely those of the authors and do not necessarily represent those of their affiliated organizations or those of the publisher, the editors, and the reviewers. Any product that may be evaluated in this article, or claim that may be made by its manufacturer, is not guaranteed or endorsed by the publisher.

frontiers in Physics

ORIGINAL RESEARCH
published: 28 January 2022
doi: 10.3389/fphy.2021.774951

Confinement of Magnetic Skyrmions to Corrals of Artificial Surface Pits with Complex Geometries

Takao Matsumoto[1]* *and Naoya Shibata*[1,2,3]

[1]Institute of Engineering Innovation, School of Engineering, The University of Tokyo, Tokyo, Japan, [2]Nanostructures Research Laboratory, Japan Fine Ceramic Center, Nagoya, Japan, [3]Department of Applied Physics and Quantum Phase Electronics Center (QPEC), University of Tokyo, Tokyo, Japan

Magnetic skyrmion is a particle-like swirling spin texture promising for future memory devices. The geometric confinement and artificial control of skyrmions are crucial for such practical applications. In a previous research, we developed a technique to confine skyrmions to simple geometric corrals, such as a rectangle and a triangle, composed of artificial surface pits with nanometer-scale dimensions fabricated by using a focused electron beam. The technique has a potential advantage of facilitating more complex geometries, which has not been fully explored yet. Here we directly visualize skyrmions confined to surface-pit corrals with several complex geometries by using differential phase contrast scanning transmission electron microscopy. We find that individual skyrmions are deformed not only in shape but also in size under a moderate-bias field. We also find that deformed skyrmionic spin textures with opposite polarities coexist in the zero-field condition. The present study provides a guide to confine skyrmions, which should be useful for future applications.

Keywords: magnetic skyrmion, geometric confinement, individual skyrmion deformation, surface-pit corral, differential-phase-contrast scanning transmission electron microscopy, complex geometry, polarity control, room temperature

OPEN ACCESS

Edited by:
Xichao Zhang,
Shinshu University, Japan

Reviewed by:
Haifeng Du,
Hefei Institutes of Physical Science (CAS), China
Marijan Beg,
Imperial College London, United Kingdom

***Correspondence:**
Takao Matsumoto
takao.matsumoto@sogo.t.u-tokyo.ac.jp

Specialty section:
This article was submitted to Condensed Matter Physics, a section of the journal Frontiers in Physics

Received: *13 September 2021*
Accepted: *21 December 2021*
Published: *28 January 2022*

Citation:
Matsumoto T and Shibata N (2022) Confinement of Magnetic Skyrmions to Corrals of Artificial Surface Pits with Complex Geometries. Front. Phys. 9:774951. doi: 10.3389/fphy.2021.774951

INTRODUCTION

Magnetic skyrmion [1–5] is a particle-like swirling spin texture arising from the competition between Heisenberg and Dzyaloshinskii–Moriya (DM) exchange interactions [6, 7]. It attracts growing attention as it is promising for future innovative devices owing to its nanometer-scale dimensions and topological stability [8, 9]. In such practical applications, skyrmions are expected to be confined in nanostructures with various geometries so that the influence of such geometric confinement on the behaviors of skyrmions is essential. In modern magnetic recording technology, such as the bit patterned media technology [10], geometric confinement is one of the key techniques to increase the stability of the elemental spin textures and hence the density of recorded information. Geometric confinement of skyrmions has been studied by micromagnetic simulations, assuming simple geometries such as nanodisks [11–15] and constricted channels [16, 17]. To realize the geometric confinement of skyrmions in experiments, conventional microfabrication techniques were used to fabricate nanodisks [18–22], nano-strips [23–25], and holes/trenches [26, 27]. In these studies, complete physical edges were utilized to confine skyrmions. Partial physical edges like the surface nano-strips with various widths and thicknesses created by using focused gallium ion beam [28] are also effective to confine skyrmions. In addition, non-physical (chemical) edges were also shown to be effective to confine skyrmions. By using helium ion beam, the DM interaction in a

localized region was modified to confine skyrmions in simple geometric shapes like nano-strips and squares [29]. Recently, it was demonstrated that skyrmions can be effectively confined in channels by fabricating stripes with modified magnetic properties in a single ferromagnetic film [30]. Alternatively, Zhang *et al.* [31] showed that skyrmions were directly created by scanning the surface of a specimen by a magnetic force microscopy (MFM) tip with bias field. Using the same technique, Ognev *et al.* [32] have demonstrated the creation of zero-bias-field skyrmion patterns with complex geometries, such as a toroid and an alphabet S. In a previous study [33], we demonstrated that even tiny surface pits with nanometer-scale dimensions fabricated by using a focused electron beam (surface-pit corral) are effective to confine stable skyrmion states. These unconventional techniques have the potential advantage of facilitating complex geometries that are difficult or even not feasible by conventional microfabrication techniques.

Unlike rigid particles, such as colloidal particles and atoms, skyrmions can change their shape. Such a deformation of individual skyrmions was first revealed in an *in situ* Lorentz transmission electron microscopy (TEM) study, demonstrating that a small uniaxial tensile strain induces a very large anisotropic deformation (elongation) of a skyrmion lattice (SkL) as well as individual skyrmions constituting the lattice [34]. We also found that individual skyrmions can flexibly change not only their shapes but also their sizes to accommodate the free volumes formed at the domain boundary cores of SkLs under the influence of the complete physical edges of a thin-plate specimen [35]. The domain boundary structure can be described by the periodic combination of fivefold-coordinated and sevenfold-coordinated structure units as frequently observed in real atomic crystals. Skyrmions at the center of fivefold-coordinated structure units are spatially compressed, while skyrmions at the center of sevenfold-coordinated structure units are spatially elongated compared with the regular circular skyrmions. Recently, such deformed skyrmions were shown to play significant roles in the spontaneous creation and annihilation of skyrmions [36]. Artificial control of such deformations (elongation and compression) of individual skyrmions is important from a viewpoint of practical applications as suggested by a recent proposal to utilize a skyrmion with an elliptical profile confined in a magnetic nanodisk as the qubits for quantum computing platforms [37]. On the other hand, artificial control of the swirling nature of skyrmions is also important from a viewpoint of practical applications. The swirling nature of a skyrmion is characterized by several parameters [21]: magnetic helicity γ_m, polarity p, and circularity c. The magnetic helicity is defined as $\gamma_m = +$ and $\gamma_m = -$ for a right-handed spin helix and a left-handed spin helix, respectively. Following the same definitions as commonly used to describe a magnetic vortex—a similar swirling spin texture—[38], skyrmions, with their out-of-plane magnetizations at the core pointing up and down, are defined by polarity $p = +1$ and $p = -1$, respectively, while skyrmions with their in-plane magnetizations rotating clockwise (CW) and counter-clockwise (CCW) around the core are defined by the circularity $c = +1$ and $c = -1$, respectively. The magnetic helicity is determined once a material is given, depending on the crystallographic chirality Γ_c and sign of the DM interaction, where Γ_c is defined as + and − for right-handed and left-handed crystallographic chirality, respectively [39, 40]. When the magnetic helicity is given, p is determined uniquely once c has been given and vice versa, depending on the direction of the bias magnetic field applied on a specimen. So far, several attempts to control the swirling parameters of skyrmions have been reported. A unique spin texture in a confined geometry called a target skyrmion, which was predicted in theoretical and numerical investigations [12, 19], was directly visualized by Lorentz TEM in a 160-nm-diameter nanodisk of FeGe [21]. In zero magnetic field, two types of target skyrmions [one is characterized by a combination of positive circularity ($c = +1$) and positive polarity ($p = +1$), while another is characterized by a combination of negative circularity ($c = -1$) and negative polarity ($p = -1$)] were observed as the material possesses the right-handed magnetic helicity ($\gamma_m = +$). The two stable ground states with opposite characteristics were demonstrated to switch each other by changing the direction of the perpendicular magnetic field applied on the thin-plate specimen. The polarity reversal of skyrmions was also feasible by thermal activation in a thin plate of barium hexaferrite [41] and by switching the magnetic helicity in a thin plate of $Mn_{1-x}Fe_xGe$ with varying compositions, resulting in the sign reversal of the DM interaction [42]. Theoretically, two degenerate skyrmion states characterized by opposite polarities can be created by applying an inclined magnetic pulse [43] that was used for magnetic vortex core reversal [35].

To investigate the deformations of individual skyrmions while distinguishing their swirling characteristics, direct real-space visualization techniques of individual skyrmions with high spatial resolutions, such as Lorentz TEM [5, 44], off-axis electron holography [45, 46], and differential phase contrast scanning TEM (DPC STEM) [33, 47], are powerful. DPC STEM is arguably the most powerful technique, particularly when the magnetic spin texture and various kinds of material defects, such as edges, grain boundaries, and surface pits, must be visualized simultaneously, as demonstrated by previous works [33, 35, 48–50]. Here we report skyrmion states confined to surface-pit corrals with complex geometries directly visualized in real-space with nanometer spatial resolution by using the DPC STEM technique.

MATERIALS AND METHODS

Bulk Polycrystal Preparation

A bulk polycrystalline β-Mn type $Co_8Zn_8Mn_4$ was synthesized by Dr. Yeong-Gi So at Akita University from highly pure Co (99.99%), Zn (99.99%), and Mn (99.99%) using an electric furnace; the constituent elements with the nominal composition of $Co_8Zn_8Mn_4$ were sealed in an evacuated silica tube, heated at 1,273 K for 12 h, subsequently cooled to 1,198 K at a cooling rate of 1 K/h, and annealed at 1,198 K for 72 h, followed by water quenching.

Thin-Plate Specimen Preparation

A (111) thin plate was fabricated from a bulk crystal by using an Ion Slicer (IS9001, JEOL, Ltd.). Prior to observation, the thin plate

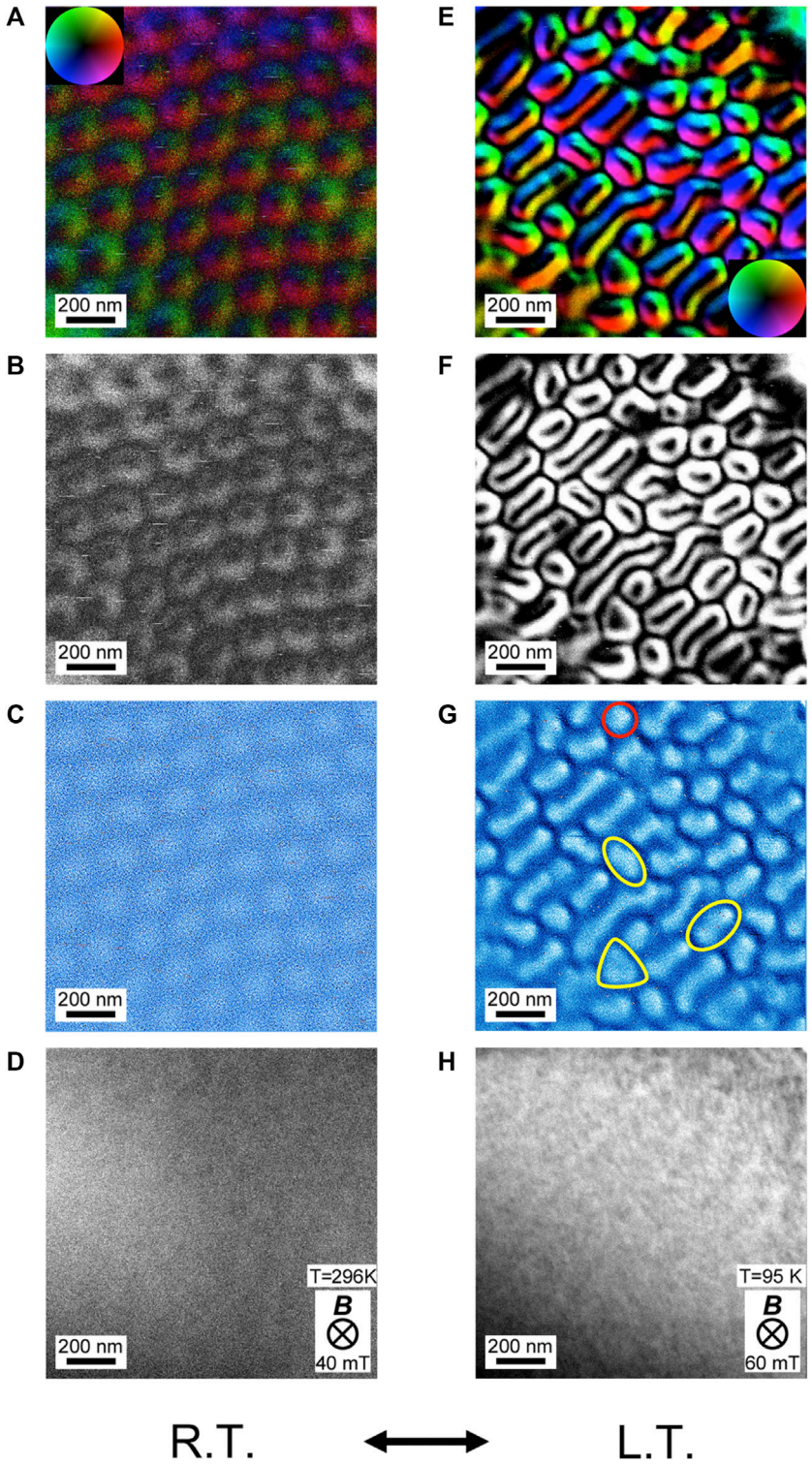

FIGURE 1 | Differential phase contrast scanning TEM images of skyrmion lattices in a thin plate of $Co_8Zn_8Mn_4$ at room temperature (296 K) **(A–D)** and at a low temperature (95 K) **(E–H)**. **(A,E)** In-plane magnetic induction as a color map and **(B,F)** intensity. **(C,G)** Magnetic helicity images [35] and **(D,H)** simultaneously acquired annular dark-field images. The same pixel dwell time of 640 μs was used to record these images. Perpendicular magnetic fields of 40 and 60 mT are applied at 296 and 95 K, respectively. Yellow shapes indicate several deformed skyrmions, not only in shape but also in size, while a red circle indicates less deformed circular skyrmions in **(G)**.

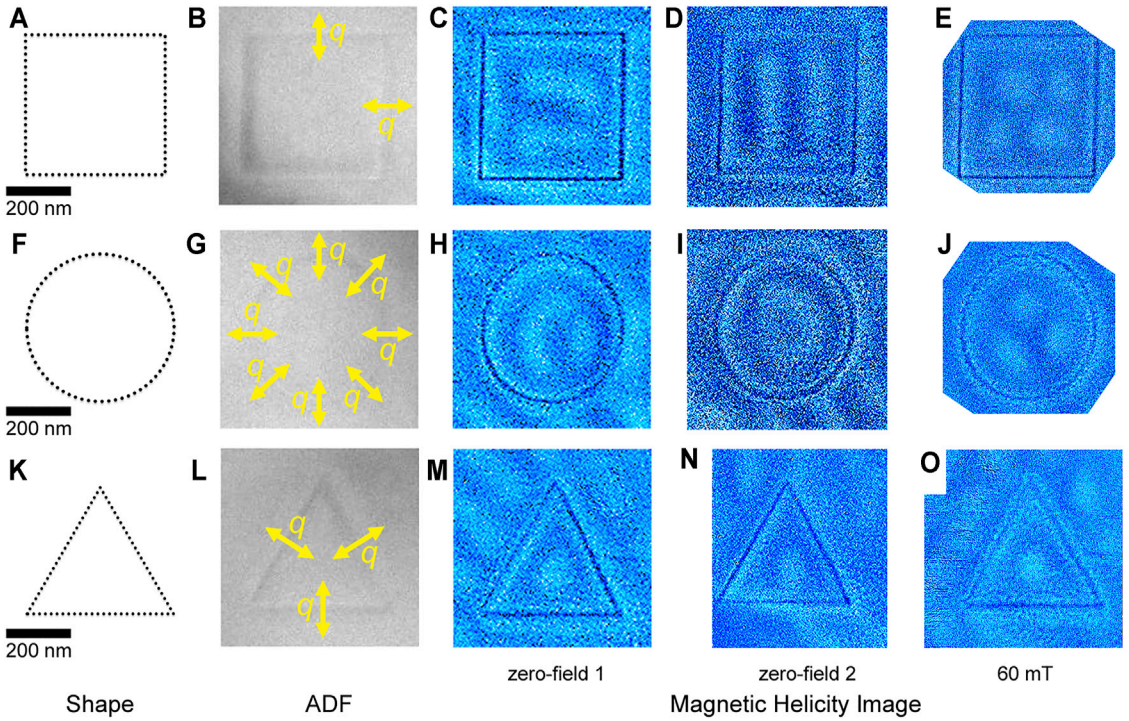

FIGURE 2 | Skyrmion states confined to surface-pit corrals with three simple geometries. Schematics of **(A)** a square, **(F)** a circle, and **(K)** a triangular corral. Annular dark-field images of fabricated corrals with a square **(B)**, a circle **(G)**, and a triangle geometry **(L)** by using a focused electron beam. The edge length of the square, diameter of the circle, and edge length of the equilateral triangle are equally 440 nm. Several q-vectors defined by each corral are indicated by yellow arrows in **(B)**, **(G)**, and **(L)**, respectively. Magnetic helicity images of spin textures confined to a square corral **(C–E)**, a circular corral **(H–J)**, and a triangular corral **(M–O)** are shown. Spin textures in two independent zero-field conditions **(C**,**D**,**H**,**I**,**M**,**N)** and under the perpendicular magnetic field of 60 mT **(E**,**J**,**O)** are shown. Skyrmions are displayed as bright particles. Pixel dwell time is 1 ms.

was further polished with a plasma cleaner (Solarus, Model 950, Gatan, Inc.). The typical thickness of the thin plate is estimated to be about 150 nm.

DPC STEM Experiments

For DPC STEM observations, we used a STEM (JEM-2100F, JEOL, Ltd.) equipped with a probe-forming aberration corrector (CEOS, GmbH) and a Schottky field emission gun operated at 200 kV. This microscope was equipped with a segmented annular all-field detector which was described in a literature in detail [51]. When observing magnetic skyrmion, the objective lens was switched off, and the illumination system was adjusted to obtain a probe size of about 3.5 nm with a probe-forming aperture semi-angle of 0.426 mrad. A perpendicular magnetic field was applied by weakly exciting the objective lens, and the field strength was calibrated by using a magnetic field measuring specimen holder equipped with three Hall-probe sensors. Even when the objective lens of the microscope is completely switched off and demagnetized several times, a small remnant perpendicular magnetic field of around 20 mT is applied on the thin-plate specimen. We use "zero-field" to refer to this experimental condition throughout the manuscript. For a probe size of 3.5 nm, the detector ranges are 0.346–0.520 and 0.78–1.35 mrad for DPC images and annular dark-field (ADF) images, respectively. To record images, we used pixel dwell time as long as 1 ms in the present study to obtain sufficient contrast at room temperature.

Surface-Pit Corral Fabrication

The same STEM (JEM-2100F, JEOL, Ltd.) used for DPC STEM observations was also used to fabricate surface-pit corrals with the objective lens strongly excited to form a smaller probe size (< 1 nm) with increasing probe current. A customized program written at the University of Tokyo was used to control the scanning of the focused electron beam to create a sequence of surface pits forming complex geometric patterns. The details of the nature of surface pits are described elsewhere [33].

RESULTS AND DISCUSSIONS

Room-Temperature Skyrmion Lattice in a Thin Plate of $Co_8Zn_8Mn_4$

For practical applications, magnetic skyrmions stable at room temperature are highly desirable. To observe stable magnetic skyrmions at room temperature (296 K), we use a (111) thin plate of $Co_8Zn_8Mn_4$ [33, 52] with the critical temperature (T_c) of 300 K. Due to the decreased magnetization at room temperature (T / T_c ~ 0.99 for T = 296 K), however, the contrast of skyrmions at room temperature is much lower than that at a low

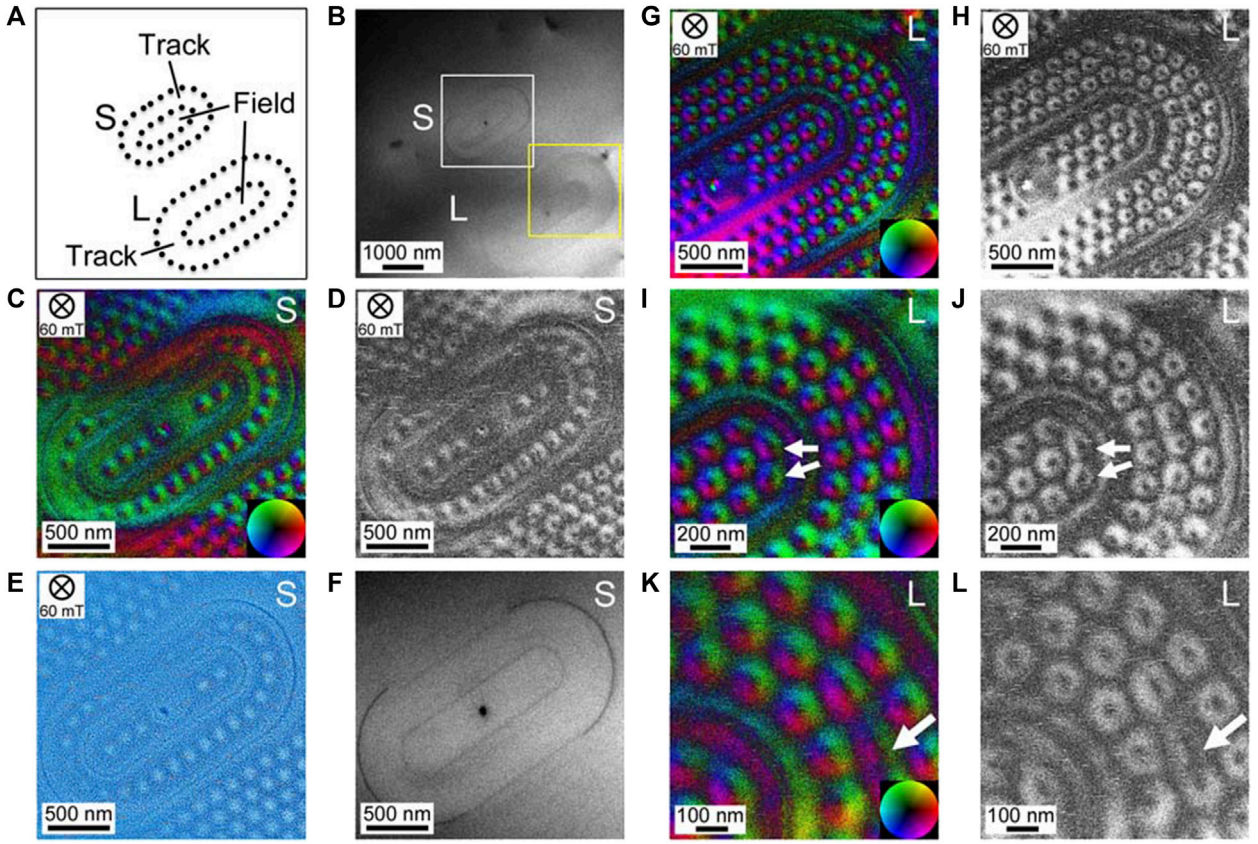

FIGURE 3 | Confinement of skyrmions to surface-pit corrals defined by two nested curved boundaries (track and field). **(A)** Schematic of the two corrals with smaller and larger sizes. **(B)** Annular dark-field (ADF) image of the two corrals fabricated by a focused electron beam on the surface of the thin-plate specimen. The track width of the smaller corral and that of the larger corral are 420 and 630 nm, respectively. **(G)** In-plane magnetic induction as a color map and **(H)** intensity obtained in the area indicated by a white square in **(B)**. **(C)** Magnetic helicity image and **(D)** ADF image of the smaller corral. **(I)** In-plane magnetic induction as a color map and **(J)** intensity confined in the larger corral. Only the field-of-view as indicated by the yellow square in **(B)** is shown. **(E)** In-plane magnetic induction as a color map and **(F)** intensity confined in the larger corral at a higher magnification. **(K)** In-plane magnetic induction as a color map and **(L)** intensity confined in the larger corral at a higher magnification. Elongated skyrmions are indicated by white arrows in **(E,F,K,L)**. The pixel dwell time is 1 ms. The S and L letters at the top-right corner of each image indicate the smaller and the larger corrals, respectively.

temperature (T / T_c ~0.32 for T = 95 K). A longer pixel dwell time than usual is hence required at room temperature to record images with sufficient contrast. **Figure 1** shows a comparison of DPC STEM images of SkLs in a thin plate of $Co_8Zn_8Mn_4$ at room temperature (296 K) under the perpendicular magnetic field of 40 mT (**Figures 1A–D**) and those at a low temperature (95 K) under the perpendicular magnetic field of 60 mT (**Figures 1E–H**) recorded with the same pixel dwell time (640 μs). In the reconstructed in-plane magnetic induction, as shown in **Figures 1A,B**, individual skyrmions with negative circularity (CCW, c = −1) are directly visualized at room temperature. Note that the in-plane magnetic induction as a color map as shown in **Figure 1A** is disturbed by diffraction contrast due to the inevitable bending of the thin-plate specimen. The swirling in-plane magnetic induction with negative circularity is correctly reconstructed only for a few individual skyrmions in the lattice. In magnetic helicity images [35] (**Figure 1C**), however, skyrmions with negative circularity are visualized as bright particles without an apparent influence of the diffraction contrast. In the ADF image (**Figure 1D**), no obvious contrast other than the diffraction contrast is observed, which proves that no apparent structural defect exists in the field-of-view of the thin-plate specimen. Since the bias magnetic field is in the down direction as indicated by the crossed circle symbols in the figure, the polarity of skyrmions as visualized in **Figures 1A–C** is inferred as positive (p = +1). It follows that the magnetic helicity of the specimen is left-handed (γ_m = −). Individual skyrmions are mostly circular in shape. In contrast, strongly deformed skyrmions are observed at a temperature of 95 K (**Figure 1E–G**). No contrast indicating the existence of apparent structural defects is observed again in the ADF image (**Figure 1H**), ensuring that the deformations are not induced by structural defects in the specimen. Note that skyrmions are deformed not only in shape but also in size as indicated by several yellow shapes, compared with the less deformed circular skyrmion as indicated by a red circle in **Figure 1G**. It appears that the deformed skyrmions prefer a few orientations rather than random orientations, which can be ascribed to the weak crystal magnetic anisotropy in the (111) plane at 95 K. Actually, in a previous Lorentz TEM study [53], it was reported that circular skyrmions created by 70 mT field-cooling at 280 K were deformed into the bar- or L-shaped form in a (001) thin plate of $Co_8Zn_8Mn_4$ when the specimen was field-cooled to a temperature of an extremely low temperature (6 K). The

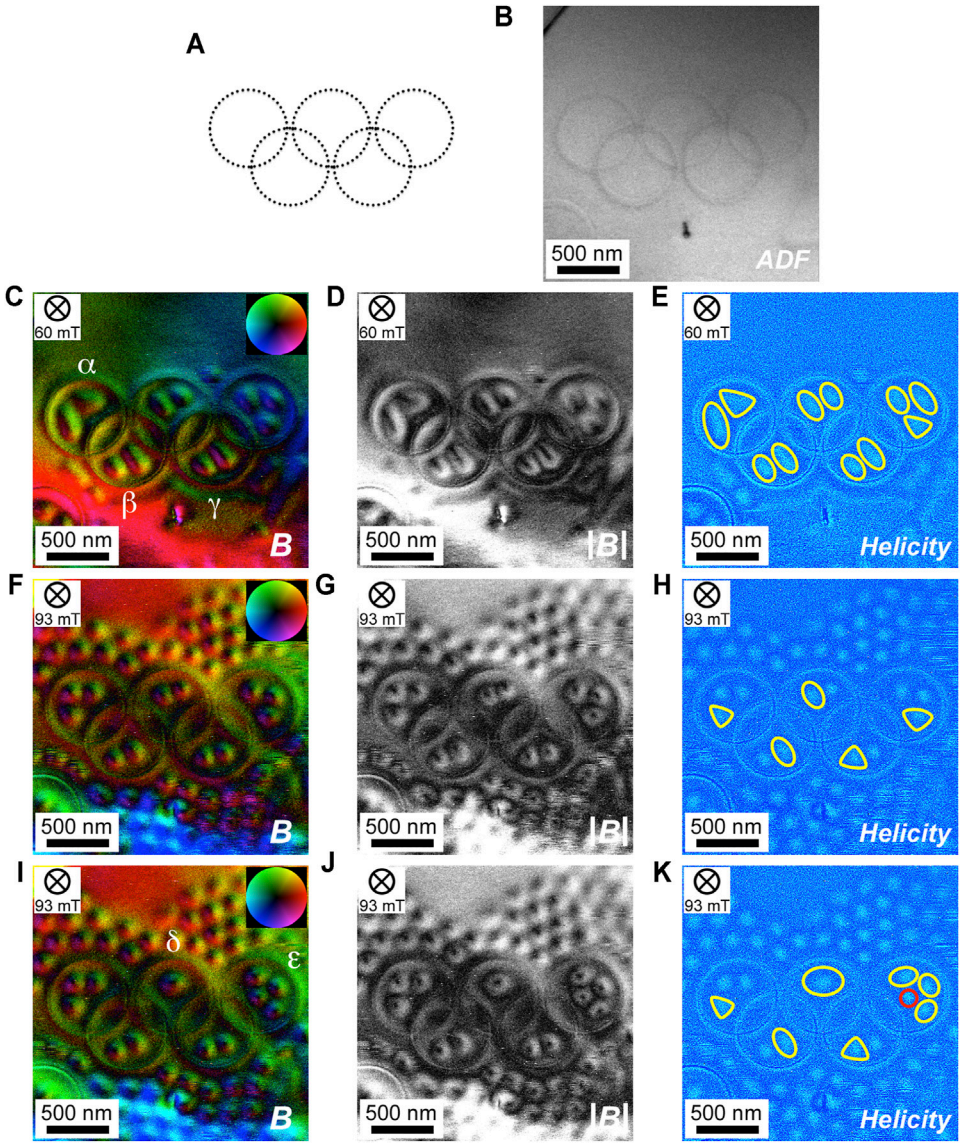

FIGURE 4 | Individual skyrmions confined to a surface-pit corral with a complex geometry (Olympic symbol) under moderate-bias fields. **(A)** A schematic of the five interlaced rings of equal dimensions (630 nm in diameter). **(B)** Annular dark-field image of the fabricated pattern on the thin-plate specimen. **(C–E)** Individual skyrmions under the perpendicular magnetic field of 60 mT. **(F–H)** Individual skyrmions under the perpendicular magnetic field of 93 mT. **(I–K)** Individual skyrmions under the perpendicular magnetic field of 93 mT with a slight change of the specimen orientation from the one shown in **(F–H)**. **(C,F,I)** In-plane magnetic induction as a color map, **(D,G,J)** as intensity, and **(E,H,K)** magnetic helicity image. Several deformed skyrmions, not only in shape but also in size, are indicated by yellow shapes in the magnetic helicity images in **(E,H,K)**. A compressed circular skyrmion is indicated by a red circle in **(K)**. Pixel dwell time is 1 ms.

elongation direction nearly aligned along the magnetic easy axis <100>, which is induced by the enhancement of magnetocrystalline anisotropy at the low temperature. Deformed skyrmions are also created at room temperature by geometric confinement as will be shown below.

Skyrmion States Confined to Surface-Pit Corrals with Simple Geometries

First, we briefly review skyrmion states confined to surface-pit corrals with three simple geometries—a square, a circle, and a triangle—as schematically shown in **Figures 2A,F,K** respectively. The ADF images of the fabricated corrals are shown in **Figures 2B,G,L**. The edge length of the square, diameter of the circle, and edge length of the equilateral triangle are equally 440 nm. Here only helicity images are shown because the reconstructed in-plane magnetic induction maps are severely disturbed by diffraction contrast (data not shown). We obtained images in the zero-field condition several times, which resulted in slightly different images. Zero-field 1 and zero-field 2 correspond to two independent experimental results. Note that the two states were not created as a result of any specific hysteresis loop as

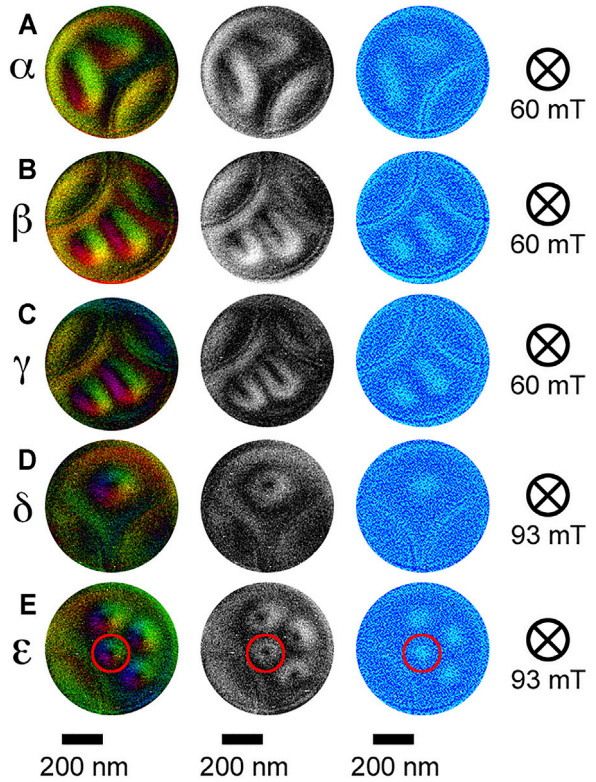

FIGURE 5 | Gallery of several deformed individual skyrmions arbitrarily extracted from **Figure 4**. From left to right, in-plane magnetic induction as a color map, in-plane magnetic induction as intensity, and magnetic helicity image are shown. **(A–E)** The confined areas as indicated by α-ε in the color maps correspond to the areas indicated in **Figures 4C,I**. A compressed circular skyrmion is indicated by a red circle in **(E)**.

described in a literature [54], but their difference was entirely due to randomness. For the square corral, two elongated skyrmions in two orthogonal (horizontal and vertical) directions can be seen in the two zero-field conditions (**Figures 2C,D**), while four circular skyrmions are created under the perpendicular magnetic field of 60 mT (**Figure 2E**). Inside the circular corral, on the other hand, strongly deformed spin textures are created in the zero-field condition (**Figures 2H,I**), which are consistent with the spin textures confined in a disk fabricated by conventional microfabrication technique reported in previous publications [20, 21]. Under the perpendicular magnetic field of 60 mT, three isolated circular skyrmions are created (**Figure 2J**). In contrast, inside the triangular corral, single isolated circular skyrmion is stabilized even in the zero-field condition (**Figures 2M,N**) as well as under the perpendicular magnetic field of 60 mT (**Figure 2O**). Since skyrmions are created by the superposition of helical spin textures propagating along multiple directions defined by q-vectors, these experimental results can be understood by considering the q-vectors defined by the boundaries as indicated by yellow arrows in **Figures 2B,G,L**. The triangular geometry is compatible with the triple-q mechanism [3] to create skyrmions. Triangular confinement of skyrmions attracted attention in several literatures, too [55, 56]. Note that, some 40 years ago, magnetic vortices stabilized in cobalt fine particles with several geometric shapes were studied by using electron holography technique in a pioneering work directed by Tonomura [57]. They reported that an isolated magnetic vortex is stabilized both in a triangular platelet with an edge length of 250 nm and in a hexagonal platelet with an edge length of 200 nm under zero-bias field. Single magnetic vortex was observed at the center of both fine particles owing to the influence of the complete physical edges.

Skyrmion States Confined to Surface-Pit Corrals with a Complex Geometry

Now, we show skyrmion states confined to surface-pit corrals with a complex geometry. **Figure 3** shows the confinement of skyrmions to surface-pit corrals with two nested curved boundaries (track and field) as schematically shown in **Figure 3A**. We fabricated two track and field corrals with two different sizes as shown in the ADF image (**Figure 3B**). The track width of the smaller corral and that of the larger corral are 420 and 630 nm, respectively. In the smaller (S) track and field corral, a linear chain and a curved chain of single skyrmions are created in the field area and track area, respectively (**Figures 3C–F**). In the larger (L) track and field, a small hexagonal array of skyrmions is created in the field area, while three strings of skyrmions are aligned in the track area (**Figures 3G–J**). Note that some skyrmions appear strongly elongated as indicated by the white arrows in **Figures 3I–L**, creating a domain boundary. Here we emphasize that skyrmions are aligned under the influence of surface-pit corrals working like physical edges with the complex geometry.

Skyrmion States Confined to Surface-Pit Corrals with a More Complex Geometry

Next, we demonstrate skyrmion states confined to surface-pit corrals with a more complex geometry—five interlaced rings of equal dimensions (Olympic symbol) as schematically shown in **Figure 4A**. **Figure 4B** shows the ADF image of the fabricated pattern on the thin-plate specimen. The diameter of each ring is 630 nm. **Figures 4C–E** show skyrmions confined to surface-pit corrals with the Olympic symbol geometry under the perpendicular magnetic field of 60 mT. Skyrmions are strongly deformed not only in shape but also in size as indicated by the yellow shapes in the magnetic helicity image (**Figure 4E**). Not only elongated skyrmions but also expanded skyrmions are observed. **Figures 4F–H** show skyrmions confined to surface-pit corrals with the Olympic symbol geometry under the perpendicular magnetic field of 93 mT. As the perpendicular magnetic field is increased, elliptical skyrmions transform into more circular ones, but with apparent deformations as indicated by the yellow shapes in the magnetic helicity image (**Figure 4H**). Note that the distribution of skyrmions is symmetric (3-2-2-2-3 from left to right). The numbers of skyrmions confined in the five defined regions are proportional to each area. After a slight change of the specimen orientations, however, the distribution of skyrmions under the same intensity of perpendicular magnetic field (93 mT) changes, as shown in **Figures 4I–K**. The numbers of skyrmions vary arbitrarily

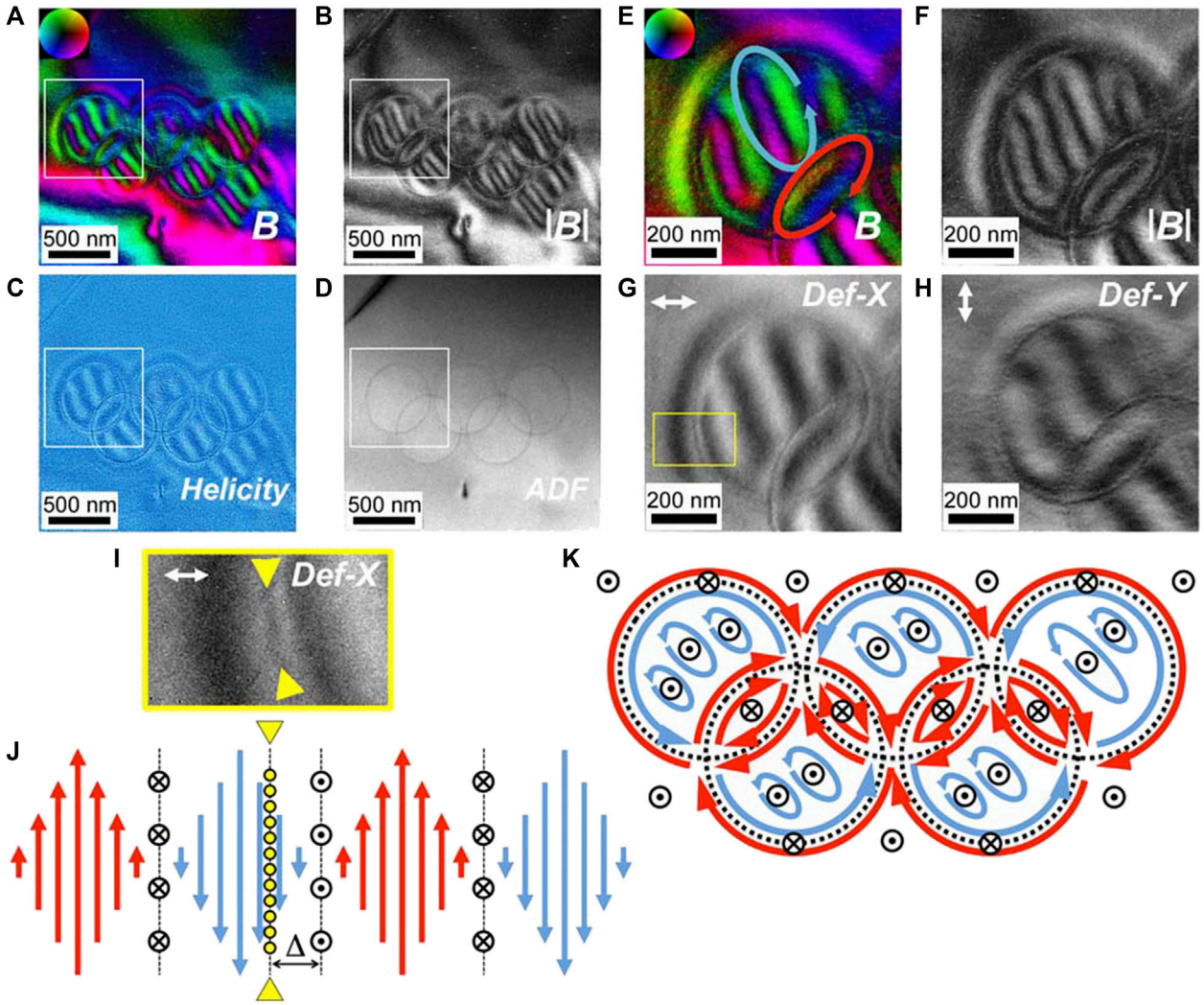

FIGURE 6 | Zero-field skyrmionic spin texture confined to a surface-pit corral with a complex geometry (Olympic symbol). **(A)** In-plane magnetic induction as a color map and **(B)** as intensity, **(E)** magnetic helicity image, and **(F)** annular dark-field (ADF) image of the whole pattern. The boxed region in **(A–D)** is observed at a higher magnification in **(C,D,G,H)**. Note that the horizontal and vertical deflection images are shown in **(G)** and **(H)**, respectively, instead of the magnetic helicity and ADF images. **(I)** The boxed area indicated by a yellow rectangle in **(G)** is enlarged. The surface-pit corral is indicated by a pair of yellow arrowheads. **(J)** Schematic of the left-handed helical spin texture corresponding to **(I)** across the surface-pit corral. The surface-pit corral is displayed as a yellow dotted line, which is indicated by a pair of yellow arrowheads. **(K)** A simplified schematic of the plausible skyrmionic spin texture confined in the Olympic symbol in zero-field condition. The target mark symbols and crossed circle symbols indicate upward and downward directions, respectively.

among the five separated regions (3-2-1-2-4 from left to right). The skyrmions are again strongly deformed not only in shape but also in size as indicated by the yellow shapes in the magnetic helicity image (**Figure 4K**). An apparently expanded skyrmion is observed in the confined area indicated as δ in **Figure 4I**. A compressed circular skyrmion is also observed as indicated by a red circle in **Figure 4K**. A gallery of several deformed individual skyrmions extracted from **Figure 4** is shown in **Figure 5**. Individual skyrmions can conform to the areas surrounded by complex boundaries, deforming into elliptical and triangular shapes with expansions (**Figure 5A**), long and short elliptical shapes (**Figures 5B,C**), an expanded elliptical shape (**Figure 5D**) as well as three short elliptical shapes and a compressed circular shape (**Figure 5E**). A rough estimate of the expansion of the skyrmion as shown in **Figure 5D** is larger than 25%. The compression of the smallest skyrmion as shown in **Figure 5E**, in contrast, is not so large (10%). Both elongation and compression of skyrmions were observed in a previous study investigating the domain boundary core formed in a SkL in a thin plate of $FeGe_{1-x}Si_x$ [35]. The ratio of compression was roughly estimated to be as small as 10%, while the ratio of elongation was as large as 60%. Furthermore, for the geometrically confined skyrmions to a triangular surface-pit corral [33] as shown in **Supplementary Figure S1**, the ratio of expansion is evaluated as 25%. More quantitative evaluations, however, should be necessary in future works. Additional demonstrations of

skyrmion states confined to surface-pit corrals with interlaced rings geometry are given in **Supplementary Figure S2**.

Zero-Field Skyrmionium Spin Textures Confined to Surface-Pit Corrals with the Olympic Symbol Geometry

Lastly, we demonstrate spin textures confined to surface-pit corrals with the Olympic symbol geometry in the zero-field condition. In-plane magnetic induction reconstructed from DPC STEM signals is shown as a color map in **Figure 6A** and as intensity in **Figure 6B**. **Figures 6C,D**, show the magnetic helicity image and ADF image, respectively. The color map at a low magnification (**Figure 6A**) is severely disturbed by diffraction contrast. The boxed region in **Figures 6A–D** is observed at a higher magnification in **Figures 6E–H**. Here horizontal and vertical deflection images are shown in **Figures 6G,H**, respectively, instead of magnetic helicity and ADF images. The color map at a higher magnification (**Figure 6E**) is not so disturbed by diffraction contrast. Note that spin textures appearing as elliptical skyrmions with opposite circularities (and hence opposite polarities) coexist as indicated by a blue oval arrow rotating CCW and a red oval arrow rotating CW in **Figure 6E**. The yellow-boxed region of the horizontal deflection image (**Figure 6G**) is enlarged as shown in **Figure 6I**. The corresponding left-handed helical spin texture is schematically shown in **Figure 6J**. Note that the position of the surface-pit corral is slightly shifted from the domain boundary (indicated by target mark symbols), which suggests that the connection between the spin texture and surface-pit corral is loosely (softly) coupled rather than the tightly (hardly) coupled connection between the spin texture and complete physical edge in conventional microfabrication techniques. It should be possible to control the connection between loose (soft) and tight (hard) by adjusting the physical parameters of surface pits, such as diameter, depth, and interdistance. The plausible skyrmionic spin textures confined to the surface-pit corral with Olympic symbol geometry are schematically shown in **Figure 6K**. Such a polarity reversal of skyrmionium spin textures in a microfabricated nanodisk was also reported in a previous literature [21]. We emphasize that the polarity reversal is only possible under a very weak perpendicular magnetic field (~20 mT). It is not clear whether the skyrmionic spin textures are actually skyrmions with opposite polarities or not. To confirm, we must check that the stray field directions at the centers of skyrmionic spin textures are actually reversed by using other experimental techniques, such as MFM, because the DPC STEM technique is not sensitive to perpendicular magnetic field (parallel with the incident electron beam).

CONCLUSION

In conclusion, we have investigated spin textures confined to surface-pit corrals with complex geometries by using the DPC STEM technique. We have found that individual skyrmions are aligned with elongation under the influence of the complex boundary defined by the surface-pit corrals. In addition, we have found that individual skyrmions are deformed not only in shape (elongation) but also in size (both expansion and compression) as influenced by the complex boundaries under a moderate-bias field. Furthermore, we have found that deformed skyrmionic spin textures with opposite polarities may coexist in zero-field condition. It is suggested that the connection between the spin texture and surface-pit corral is loosely (softly) coupled rather than the tightly (hardly) coupled connection found between the spin texture and complete physical edge in conventional microfabrication techniques. It should be possible to control the connection between loose (soft) and tight (hard) by adjusting the physical parameters of surface pits, such as diameter, depth, and interdistance. We hope that our experimental observations stimulate theoretical and micro-magnetic simulation studies on the controlled deformation of skyrmions. We also hope that the present study provides a guidance to arrange skyrmions with controlled swirling parameters, which should be explored for future applications.

DATA AVAILABILITY STATEMENT

The original contributions presented in the study are included in the article/**Supplementary Material**. Further inquiries can be directed to the corresponding author.

AUTHOR CONTRIBUTIONS

TM designed and conducted the TEM/STEM experiments, processed the images, and wrote the manuscript. NS developed the aberration-corrected DPC STEM system, directed the study, and read and commented on the manuscript.

FUNDING

A part of this work was supported by the Japan Science and Technology Agency SENTAN grant number JPMJSN14A1. A part of this work was conducted at the Research Hub for Advanced Nano Characterization, The University of Tokyo, supported under "Nanotechnology Platform" (project no. 12024046) sponsored by MEXT, Japan. TM and NS acknowledge support from the JSPS KAKENHI grant number 20H05659. NS acknowledges support from the JSPS KAKENHI grant number 19H05788.

ACKNOWLEDGMENTS

The authors acknowledge M. Nakabayashi at The University of Tokyo for her help in the thin plate preparation. We thank Dr. Y.

Kohno and Dr. H. Sawada at JEOL, Ltd., for their assistance in DPC STEM. We thank Prof. Yeong-Gi So at Akita University for preparing the bulk crystal of $Co_8Zn_8Mn_4$. Lastly, we acknowledge Prof. Y. Ikuhara at The University of Tokyo for his support and assistance throughout the study.

REFERENCES

1. Skyrme THR. A Unified Field Theory of Mesons and Baryons. *Nucl Phys* (1962) 31:556–69. doi:10.1016/0029-5582(62)90775-7
2. Rößler UK, Bogdanov AN, Pfleiderer C. Spontaneous Skyrmion Ground States in Magnetic Metals. *Nature* (2006) 442:797–801. doi:10.1038/nature05056
3. Muhlbauer S, Binz B, Jonietz F, Pfleiderer C, Rosch A, Neubauer A, et al. Skyrmion Lattice in a Chiral Magnet. *Science* (2009) 323:915–9. doi:10.1126/science.1166767
4. Münzer W, Neubauer A, Adams T, Mühlbauer S, Franz C, Jonietz F, et al. Skyrmion Lattice in the Doped semiconductorFe1−xCoxSi. *Phys Rev B* (2010) 81:041203. doi:10.1103/PhysRevB.81.041203
5. Yu XZ, Onose Y, Kanazawa N, Park JH, Han JH, Matsui Y, et al. Real-space Observation of a Two-Dimensional Skyrmion crystal. *Nature* (2010) 465:901–4. doi:10.1038/nature09124
6. Dzyaloshinsky I. A Thermodynamic Theory of "weak" Ferromagnetism of Antiferromagnetics. *J Phys Chem Sol* (1958) 4:241–55. doi:10.1016/0022-3697(58)90076-3
7. Moriya T. Anisotropic Superexchange Interaction and Weak Ferromagnetism. *Phys Rev* (1960) 120:91–8. doi:10.1103/PhysRev.120.91
8. Nagaosa N, Tokura Y. Topological Properties and Dynamics of Magnetic Skyrmions. *Nat Nanotech* (2013) 8:899–911. doi:10.1038/nnano.2013.243
9. Fert A, Cros V, Sampaio J. Skyrmions on the Track. *Nat Nanotech* (2013) 8:152–6. doi:10.1038/nnano.2013.29
10. Albrecht TR, Arora H, Ayanoor-Vitikkate V, Beaujour J-M, Bedau D, Berman D, et al. Bit-Patterned Magnetic Recording: Theory, Media Fabrication, and Recording Performance. *IEEE Trans Magn* (2015) 51–42. doi:10.1109/TMAG.2015.2397880
11. Rohart S, Thiaville A. Skyrmion Confinement in Ultrathin Film Nanostructures in the Presence of Dzyaloshinskii-Moriya Interaction. *Phys Rev B* (2013) 88:184422. doi:10.1103/PhysRevB.88.184422
12. Leonov AO, Rößler UK, Mostovoy M. Target-skyrmions and Skyrmion Clusters in Nanowires of Chiral Magnets. *EPJ Web of Conferences* (2014) 75:05002. doi:10.1051/epjconf/20147505002
13. Liu Y, Xuan S, Jia M, Yan H. Polarity Control of a Skyrmion in a Helimagnet Nanodisk by Fixing Magnetization at the Boundary. *J Phys D: Appl Phys* (2017) 50:48LT01. doi:10.1088/1361-6463/aa920a
14. Göbel B, Henk J, Mertig I. Forming Individual Magnetic Biskyrmions by Merging Two Skyrmions in a Centrosymmetric Nanodisk. *Sci Rep* (2019) 9:9521. doi:10.1038/s41598-019-45965-8
15. Li H, Akosa CA, Yan P, Wang Y, Cheng Z. Stabilization of Skyrmions in a Nanodisk without an External Magnetic Field. *Phys Rev Appl* (2020) 13:034046. doi:10.1103/PhysRevApplied.13.034046
16. Iwasaki J, Mochizuki M, Nagaosa N. Universal Current-Velocity Relation of Skyrmion Motion in Chiral Magnets. *Nat Commun* (2013) 4:1463. doi:10.1038/ncomms2442
17. Zhang SS-L, Phatak C, Petford-Long AK, Heinonen OG. Tailoring Magnetic Skyrmions by Geometric Confinement of Magnetic Structures. *Appl Phys Lett* (2017) 111:242405. doi:10.1063/1.5005904
18. Du H, Ning W, Tian M, Zhang Y. Magnetic Vortex with Skyrmionic Core in a Thin Nanodisk of Chiral Magnets. *Epl* (2013) 101:37001. doi:10.1209/0295-5075/101/37001
19. Beg M, Carey R, Wang W, Cortés-Ortuño D, Vousden M, Bisotti M-A, et al. Ground State Search, Hysteretic Behaviour and Reversal Mechanism of Skyrmionic Textures in Confined Helimagnetic Nanostructures. *Sci Rep* (2015) 5:17137. doi:10.1038/srep17137
20. Zhao X, Jin C, Wang C, Du H, Zang J, Tian M, et al. Direct Imaging of Magnetic Field-Driven Transitions of Skyrmion Cluster States in FeGe Nanodisks. *Proc Natl Acad Sci USA* (2016) 113:4918–23. doi:10.1073/pnas.1600197113
21. Zheng F, Li H, Wang S, Song D, Jin C, Wei W, et al. Direct Imaging of a Zero-Field Target Skyrmion and its Polarity Switch in a Chiral Magnetic Nanodisk. *Phys Rev Lett* (2017) 119:197205. doi:10.1103/PhysRevLett.119.197205
22. Cortés-Ortuño D, Romming N, Beg M, von Bergmann K, Kubetzka A, Hovorka O, et al. Nanoscale Magnetic Skyrmions and Target States in Confined Geometries. *Phys Rev B* (2019) 99:214408. doi:10.1103/PhysRevB.99.214408
23. Du H, Che R, Kong L, Zhao X, Jin C, Wang C, et al. Edge-mediated Skyrmion Chain and its Collective Dynamics in a Confined Geometry. *Nat Commun* (2015) 6:8504. doi:10.1038/ncomms9504
24. Jin C, Li Z-A, Kovács A, Caron J, Zheng F, Rybakov FN, et al. Control of Morphology and Formation of Highly Geometrically Confined Magnetic Skyrmions. *Nat Commun* (2017) 8:15569. doi:10.1038/ncomms15569
25. Hou Z, Zhang Q, Xu G, Gong C, Ding B, Wang Y, et al. Creation of Single Chain of Nanoscale Skyrmion Bubbles with Record-High Temperature Stability in a Geometrically Confined Nanostripe. *Nano Lett* (2018) 18:1274–9. doi:10.1021/acs.nanolett.7b04900
26. Birch MT, Cortés-Ortuño D, Turnbull LA, Wilson MN, Groß F, Träger N, et al. Real-space Imaging of Confined Magnetic Skyrmion Tubes. *Nat Commun* (2020) 11:1726. doi:10.1038/s41467-020-15474-8
27. Qin G, Wang Y, Pei K, Zhang R, Zhang C, Luo Y, et al. Skyrmion Bubbles Stabilization in Confined Hole and Trench Materials. *Appl Phys Lett* (2020) 117:052405. doi:10.1063/5.0013257
28. Bagués N, Esser BD, Ahmed AS, Rowland J, Yan J-Q, Huber DE, et al. *In Situ* Lorentz Electron Microscopy Imaging of Skyrmions in Geometric Confined Structures. *Microsc Microanal* (2019) 25(Suppl. 2):34–5. doi:10.1017/S1431927619000904
29. Juge R, Bairagi K, Rana KG, Vogel J, Sall M, Mailly D, et al. Helium Ions Put Magnetic Skyrmions on the Track. *Nano Lett* (2021) 21:2989–96. doi:10.1021/acs.nanolett.1c00136
30. Ohara K, Zhang X, Chen Y, Wei Z, Ma Y, Xia J, et al. Confinement and Protection of Skyrmions by Patterns of Modified Magnetic Properties. *Nano Lett* (2021) 21:4320–6. doi:10.1021/acs.nanolett.1c00865
31. Zhang S, Zhang J, Zhang Q, Barton C, Neu V, Zhao Y, et al. Direct Writing of Room Temperature and Zero Field Skyrmion Lattices by a Scanning Local Magnetic Field. *Appl Phys Lett* (2018) 112:132405. doi:10.1063/1.5021172
32. Ognev AV, Kolesnikov AG, Kim YJ, Cha IH, Sadovnikov AV, Nikitov SA, et al. Magnetic Direct-Write Skyrmion Nanolithography. *ACS Nano* (2020) 14:14960–70. doi:10.1021/acsnano.0c04748
33. Matsumoto T, So Y-G, Kohno Y, Ikuhara Y, Shibata N. Stable Magnetic Skyrmion States at Room Temperature Confined to Corrals of Artificial Surface Pits Fabricated by a Focused Electron Beam. *Nano Lett* (2018) 18:754–62. doi:10.1021/acs.nanolett.7b03967
34. Shibata K, Iwasaki J, Kanazawa N, Aizawa S, Tanigaki T, Shirai M, et al. Large Anisotropic Deformation of Skyrmions in Strained crystal. *Nat Nanotech* (2015) 10:589–92. doi:10.1038/nnano.2015.113
35. Matsumoto T, So Y-G, Kohno Y, Sawada H, Ikuhara Y, Shibata N. Direct Observation of Σ7 Domain Boundary Core Structure in Magnetic Skyrmion Lattice. *Sci Adv* (2016) 2:e1501280. doi:10.1126/sciadv.1501280
36. Rendell-Bhatti F, Lamb RJ, van der Jagt JW, Paterson GW, Swagten HJM, McGrouther D. Spontaneous Creation and Annihilation Dynamics and Strain-Limited Stability of Magnetic Skyrmions. *Nat Commun* (2020) 11:3536. doi:10.1038/s41467-020-17338-7
37. Psaroudaki C, Panagopoulos C. Skyrmion Qubits: A New Class of Quantum Logic Elements Based on Nanoscale Magnetization. *Phys Rev Lett* (2021) 127:067201. doi:10.1103/PhysRevLett.127.067201
38. Kammerer M, Weigand M, Curcic M, Noske M, Sproll M, Vansteenkiste A, et al. Magnetic Vortex Core Reversal by Excitation of Spin Waves. *Nat Commun* (2011) 2:279. doi:10.1038/ncomms1277

SUPPLEMENTARY MATERIAL

The Supplementary Material for this article can be found online at: https://www.frontiersin.org/articles/10.3389/fphy.2021.774951/full#supplementary-material

39. Grigoriev SV, Chernyshov D, Dyadkin VA, Dmitriev V, Maleyev SV, Moskvin EV, et al. Crystal Handedness and Spin Helix Chirality inFe1−xCoxSi. *Phys Rev Lett* (2009) 102:037204. doi:10.1103/PhysRevLett.102.037204
40. Grigoriev SV, Chernyshov D, Dyadkin VA, Dmitriev V, Moskvin EV, Lamago D, et al. Interplay between Crystalline Chirality and Magnetic Structure inMn1−xFexSi. *Phys Rev B* (2010) 81:012408. doi:10.1103/PhysRevB.81.012408
41. Yu XZ, Shibata K, Koshibae W, Tokunaga Y, Kaneko Y, Nagai T, et al. Thermally Activated Helicity Reversals of Skyrmions. *Phys Rev B* (2016) 93:134417. doi:10.1103/PhysRevB.93.134417
42. Shibata K, Yu XZ, Hara T, Morikawa D, Kanazawa N, Kimoto K, et al. Towards Control of the Size and Helicity of Skyrmions in Helimagnetic Alloys by Spin-Orbit Coupling. *Nat Nanotech* (2013) 8:723–8. doi:10.1038/nnano.2013.174
43. Heo C, Kiselev NS, Nandy AK, Blügel S, Rasing T. Switching of Chiral Magnetic Skyrmions by Picosecond Magnetic Field Pulses via Transient Topological States. *Sci Rep* (2016) 6:27146. doi:10.1038/srep27146
44. Tonomura A, Yu X, Yanagisawa K, Matsuda T, Onose Y, Kanazawa N, et al. Real-space Observation of Skyrmion Lattice in Helimagnet MnSi Thin Samples. *Nano Lett* (2012) 12:1673–7. doi:10.1021/nl300073m
45. Park HS, Yu X, Aizawa S, Tanigaki T, Akashi T, Takahashi Y, et al. Observation of the Magnetic Flux and Three-Dimensional Structure of Skyrmion Lattices by Electron Holography. *Nat Nanotech* (2014) 9:337–42. doi:10.1038/nnano.2014.52
46. Li Z-A, Zheng F, Tavabi AH, Caron J, Jin C, Du H, et al. Magnetic Skyrmion Formation at Lattice Defects and Grain Boundaries Studied by Quantitative off-Axis Electron Holography. *Nano Lett* (2017) 17:1395–401. doi:10.1021/acs.nanolett.6b04280
47. McGrouther D, Lamb RJ, Krajnak M, McFadzean S, McVitie S, Stamps RL, et al. Internal Structure of Hexagonal Skyrmion Lattices in Cubic Helimagnets. *New J Phys* (2016) 18:095004. doi:10.1088/1367-2630/18/9/095004
48. Matsumoto T, So Y-G, Kohno Y, Sawada H, Ishikawa R, Ikuhara Y, et al. Jointed Magnetic Skyrmion Lattices at a Small-Angle Grain Boundary Directly Visualized by Advanced Electron Microscopy. *Sci Rep* (2016) 6:35880. doi:10.1038/srep35880
49. Matsumoto T, So Y-G, Ikuhara Y, Shibata N. Direct Visualization of Nucleation Intermediate State of Magnetic Skyrmion from Helical Stripes Assisted by Artificial Surface Pits. *J Magnetism Magn Mater* (2021) 531:167976. doi:10.1016/j.jmmm.2021.167976
50. Shibata N, Findlay SD, Matsumoto T, Kohno Y, Seki T, Sánchez-Santolino G, et al. Direct Visualization of Local Electromagnetic Field Structures by Scanning Transmission Electron Microscopy. *Acc Chem Res* (2017) 50:1502–12. doi:10.1021/acs.accounts.7b00123
51. Shibata N, Kohno Y, Findlay SD, Sawada H, Kondo Y, Ikuhara Y. New Area Detector for Atomic-Resolution Scanning Transmission Electron Microscopy. *J Electron Microsc* (2010) 59:473–9. doi:10.1093/jmicro/dfq014
52. Karube K, White JS, Reynolds N, Gavilano JL, Oike H, Kikkawa A, et al. Robust Metastable Skyrmions and Their Triangular-Square Lattice Structural Transition in a High-Temperature Chiral Magnet. *Nat Mater* (2016) 15:1237–42. doi:10.1038/nmat4752
53. Morikawa D, Yu X, Karube K, Tokunaga Y, Taguchi Y, Arima T-h., et al. Deformation of Topologically-Protected Supercooled Skyrmions in a Thin Plate of Chiral Magnet Co8Zn8Mn4. *Nano Lett* (2017) 17:1637–41. doi:10.1021/acs.nanolett.6b04821
54. Carey R, Beg M, Albert M, Bisotti M-A, Cortés-Ortuño D, Vousden M, et al. Hysteresis of Nanocylinders with Dzyaloshinskii-Moriya Interaction. *Appl Phys Lett* (2016) 109:122401. doi:10.1063/1.4962726
55. Hagemeister J, Iaia D, Vedmedenko EY, von Bergmann K, Kubetzka A, Wiesendanger R. Skyrmions at the Edge: Confinement Effects in Fe/Ir(111). *Phys Rev Lett* (2016) 117:207202. doi:10.1103/PhysRevLett.117.207202
56. Pepper RA, Beg M, Cortés-Ortuño D, Kluyver T, Bisotti M-A, Carey R, et al. Skyrmion States in Thin Confined Polygonal Nanostructures. *J Appl Phys* (2018) 123:093903. doi:10.1063/1.5022567
57. Tonomura A. Applications of Electron Holography. *Rev Mod Phys* (1987) 59:639–69. doi:10.1103/RevModPhys.59.639

Conflict of Interest: The authors declare that the research was conducted in the absence of any commercial or financial relationships that could be construed as a potential conflict of interest.

Publisher's Note: All claims expressed in this article are solely those of the authors and do not necessarily represent those of their affiliated organizations or those of the publisher, the editors, and the reviewers. Any product that may be evaluated in this article or claim that may be made by its manufacturer is not guaranteed or endorsed by the publisher.

frontiers in Physics

PERSPECTIVE
published: 16 February 2022
doi: 10.3389/fphy.2022.769904

From Thermodynamics to Information: Landauer's Limit and Negentropy Principle Applied to Magnetic Skyrmions

Roberto Zivieri *

National Institute of High Mathematics, Rome, Italy

Magnetic skyrmions are topological swirling spin textures objects that can be manipulated and employed as information carriers. This is accomplished based either on their ground-state properties or their thermodynamic properties. Landauer's principle establishes an irreversible conversion from information to physics. The inverse mechanism, the inverse mechanism is proposed for magnetic topological defects forming in magnetic nanostructures that are regarded as closed thermodynamic systems confirming Szilard's and Brillouin's hypotheses. This mechanism consists of the creation of bits of information using a thermodynamic source having a form of negentropy. In this perspective article, the following are proved for magnetic skyrmions: 1) Landauer's principle expressed in terms of negentropy and 2) the generalized second principle of thermodynamics based on Brillouin's negentropy principle of information. The thermodynamic entropy is converted into information entropy at the expense of negentropy, "negative entropy" corresponding to the loss of thermodynamic entropy from the magnetic skyrmion itself. A recently proposed practical device enables the verification of points 1) and 2) and allows a full understanding of the interchange between thermodynamics and information and vice versa regarding skyrmions as information units and showing, in perspective, the considerable advantages offered by this type of storing and coding information.

Keywords: magnetic skyrmion, information and thermodynamics, Landauer's limit, Landauer's principle, Brillouin's negentropy, generalized second principle of thermodynamics, information unit, bits

OPEN ACCESS

Edited by:
Huaiyang Yuan,
Utrecht University, Netherlands

Reviewed by:
Xiangrong Wang,
Hong Kong University of Science and Technology, Hong Kong SAR, China
Fatima Sayed,
Lebanese University, Lebanon

***Correspondence:**
Roberto Zivieri
roberto.zivieri@unife.it

Specialty section:
This article was submitted to Condensed Matter Physics, a section of the journal Frontiers in Physics

Received: *02 September 2021*
Accepted: *05 January 2022*
Published: *16 February 2022*

Citation:
Zivieri R (2022) From Thermodynamics to Information: Landauer's Limit and Negentropy Principle Applied to Magnetic Skyrmions. Front. Phys. 10:769904. doi: 10.3389/fphy.2022.769904

INTRODUCTION

Magnetic skyrmions are axisymmetric topological solitons of vortex-like character hosted in ferromagnetic materials. Generally, they are stabilized by an exchange interaction of relativistic nature called Dzyaloshinskii–Moriya interaction (DMI) [1, 2]. Magnetic skyrmions are characterized by 1) a skyrmion number S (otherwise called the topological charge), an integer that indicates how many times magnetic moments within a skyrmion wrap a sphere; 2) helicity number, the phase appearing in the in-plane spin texture; and 3) a fixed rotation fashion called chirality χ. The skyrmion number is expressed as $S = 1/(4\pi) \int d^2\boldsymbol{\rho}\, \mathbf{m}\cdot(\partial\mathbf{m}/\partial x \times \partial\mathbf{m}/\partial y)$ where $\mathbf{m}(\boldsymbol{\rho}) = \mathbf{M}(\boldsymbol{\rho})/M_s$ is the dimensionless magnetization vector with $\mathbf{M}$ representing the magnetization, $\boldsymbol{\rho} = (x, y)$ the in-plane coordinates, M_s representing the saturation magnetization, and $\partial/\partial x$ and $\partial/\partial y$ are first partial derivatives.

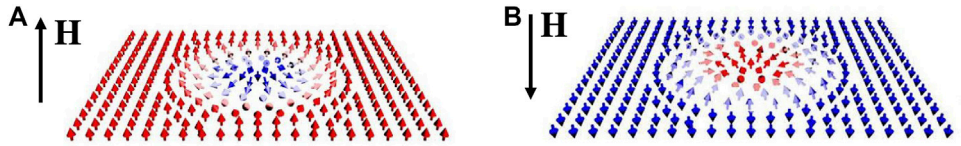

FIGURE 1 | Pictorial representation of a Néel magnetic skyrmion in two magnetization textures. **(A)** Perpendicularly magnetized ferromagnet hosting an outwardly (chirality $\chi = +1$) Néel magnetic skyrmion with polarity $p = -1$. **(B)** Perpendicularly magnetized ferromagnet hosting an inwardly (chirality $\chi = -1$) Néel magnetic skyrmion with polarity $p = +1$. **H** lies along the z-axis [positive direction in **(A)** and negative direction in **(B)**].

Recently, great efforts have been devoted to the manipulation of magnetic skyrmions forming in magnetic nanostructures based on their ground-state magnetic properties and giving rise to spintronic applications [1–4]. Very recently, magnetic skyrmions have been employed as qubits, a new class of quantum logic elements [5]. It has also been proposed the employment of magnetic skyrmions as information entropy carriers suggesting a data communication system based on the coding of information entropy [6]. This investigation stemmed from the theoretical and numerical exploration of the thermodynamic properties of magnetic skyrmions [7–10]. In this respect, the link between the physical and information entropies has been a subject matter of several studies [11–15]. On the other hand, the concept of negentropy was introduced first by Szilard who solved Maxwell's demon paradox [16, 17], and then by Brillouin [18–23] who continued Szilard's and Shannon's investigations. After the discovery and formulation of Landauer's principle [24–27], in recent decades, great efforts were made for the full understanding of information erasure and its relation with thermodynamics and logical computation from a philosophical, theoretical, and experimental viewpoints [28–47].

In this perspective article, this kind of investigation was applied to magnetic skyrmions. The aim of this study was threefold: 1) to show that Landauer's limit is expressed in terms of variation of negentropy for a Néel skyrmion; 2) to show that the generalized second principle of thermodynamics based on Brillouin's negentropy principle can be applied to a Néel skyrmion; and 3) to explain the interplay between information and negentropy and vice versa of a Néel skyrmion [6, 8]. This discussion could open the route in prospect for a new way of storing and coding information by using magnetic topological defects.

NEGENTROPY AND LANDAUER'S LIMIT FOR A MAGNETIC SKYRMION

A Néel skyrmion (or hedgehog skyrmion) forming in magnetic nanostructures as a result of the interfacial DMI is characterized by the magnetization texture $\mathbf{m} = \chi \sin\theta\,\hat{\rho} + \cos\theta\,\hat{z}$ in a cylindrical reference frame (ρ, φ, z) where $\chi = \pm 1$ is the chirality (+1 outwardly magnetization, −1 inwardly magnetization), and θ is the polar angle with $0 \le \theta \le \pi$. **Figure 1A** shows an outwardly Néel skyrmion ($\chi = +1$) with a negative polarity ($\theta = \pi$) and skyrmion number $S = -1$ subjected to an external magnetic field **H** along the $+ z$ direction, while **Figure 1B** displays an inwardly Néel skyrmion ($\chi = -1$) with a positive polarity ($\theta = 0$) and skyrmion number $S = +1$ subjected to an external magnetic field **H** along the $- z$ direction. In the following discussion, the Néel skyrmion texture shown in **Figure 1A** was taken into account to be consistent with the results of micromagnetic simulations carried out on a Néel skyrmion with $\chi = +1$, negative polarity, and $S = -1$ [7]. However, note that this choice is purely arbitrary and the same conclusion would be drawn taking into account the Néel skyrmion with $\chi = -1$, a positive polarity, and $S = +1$.

The skyrmion energy was calculated from the microscopic micromagnetic Hamiltonian as a spatial integral of the skyrmion energy density within the thin-film limit including exchange, interfacial DMI, magnetostatic and perpendicular anisotropy contributions, and external magnetic field interaction [7–9]. Within this model, the exchange interaction among spins forming the magnetic skyrmion was rigorously taken into account. It was found that, in the vicinity of the absolute energy minimum at the equilibrium skyrmion diameter $D_{0\mathrm{sky}}$, the skyrmion energy can be fitted by means of a parabolic curve for any temperature T and bias field amplitude H in the region of skyrmion metastability ($0 \le T \le 300$ K for $\mu_0 H > 5$ mT and $0 \le T \le 200$ K for $\mu_0 H = 0$ mT) [7]. Importantly, $D_{0\mathrm{sky}}$ strictly depends on the parameters of the microscopic Hamiltonian. In this respect, the determination of the skyrmion size for an isolated skyrmion by computing the skyrmion radius (both equilibrium and average) has recently been proved according to different analytical theories based on the minimization of the skyrmion energy with respect to the skyrmion radius [9, 48, 49]. In particular, it has been shown that both the average skyrmion size and the wall width separating the core from the outer domain of the skyrmion can be accurately computed [48]. This investigation has been generalized by studying the magnetic skyrmion's size and spin profile in a condensed phase forming a skyrmion crystal at high skyrmion density [49]. In this latter case, it has been demonstrated that the dependence of skyrmion size on magnetic parameters is different compared to isolated skyrmions or to skyrmion stripes forming at low skyrmion density.

According to micromagnetic simulations, it was observed that the value of the Néel skyrmion diameters obeys a distribution analogous to Maxwell–Boltzmann (MB) of the molecules of an ideal gas at any T and for any H in the region of metastability [7]. Exploiting this physical analogy with ideal gases, an analytical MB distribution for a 3D skyrmion diameter population [7, 9] was proposed, and it was found an excellent agreement between the micromagnetic and the analytical results [7]. This analogy was

also extended to the 2D skyrmion diameter distribution [8]. From the analogy with the 3D MB distribution of an ideal gas, the Gaussian distribution at the thermodynamic equilibrium at a given T and H for both 3D and 2D skyrmion diameter distribution can be written in the form

$$f_0\left(D_{\mathrm{sky}}\right) = C_{\mathrm{av}} \quad e^{-\frac{a}{k_B T}\left(\Delta\langle D_{\mathrm{sky}}\rangle\right)^2}, \tag{1}$$

where C_{av} is the normalization constant (in m^{-2}), k_{B} is the Boltzmann constant, a is a coefficient proportional to the skyrmion energy curvature, $\Delta\langle D_{\mathrm{sky}}\rangle = D_{\mathrm{sky}} - \langle D_{\mathrm{sky}}\rangle$, D_{sky} the skyrmion diameter, and $\langle D_{\mathrm{sky}}\rangle$ the average skyrmion diameter with $\langle D_{\mathrm{sky}}\rangle = \langle D_{\mathrm{sky}}(T)\rangle$.

Owing to the mentioned analogy, it is useful to relate the diameter distribution depending on T and H to skyrmion's thermodynamic entropy as occurs for the thermodynamic entropy of an ideal gas. Regarding this, it is important to note that the main source of entropy for domains forming in ferromagnets is represented by spin waves (or magnons). Recently, it has been found that the source of entropy and free energy for a domain and a domain wall (DW) in a magnetic nanowire is due to thermally activated magnons [50]. In this system, it has been demonstrated that the larger domain wall entropy is due to the increase in the magnon density of states at low energy, and the driving force allowing DW propagation under a temperature gradient towards the hotter region is the thermodynamic entropy itself. Under this condition, the system evolves toward a state that lowers its free energy by exploiting DW's larger entropy [50]. The DW movement toward a hotter region driven by thermal gradients has also been proved in antiferromagnets and can be understood by means of the minimization of the free energy [51]. Also, the main source of the configurational entropy of a classical Néel magnetic skyrmion has been attributed to the thermal-breathing mode, a type of spin wave as observed in micromagnetic simulations [7].

The configurational entropy at thermodynamic equilibrium related to a classical Néel magnetic skyrmion diameter distribution was computed, at each T and H, as the Gibbs–Boltzmann's statistical thermodynamic entropy, a quantity proportional to the statistical average $H_0 = \langle \ln f_0 \rangle$, the Boltzmann order function at thermodynamic equilibrium, namely as $S = -k_{\mathrm{B}} H_0$ with $S = S(T)$ [7–9]. This entropy is the generalization of the Boltzmann entropy when the microstates of the statistical ensemble are not equiprobable. For a 2D skyrmion diameter population, after performing the statistical average H_0 within the continuous limit, it takes the form [8]

$$S = -k_B \pi \int_0^{\infty} dD_{\mathrm{sky}} D_{\mathrm{sky}} f_0\left(D_{\mathrm{sky}}\right) \ln\left(f_{01}\left(D_{\mathrm{sky}}\right)\right). \tag{2}$$

Here, $f_{01}(D_{\mathrm{sky}}) = f_0 \langle A_{\mathrm{sky}}\rangle$ with $\langle A_{\mathrm{sky}}\rangle \approx 1/4\ \pi \langle D_{\mathrm{sky}}\rangle^2$ the average skyrmion area and $S > 0$ (in J/K). The Gaussian distribution f_0 is the one that realizes the largest thermodynamic entropy according to the maximum entropy principle. In turn, $\langle D_{\mathrm{sky}}(T)\rangle \approx D_{0\mathrm{sky}} [1 + k_{\mathrm{B}} T/(2a\ D_{0\mathrm{sky}}{}^2)]$ with $D_{0\mathrm{sky}} = D_{0\mathrm{sky}}(T)$ defined as the diameter at which the total skyrmion energy attains its absolute minimum. In turn, the value of $D_{0\mathrm{sky}}$ strictly depends on the magnetic parameters appearing as coefficients in the micromagnetic Hamiltonian such as the exchange stiffness constant A, the interfacial Dzyaloshinskii–Moriya parameter D, the uniaxial perpendicular anisotropy constant K_{u}, and on the external magnetic field amplitude H. The statistical thermodynamic entropy is also referred to as thermal entropy [52, 53] and is an increasing monotonic function of T.

The information entropy (expressed in terms of the number of bits) was calculated according to Jaynes's information framework [11–15] and taking into account **Eq. 2**. The use of continuous variables was suggested by Jayne in [13, 14] and was applied to the definition of information entropy in the continuum case [15]. The information entropy (in bits) was determined as the 2D statistical average of the information content $I(D_{\mathrm{sky}}) = -\log_2(f_{01}(D_{\mathrm{sky}}))$ (2 is the logarithm basis) [6] and can be rewritten in the form

$$H_I = \pi \int_0^{\infty} dD_{\mathrm{sky}} D_{\mathrm{sky}} f_0\left(D_{\mathrm{sky}}\right) I\left(D_{\mathrm{sky}}\right), \tag{3}$$

with $H_I > 0$.

Landauer's limit is derived starting from the configurational entropy and the corresponding information entropy. To create bits of information, S must decrease passing from an initial temperature T_{i} to a final temperature T_{f} with $T_{\mathrm{f}} < T_{\mathrm{i}}$. Starting from **Eq. 1** and using some logarithm rules, the entropy variation $\Delta S = S(T = T_{\mathrm{f}}) - S(T = T_{\mathrm{i}})$ with $S(T = T_{\mathrm{f}}) < S(T = T_{\mathrm{i}})$ such that $\Delta S < 0$ can be written in a compact form as

$$\Delta S = k_B \pi \left[\int_0^{\infty} dD_{\mathrm{sky}} D_{\mathrm{sky}} \ln\left(\frac{f_{01}(T = T_{\mathrm{i}})^{f_0(T=T_{\mathrm{i}})}}{f_{01}(T = T_{\mathrm{f}})^{f_0(T=T_{\mathrm{f}})}} \right) \right], \tag{4}$$

where the dependence of f_{01} and f_0 on D_{sky} is omitted. Analogously, the variation of the information entropy coded by the magnetic skyrmion, $\Delta H_I = H_I(T = T_{\mathrm{f}}) - H_I(T = T_{\mathrm{i}})$ with $T_{\mathrm{f}} > T_{\mathrm{i}}$ (the temperature T_{f} appearing in H_I corresponds to the temperature T_{i} appearing in S and vice versa) and $H_I(T = T_{\mathrm{f}}) > H_I(T = T_{\mathrm{i}})$ such that $\Delta H_I > 0$ takes the form

$$\Delta H_I = \pi \left[\int_0^{\infty} dD_{\mathrm{sky}} D_{\mathrm{sky}} \log_2\left(\frac{f_{01}(T = T_{\mathrm{i}})^{f_0(T=T_{\mathrm{i}})}}{f_{01}(T = T_{\mathrm{f}})^{f_0(T=T_{\mathrm{f}})}} \right) \right]. \tag{5}$$

It is useful to introduce the corresponding thermodynamic variation of information entropy by defining $S_I = k_{\mathrm{B}} H_I$. By comparing **Eqs 4**, **5** and taking into account that $S_I = k_{\mathrm{B}} H_I$, Landauer's limit can be derived. Indeed, substituting $\ln(f_{01}) = \log_2(f_{01}) \ln 2$ in **Eq. 2** and comparing **Eq. 2** with **Eq. 3**, one gets, *via* $\Delta S_I = k_{\mathrm{B}} \Delta H_I$, $\Delta S = -\Delta S_I \ln 2$. The creation of 1 bit of information leads to a variation $\Delta H_I = 1$ bit and to an increment $\Delta S_I = k_{\mathrm{B}}$ (units of 1 bit) yielding

$$\Delta S = -k_B \ln 2. \tag{6}$$

Therefore, Landauer's limit corresponds to the lower limit of the entropy lost in an observation as a result of the creation of 1 bit. In the present case, the thermodynamic entropy was lowered to create 1 bit of information and the minimum energy,

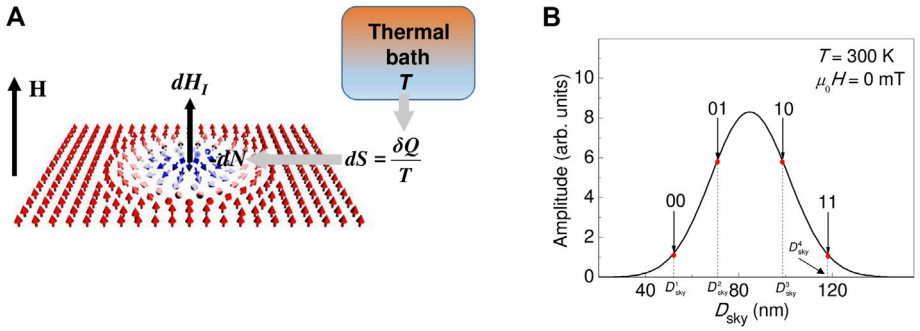

FIGURE 2 | (A) Sketch of the ferromagnetic nanostructure (film) hosting a Néel magnetic skyrmion (outwardly magnetized and negative $p = -1$) regarded as a closed thermodynamic system. The infinitesimal reversible exchange of entropy dS (δQ is the infinitesimal absorbed heat) between the thermal bath and the film at temperature T and between the film and the skyrmion is indicated. dN is the infinitesimal skyrmion negentropy, and dH_I is the infinitesimal information entropy. **(B)** The sampling of the skyrmions' diameter distribution at $T = 300$ K and $\mu_0 H = 0$ mT *via* the assignment of the 4-bit configurations 00, 01, 10, and 11 to the skyrmion diameters, $D_{sky}{}^1$, $D_{sky}{}^2$, $D_{sky}{}^3$, and $D_{sky}{}^4$, respectively. For the parameters used [6], $H_I \approx 2$ bits and the number of bit configurations is 4.

$$E = -k_B T \ln 2, \tag{7}$$

was subtracted from the system. The amount of energy is the minimal work $W = -k_B T \ln 2$ ($W < 0$) that must be extracted to create 1 bit of information, as established by Landauer's principle. This is a different case with respect to that was considered by Landauer for which the logical irreversibility implies the thermodynamic irreversibility. The information coding by a magnetic skyrmion can be regarded as a thermodynamically reversible process. By introducing the negentropy, the entropic equivalent of degradation of energy [18], namely $N = -S$ ($N < 0$ and $S > 0$) and $\Delta N = -\Delta S > 0$ being $\Delta N = N(T = T_f) - N(T = T_i)$, $N(T = T_f) < 0$ and $N(T = T_i) < 0$ but $N(T = T_f) > N(T = T_i)$ we get

$$\Delta N = k_B \ln 2. \tag{8}$$

Therefore, Landauer's limit can be regarded as the negentropy acquired by the system.

THE BRILLOUIN'S NEGENTROPY SECOND PRINCIPLE OF THERMODYNAMICS FOR A MAGNETIC SKYRMION

According to the second principle of thermodynamics, a magnetic system moves towards a state with a larger entropy or lower free energy [50]. The magnetic skyrmion's Helmholtz free energy, *viz.* $F = \langle E \rangle - T S$ with $\langle E \rangle = \langle E(T) \rangle$ the average skyrmion energy, in the absence of an external magnetic field, diminishes with increasing T and attains a minimum at the upper limit of the region of metastability at $T = 300$ K. With the magnetic parameters used (see the following section), $F \approx 5.5\ 10^{-20}$ J at $T = 150$ K [9] corresponds to 1 bit of information.

Here, the generalized second principle of thermodynamics for a closed thermodynamic system such as a magnetic skyrmion in terms of Brillouin's negentropy principle $\Delta S_{tot} = \Delta S - \Delta S_I \geq 0$ is discussed [18]. Therefore, the total entropy S_{tot} of a magnetic skyrmion does not decrease. In particular, $\Delta S_{tot} = S_{tot\ f} - S_{tot\ i}$ is the total entropy variation from the initial state i to the final state f, and $\Delta S = S_f - S_i > 0$ is the variation of the thermal entropy from the initial state to the final state (by the convention of an opposite sign with respect to that in **Eq. 4**), while $\Delta S_I = S_{If} - S_{Ii} > 0$ is the increment of information entropy in thermodynamic units owing to the creation of bits of information. By introducing the negentropy variation $\Delta N = -\Delta S < 0$, the generalized second principle of thermodynamics is expressed in terms of Brillouin's negentropy

$$\Delta (N + S_I) \leq 0. \tag{9}$$

Eq. 9 expresses thermodynamic reversibility when $\Delta(N + S_I) = 0$, *viz.* $\Delta N = -\Delta S_I$ but it does not state that physical reversibility necessarily implies logical reversibility.

NEW PERSPECTIVES IN INFORMATION THEORY: THE SKYRMION UNIT

In this section, new perspectives in information theory based on the use of the magnetic skyrmion as a unit of information entropy are outlined [6, 8].

The Role of the Sender and the Receiver in a Data Communication System

In a data communication system, it is crucial to understand how the information from the sender allows an amount of negentropy N to get converted into information entropy H_I. This occurs because the sender sends to the magnetic skyrmion a binary input of amplitude 2^n where n is the number of bits of information entropy. This binary input might be regarded in a way similar to a light input interacting with matter (e.g., a laser source), and this interaction with the skyrmion allows rewriting its thermodynamic configuration and its corresponding entropy. For example, for $n = 2$ bits, there are $g = 4$ binary configurations [6] that refer to an average skyrmion diameter $\langle D_{sky} \rangle$ and to the average entropy S according, for instance, to

the sampling: $00 \rightarrow {D_{\rm sky}}^1$, $01 \rightarrow {D_{\rm sky}}^2$, $10 \rightarrow {D_{\rm sky}}^3$, $11 \rightarrow {D_{\rm sky}}^4$ with ${D_{\rm sky}}^j$ (j = 1,2,3,4). This means that the jth binary configuration fixes the thermodynamic configuration corresponding to the jth entropy density $s(D_{\rm sky}^j) = -k_B f_0(D_{\rm sky}^j)\ln(f_{01}(D_{\rm sky}^j))$. This is accomplished by viewing the sender involved in a "writing" operation linking the jth binary configuration to the jth entropy density $s(D_{\rm sky}^j)$. The general effect of these subsequent reading operations is accounted in the calculation of a statistical average corresponding to S. The entropy cost of this operation is $\Delta N = -\Delta S < 0$ ($dN = -dS$), an entropy source employed as a reservoir for increasing the information entropy which causes a variation $\Delta S_I > 0$ ($dS_I > 0$) that, in bit units, is $\Delta H_I > 0$ ($dH_I > 0$) (see **Figure 2A**). If the process is reversible $\Delta N = -\Delta S_I$, while if it is irreversible $\Delta N < -\Delta S_I$ (**Eq. 9**). **Figure 2B** shows the binary–thermodynamic correspondence in terms of signal sampling for a 2D MB population of magnetic skyrmion diameters of the form $\frac{dn}{dD_{\rm sky}} = C_{\rm sky} D_{\rm sky} e^{-\frac{a}{k_B T}(D_{\rm sky} - D_{0\rm sky})^2}$ at T = 300 K and $\mu_0 H$ = 0 mT with $dn/dD_{\rm sky}$, the number of diameters ranging between $D_{\rm sky}$ and $D_{\rm sky} + dD_{\rm sky}$, $C_{\rm sky}$ the normalization constant (in m^{-2}). In the numerical calculations performed for ferromagnetic dot/heavy metal systems (e.g., Co/Pt), we employed the following geometric and magnetic parameters: dot radius R = 200 nm and Co thickness t = 0.8 nm, M_s (T = 0 K) = 6.0×10^5 A/m, A (T = 0 K) = 2.0×10^{-11} J/m, D (T = 0 K) = 3.0×10^{-6} J/m^2, and K_u (T = 0 K) = 0.6×10^6 J/m^3 [6–9, 54]. A, D, and K_u were scaled from their zero temperature values at non-zero temperature by using scaling laws [54]. For the parameters used, a = 0.71 × 10^{-5} J/m^2, $D_{0\rm sky}$ = 81.28 nm, and $n \approx 2$. The coded information is read by the receiver as a sequence of 4 binary configurations (00, 01, 10, 11), the binary interpretation of the negentropy resulting from the information entropy. The receiver consists of a binary sensor made by binary inputs enabling to read the discrete signal corresponding to a sequence of binary configurations assigned to a given entropy density. This coding has the considerable advantage to potentially create more bits for an equal number of skyrmions. The employment of 4 magnetic skyrmions heated at room temperature could lead to the coding of 1 byte of information which represents a unit of computer information and g = 256 binary configurations.

CONCLUSION

In this study, the interplay between thermodynamics and information occurring in easily manipulated magnetic skyrmions forming in magnetic nanostructures was discussed. It has been proved that Landauer's limit for a magnetic skyrmion can be expressed in terms of negentropy variation. It has been shown that the interchange between thermodynamic entropy and information entropy to create bits of information occurs by using a reservoir of negentropy that fulfills Brillouin's negentropy second principle of thermodynamics. This type of coding information based on the information entropy could be employed in prospect for improving data transmission.

DATA AVAILABILITY STATEMENT

The original contributions presented in the study are included in the article/Supplementary Material; further inquiries can be directed to the corresponding author.

AUTHOR CONTRIBUTIONS

RZ conceived the theme, developed the physical ideas, and suggested the applications based on the relation between thermodynamics and information for magnetic skyrmions.

ACKNOWLEDGMENTS

The author acknowledges support from Gruppo Nazionale per la Fisica Matematica (GNFM) and Istituto Nazionale di Alta Matematica (INdAM) "F. Severi."

REFERENCES

1. Fert A, Cros V, Sampaio J. Skyrmions on the Track. *Nat Nanotech* (2013) 8: 152–6. doi:10.1038/nnano.2013.29
2. Fert A, Reyren N, Cros V. Magnetic Skyrmions: Advances in Physics and Potential Applications. *Nat Rev Mater* (2017) 2:17031. doi:10.1038/natrevmats.2017.31
3. Müller J. Magnetic Skyrmions on a Two-Lane Racetrack. *New J Phys* (2017) 19: 025002. doi:10.1088/1367-2630/aa5b55
4. Zhang X, Zhou Y, Mee Song K, Park T-E, Xia J, Ezawa M, et al. Skyrmion-electronics: Writing, Deleting, reading and Processing Magnetic Skyrmions toward Spintronic Applications. *J Phys Condens Matter* (2020) 32:143001. doi:10.1088/1361-648X/ab5488
5. Psaroudaki C, Panagopoulos C. Skyrmion Qubits: A New Class of Quantum Logic Elements Based on Nanoscale Magnetization. *Phys Rev Lett* (2021) 127:067201. doi:10.1103/PhysRevLett.127.0672010.1103/PhysRevLett.127.067201
6. Zivieri R. Magnetic Skyrmions as Information Entropy Carriers. *IEEE Trans Magn* (2022) 58:1500105. doi:10.1109/TMAG.2021.3092693
7. Zivieri R, Tomasello R, Chubykalo-Fesenko O, Tiberkevich V, Carpentieri M, Finocchio G. Configurational Entropy of Magnetic Skyrmions as an Ideal Gas. *Phys Rev B* (2019) 99:174440. doi:10.1103/PhysRevB.99.174440
8. Zivieri R. Statistical Properties and Configurational Entropy of a Two-Dimensional Néel Magnetic Skyrmions Population. *Appl Sci* (2020) 10:352. doi:10.3390/app10010352
9. Zivieri R. Statistical Thermodynamics of Chiral Skyrmions in a Ferromagnetic Material. *Materials* (2019) 12:3702. doi:10.3390/ma12223702
10. Zivieri R, Chubykalo-Fesenko O. Static Properties of Magnetic Skyrmions, Chapt. 6. In: G Finocchio C Panagopoulus, editors. *Magnetic Skyrmions and Their Applications*. Sawston: Woodhead Publishing Series in Electronic and Optical Materials (2021). p. 181–231. doi:10.1016/b978-0-12-820815-1.00010-9
11. Shannon CE. A Mathematical Theory of Communication. *Bell Syst Tech J* (1948) 27:379–423. doi:10.1002/j.1538-7305.1948.tb01338.x
12. Shannon CE, Weaver W. *The Mathematical Theory of Communication*. Urbana, IL, USA: University of Illinois Press (1949).
13. Jaynes ET. Information Theory and Statistical Mechanics. *Phys Rev* (1957) 106: 620–30. doi:10.1103/PhysRev.106.620
14. Jaynes ET. Information Theory and Statistical Mechanics. II. *Phys Rev* (1957) 108:171–90. doi:10.1103/physrev.108.171

15. Jaynes ET. Prior Probabilities. *IEEE Trans Syst Sci Cybern* (1968) 4:227. doi:10.1109/TSSC.1968.300117
16. Szilard L. über die Entropieverminderung in einem thermodynamischen System bei Eingriffen intelligenter Wesen. *Z Physik* (1929) 53:840–56. doi:10.1007/BF01341281
17. Szilard L. On the Decrease of Entropy in a Thermodynamic System by the Intervention of Intelligent Beings. *Syst Res* (1964) 9:301–10. doi:10.1002/bs.3830090402
18. Brillouin L. The Negentropy Principle of Information. *J Appl Phys* (1953) 24:1152–63. doi:10.1063/1.1721463
19. Brillouin L. Maxwell's Demon Cannot Operate: Information and Entropy. *IJournal Appl Phys* (1951) 22:334–7. doi:10.1063/1.1699951
20. Brillouin L. Physical Entropy and Information. II. *J Appl Phys* (1951) 22:338–43. doi:10.1063/1.1699952
21. Brillouin L. Information Theory and Most Efficient Codings for Communication or Memory Devices. *J Appl Phys* (1951) 22:1108–11. doi:10.1063/1.1700116
22. Brillouin L. Negentropy and Information in Telecommunications, Writing, and Reading. *J Appl Phys* (1954) 25:595–9. doi:10.1063/1.1721696
23. Brillouin L. *Science and Information Theory*. Cambridge, USA: Academic Press (1956).
24. Landauer R. Irreversibility and Heat Generation in the Computing Process. *IBM J Res Dev* (1961) 5:183–91. doi:10.1147/rd.53.0183
25. Landauer R. Information Is Physical. *Phys Today* (1991) 44:23–9. doi:10.1063/1.881299
26. Landauer R. Dissipation and Noise Immunity in Computation and Communication. *Nature* (1988) 335:779–84. doi:10.1038/335779a0
27. Landauer R. The Physical Nature of Information. *Phys Lett A* (1996) 217:188–93. doi:10.1016/0375-9601(96)00453-7
28. Bennett CH. Logical Reversibility of Computation. *IBM J Res Dev* (1973) 17:525–32. doi:10.1147/rd.176.0525
29. Bennett CH. The Thermodynamics of Computation: a Review. *Int J Theor Phys* (1982) 21:905–40. doi:10.1007/BF02084158
30. Shizume K. Heat Generation Required by Information Erasure. *Phys Rev E* (1995) 52:3495–9. doi:10.1103/PhysRevE.52.3495
31. Earman J, Norton JD. EXORCIST XIV: The Wrath of Maxwell's Demon. Part II. From Szilard to Landauer and beyond. *Stud Hist Philos Sci B: Stud Hist Philos Mod Phys* (1999) 30:1–40. doi:10.1016/S1355-2198(98)00026-4
32. Piechocinska B. Information Erasure. *Phys Rev A* (2000) 61:062314. doi:10.1103/PhysRevA.61.062314
33. Frank MP. The Physical Limits of Computing. *Comput Sci Eng* (2002) 4:16–26. doi:10.1109/5992.998637
34. Wang GM, Sevick EM, Mittag E, Searles DJ, Evans DJ. Experimental Demonstration of Violations of the Second Law of Thermodynamics for Small Systems and Short Time Scales. *Phys Rev Lett* (2002) 89:05060. doi:10.1103/PhysRevLett.89.050601
35. Bennett CH. Notes on Landauer's Principle, Reversible Computation and Maxwell's Demon. *Stud Hist Philos M P* (2002) 34:501–10. doi:10.1016/S1355-2198(03)00039-X
36. Maroney OJE. The (Absence of a) Relationship between Thermodynamic and Logical Reversibility. *Stud Hist Philos Sci Part B: Stud Hist Philos Mod Phys* (2005) 36:355–74. doi:10.1016/j.shpsb.2004.11.006
37. Norton JD. Eaters of the lotus: Landauer's Principle and the Return of Maxwell's Demon. *Stud Hist Philos Sci Part B: Stud Hist Philos Mod Phys* (2005) 36:375–411. doi:10.1016/j.shpsb.2004.12.002
38. Sagawa T, Ueda M. Minimal Energy Cost for Thermodynamic Information Processing: Measurement and Information Erasure. *Phys Rev Lett* (2009) 102:250602. doi:10.1103/PhysRevLett.102.250602
39. Dillenschneider R, Lutz E. Memory Erasure in Small Systems. *Phys Rev Lett* (2009) 102:210601. doi:10.1103/PhysRevLett.102.210601
40. Vaccaro JA, Barnett SM. Information Erasure without an Energy Cost. *Proc R Soc A* (2011) 467:1770–8. doi:10.1098/rspa.2010.0577
41. Pop E. Energy Dissipation and Transport in Nanoscale Devices. *Nano Res* (2010) 3:147–69. doi:10.1007/s12274-010-1019-z
42. Norton JD. Waiting for Landauer. *Stud Hist Philos Sci Part B: Stud Hist Philos Mod Phys* (2011) 42:184–98. doi:10.1016/J.SHPSB.2011.05.002
43. Bérut A, Arakelyan A, Petrosyan A, Ciliberto S, Dillenschneider R, Lutz E, et al. Experimental Verification of Landauer's Principle Linking Information and Thermodynamics. *Nature* (2012) 483:187–9. doi:10.1038/nature10872
44. Sagawa T. Thermodynamic and Logical Reversibilities Revisited. *J Stat Mech* (2014) 2014:P03025. doi:10.1088/1742-5468/2014/03/P03025
45. Jun Y, Gavrilov M, Bechhoefer J. High-Precision Test of Landauer's Principle in a Feedback Trap. *Phys Rev Lett* (2014) 113:190601. doi:10.1103/PhysRevLett.113.190601
46. Hong J, Lambson B, Dhuey S, Bokor J. Experimental Test of Landauer's Principle in Single-Bit Operations on Nanomagnetic Memory Bits. *Sci Adv* (2016) 2:e1501492. doi:10.1126/sciadv.1501492
47. Wolpert DH. The Stochastic Thermodynamics of Computation. *J Phys A: Math Theor* (2019) 52:193001. doi:10.1088/1751-8121/ab0850
48. Wang XS, Yuan HY, Wang XR. A Theory on Skyrmion Size. *Commun Phys* (2018) 1:31. doi:10.1038/s42005-018-0029-0
49. Wu H, Hu X, Jing K, Wang XR. Size and Profile of Skyrmions in Skyrmion Crystals. *Commun Phys* (2021) 4:210. doi:10.1038/s42005-021-00716-y
50. Wang XS, Wang XR. Thermodynamic Theory for thermal-gradient-driven Domain-wall Motion. *Phys Rev B* (2014) 90:014414. doi:10.1103/PhysRevB.90.014414
51. Selzer S, Atxitia U, Ritzmann U, Hinzke D, Nowak U. Inertia-Free Thermally Driven Domain-Wall Motion in Antiferromagnets. *Phys Rev Lett* (2016) 117:107201. doi:10.1103/PhysRevLett.117.107201
52. Simon F. On the Third Law of Thermodynamics. *Physica* (1937) 4:1089–96. doi:10.1016/s0031-8914(37)80205-0
53. Feistel R. Distinguishing between Clausius, Boltzmann and Pauling Entropies of Frozen Non-equilibrium States. *Entropy* (2019) 21:799. doi:10.3390/e21080799
54. Tomasello R, Guslienko KY, Ricci M, Giordano A, Barker J, Carpentieri M, et al. Origin of Temperature and Field Dependence of Magnetic Skyrmion Size in Ultrathin Nanodots. *Phys Rev B* (2018) 97:060402. doi:10.1103/physrevb.97.060402

Conflict of Interest: The author declares that the research was conducted in the absence of any commercial or financial relationships that could be construed as a potential conflict of interest.

Publisher's Note: All claims expressed in this article are solely those of the authors and do not necessarily represent those of their affiliated organizations, or those of the publisher, the editors, and the reviewers. Any product that may be evaluated in this article, or claim that may be made by its manufacturer, is not guaranteed or endorsed by the publisher.

Advantages of publishing in Frontiers

OPEN ACCESS
Articles are free to read for greatest visibility and readership

FAST PUBLICATION
Around 90 days from submission to decision

HIGH QUALITY PEER-REVIEW
Rigorous, collaborative, and constructive peer-review

TRANSPARENT PEER-REVIEW
Editors and reviewers acknowledged by name on published articles

Frontiers
Avenue du Tribunal-Fédéral 34
1005 Lausanne | Switzerland

Visit us: www.frontiersin.org
Contact us: frontiersin.org/about/contact

REPRODUCIBILITY OF RESEARCH
Support open data and methods to enhance research reproducibility

DIGITAL PUBLISHING
Articles designed for optimal readership across devices

FOLLOW US
@frontiersin

IMPACT METRICS
Advanced article metrics track visibility across digital media

EXTENSIVE PROMOTION
Marketing and promotion of impactful research

LOOP RESEARCH NETWORK
Our network increases your article's readership